DESIGN A NOVEL METHODOLOGY FOR THE GOAL-DIRECTED CONTROL OF EPITAXIAL GRAPHENE FABRICATION

A thesis submitted for the degree of Doctor of Philosophy

by

Nikolai Issakov

School of Engineering & Design
Brunel University

November 2013

DESIGN A NOVEL METHODOLOGY FOR THE GOAL-DIRECTED CONTROL OF EPITAXIAL GRAPHENE FABRICATION

by
Nikolai Issakov

Acknowledgements

My research was financially supported by Brunel University's EPSRC Doctoral Training Account from October 2007 to September 2010. I would like to thank the School of Engineering and Design and the UK Engineering and Physical Sciences Research Council (EPSRC) for their kind support during this period. My project was linked to the EPSRC-funded project with title "The Matter Compiler" (EP/F009801/1) and has been focused on the development of a process for scalable graphene fabrication. I conducted my research in the Multi-Scale Engineering Laboratory in the Advanced Manufacturing and Enterprise Engineering Division of the School of Engineering and Design in Brunel University London, under the supervision of Dr. Charalampos Makatsoris. Many people helped me to complete this thesis, firstly my supervisor, Dr. Charalampos Makatsoris. We spent a lot of time together from conception of the research to its design and execution. During our collaboration on the project he was for me a personification of enthusiasm and patience. I am extremely grateful for his support.

Secondly, I am grateful to the collective of The Advanced Manufacturing and Enterprise Engineering School who facilitated my adaptation to a new human environment. I express my sincere thanks to Dr. Leonid Paramonov for practical help and useful scientific discussions. Also, I am very pleased to thank my colleagues for their benevolent support and discussion of my results and reports during different meetings. I would also like to present my acknowledgement to everybody who in any event expressed to me their own goodwill throughout my stay in the University.

I express a particular gratitude to my first teacher, Ms. Nadejda Moskovtchenko, Professor Emeritus from The Russian Academy of Science, for believing in my capability and her useful advice.

Nikolai Issakov

Abstract

The elusive 2D carbon poly-type was argued more than 70 years ago. Meanwhile, the recent discovery of graphene has proved that such materials can indeed be obtained and are thermodynamically stable. Graphene has demonstrated the unique properties that lead to many innovations in laboratory conditions. However, the current approaches available for the industrial fabrication yield the low graphene quality against the theoretical predictions. Furthermore, any graphene combination with the supporting units causes a newly-induced quality for adaptation to the other condensed matters. Therefore, the unusual ability for sensitive alteration in the external world has turned into a regulation for intended graphene engineering.

The submitted investigation has been undertaken to elaborate a novel methodology for the goal-directed control of epitaxial graphene fabrication by using interaction design. This is the most perspective pathway to scale-up production of intended quality subjected to the manufacturing of novel carbide derived carbon (CDC) patterns via interaction with specific substrates under hydrogen halides impact. The graphene layers and structural arrangement of the composite systems, as well as their electronic properties depend on the particular substrate, coherent commensuration of the adjacent units, interaction between them and the physical environment of fabrication. It is crucial to understand the interaction processes leading to stable construction. Density Functional Theory (DFT) implemented in the CASTEP system has been employed in this research in order to develop this knowledge and also to determine how to tune and engineer the band gaps of such composite assemblies.

The substrate alternating reconstructions, polarity of surface terminations, commensuration and number of layers, their stacking order and distances between constituting units are taken into consideration for intended simulation. The (3×3) and $\left(\sqrt{3}\times\sqrt{3}\right)R30°$ reconstructions of 4H-*SiC* poly-type are the starting points for epitaxial growth (EG) on the *Si*-face and *C*-face unit cells. The results of the substrate induced interaction are interpreted via the versatility of band states gradually traced from the dehydrogenated *SiC* framework to CDC bi-layer. The distinctive feature resulted from the substrate influence is kept as the transitional band for different arrangements and locations in vicinity of the Fermi level. The first buffering *C*-plane reinforces substrate distinctions between the initial configurations and polarities. The *n*-type of gap state is the characteristic of the *Si*-face termination, whereas, the *p*-type is found for the *C*-face case. Both structures are devoid of the freestanding graphene signs. The appropriate indications of dominant graphene identity are found for the (0001) - $\left(\sqrt{3}\times\sqrt{3}\right)R30°$ substrate only, at a close distance between two upper *C*-planes acceptable for covalent bonds.

As for graphene EG the chemical conversion by using fluorination is employed to avoid the possible damage inspired by initial substrate roughness. The few layered CDC assemblage on the (0001) - $\left(\sqrt{3}\times\sqrt{3}\right)R30°$ support is trailed via gradual $Si-F$ interaction and SiF_x groups penetrating through the bulk. Regular control over potential energy surfaces, minimal energy pathways, transition states and activation barriers enable the indicative indexes for reaction credibility and progress. By means of the Arrhenius equation using the activation energy values the average temperature of 1500 - 2000℃ are predicted for the real conversion events. Under these conditions the wet surface etching for the topmost *Si*-atoms and release of oxidised CDC are accompanied with a complementary promotion mechanism which resulted in a highly ordered graphene structure.

CONTENT:

Chapter 5. THEORETICAL BASIS

Chapter 6. SIMULATION AND COMPUTATIONAL DESIGN OF CDC SYSTEMS

Chapter 7. DETERMINATION OF ELECTRONIC STATES

Chapter 8. SURFACE CONVERSION UNDER *HF* IMPACT

List of Figures:

List of Abbreviations:

AB – Bernal-Stacking Order;
AFM – Atomic Force Microscopy;
AO – Atomic Orbital;
BL – Bi-layer;
BP – Barrier from Product;
BR – Barrier from Reactant (Activation Energy);
BS – Band Structure;
BZ – Brillouin Zone;
CDC – Carbide Derived Carbon;
CM-AFM – Contact Mode of AFM;
CVD – Chemical Vapor Deposition;
2D – Two Dimensional;
3D – Three Dimensional;
DFT – Density Functional Theory;
DMS – Diamond Mechanosynthesis;
DOS – Density of State;
DPN – Dip Pen Nanolithography;
EG – Epitaxial Growth;
ER – Energy of Reaction;
FL – Few-layer;
FLG – Few-layered Graphene;
FM-AFM – Force Mode of AFM;
GGA – Generalised Gradient Approximation;
GS – Gap State;
HF – Hartree-Fock;
IRC – Intrinsic Reaction Coordinate;
KS – Kohn-Sham;
LDA – Local Density Approximation;
LO – Local Oxidation;
LPE – Liquid Phase Epitaxy;
LST – Linear Synchronous Transit;
MBB – Molecular Building Blocks;
MBE – Molecular Beam Epitaxy;
MD – Molecular Dynamics;
MEP – Minimum Energy Path;
ML – Monolayer;
MO – Molecular Orbital;
MP – Monkhorst-Pack;
MWNT – Multi-Walled Nanotube;
NC-AFM – Non-Contact Mode of AFM;
PES – Potential Energy Surface;
PA – Pseudopotential Approximation;
PW – Plane Wave;
PWP – Plane Wave Pseudopotential;
QST – Quadratic Synchronous Transit;
RA – Retrosynthetic Analysis;

SPM – Scanning Probe Microscopy;
STM – Scanning Tunnelling Microscopy;
SPML – Scanning Probe Microscopy Lithography;
SWNT – Single-Walled Nanotube;
TM – Transform Materials;
TM-AFM – Tapping Mode of AFM;
TS – Transition State;
TST – Transition State Theory;
UHV – Ultra-High Vacuum.

Chapter 1 Introduction

1. 1 Research subject and rationale

The materials of the carbon group including the different dimensional allotropes of various properties (Fig. 1.1) – 3D crystalline diamond and graphite, 1D nano-tubes and 0D fullerenes – are a significant manufacturing requirement.

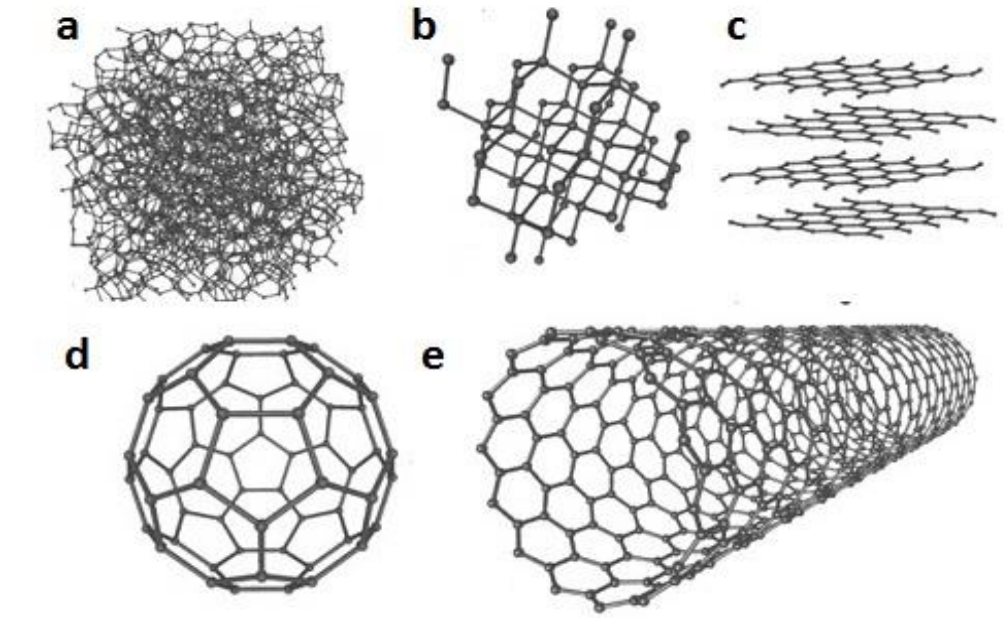

Figure 1. 1. The main allotropes of carbon materials: a) Amorphous carbon, Crystalline carbon; b) Diamond; c) Graphite; d) C_{60} buckyball; e) Single-walled nano-tube (General Chemistry, Chapter 11, Prentice Hall, 2007).

Carbon – carbon bonds are especially strong and used for a wide range of nano-manufacturing. Along with the multiple interests in advanced carbon composites, the accessibility of the elusive 2D dimension poly-type – graphene has been argued against since the mid-1930s. The atomically single 2D structures were assessed only as the upper part of 3D crystal lattice (Peierls, 1935; Landau, 1937; Mermin, 1968) and deemed to be thermodynamically unstable. After the detailed arguments against its independent existence, real graphene was recently discovered (Novoselov et al., 2004, 2005, 2007; Geim and Novoselov, 2007), and has nowadays turned into a subject of high priority for molecular compilation. This discovery triggered an avalanche of scientific research comparable with a “gold rush”. The numerous theoretical and experimental investigations are especially concerned with the novel properties, advanced routes of synthesis and assembly fabrication

(Berger et al., 2004, 2006; Novoselov et al., 2005; Hass et al., 2006, 2008; Rollings et al., 2006; Schniepp et al., 2006; Stankovich et al., 2006, 2007; Geim and MacDonald, 2007; Katsnelson, 2007; Miao et al., 2007; Pisana et al., 2007; Stolyarova et al., 2007; Andres et al., 2008; Freitag, 2008; Morozov et al., 2008; Seyller et al., 2008; Hibino et al., 2009; Magaud et al., 2009; Hofrichter et al., 2010; Nair et al., 2010; Sprinkle et al., 2010; Heer et al., 2011; Kuroda et al., 2011; Presser et al., 2011; Novoselov et al., 2012).

Graphene is a giant aromatic macromolecule of covalently bonded carbon atoms arranged into a 2D honeycomb crystalline lattice of specific electron configuration (Novoselov et al., 2005; Geim and MacDonald, 2007; Katsnelson, 2007; Pisana et al., 2007; Freitag, 2008). As regards the atomically single 2D structures, the moving electrons that are confined in two dimensions behave like mass-less relativistic particles while causing exceptional physical qualities and behaviour. The long-range hopping processes result in graphene's unique electronic properties interpreted by using the nearest-neighbour tight-binding approximation. The ballistic transport under the large electron free path, giant charge carrier mobility, the superior conductivity, tuneable electronic capacity, control on electron spin, etc. promise a great breakthrough in the fields of electronics and medicine.

With a view to developing graphene-based manufacturing, some advancement in scale-up production, patterning and tailoring technology, fabrication of building blocks and settling into designed systems proved to be immediate industrial tasks (Berger et al., 2004, 2006; Hass et al., 2006, 2008; Stankovich et al., 2006, 2007; Miao et al., 2007; Stolyarova et al., 2007; Andres et al., 2008; Morozov et al., 2008; Seyller et al., 2008; Hibino et al., 2009; Nair et al., 2010; Kuroda et al., 2011). These requirements consider graphene in combination with other condensed materials that should be elaborated on the basis of graphene mutability in the external environment. It is already known that graphene qualities are sensitively changed under general external factors. In particular, very strong alterations occur under the influence of substrate induced interactions. Moreover, any practical applications require proper graphene adjustment with the other condensed materials. The electronic properties also change as a layer number runs from the basal plane to 3D. Thus, the unusual graphene alterations proved to be a critical confinement for manufacturing aims. All of these concern both graphene synthesis and fabrication.

The reliable routes for a scale-up production have long been considered an important problem (Rollings et al., 2006; Schniepp et al., 2006; Magaud et al., 2009; Hofrichter et al., 2010; Sprinkle et al., 2010; Heer et al., 2011; Presser et al., 2011; Novoselov et al., 2012). It is still a great challenge to produce large quantities of high quality because graphene sheets have a strong tendency for alteration, while growth depends on the surrounding environment, arrangement and number of layers. The industrial demands are satisfied at the expense of epitaxial growth (EG) – a very sensitive process as regards the physical and chemical conditions. Therefore, the priority of research has gradually moved towards epitaxial graphene evolving in combination together with the other solids without structural rearrangement. The composite graphene assemblies alternating in dependence on design features and processing methods are considered as a worthy subject for updated manufacturing aims. The tendencies of graphene behaviour under variable external conditions emerge as the key factors for directed control over the most reproducible films. The new data on mutability and the development of foliated composite assemblies are considered as a theoretical basis for the most advanced and steady growth of high quality epitaxial graphene.

1. 2 Aim and objectives

The current research is intended for the improvement of scale-up and qualitative graphene acceptable for high performance manufacturing. The **ultimate aim** is directed to the elaboration of a novel methodology for new epitaxial graphene fabrication, which is potentially scalable, by using graphene mutability tendencies in dependence on external environment influences and fabrication methods. The key-factors of goal-directed control over intended properties are explored as a consequence from graphene alteration in the external environment. The investigation undertaken examines this unique mutability and adaptation of graphene to the external environment resulting from substrate induced interaction and chemical environmental conditions. The stepwise epitaxial processes of carbide derived carbon (CDC) growth on 4H-*SiC* substrate are studied by means of computational design on the basis of DFT first principles calculations. As a result, the novel pathway to graphene epitaxial growth via *SiC* chemical conversion and selective material removal is performed. The relevant research subject, rationale and justification are

presented in Chapter 1, “Introduction”, formulating the general graphene database and topical principles taken into account for the investigation undertaken.

The subsequent **particular objectives** of this work are elaborated to be the key-factors subordinated to directed regulation for intended graphene fabrication via interaction design of graphene composite patterns.

1. The useful information and knowledge concerning the updated approach as regards the advanced molecular compilation are collected in Chapter 2, “Review of molecular compilation”. This topical review and literature data – concerning the physical and chemical methods of molecular compilation for nano-scaled investigations; the general principles of mechanical chemistry and self-organisation; procedures for atomically precise manufacture and surface modifications; relevant technics, processing and tools; some achievements of molecular architecture, perspective nano-materials, etc. – is intended to ensure the proper approaches and preconditions acceptable for the investigations undertaken.
2. In order to outline graphene topical database and challenges, a purposive roadmap is drawn up and presented in Chapter 3, “The rise of graphene”. The history of graphene discovery, its atomic and physical properties, advanced routes to synthesis and fabrication, industrial application and perspective potentiality for production are overviewed in anticipation of expanding graphene application and market.
3. The available technics and capability resulting from the surface transformation of solid substrate as regards the EG processes and release of CDC are presented in Chapter 4, “Surface engineering of *SiC* substrates”. Two contrasting approaches to graphene epitaxial growth via CDC advanced synthesis are considered through the material deposition (CVD) and material removal via thermal and chemical conversions.
4. A generalised resume from the fundamental quantum mechanics laws provides the theoretical basis for analysis and elaboration of CDC systems (Chapter 5). The “Theoretical basis” is devoted to the solution of electron interactions in a many-body system by means of the DFT first principles calculations.

5. Simulations of many-layered composite patterns to reveal the alteration of graphene qualities during successive epitaxial growth on alternating structural modifications of supporting 4H-*SiC* substrate are considered in Chapter 6. The "Simulation and computational design of CDC systems" examines the successive simulation of many-layered assemblies of two CDC planes on alternating 4H-*SiC* substrate surfaces.
6. The influence of substrate induced interaction as the increasing number of carbon layers and thickness of designed construction is considered in Chapter 7. The "Determination of electronic states" considers a divergent alteration of electronic states during gradual growth of few-layered systems.
7. Elaboration of a novel pathway to carbide derived carbon resulted from self-organisation transformations under substrate chemical conversion in *HF* medium at an elevated temperature is considered in Chapter 8. The "Surface conversion under *HF* impact" is subjected to CDC epitaxial growth under *HF* etching. Dynamics of *Si – F* interaction as penetration into the deeper bi-layers is analysed through the transition states, energy of reaction, activation energy and barrier from product values.
8. Estimation of real physical conditions for *Si – F* interaction, removal of SiF_4 volatile phase, oxidation of *C*-atoms, analysis of energy dispersion for promotion from amorphous carbon into highly ordered graphene structure – all of these are discussed in Chapter 9. The "Stable epitaxial graphene via 4H-*SiC* chemical conversion" considers kinetics and physical conditions calculated on the basis of Arrhenius equation for the real process of CDC chemical growth. The driving mechanism of promotion into highly ordered graphene structure is shown.

1. 3 Methodology of current research

The exploration undertaken is realised through the interaction design of the few-layered graphene composite systems and operations for their epitaxial growth by means of the 4H-*SiC* substrate surface conversion, as follows:

(1) Computational design of composite assemblies alternating under substrate induced interaction and regular adjustment of constituting units is initiated to reveal graphene mutability during stepwise chemical conversion. The few-layered CDC patterns of systematic study are composed on the

variable supporting frameworks grown under standard Bernal (AB) stacking order. Two general contrast reconstructions of 4H-*SiC* poly-type of both polar *Si*-face and *C*-face terminations are chosen to be the initial points. The framework is grown on the top by succeeding CDC planes without structural reorientation. Thus, the systems under consideration are composed for the variable supporting materials, commensurations and adjustment of constituting units stacked in the standard Bernal stacking order.

(2) Arrangements and distances for the constituting layers are chosen to hold the strong covalent bonds between substrate and buffering graphene monolayer (ML). Elastic commensuration of adjacent crystalline lattices and slight distortion of flattened graphene ML are admitted above a little warped *SiC* surface. For remote layers only the Van der Waals forces are taken into account.

(3) At every stage of conversion the electronic structures are determined by means of the CASTEP code elaborated on the basis of DFT first principles calculations. By using the DFT first principles calculations the resulting changeable electronic structures are recognised for every calculation step to be criteria for proximity to graphene quality and for mutability of evolving a multisystem as a whole.

(4) The epitaxial growth under halogenations via *SiC* unit cells interaction with *HF* is traced and tested on three different *SiC* bi-layers. The driving mechanism and dynamics of chemical conversion under penetrating *Si – F* interaction are interpreted through the advanced transition states and activation energy values. The revealed transition states gradually propagated into the substrate depth are used to verify reaction feasibility and estimate the real kinetics and temperature of the chemical process. The temperature conditions for real CDC formation are found for all three substrate bi-layers by using Arrhenius equation.

(5) The complementary mechanism for promotion of amorphous carbon into highly ordered graphene structure is estimated and investigated by using TST at every calculation step of this self-organisation process.

Thus, the novel way to improved graphene structures is elaborated in terms of the surface chemistry methods.

1. 4 Key contributions

As a result of this investigation, it was shown that at least three groups of general factors for quality regulation are significant for intended graphene engineering.

- The composite factors admit a variable substrate induced interaction and the influence of intervening intercalation. Especially interesting effects are referred to by applications of carbides and metals of hexagonal symmetry as well as combination with the novel 2D materials (Novoselov et al., 2012).
- The structural factors mean geometric specification of designed many-layered assemblies. Their electronic properties will sensitively change in dependence on the number and structural arrangement of carbon layers, adjustment distances and stacking order of constituting units.
- The environmental factors are concerned with external conditions and medium during graphene production. The tuning of chemically functionalised systems may be realised via regulation of medium parameters, including temperature values, gaseous environment, using of halogenations, doping and catalytic surfactants.

This investigation results in test and trace of these mutability factors with respect to an experimentally advanced model of epitaxial graphene grown on the *SiC* substrate. The following tenets are considered as the new defended assertions:

1. Alternatives to divergent assemblies of variable proximity to graphene quality are capable of control depending on substrate induced interaction, number, distance and adjustment of constituting units.
2. Substrate influence forcing the strong covalent bonds and mixed properties in interface gives up to dominant graphene identity for many-layered systems as gradual epitaxial growth in progress.
3. The driving mechanism and dynamics of chemical conversion via *HF* etching are restored through the trace of advanced transition states.
4. The irreversible trend for penetrating process via *Si – F* interaction is found.
5. The temperature conditions for real CDC formation are found by using the activation energy values.

6. The complementary mechanism for CDC promotion into highly ordered graphene structure is revealed via the calculation steps of this self-assembly event.
7. The novel pathway to graphene growth is based on the mutual processes of surface chemistry including the material deposition and material removal.

As a summary, the submitted work elaborates the novel design for epitaxial graphene fabrication via 4H-*SiC* substrate induced interaction in halogenated environment.

Chapter 2 Review of molecular compilation

2. 1 Background

Whereas there has been a long history of sporadic knowledge concerning small-size phenomena, regular experiences have given rise to nanotechnology as a new independent science. On the threshold of intended research, this topical review presents the principal advancements regarding molecular compilation and nanotechnology.

General ideas and concepts of nanotechnology can be traced back to Michael Faraday's experiments. He was the first to reveal that the matter on a micro-level dimension acquires properties unusual for the bulk (Faraday, 1857). Also, in the kinetic theory of gases, J. C. Maxwell formulated the concept of "finite being": the tiny pieces move at a specified high velocity owing to the small mass and the above average kinetic energy (Maxwell, 1867–1868). The idea of "neglected dimensions" and gradual transition between molecular and colloidal states was associated with the advent of colloidal science (Ostwald, 1907, 1915). The first observations and size measurements of nano-particles are associated with Zsigmondy, who studied gold sols in detail and other materials with sizes 10 nm and less (Zsigmondy, 1914).

By the 1950s the explorations became more systematic. The colloidal metal suspensions and the small metal particles became a subject of great importance because of the special behaviour in the intermediate between pure solutions and emulsions. The ability to operate with the individual atoms by means of precise tools was, in this period, firstly considered (Feynman, 1959). The new term "nanotechnology" (Taniguchi, 1974) was introduced to describe the development of materials up to the size of 100 nm. Eventually, the technological significance of the nano-scale phenomena was recognised.

Since the 1980s, the systematic investigations for molecular manufacturing have advanced on the basis of different approaches and methods. Scientific conceptions and experiments are directed towards the synthesis and properties of the metal particles as a transition from the bulk through the domains of intermediate quantum size effects to the molecules and clusters. Reproduced Faraday experiments (Thomas, 1988) showed that the gold sols contain particles of 3 – 30 nm in diameter known as "nano-particles". The earlier researches were conducted in the area of

colloidal chemistry. The experience of the nucleation, growth and agglomeration allowed the preparation of sols with narrow particle size distribution and mean size of 20 nm. The small sizes were achieved by restriction of growth by using either the kinetic factor or ligands for surface stabilisation and reducing particle dimension. There were many studies of periodic colloidal structures and principles of self-assembly (Yuan et al., 1992; Sankaran et al., 1993; Bradley, 1994; Brust et al., 1994; Schmid, 1994; Muller et al., 1995; Kung and Ko, 1996; Martin et al., 2004, 2007; Pauliac-Vaujour and Moriarty, 2007; Siepmann et al., 2007). The growth from clusters of few metal atoms up to colloids with thousands of atoms stimulated progress in organometallic chemistry developed into the area of interdisciplinary science.

Another route of wet chemistry based on the catalytic effects resulted in surface-anchored nano-particles and clusters on a solid substrate (Haruta et al., 1989, 1993; Sugawara et al., 1995; Hayashi et al., 1996; Haruta, 1997, 2001; Gacoin et al., 1997; Kiely et al., 1998; Teranishi and Miyake, 1998; Teranishi et al., 1998, 2000, 2001, 2002; Hoffmann et al., 2001; Meusel et al., 2001; Wang R. et al., 2001; Giorgi et al., 2002). A great new approach to nano-scaled compilation is developed through directed control over precise atomic position by using advanced scanning techniques (Drexler, 1981, 1991, 1992, 1994; Farrell and Levinson, 1985; Gomer, 1986; Merkle, 1993, 1997, 2000; Walch and Merkle, 1998; Merkle and Freitas, 2003; Temelso et al., 2006, 2007).

2. 2 Recent advance in nano-structures

From the beginning, the major approaches to nano-particle synthesis were concentrated around two areas: physical and chemical routes. The general requirements for update nano-materials are as follows: control for the sizes and compositions of nano-scale components, whether they are aerosol particles or powders or products of sol-gel processing; control for the characteristics of particle size distributions and structure of interface within the fully formed products; the chemical and thermal stability of formed structures; the ability for scale-up synthesis.

2. 2. 1 Physical methods

The methods of gas phase evaporation and condensation were the best concerning mono-dispersion size (Gleiter, 1989; Siegel, 1991; Murray et al., 1993). As a

development of these methods, the various aerosol techniques were worked out to produce the high yields including the synthesis by flame combustion, laser ablation, spray pyrolysis, plasma spray and electro spray. Gas synthesis has a low production rate. The typical rate of process is about 100 mg per hour. A higher rate of about 1 kg per hour was recently developed. The aerosol technology fits the large-scale production. It allows the formation of nano-particles below 20 nm in diameter with narrow particle size distribution (Murray et al., 1993). The particles may be deposited on any substrate by means of electric field and under very high temperature, over 1500°C. By means of thermal decomposition the nano-particles of gold, silver, tungsten, gallium, lead and indium were deposited by evaporation of volatile component or by cracking of metals (Leslie-Pelecky et al., 1996; Sunstrom et al., 1996; Suslick et al., 1996; Deppert et al., 1998; Magnusson et al., 1999, 2000; Bovin et al., 2000).

In the course of time, some other physical methods were developed, e.g. the methods of ion implantation, electron-beam evaporation, pulsed laser vaporisation with controlled condensation under the well-defined conditions of temperature and pressure. Some mixed routes of synthesis include the cavitation processing, micro-emulsion method and method of high-energy ball milling. The cavitation processing with generation of local zone of extremely high gradients of temperature and pressure can assist the destruction of introduced organometallic solution (Suslick et al., 1996). In a hydrodynamic cavitation the particles are formed by creation of released gas bubbles inside sol-gel solutions. The bubbles are responsible for the nucleation and growth of nano-particles that are generated under rapid increase of the pressure in a drying chamber (Sunstrom et al., 1996). The sizes of particles are mostly controlled by pressure in this chamber. Another method uses the low interfacial tension in the micro-emulsions. This method involves the addition of a surfactant, e.g. alcohol (Higgins, 1997). As a result, the micro-emulsions can spontaneously produce the nano-particles with no additional mechanical procedure.

The method of high energy ball milling was used for the structural nano-particles (Koch C., 1989), the magnetic (Leslie-Pelecky and Reike, 1996) and the catalytic ones (Ying and Sun, 1997). This technique, which is already a commercial technology, is considered as dirty because of contamination problems in ball milling processes. However, increase of synthesis is of great importance. This is why the route of high energy ball milling may be regarded as a commercial high volume

process that enables the generation of nano-particles for magnetic and catalytic materials.

2. 2. 2 Colloidal chemistry

Development of chemical nano-synthesis started in the area of colloidal and organometallic chemistry. The different methods for preparation of colloidal metals were elaborated. This knowledge enables the reproducible preparation of sols with narrow particle size distribution (Turkevich, 1985). The small sizes were achieved by restriction of growth while depressing the dimensions of particles. The most challenging problems were concerned with control for generation of the finest and most mono-dispersed nano-particles. Sol-gel processing enables the production of the highly mono-dispersed colloidal nano-particles with sizes about 1 nm (Kung and Ko, 1996). However, in this case, the specific chemical control is required. The sizes and character of distribution are manipulated by means of either introduction of the chemicals (Kyprianidou - Leodidou et al., 1994) or change of the physical conditions (Wang C. et al., 1997). Small size and stability are achieved by addition of inverted micelles, polymer blends, ligands and porous glasses. There are a large number of organic compounds that may be used. The right choice enables preparation of fine nano-particles, which are not only coated and protected, but may also be combined with other chemical compounds. The effects of this chemical control were expanded by some experiments with the finest *Pt, Pd* and *Au* particles and clusters (Yuan et al., 1992; Sankaran et al., 1993; Gacoin et al., 1997).

2. 2. 3 Progress in mechanical chemistry

The atomically controlled synthesis under the influence of mechanical energy is nowadays the most advanced branch of nano-manufacturing based on the principles of mechanical chemistry (Farrell and Levinson, 1985; Gomer, 1986; Foster and Frommer, 1988; Miller and Drexler, 1988; Eigler and Schweizer, 1990; Drexler and Foster, 1990; Drexler, 1991, 1992). The reactions directed towards precise arrangement of atoms and molecules in the desired order on the solids are carried out by the SPM modes due to the energy dissipation from the tool-tip as it approaches solid surface. The covalent and ionic chemical bonds are formed by means of the mechanical forces precisely applied to the solids. Vertical or lateral manipulation involves holding atoms, molecules and growing surface of target work-piece. These two components should be located in the proper relative positions and coupled

together in the desired manner. The mechanical synthesis is intended for creation of molecular building blocks for future micro devices. The direct control methods are generally aimed at the old bonds breaking, existing atoms removal and precise vacancy occupation with the new atoms. The lateral and vertical manipulations of single atoms or molecules let usually form the nanostructures with the covalent or ionic chemical bonds. The most crucial factors in the course of atom manipulations are the following:

– vibration and excitation of ad-atom/substrate bond;

– tip/ad-atom interaction.

The vibration can raise the atom closer to the activation barrier for transfer between the sites. The latter factor affects the surface and controls the atom dynamics. The new bonds are formed by means of external mechanical force.

The operations for similar transformations are determined as the “Pick and Place” reactions. Two fundamental requirements are characteristics of this approach. The first is concerned with the feedstock of atoms, molecules and molecular pieces that are considered as the ready molecular building blocks for mechanical fabrication. The most attractive materials for these aims are diamond and diamond-like structures. The second necessary requirement concerns the special positional devices that allow adjoining the different mechanical parts in assembles. The tip-driving synthesis by means of mechanical manipulation affords the new possibility where direct attack is able to protect the sensitive functional groups.

2. 3 Control of molecular assembly

Molecular compilation of complex intended product is usually unrealistic during one act event and might be realised by means of the multi-stage transformations as a succession of easy operations that are in total accordance with the physical laws. The main approaches to molecular compilations are nowadays performed in terms of either the self-assembly processes or by means of the precise positional control. These approaches may be based on the different operations.

The self-assembly approach arose in the field of colloidal and organometallic chemistry (Yuan et al., 1992; Sankaran et al., 1993; Bradley, 1994; Brust et al., 1994; Schmid, 1994; Muller et al., 1995; Kung and Ko, 1996; Martin C. et al., 2004, 2007; Pauliac-Vaujour and Moriarty, 2007; Siepmann et al., 2007). A processing involves gelation, precipitation, thermal treatment and adding a wide range of reducing

agents. The best strategy is concerned with the reduction of metal salts in solution isolated in a solid state by the protecting ligands. The serious disadvantages are caused by poor product safety because of its decomposition after reactions.

The other pathway of self-organisation is approved by using the catalytic effects under crystallisation and epitaxial growth on the solid substrates**.** The wet chemistry methods can produce assemblies of surface-anchored particles and clusters. The mechanism implies a deposition on the solids due to surface effects. This method allows the various highly ordered arrays patterned in dependence on the interface structures and binding energy between nano-particles and supporting materials (Haruta et al., 1989, 1993; Sugawara et al., 1995; Hayashi et al., 1996; Haruta, 1997, 2001; Gacoin et al., 1997; Kiely et al., 1998; Teranishi and Miyake, 1998; Teranishi et al., 1998, 2000, 2001, 2002; Hoffmann et al., 2001; Meusel et al., 2001; Wang R. et al., 2001; Giorgi et al., 2002).

The positional assembly and directly precise control over atoms allow the synthesis of a much wider range of nanostructures. Many atomic arrangements are either difficult or impossible to produce by means of self-assembly methods alone. Contrariwise, the positional assembly is a new approach for the wide range of nano-materials. The foundations of mechanical synthesis are supported by the relevant theoretical studies and calculations (Drexler, 1981, 1991, 1992, 1994; Farrell and Levinson, 1985; Gomer, 1986; Merkle, 1993, 1997, 2000; Walch and Merkle, 1998; Merkle and Freitas, 2003; Temelso et al., 2006, 2007). The direct manipulations on the solids are based on the general principles of mechanical chemistry using mechanical energy, pulling, pushing, replacement of atoms and molecules for atomically precise fabrication of metallic, dielectric, organic, etc. nanostructures on different surface (Farrell and Levinson, 1985; Eigler and Schweizer, 1990; Drexler, 1991, 1992).

The great progress in this area became possible by using the scanning probe microscopy (Lyo and Avouris, 1991; Strocio and Eigler, 1991; Aono et al., 1993; Salling and Lagally, 1994; Avouris, 1995; Meyer et al., 1995; Jung et al., 1996; Meyer and Rieder, 1997; Bartels et al., 1997; Stipe et al., 1997, 1998; Dujardin et al., 1998; Hla and Rieder, 2002, 2003; Stroscio and Celotta, 2004). The technique for these manipulations was observed in detail (Hla and Rieder, 2002, 2003). Tunnelling electrons from the tip were used to induce reversible rotation. The displacements were determined as a function of current, bias voltage and lateral distance from the

tip (Stipe et al., 1997, 1998). Direct position control by using the AFM was theoretically elaborated at the beginning of the 1990s (Meyer and Amer, 1988) and demonstrated for the different surfaces: e.g. for $Si\ (111) - (7 \times 7)$ surface (Giessibl, 1995), *InP* (110) surface (Sugawara et al., 1995), *Ag* (111) surface (Orisaka et al., 1999), *Cu* (111), (100) surfaces (Loppacher et al., 2000). The vertical manipulations by means of soft indentation on $Si\ (111) - (7 \times 7)$ was implemented under UHV and 78°K (Oyabu et al., 2003, 2006) and under room temperature (Sugimoto et al., 2005, 2007, 2008).

2. 3. 1 Self-assembly routes

This approach gives us many highly ordered arrays from the gas, colloidal and catalytic systems. Among these forms, there are nano-cubes, nano-tubes and hollow structures that were developed in the field of colloidal and organometallic chemistry. The different methods for the preparation of colloidal metals and synthesis were elaborated (Yuan et al., 1992; Sankaran et al., 1993; Bradley, 1994; Brust et al., 1994; Schmid, 1994; Muller et al., 1995; Kung and Ko, 1996; Martin C. et al., 2004, 2007; Pauliac-Vaujour and Moriarty, 2007; Siepmann et al., 2007) and applied to industry aims (Haruta et al., 1989, 1993; Sugawara et al., 1995; Hayashi et al., 1996; Haruta, 1997, 2001; Gacoin et al., 1997; Kiely et al., 1998; Teranishi and Miyake, 1998; Teranishi et al., 1998, 2000, 2001, 2002; Hoffmann et al., 2001; Meusel et al., 2001; Wang R. et al., 2001; Giorgi et al., 2002).

Sol-gel processing was the main route to nano-particle synthesis. The best strategy to generate uniform nano-particles is concerned with the reduction of metal salts in solution. Chemically prepared metal colloids are stable only in the solution, protected by the solvent molecules preventing coagulation. To isolate them in the solid state, the different ways of stabilisation are used, including so-called protecting ligands. The colloids and clusters stabilised by ligand do not have the same properties as the particles without protecting ligand. For example, the easiest procedure for preparation of the gold colloids involves the dissolution of gold salt in a solvent mixture with the added organic acids. This mixture is treated with the sulphur compounds and additional chemicals that convert the gold from the solution into the metallic state. The sulphur ligands form the envelope surrounding the particles and act as a protective coating. All these prevent the nano-particles from sticking to each other, i.e. the normal process that would take place in the absence of

the sulphur component. Among the various chemical methods, there is the reduction of aqueous solutions by citric acid, sodium citrate, *NaSCN, KSCN* and the reduction in aqueous solution. Aqueous and alcohol solutions are mixed with polymers, ligands, with various surfactants containing cyano (-*CN*) and mercapto (-*SH*) groups. Hydrazine hydrate may also be used for the colloidal *Au, Pt, Cu* particles and for the *Pd/Pt* alloy. Decomposition by the reducing agents results in nano-particles in the range from few to hundreds of nanometres, sometimes even smaller than two nanometres. Sol-gel processing, including gelation, precipitation, thermal treatment, adding a wide range of reducing agents, enables the generation of particles for various elements. The sizes and dispersion are controlled by the reaction conditions. By means of certain ligands, the surface of particles may be protected. Subsequently, the samples may be dried and re-dissolved again without any changes of material properties (Van Rheenen et al., 1987; Ishizuka et al., 1992; Schmid, 1994; Bradley, 1994; Brust et al., 1994; Badia et al., 1997; Teranishi et al., 1998, 2000; Wang R. et al., 2001).

The regular motifs in the self-organised nano-assemblies are very susceptible to change of physical and chemical conditions. Hence, the 2D patterns were recently formed from the colloidal *Au* nano-particles adsorbed on the hydrogen passivated *Si* (111) surface under direct modification of solvent dynamics (Zareie et al., 2003; Martin C. et al., 2004, 2007; Blunt et al., 2007; Siepmann et al., 2007; Pauliac-Vaujour and Moriarty, 2007). In dependence on the experimental conditions, *Au* nano-particles formed the most typical patterns: the isolated islands, labyrinthine, cellular and worm like networks. The simulations were programmed to be stochastic processes and resulted in random events. Nevertheless, the patterns preliminary described in terms of the Monte Carlo code proved to be in good agreement with the experimental validation. It was shown that the distribution of nano-particles in the interface area and the patterns on the nano-structured surface are non-random. We are able, therefore, to suppose the possible mechanisms for self-assembly. At the beginning of the colloidal dewetting under defined temperature, the vapour volatility, the balance of interfacial energy and viscosity and the specific nucleation rate result in a certain number of events per unit area and per unit time. As a consequence, the vapour bubbles are clustered within some areas, though in other areas there is no nucleation. In time, as vapour bubbles expand, the nucleation rate rapidly decreases, whereas the holes are enlarged. This implies that the nucleation events may only take

place within the limited time interval. Nucleation occurs near the frontiers of vapour bubbles that coincide with each other. A cellular structure is envisaged as the most regular result of these events. The morphology and image of final nanostructure are considered to be in strong dependence on the solvent vapour pressure, the particle concentration and interaction with substrate determining the particle mobility (Martin C. et al., 2004).

Although the sol-gel processing produces the particles and clusters with intended sizes and properties, this mode has some serious disadvantages caused by the decomposition of nano-particles in solution after reactions and the problems of product safety. This is why the other wet chemical methods based on the surface effects and crystallisation of metal nano-particles on the solid substrates were examined**.** The wet chemistry methods may produce the assemblies of surface-anchored nano-particles and clusters. The surface-anchored *Au* nano-particles and clusters were produced by the crystallisation on the surfaces of both insulator (sapphire (0001)) and conductor (titanium oxide (110)). It was implemented under elevating temperature from 200°C up to 850°C and more after treatment of the samples with $HAuCl_4$ solutions of different concentrations, *pH* and solvents. By analogy with the dewetting of colloidal solutions, the crystallisation of surface-anchored *Au* nano-particles proved to be in strong dependence on the structure of solids, temperature, *pH* and type of solvent. The surface-anchored *Au* nano-particles turned into the main objects of appropriate explorations with the aim of novel catalysts (Haruta et al., 1989, 1993; Haruta, 1997, 2001; Horvath et al., 2000). Gold at the bulk is too poor as a catalyst. However, dispersed on the solid substrate as *Au* nano-particles, it possesses the unique catalytic properties. The catalysts supported by the finest and highly dispersed nano-particles of 1-5 nanometres are active at very low temperature. Thus, *CO* oxidation occurs at T = – 70°C. Some gold catalysts demonstrate a high selectivity for partial oxidation reactions. Oxidation of propylene to propylene oxide occurs with 100% selectivity at 50°C, whereas the experiments with *Pd* and *Pt* catalysts show no propylene oxide yields, but only about 100% conversion to propane. The use of sputtered gold or gold colloids deposited on the transition metal oxides may produce the surfaces with selective adsorption of H_2 and *CO* gases.

The study of surface effects methods was stimulated by the recent discoveries of nano-scale materials catalytic properties. Surface-anchored mechanisms imply the

process of transition metals depositions on the solids due to the surface phenomena. The relevant crystallisation under different physical and chemical conditions has been thoroughly studied since the late of 1990s (Haruta et al., 1989, 1993; Boccuzzi et al., 1996; Hayashi et al., 1996; Haruta, 1997, 2001; Moriarty et al., 1998; Horvath et al., 2000; Guczi et al., 2000; Baumer et al., 2000; Meusel et al., 2001; Hoffmann et al., 2001; Giorgi et al., 2002). This method allows the various self-organised assemblies and nano-patterned structures. Catalytic properties depend on the differences of interface structures and binding energy between metal particles and supporting materials. The required catalyst properties are as follows:

- the strong binding energy between nano-particles and support;
- the large interface area;
- the proper selection of crystalline substrate;
- the sizes of nano-particles.

Thus, the self-organisations in nano-assemblages produced from both colloidal and wet chemical systems lead to highly ordered array and may be regulated on the basis of compatibility between theoretical simulation and proof of principle experiment.

2. 3. 2 Direct position control

The direct position control assembly represents the new, but very perspective approach of a great potentiality to make the wide range of nano-materials. There are many atomic arrangements that are either difficult or impossible to produce by means of the self-assembly methods alone. The direct position control over atoms and molecules allows the synthesis of a much wider range of nanostructures. The criteria of positional assembly differ in many aspects as against the self-organised events. The relevant theoretical analysis and calculations are the foundations of mechanical synthesis (Farrell and Levinson, 1985; Gomer, 1986; Drexler, 1991, 1992, 1994; Merkle, 1993, 1997, 2000; Walch and Merkle, 1998; Merkle and Freitas, 2003; Temelso et al., 2006, 2007).

The direct manipulations on the solids are based on the general principles of mechanical chemistry using mechanical energy, pulling, pushing, replacement of atoms and molecules for atomically precise fabrication of metallic, dielectric, organic, etc. nanostructures on different surfaces. The great progress in this area was made simultaneously with the improvement of the scanning probe microscopy

(SPM). The general idea of the mechanical displacements, motions and positions of the atoms and molecules in precise locations by means of the tiny robotic arms was proposed (Farrell and Levinson, 1985; Eigler and Schweizer, 1990; Drexler, 1991, 1992). This approach was successfully developed by the SPM. The various lateral and vertical manipulations were advanced under different conditions (Lyo and Avouris, 1991; Strocio and Eigler, 1991; Aono et al., 1993; Salling and Lagally, 1994; Avouris, 1995; Meyer et al., 1995; Jung et al., 1996; Meyer and Rieder, 1997; Bartels et al., 1997; Stipe et al., 1997, 1998; Dujardin et al., 1998; Hla and Rieder, 2002, 2003; Stroscio and Celotta, 2004). Techniques of direct manipulations are observed in details (Hla and Rieder, 2002, 2003). The first experiments were carried out by means of the STM on the different surfaces: *Si* (100) and (001), *Cu* (111) and (211), *Ag* (110), *Ge* (111), *Pt* (111) involving *Fe, Co, Cu, Pb, CO,* O_2. The reactions such as dissociation, diffusion, adsorption, desorption and bond-formation, became available on the atomic level, including the reactant preparation, contact of mechanical parts together and formation of chemical bonds by using the STM tip.

The technique of atomically directed position was thoroughly explored for the *Si* (100) and (001) surfaces (Salling and Lagally, 1994; Avouris, 1995; Hersam et al., 1999). One of the early mechanical manipulations using the deposition and removal of single *Si*-atoms from *Si* (111) - (7×7) surface was demonstrated (Huang H. et al., 1994), as well as the combination of letters F and U corresponding to the logo of the Freie University (Meyer et al., 1995) was formed by the *CO* molecules on the *Cu* (211). Lateral manipulations on the *Cu* (211) involving *Cu*-, *Pb*-atoms, *Pb*-dimer, *CO*, C_2H_4 were carried out under low temperature (15 - 80°K) in UHV conditions (Meyer and Rieder, 1997; Bartels et al., 1997). *Cu*- and *Pb*-atoms were pulled from the one adsorption site to the nearest one. Tunnelling electrons from the tip were used to induce the reversible rotation of *O*-atoms on the *Pt* (111). This procedure demonstrated the ability to control the single molecules motion as well as the reversible displacement of *Si*-ad-atoms on the *Si* (111) - (7×7) surface. These displacements were determined as a function of current, sample bias voltage and lateral distance from the tip (Stipe et al., 1997, 1998). The direct tip-surface contact to replace *Ge*-atoms on the (111) surface was also investigated (Dujardin et al., 1998).

The STM was probated with a view to formation of the ionic bonds between molecules and atoms on the metallic surfaces (Lee and Ho, 1999). The goal of this experiment was to create bonds by means of the direct position of atoms. Mechanical manipulations with *CO* and *Fe* on the *Ag* (110) surface were carried out under UHV at 13°K by using the STM tip. At the first stage, the *Fe*-atoms were evaporated and adsorbed along with the *CO* molecules on the surface. Then, the *CO* molecules were transferred from the surface to the STM tip and bonded with the *Fe*-atoms to form *Fe(CO)*. At the second stage, the second *CO* molecules were manipulated in the same mode to form $Fe(CO)_2$. The reactants and products were identified with the spatial imaging and vibration energy spectroscopy. The adsorption of *CO* is initiated with the occupation of sites that form the strongest bonds. The *Fe – CO* bond energy is of 11 +/- 4 kcal/mol. Activation energy for desorption of *CO* from atop sites of *Fe* (100) is about 12.8 kcal/mole, whereas for *Ag* (110) is 5.5 +/- 0.4 kcal/mole. Thus, *CO* forms stronger bonds with the *Fe*-atoms rather than with the *Ag* surface or the tip. Because of weak diffusion of *CO* on *Ag* (110) surface, the molecule impinges directly on the *Fe*-atom. The chemical processes are characterised in terms of the STM feedback information. The succession of images and single-molecular vibration spectrum are shown. The bond formation control of adsorbed species at the single molecular levels provides a real space for understanding and visualisation of the chemical bond formation nature.

The catalytic mechanism of oxidation from *CO* to CO_2 at 13°K by means of the manipulation on *Ag* (110) using the tunnelling electrons was also studied (Hahn and Ho, 2001). The *Cu* (111) surface was used as the substrate for the *Co*-atom. It reveals the most suitable locations for the positions of atoms (Stroscio and Celotta, 2004).

The direct position control by using the AFM was theoretically elaborated at the beginning of the 1990s (Meyer and Amer, 1988). The general capability for atomically direct manipulation using the NC-AFM owing to its high resolution was demonstrated later on the *Si* (111) - (7×7) surface (Giessibl, 1995), *InP* (110) surface (Sugawara et al., 1995), *Ag* (111) surface (Orisaka et al., 1999) and *Cu* (111), (100) surfaces (Loppacher et al., 2000). These investigations took place under UHV and at low or room temperature. Finally, the vertical manipulations by means of the soft nano-indentation on the *Si* (111) - (7×7) surface were implemented under UHV and 78°K (Oyabu et al., 2003, 2006). A similar experiment under room temperature

was reproduced few years later (Sugimoto et al., 2005, 2007). The atomic manipulation on the *KCl* (100) surface using the NC-AFM under room temperature and UHV conditions was recently demonstrated as well (Nishi et al., 2006).

2. 3. 3 Molecular building blocks

The main advantage of the positional control approach is concerned with using molecular building blocks (MBB). General concept, strategy and principles for design and application of the MBB have been examined (Merkle, 2000). The long-term goals must be the building of complex molecular machines, whereas the construction of key MBB components should be in the short term. The manufacturing of molecular machines requires the positional devices, on the one hand, and constituting parts of assembly, on the other. The MBB are composed of a few tens to several thousands of atoms. Furthermore, the multiple linking groups of radicals are required to bond the building blocks together. Three bonds are necessary at least. However, four or more bonds would be preferable for a stronger assembly as a whole. The MBB and all supporting units should be made from the stiff hydrocarbons. The advantages of the MBB are as follows: larger sizes, more links between separate blocks, greater tolerance for contaminants, experimental accessibility, ease of synthesis, a larger design space. The characteristics of MBB intended properties and relevant molecular structures are analysed. Special attention is given to the linking groups capable of connecting the blocks by involving dipolar bonds, hydrogen bonds, transition metal complexes, traditional amide and ester linkages. The MBB should be stiff, strong and synthesised by means of the available methods. Tetrahedral assembled MBB appears to be more attractive, e.g. tetrahedral molecules including adamantine. The other small stiff structures might be represented by cyclophanes, iceanes (small pieces of hexagonal diamond), buckyballs, buckytubes, alpha helical proteins. The larger MBB are more useful because they are easier to be manipulated. Also, their surface areas provide more sites for binding to the other blocks.

Modern nano-manufacturing enables MBB of very different molecular architectures to be designed, only if consistent with the laws of physical chemistry (Merkle, 2000). Quantum chemistry methods are capable of ensuring a theoretical basis and relevant calculations to estimate a probability of proposed reaction and its thermodynamic parameters. The interaction of building blocks performing some

bridge with the radical sites of surface was examined and applied directly to the molecular architecture of diamond or diamondoid surfaces (Walch and Merkle, 1998; Merkle and Freitas, 2003). The theoretical and computational investigations of vacuum mechano-synthesis on the *C* (110) diamond surface from *C* – *C* dimer precursors by using the *Si*, *Ge* and *Sn* substituting triadamantane derivatives were undertaken (Merkle and Freitas, 2003). The new families of synthetic tool-tips capable for the precise placement of the *C* – *C* dimers on a growing diamond surface were analysed by using DFT. The functional group of two carbon atoms held together by a triple bond with a placement tool is to be positioned and bonded to a precise location of growing work piece. The dimers are required to be weakly bonded to the tool-tips and also highly reactive and easily bonded with intended structure. The dimer should be bonded with two atoms of supporting structure: carbon, silicon, germanium, tin and lead. These supporting atoms are included as a part substituting the adamantine ($C_{10}H_{16}$) frameworks. The DFT analysis of this type of structure suggests that the adamantine framework substituted by the supporting atoms of IV group can interact with any surface and remain weakly bonded to the *C* – *C* dimer orientated appropriately. Each tool structure is the minimum of potential energy surface (PES). The *C* – *C* dimers are bonded to these tools by progressively weaker bonds moving from *Si* to *Pb*. Encounters between the tool-tips and the growing surfaces occur at desired position and orientation. The *C* – *C* dimers should remain in horizontal position. An alternative pathway is eliminated by this approach.

Interactions between the dimer placement tools and the diamond surfaces were studied by means of constructing the reaction path, potential energy profiles and ab initio molecular dynamics simulation by using DFT with GGA (Generalised Gradient Approximation) (Peng et al., 2004, 2006; Mann et al., 2004). Good operations as regards the *Ge*-based and the *Si*-based tool tips were shown. The *Ge*-based one provides the better functionality over a wide range of temperature. Several representative hydrogenation reactions were also studied by using the state-of-the-art ab initio electronic structure methods. It resulted in the determination of transition states geometry, activation barriers and thermodynamic characteristics (Temelso et al., 2006, 2007). As for kinetics and thermodynamics, it was concluded that hydrogen attached to the group IV elements might be successfully used as the *H*-donation tool.

2. 3. 4 Surface transformations

Surface transformations by using epitaxial techniques were developed as convenient methods for the synthesis of mono-crystalline films on mono-crystalline substrates. This process, called epitaxy, can be used to deposit a microscopic layer of crystal material on the top of a substrate that is also made of crystal. The deposition process, called epitaxial growth (EG), means the operation of growing a crystal of a particular orientation on top of another crystal, where the orientation is determined by the underlying crystal. The atoms in an epitaxial layer have a particular locations relative to the underlying crystal (King and Woodruff, 1997). Epitaxial growth has become increasingly important for growing crystalline thin films with tailored electronic, optical and magnetic properties for technological applications. This approach is limited by the high structural similarities required between an underlying substrate and a growing crystal layer on the top of it. Homoepitaxy is a kind of epitaxy performed with only one material. In homoepitaxy, a crystalline film is grown on a substrate or film of the same material. Heteroepitaxy is a kind of epitaxy performed with materials that are different from each other.

Depending on the materials and the layer structure, epitaxy can be performed from the vapour, liquid or solid phases, or in the form of molecular beams in ultra-high vacuum. There are a number of approaches to vapour phase epitaxy, which is the most common process for epitaxial layer growth. The deposition atoms come from a vapour, so that growth occurs in the interface between gaseous and solid phases of matter. Examples include growth from thermally vaporised material such as silicon or from gases such as silane (SiH_4), which reacts with a hot surface to leave behind the silicon atoms and to release the hydrogen back into the gaseous phase. In chemical vapor deposition (CVD) the atoms for epitaxial growth are supplied from a precursor gas source (e.g. silane). Metal-organic chemical vapor deposition is similar, except that it uses metal-organic species such as trimethyl gallium (which are usually liquid at room temperature) as a source for one of the elements. For example, trimethyl gallium and arsine are often used for epitaxial gallium arsenide growth.

In liquid phase epitaxy (LPE) layers grow from a liquid source at a liquid-solid interface. Epitaxy involves the precipitation of a crystalline film from a supersaturated melt onto a substrate. In solid phase a thin amorphous (noncrystalline) film layer is first deposited on a crystalline substrate, which is then heated to convert the film into a crystalline layer. The epitaxial growth then proceeds by a layer-by-

layer process in the solid phase through atomic motion during the recrystallisation at the crystal-amorphous interface.

Molecular beam epitaxy (MBE) is one or more evaporated beams of atoms which react with the substrate to yield a film. The process provides a pure stream of atomic vapour by thermally heating the constituent source materials. For example, silicon can be placed in a crucible or cell for silicon epitaxy, or gallium and arsenic can be placed in separate cells for gallium arsenide epitaxy. Chemical beam epitaxy uses a gas as one of its sources in a system similar to molecular beam epitaxy. Atomic layer epitaxy is based on introducing one gas that will absorb only a single atomic layer on the surface and following it with another gas that reacts with the preceding layer.

The hydrogen abstraction and donation are crucial operations for surface treatment. Any invented surfaces are covered with hydrogen atoms to avoid the high reactivity for free bonds on the top-level terminations. To add the carbon or another atom on the inert surface is an absolutely unrealisable task unless hydrogen atoms are removed. To overcome this task and prepare the reactive surface for the following events, the special nano-scale tool-tips are used. The hydrogen abstraction via free radicals is the main mechanism resulting in activation of surface for the further creation of intended assemblies. Hydrogenation of single molecules, hydrogen deposition and abstraction from the different surfaces (*C, Si, SiC, S, Ge, Sn, Pt*), including diamondoid surfaces, were studied both in computation and experiments (Lyding et al., 1994, 1998; McIntyre et al., 1994; Huang and Yamamoto, 1997; Foley et al., 1998; Hersam et al., 1999; Lauhon and Ho, 2000).

The diamond-like structures proved to be preferable for molecular compilation because $C - C$ bonds are especially strong. These works proved to be pioneering in terms of the fundamental principles of mechanical nano-engineering advanced for diamond mechanical synthesis (DMS). For the beginning of chemical vapor deposition (CVD) diamond growth occurs from hydrocarbon gases. The processes of hydrogen abstraction from methane CH_4, acetylene C_2H_2, benzene C_6H_6 and isobutane $CH\ (CH_3)_3$ using the radical species serve as suitable for diamond *C* (111) synthesis (Musgrave et al., 1991). The hydrogen abstraction from diamond surfaces was also theoretically studied. The activation energy for hydrogen abstraction on the diamond surface was estimated by using the constrained isobutane as a model on the basis of multi-configuration self-consistent-field methods (Page

and Brenner, 1991). The specific example of hydrogen abstraction from *C* (111) surface in strong electric uniform fields was simulated with the result of $C - H$ dissociation to yield $R^+ + H^-$. Reaction probability, cross sections, rate coefficients, frequency factors and activation energy were computed (Chang X. et al., 1993).

The hydrogen abstraction activation energies were calculated for several representative reactions involving hydrocarbons (Zavitsas and Chatgilialogu, 1995). The activation barriers and enthalpy for dehydrogenation from silicon mono-hydride and silicon bi-hydride were estimated (Srinivasan et al., 1996; Srinivasan and Parsons, 1998). The first successful deposition of individual hydrogen atoms demonstrated that the adsorbed *H*-atoms can be diffused and then deposited on the mono-hydride *Si* (100) - (2×1) - *H* surface. This mechanism involved *H*-diffusion on the STM tungsten tip followed by deposition due to the electronic excitation (Huang and Yamamoto, 1997). The electrons also stimulated the abstraction of hydrogen and deuterium from the *Si* (100). This process was explored under various temperatures. The large temperature dependence was revealed and explained by the multiple vibration effects (Foley et al., 1998). The different circumstances were taken into consideration for the experiments with atomic scale desorption and deposition of hydrogen atoms on the hydrogen-terminated *Si* (001) - (2×1) - *H* and *Si* (001) - (3×1) - *H* surfaces by using the clean and *H*-covered tips resulted in the different conclusions (Thirstrup et al., 1998). The studies of hydrogen and deuterium desorption from the *H*-passivated *Si* (100) surfaces discovered that deuterium is more difficult to be desorbed as against hydrogen. Desorption has no temperature dependence in the high energy electronic regime. However, under low energy regime hydrogen is much easier to be desorbed at low temperature (Lyding et al., 1994, 1998; Hersam et al., 1999). The carbon atoms at the sides and bottom of different *Si*-clusters were applied. Energy barriers proved to be very sensitive to the cluster sizes (Ricca et al., 1999).

Quantum chemical simulation with a view to the mechanical synthesis of sila-adamantane ($Si_{10}H_{16}$) on the hydrogenated *Si* (111) surface was examined. The potential energy of sila-adamantane and its intermediate surfaces were estimated by using the molecular dynamic and molecular orbital method (Herman, 1997, 1999).

The hydrogen abstraction by gaseous radicals - *H, F, Cl* and *Br* from the *H*-terminated surfaces of silicon carbide (4H-*SiC*) was theoretically studied (Olander and Larsson, 2004). Both *Si*-terminated (0001) and *C*-terminated ($000\bar{1}$)

surfaces were investigated for $1873°K$ and $2573°K$. The hydrogen abstraction energy was calculated on the basis of average energies obtained from the MD simulations at different temperatures. The combined methods of MD/DFT calculations were used (Hohenberg and Kohn, 1964; Kohn and Sham, 1965; Payne et al., 1992).

The atomic hydrogen induced abstraction of methyl group on the both *Ge* (111) and *Ge* (100) surfaces allows the estimation of very large activation energy that depends on the surface coverage by methyl group. The strong differences of atomic layer epitaxy characteristics between (100) and (111) surfaces are explained by either the different mechanisms of methyl groups thermal desorption or the different surface structures (Sugahara et al., 1998).

2. 4 Retro-synthetic analysis

The molecular compilation of complex intended product might be realised by means of the multi-stage transformations as a succession of more easy operations in total accordance with the physical laws. The different routes to multistage synthesis may be run by either self-assembly or positional assembly. In the wet chemistry the reagents can interact with any part of molecule. However, the mechanical chemistry under precise position control seems also to have another advantage. The hybrid approach implies that some processes are the subject of self-organisation, whereas the others are running via mechanical manipulations.

In order to obtain useful information about final products every intermediate state should be firstly examined by using the first principles of quantum mechanics. The general approach to the pathway for arbitrary complex compound is elaborated by means of retro-synthetic analysis (RA) based on the decomposition from the intended product backwards to the starting components. It is carried out through gradual reduction of molecular complexity until the commercially available components are reached. The ideas to analyse a target product towards reverse direction of synthesis were developed in the 1970s and especially improved in the field of organic chemistry (Corey, 1967, 1971, 1988, 1990; Corey and Wipke, 1969; Corey and Cheng, 1989; Corey et al., 1961, 1968, 1972, 1985).

The RA represents the chain of transformations and intermediate states in the opposite direction of their succession. The same compounds may be synthesised by different pathways. Therefore, they say about the “retro-synthesis” tree inducing a

cyclic graph of possible pathways for the transform materials (TM) from the single product. Every transform implies the real reaction resulted in approach to the synthetic precursor. The aim of any transform is to reduce the molecular complexity. A tree of alternative routes should be restored with a view to the well-grounded pathway.

The great arsenal of reactions between the fragments results in the precursor. In turn, every precursor becomes the subject of reverse analysis, until the available starting compound is determined. Different types of transforms exist based on the decomposition or bond breaking in chain, ring or functional group. This step involves the bond breaking and forms two or more synthons as the idealised molecular fragments resulted from the transform. The synthons may be positive charged (with acceptor atom) or negative charged (with donor atom). A minimal molecular substructure that enables certain transformations is called retron. Ability for retron finding is the pledge of retro-synthesis success. The RA should begin from the study of TM composition and structure. It is very important to define:

- which functional groups are present;
- whether there is any sign of symmetry;
- whether there is some analogy with the synthesis produced previously;
- possibility to imagine TM from the available fragments.

There are at least five types of strategies for the RA implementation:

Transform-based strategies are aimed at the search for the most powerful and simplifying transform that makes up the greatest contribution to the retro-synthesis. Structure-goal strategies. The most important role belongs to the starting compound in the TM, i.e. the subunit that corresponds to retron.

Topological strategies are based on the search of bond (or bonds) that leads to the maximum reduction of molecular complexity.

Functional group strategies mean that manipulation of functional groups can lead to the significant reductions in molecular complexity.

Stereo-chemical strategies are directed towards the search for stereo-chemical analogies, while taking into account that the numerous chemical targets have different demands.

Ideas and methods of the RA are experienced in mechanical chemistry that would mean a new strategy and great challenges for nano-manufacturing. The overall knowledge of synthesis is integrated into a well-grounded “pick and place” system

and converted into machine readable instruction governing the SPM operations as follows:

(a) – chemical activation by means of shifting the Fermi level with tip bias;
(b) – using a chemically functionalised tool-tip to perform bond breaking and bond formation;
(c) – hydrogenation, dehydrogenation, oxidation and other reactions;
(d) – application of tip functionalised with the conventional catalysts;
(e) – using tip able to excite a certain molecular vibration mode.

Checking and validation of the invented system are possible by the "proof of principle" experiments carried out by the tip-driven techniques. In the course of experiments, a visualisation and study of interface quality provide better understanding and insight into the nano-assembly processes in real time. The relevant monitoring and feedback strategy inform about some characteristics of the tip and possible defects on the work-piece surface.

2. 5 Scanning probe microscopy

The new strategies for nanotechnology would be inconceivable without a progress in the scanning probe technique. That proved to be very important both for development of the self-organised assembly and the mechanical synthesis. The scanning tunnelling microscopy (STM) was the first proper tool not only with regard to images and mapping of surfaces, but for the different mechanical manipulations to arrange the atoms in intended order (Eigler and Schweizer, 1990). However, this system proved to be limited by the weakly adsorbed species on the conducting surface. The updated nano-engineering needs the wide range of structures with strongly adsorbed atoms and molecules on the very different surfaces. This necessity became possible by using atomic force microscopy (AFM), the last generation of scanning devices.

For the resolving atoms on the insulating surface, Gerd Binnig and Christoph Gerber introduced the method that was very similar to the STM. The flexible force-sensing cantilever stylus scanning over the sample was used (Binnig et al., 1986). The forces acting in the system between cantilever and sample caused the minute deflections of cantilever that were detected and utilised as the feedback signal. The topographic image of high resolution was obtained by keeping the force constant. The AFM has some common properties with its precursor: a piezoelectric scanner,

feedback electronics, system of isolation against vibration, coarse positioning mechanism and automated control system via computer. However, the AFM proved to be much more attractive in terms of its versatility, in particular in the application for both conductors and insulators. This system is easy to operate in a liquid environment. The AFM allows to be obtained the most useful information of the surface forces acting in the systems. With regard to the Scanning Electron Microscope, the AFM provides extraordinary contrast of topography. As against the Transmission Electron Microscopes, 3D images may be obtained without special preparation. The great advantage of the AFM concerns its capability to research the non-conducting surfaces. The system allows the study of different surface modifications where the energetic effects occur in the interfaces while giving rise to forces not presented otherwise. Besides the classical Van der Waals forces, the salvation and depletion forces, electrostatic forces and hydrophobic effects are characteristic of the interface. The dissipation energy is based on the two mechanisms (Shluger et al., 1997; Kantorovich, 2002; Kantorovich and Trevethan, 2004; Trevethan et al., 2007 a, b):

(1) – the Brownian motion mechanism caused by the vibrations of surface atoms resulted in the friction force acting on the tip;

(2) – the adhesion hysteresis mechanism resulting in different surface-tip forces as the approach and retraction events.

The manipulation events should result in the sudden changes in the force field. These forces are of great importance for the complex processes governing the fine pieces. Many dissolved substances tend to concentrate close to the interface where all the chemical reactions start. The surface modifications are different and may alter the properties of the whole system.

Construction of the AFM is universal for different models. A cantilever with sharp tip scans over the surfaces. The photo-detection and feedback enable the piezo-electric scanner to maintain the tip either at constant force to obtain height information or at constant height to obtain force information. The cantilever and small hook at the end press against the surface while the sample is scanned. To achieve the atomically high resolution, the cantilever-tip assembly should be flexible with a force constant from 10^{-2} to 10^{2} nano-newtons (nN) to detect a change of force of a small fraction of a nano-newton. The resonance frequency of cantilever must be high enough to follow the surface contours. Usually, the frequency of

corrugation signal is up to a few kHz while scanning. The natural frequency of cantilever must be greater than 10 kHz. The cantilever should be small, much lighter in weight than 1 mg, whereas its length should be of the order of 100 micrometers. The stiffness in vertical and horizontal directions should strongly differ to minimise the image artefacts. Some artificial effects caused by the disturbing frictional forces may occur when the AFM operates in the repulsive-force mode. Therefore, the substantial lateral stiffness should be chosen by means of the appropriate geometry of cantilever shape. The slope of tip should be very steep as well as very smooth.

The AFM would be probably a curiosity without the great breakthrough in the manufacturing of tip-cantilever pair. The first silicon cantilever was produced for the study of boron nitride structure (Albrecht et al., 1990; Chen C., 1993). It was developed afterwards for the mass production of cantilever-tip assembly (Akamine et al., 1990). Nowadays, the tips are fabricated from *Si* or Si_3N_4. 3D image and lateral resolution depend on apical tip and sample geometry. The radius of curvature usually influences the resolution ability. The sharp tip can give great improvements.

The forces within the tip-sample pair are less than 10^{-9} N, which requires a very sensitive detection system. This system does not measure these forces directly, but senses the deflection of the cantilever. The detecting system was developed over time and may be represented by several types. Binnig and colleagues used the tunnelling tip placed above the upper surface of the cantilever with the force-sensitive tip separated by the vacuum gap. The central piezo element and the flank piezo drivers were designed to control the spacing between the cantilever and the tip. This was a sensitive system where a change in spacing of 1 *A* between tunnelling tip and cantilever changes the tunnelling current.

Up-to-date detecting systems are based on the optical techniques, using the most sensitive but rather complicated interferometer method (Erlandsson et al., 1988; Martin Y. et al., 1988) or the beam reflect method (Meyer and Amer, 1988). The latter is set in many modifications using the light beam reflected from the mirrored surface of cantilever. The other system uses the cantilever as one of the mirrors in the cavity of a diode laser (Sarid, 1991). The cantilever motion has strong effect on the laser output exploited as a motion detector. As the tip scans the surface by moving up and down, the beam is deflected off the cantilever into a photodiode. The photo-detector measures the difference in light intensities between the upper and lower

elements and converts this into a voltage. The feedback maintains a constant force or constant height above the sample. Under the constant force the driver monitors the height deviation in real time. The constant height allows records for deflection forces.

Operation modes depend on the interactions between the tip and the sample that may be repulsive for the contact mode (CM-AFM) or attractive for the non-contact mode (NC-AFM) and the tapping mode (TM-AFM) with intermittent contact. Different modes might serve for different tasks during the same experiment. Furthermore, as the tip is brought close to the sample and pulled away the forces may be recorded while providing the useful information about atomic- and molecular-scale adhesive and elastic response. The force mode (FM-AFM) operated under frequency modulation detection enables the attractive or repulsive forces to be measured, while elucidating the local chemical and mechanical properties of sample, thickness of adsorbed molecular layer, etc. As the free end of cantilever is brought towards and away from the sample, it causes the scanner to expand and contract in a vertical direction. The deflection of free end is measured and plotted at many points as the Z-scanner. The distance and speed of the tip travelling during the force measurements may be controlled in terms of the amplitude and frequency of the voltage. The amplitude of cantilever oscillation versus the separation distance measured by the oscillation probe provides the information about the magnetic fields and visco-elastic properties.

The highest resolution based on the principles of vibrating cantilever is general for the NC-AFM and TM-AFM and especially appropriate for the insulators and semiconductors. By this mode the tip hovers above the sample and keeps the spacing of the order of 10-100 *A*. The Van der Waals forces are much weaker as against the CM-AFM and difficult to be measured. These forces are detected by means of the sensitive system with the small oscillations of probe. The oscillation with the amplitude about 20 nm is given to the tip-cantilever assembly before the approach to sample. The system vibrates near its resonant frequency of 100 – 400 kHz. The amplitude changes in response to the tip-sample spacing and the image of surface. The oscillating while scanning takes place at a frequency from 50,000 to 500,000 cycles per second. Over a raised area the amplitude is decreased. Conversely, if the tip passes over a depression the amplitude is increased. These changes are used for the identification of the surfaces. The cantilever used for the

TM-AFM must be very stiff. It is the additional reason that makes the signal small and difficult to be measured. By means of the feedback loop the amplitude of oscillation is kept constant. Consequently, the force on the sample is automatically maintained at the lowest level. In order to have good images the special system of vibration isolation is used. This system saves the images, avoids as far as possible the undesirable effects of tip influence (Baumer et al., 2000) and obtains the highest atomic resolution. By these reasons the TM-AFM is considered to be the most advanced technique.

2. 6 Atomically precise architecture

Atomically precise manufacture means the fabrication of molecular assemblies by using the sequences of chemical reactions directed by the mechanical forces of machinery. It is a particular area of nanotechnology together with its techniques, products, design and theoretical analysis. The approaches to synthesis are based on either self-organisation or positional assembly under tool-tip operations resulting in desired molecular architecture. Up-dated atomically precise manufacturing mostly results from the great breakthrough in the area of diamond mechanical synthesis (DMS) that stimulates the further progress for material engineering.

The general ideas and principles of nano-manufacturing go back to the 1980s when the capability of mechanical energy for the molecular manipulations was proposed. The first investigations were aimed at the special properties of the tool that, jointed to the SPM tip, would be able to manoeuvre with the single reactive pieces (Drexler, 1981; Farrell and Levinson, 1985; Gomer, 1986; Saunders and Jarret, 1986; Becker et al., 1987; Miller and Drexler, 1988; Drexler and Foster, 1990; Eigler and Schweizer, 1990; Musgrave et al., 1991; Drexler, 1991, 1992, 1994; Muller et al., 1995). The molecular tool-tip made from the ethynyl radical ($C = C - H$) was further improved under thorough examination (Drexler, 1992). As for the "tool-tip-surface" operation, it was shown that this system:

- should be of high affinity for hydrogen easily made;
- should not be encumbered by surrounding groups;
- should be a part of handle attached to tip;
- should be stable both mechanically and chemically while positioning;
- should have a good ability for selection of alternative reactions.

The mechanical control enables a much wider range of molecular structures to be synthesised. However, the self-organisation allows the involvement of the large number of transition metals, which is very important for the novel catalytic and other properties. Therefore, the combined approach including the mechano-chemistry conversions with the covalent attachment of molecules superimposed on the self-assembly structures should allow the great capability of nano-scale engineering (Muller et al., 1995). The general approach to this pathway is based on the decomposition backwards from the desired product to the available compound.

Precise positional operations include a manoeuvring, torsion and insertion into structure, preparation of reactive sites by removing unwanted moieties and placement of the new pieces. This results in the desired molecular architecture. The operations are realised by means of the attachment and withdrawal of molecular tool-tips that perform different operations with reactive pieces on the growing surface: abstraction, donation, position, replacement, etc. The surfaces are structurally fabricated with single atoms, molecules, dimers, tiny building blocks, etc. A very stiff material should be properly selected with regard to the tool-tips, growing surfaces and supporting structures connected by strong covalent bonds. The reactive pieces should be positioned one after another until the intended architecture occurs. The fabrication is developed in an ultra-high vacuum. A noble gas or chemically inert fluid might be performed as well. Several tasks are the main challenge for the creation of artificial molecular architecture. The mechanical manipulation experiments serve as the useful precedent for the subsequent development. The first samples of molecular architecture were synthesised on the different metallic surfaces. For instance, the multi-stage fabrications were performed on the *Pt* (111) surface. The carbon fragments were initially produced by the partial dehydrogenation of propylene. Afterwards, the repeated hydrogenation for carbonaceous fragments was locally undertaken. The *Pt* - *Rh* tip of the STM acted as a catalyst (McIntyre et al., 1994). Another experiment demonstrated the oxidation of carbon monoxide (*CO*) molecule positioned at the closest distance from the *O*-atom on the *Ag* (110) surface. The carbon dioxide CO_2 formation was produced while illustrating the catalytic oxidation mechanism (Hahn and Ho, 2001). By employment of the mechanical mechanism, the more complex biphenyl molecule $C_{12}H_{10}$ was fabricated on the *Cu* (111) surface. The multi-step reaction involves the separation of iodine from iodo-benzene. During this fabrication chemical reactants were prepared, brought

together mechanically and finally welded together chemically (Hla et al., 2000). One more important experiment demonstrated the selective break of $N - H$ bond for methyl-amino-carbene ($CNHCH_3$) on the *Pt* (111) surface and formation of $CNCH_3$ molecules. The dehydrogenation together with regenerated hydrogenation allows a completely reversible cycle to be established at molecular level (Katano et al., 2007).

From the available experimental works interesting results were demonstrated as regards the reconstruction of silicon surface (Giessibl, 1995) and rearrangement single atoms on the *Si* (100) - (2×1) surface, *Si* (111) - (7×7) surface and *Ge* (111) - (2×8) surface (Moriarty et al., 1998; Morita et al., 2004; Sugimoto et al., 2005, 2007, 2008; Oyabu et al., 2003, 2006). The high resolution images were achieved for the *InP* (110) semi-conductor (Sugawara et al., 1995) and the CaF_2 insulator surfaces (Reichling and Barth, 1999). Mechanical vertical manipulations were carried out for the *KCl* (100) insulator surface (Nishi et al., 2006).

2. 7 Novel nano-materials

The novel properties of highly ordered nano-assemblies are determined by the electronic structure of material and the characteristics of nano-particles depending on sizes and particle size distributions. It especially concerns the sizes of few nano-metres when the novel properties are size-dependent and correspond neither to those of the molecules nor to those of the bulk. The nano-particles in the range of 1-10 nm display the electronic properties arisen from confinement of electrons in very small volume. The quantum size effects are attributed to the reduction of the free electrons for large fraction of low coordinated atoms. The finest particles are considered as “quantum dots” for electrons restricted near nano-crystal cores. This phenomenon is characteristics of intrinsic band structure due to density of states in the valence and conduction bands (Halperin, 1986; Schmid, 1992, 1994; Rosch and Pacchioni, 1994; Grabar et al., 1995; Galletto et al., 1999). The quantum effects in so-called "quantum dots" are of great importance and used for new generations of computers with an extremely high capacity. As a result, it leads to miniaturisation of electronic devices.

The highly ordered metal nano-particles with well-defined two-dimensions would enable the development of novel materials for the optical and electronic industries. The magnetic properties of small nano-particles are also of high technological interest. *Fe*, *Co* and *Ni* nano-particles dispersed on semiconductor substrate are important for the development of magnetic data storage. Metal clusters

separated by nonmetal atoms or ligand may lead to the new magnetic materials (Hill et al., 1998, 1999; Sun et al., 2000; Mozaffari-Afshar et al., 2001). Mixed nano-particles are considered as a basis for the novel alloys. Transition metal clusters combined with *S* or *P* predict the semi-conducting materials (Schmid, 1994; Bradley, 1994).

With a view to nano-manufacturing operations the significance of α-Al_2O_3 should be emphasised (Barth and Reichling, 2001). Its practical application is enhanced due to stability under variable temperatures and used as a supporting material for catalysis. The α-Al_2O_3 surface demonstrates high ability to self-organisation during chemical transformations. Moreover, some alumina varieties belong to the diamondoids group (sapphire, corundum) and can be used for mechanical chemistry. The well-grounded crystalline structure is evident advantage for control over surface modifications.

At every stage of nanotechnology progress the elements of gold group (*Cu*, *Ag* and *Au*) as well as *Pd* and *Pt* were the subject of systematic research. Despite the restricted bulk properties the gold in nanostructures has great possibilities comparable perhaps with the carbon group. The properties of nano-scaled structures depend on the nano-particle sizes, shape, density, dispersion and the other surface characteristics. The highest medical effects including drug delivery, therapy treatment and recovering are determined by *Au* nano-particle parameters (Shipway et al., 2000; Wang D. et al., 2002; Chithrani et al., 2006; Jiang W. et al., 2008).

The first experience with gold sols launched the great scientific interest in colloidal and organometallic chemistry (Yuan et al., 1992; Sankaran et al., 1993; Bradley, 1994; Brust et al., 1994; Muller et al., 1995; Kung and Ko, 1996; Martin C. et al., 2004, 2007; Pauliac-Vaujour and Moriarty, 2007; Siepmann et al., 2007). However, the main importance stimulating the most intense investigations aimed at the self-organisation processes was concerned with the high catalytic activities of metallic nano-particles. The unique properties of the *Au, Pt* and *Pd* nano-particles proved to depend on temperature, concentration, *pH*, type of the solvent, characteristics of solid substrate and its top-level termination. Numerous experiments with the *Au, Pt* and *Pd* nano-particles showed the variable and unique properties of catalysts as a function of nano-particle characteristics (Haruta et al., 1989, 1993; Haruta, 1997, 2001; Horvath et al., 2000; Baumer et al., 2000; Hoffmann et al., 2001;

Meusel et al., 2001; Giorgi et al., 2002). Deposited on the different solids the same metal nano-particles produce the surfaces of selective adsorption of H_2 and *CO*. The differences of interface structures and binding energy of *Au* and supporting materials are considered to determine the various catalytic properties. For instance, the *Au* nano-particles on *NiO* increase selectivity of catalysts for both *CO* and H_2, whereas the *Au* nano-particles on *CuO* show large selectivity and sensitivity for *CO* only. *Au* deposition on *CoO* showed enhanced selectivity for H_2 (Haruta et al., 1989, 1993; Hayashi et al., 1996; Boccuzzi et al., 1996; Kamimoto et al., 1998).

Semiconductors and computer circuits are often manufactured using crystalline materials produced via epitaxial growth. In homoepitaxy the film and the substrate are the same material. The growth layers are made up of the same material as the substrate. In heteroepitaxy the growth layers are of a material different from the substrate. Film and substrate are different materials, for instance *AlAs* on *GaAs*. The commercial importance of epitaxy comes mostly from its use in the growth of semiconductor. Metal-semiconductor structures are used for contact applications. For example, since the small lattice mismatch for $CoSi_2$ or $NiSi_2$ on *Si*, interfaces are defect free. *Fe* on *GaAs* is similarly possible since the lattice size of *Fe* is about half of *GaAs*. Epitaxy of compound semiconductors from the III-V groups of materials (*GaAs, InP*, etc.) and the II-VI groups of materials (*ZnO*, *CdSe*, *CdS*) are also used in computer, video display and telecommunications applications (Adachi et al., 2009).

A wide range of novel epitaxial materials is nowadays synthesised, including oxides, magnetic materials, superconductors, metals and organics (King and Woodruff, 1997; Kittel, 2005). Materials grown through such techniques have become common constituents of devices in fields ranging from nano- and optoelectronics, to photonics, energy production, sensors for biological and environmental applications. Besides, special modifications of epitaxial techniques allow the synthesis of low-dimensional structures, such as quantum dots, nanowires, carbon nanotubes and graphene.

The materials of carbon group comprise the different dimensional allotropes of various properties (Fig. 1.1); 3D diamond and graphite, 1D nano-tubes and 0D fullerenes have been of great manufacturing requirement for a long time. Carbon – carbon bonds are especially strong and used for a wide range of nano-manufactory. First of all, this concerns a diamond, diamondoids and structurally diamond-like materials. Each carbon atom in a diamond is covalently bonded to four

other carbons in a tetrahedron. All together these tetrahedrons form a three-dimensional network of six-sided carbon rings. Examples of other carbon materials are carbon nano-tubes, fullerenes and very stiff ionic ceramics such as sapphire that can be covalently bonded to diamond. The fullerenes are molecules of varying sizes composed entirely of carbon, which take the form of a hollow sphere, ellipsoid, or tube. The chemical and physical properties of fullerenes are still under thorough study for potential medicinal aims. In particular, it concerns spherical fullerenes with the formula C_{60}. The carbon nano-tubes related to the fullerene's structural family divided into single-wall (SWNTs) and multi-wall (MWNTs) nano-tubes, are the cylindrical carbon molecules with the novel properties that make them potentially useful in a wide variety of nano-electronics, optics, etc.

Diamond is considered to be the most attractive for nano-scale manufacturing. However, diamond is a very brittle material. Therefore, the diamond-like structures are mostly preferable for molecular compilations. The structures with the properties resembling diamond are strong, stiff, with dense 3D networks of bonds for the first and the second rows of atoms with a valence of three or more. A diamondoid is a hydrocarbon molecule with a three-dimensional structure whose carbon – carbon framework represents the fundamental repeating unit in the diamond lattice. This group comprises a crystalline diamond, sapphire and the other crystalline structures whose top-level atoms are capable of being substituted with *N, O, Si, S,* etc. Diamondoid materials are constructed from the atoms of 12 elements: *C, Si* or *Ge* (group IV); *N* or *P* (group V); *O* or *S* (group VI); *F* or *Cl* (group VII); *B* or *Al* (group III) and hydrogen (*H*). Diamondoids are considered to be the ideal building blocks for nano-assemblies. These materials might be 100 – 250 times stronger than titanium and much lighter. The simplest diamondoid is adamantane ($C_{10}H_{16}$) that has 10 carbon atoms arranged in a cage-like structure that looks like a small part of a diamond. Larger diamondoids are diamantane ($C_{14}H_{20}$), triamantane ($C_{18}H_{24}$) and poly-mantanes ($C_{4n+6}H_{4n+12}$, $n = 0,1,2...$).

The great progress in diamond mechanical synthesis (DMS) producing the novel carbon materials worked up the new advanced technology for synthesis and fabrication applicable for the other carbon materials. The hydrogenation reactions are of great significance, first of all taking into consideration the DMS requirements. The crucial procedures of hydrogen abstraction and donation are used from the beginning

of chemical vapor deposition (CVD) for diamond growth from hydrocarbon gases. The same methods may be applicable for treatment of the other carbon materials. Diamond surfaces are passivated with hydrogen atoms to avoid a high reactivity on the top-levels. Any operation on the inert surface is impossible unless hydrogen atoms are removed. To overcome this situation and prepare the reactive surface, hydrogen should be abstracted by using different radicals delivered by means of differently coated tool-tips. This is the main mechanism resulting in the activation of a diamond surface for the further creation of invented molecular architecture.

The intended diamond surface is fabricated via three stages of positional control. At least three basic tool-tips were already theoretically elaborated: (1) – hydrogen abstraction tools, (2) – dimer placement tools and (3) – hydrogen donation tools. The general strategy and principles relevant to the DMS manufacturing founded by the first theoretical works (Merkle, 1993, 1997, 2000; Brenner et al., 1996; Walch and Merkle, 1998) were advanced to practical realisation during the last few years. The new family of tool-tips operating on the surface of diamond or diamondoids was simulated (Merkle and Freitas, 2003; Allis and Drexler, 2005; Freitas et al., 2007). The terms of stability and strength for new bonds were calculated for the placement of $C - C$ dimer with the supporting atoms of IV group. They substitute the bi-adamantine structure at the specific site of a growing diamond surface (Merkle and Freitas, 2003) and at the position of several dimers (Peng et al., 2004). The interactions between the clean diamond (110) surfaces and the dimer placement tools were examined. The *Si*-based and *Ge*-based tool-tips can successfully operate for the multi-stage fabrications in a wide range of temperatures (Mann et al., 2004; Peng et al., 2006).

On the basis of DFT and by using the semi-empirical method AM1 (Austin Model), the classical molecular methods and series of 24 potentially useful tool-tip structures were theoretically examined. Some members enable the $C - C$ dimer to be held and positioned for controlled DMS reactions under room temperature and vacuum condition (Freitas et al., 2007). The explored tool-tips should have two main components: the chemically active tool-tip and the chemically inert handle to which this tool tip is covalently bonded. The handle is adjusted to the AFM for positional manipulations. At the first stage of DMS, the hydrogen atoms should be removed from each of the two adjacent spots and left behind two reactive dangling bonds. This manipulation is possible by using the hydrogen abstraction tool that should have

a high chemical affinity for hydrogen. The other domains of tool should be inert and serve as a handle attachment point. The tool should be held by either the SPM tip or molecular robotic arms and move directly over particular hydrogen atoms on the surface. One of the most suitable molecules for hydrogen abstraction is $C - C$ dimer. The dimer is a molecule consisting of two same atoms or molecules bonded together. In this case, the dimer would be C_2, *i.e.* two carbon atoms connected by a triple bond. Each carbon atom in this dimer is connected to a handle structure that is not reactive. The environment around the tool has to be inert, e.g. vacuum or a noble gas (neon). During the abstraction the force or the current is monitored with the SPM in terms of the correct signals that indicate the termination of an event. Once the first stage is completed, the molecular structure has a high chemical affinity for hydrogen. The reactive spots on the diamond surface occur. Therefore, the carbon atoms' deposition at the desired sites becomes possible.

The second stage of operation demands another tip that should turn into the $C - C$ dimer placement tool. The dimer placement tool held by the AFM is brought close to the reactive spots along a particular trajectory. The two surface dangling bonds react with the ends of dimer. The relevant monitoring for current and force tests the dimer emplacement events. Then, the tool is withdrawn. The weaker bonds with the $C - C$ dimer are broken resulting in the transfer of dimer from the tool to the surface. This manipulation makes possible to position $C - C$ dimer and create any forms on the growing surface.

Once a new molecular structure is fabricated it should be made inert again. Therefore, a hydrogen donation tool does the opposite transformation. It makes a passive surface by terminating the dangling bonds. Such stabilisation is necessary to prevent the new atomic structure from unexpected rearrangements. The general requirements for this tool include the weekly attached hydrogen atoms. For example, the most effective *Ge*-based or *Sn*-based hydrogen donation tools are used.

Chapter 3 The rise of graphene (structure, properties and fabrication)

3. 1 Introduction

Taking into consideration that graphene crystalline and electronic properties are of a great exception, their specifications, immediate industrial tasks and utilisation are further reviewed to be the relevant database for the novel methodological exploration.

Along with many sided interest to carbon composites, the elusive 2D form – graphene – was argued more than 70 years ago. Since the mid-1930s, it has been assessed to be unstable thermodynamically and existing only as the upper part of a 3D crystal lattice. This continued to be the case until the practical discovery in 2004 of freestanding graphene. This discovery triggered an avalanche of scientific research papers comparable with the "gold rush" (Novoselov et al., 2004; Geim and Novoselov, 2007). Graphene sheets comprise carbon atoms bonded together in a flat hexagonal array constituting graphite when they are stacked in layers. For the atomically single 2D structures the moving electrons confined in two dimensions behave like mass-less relativistic particles while causing the unique electronic properties.

The ballistic transport and giant charge carrier mobility under large electron free path extending through the thousands of inter-atomic distances without scattering, superior conductivity for electricity and heat, tuneable electronic capacity, control on electron spin, while enhancing Coulomb interaction, etc., make graphene a perspective material for "spintronic" electronics (Goldman and Nishioka, 2007). With a view to progressing novel graphene-based technology some advancement concerning the scale-up production, patterning and tailoring, fabrication of building blocks and settling together with other condensed materials should be worked up on the basis of graphene behaviour in an external situation.

Graphene properties alter under its excitation and interaction in combination with different assemblies. Graphene sheets have a strong tendency to decay and stick as a number of layers is grown. Treatment using strong acids prevents this aggregation, but affects the useful electronic properties (Si and Samulski, 2008). Therefore, the main attention should be focused on many-layered graphene-substrate systems formed step-by-step on different solids. Identification of electronic

properties as the number of carbon layers run from zero to 3D dimension is of special importance. The interfacial processes leading to different graphene layers turn into exclusive knowledge that enables control and regulating of the graphene-forming processes in dependence on the external conditions.

Since real graphene discovery, the scientific activity has been concentrated on immediate tasks of fundamental and industrial signification. The unique graphene properties, including its mutability under variable conditions, are determined by electrons moving in 2D confinement. The problem of interaction with another condensed material proved to be of special importance. The composite systems of layered graphene on the solid support attract the particular attention. Two layers jointed together reveal the spectrum approximating to freestanding graphene, whereas the every subsequent layer adds the novel features. The new material is made up of the few layers stacked one on top of the other, meaning that each layer is electronically independent. This is why the new composite assemblies in the alternating combinations are designed and studied, including the submitted investigation, with the subject of substrate induced interaction. The novel composite structures integrated into the external medium emerge in anticipation of future graphene utilisation.

3. 2 Atomic and electronic structure

With regard to the quantum theory of condensed matters, graphene is a great exception. Moving electrons involved in the long-range hopping processes result in graphene unique electronic properties. An exceptional ability for graphene adaptation to physical conditions is interpreted as a consequence of a particular crystalline structure. Graphene hexagonal lattice is disintegrated into equivalent triangle sub-lattices providing the quantum long-range hopping effects (Katsnelson, 2007). Two nearest atoms of the opposite triangles compile the primitive unit cell responsible for electronic symmetry while following the tight-binding approximation (Wallace, 1947). The exclusive electronic structure arises from the symmetry of the crystalline structure. The periodicity in graphene honeycomb lattice is conventionally expressed in terms of two sub-lattices as the equivalent and interpenetrating triangles **A** and **B**. The bonds between carbon atoms form the hexagonal lattice where each atom of sub-lattice **A** is connected to three atoms of sub-lattice **B** and vice versa (Fig. 3. 1_a). Both sub-lattices are interchanged by rotation in the 2D plane for 120°.

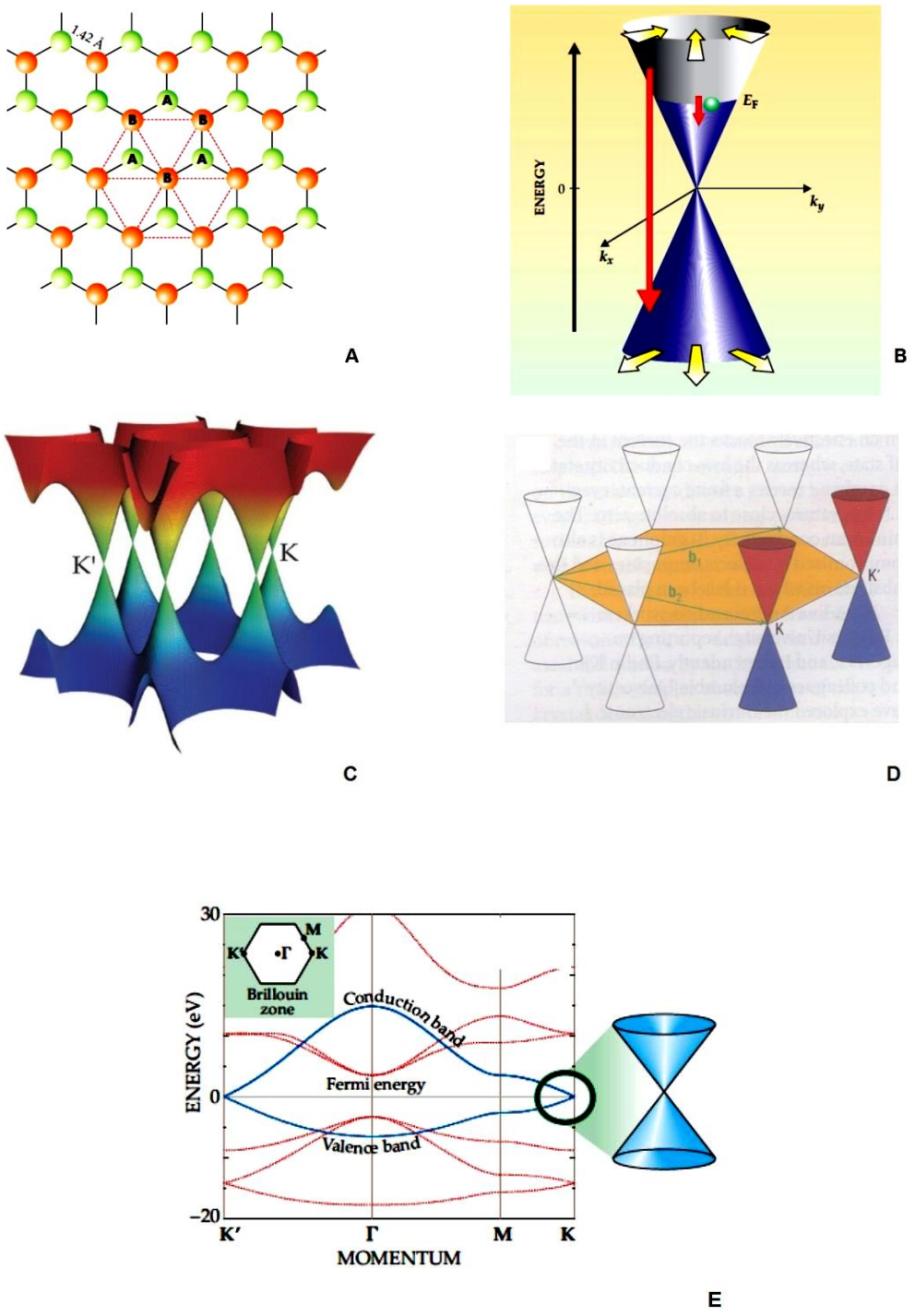

Figure 3. 1. Crystalline and electronic structures of graphene:
(a)- graphene honeycomb lattice comprising two interpenetrating triangle sub-lattices **A** and **B**; the nearest and far bonds are shown (Geim and MacDonald, 2007). **(b, c, d)** – the low-energy conical valleys of energy dispersion in dependence on the Dirac's points *K* and *K'* in the BZ (Geim and MacDonald, 2007; Katsnelson, 2007; Freitag, 2008). **(e) –** Fermi level going through the Dirac's points (Geim and MacDonald, 2007).

Thus, graphene unit cell has two carbon atoms that belong to the different sub-lattices. Each atom of the sub-lattice **A** is surrounded with the nearest neighbours constituting the opposite sub-lattice **B**.

Graphene electronic exception is caused by the unusual behaviour of its charge carriers (Wallace, 1947; Novoselov et al., 2007; Geim and Novoselov, 2007; Geim and MacDonald, 2007; Katsnelson, 2007; Freitag, 2008). Four valence electrons corresponding to each *C*-atom are conventionally expressed as $2s^2 2p_x^1 2p_y^1$. Owing to promotion effect in graphene, they are modified into $2s2p_x^1 2p_y^1 2p_z^1$. It means that the valence level has one *s* orbital and three *p* orbitals. Three atomic orbitals *2s, $2p_x$* and *$2p_y$* tied up by strong covalent bonds are *sp^2* hybridised and form three new molecular orbitals. Their electrons while forming the σ states (bonds) in the *XY* plane with the appropriate σ and σ' bands join carbon atom to three neighbours. The remaining $2p_z$ orbital perpendicular to the plane is characteristic of the fourth valence electron corresponding to the π state (bond). These electrons form the valence π and conduction π' bands responsible for conductivity.

The low and high energy states are made up with the valence and conduction bands. While the valence electrons move, the π bands are decoupled from σ and σ' bands while separating the occupied and empty states in some energy range.

The interaction between energy spectrums is formed appropriately for the *$2p_z$* states. The conical valleys of energy arise at the edges of the first Brillouin zone (**BZ**), where π and π' bands intersect (Fig. 3. 1_b, c, d). The cone-shape structure corresponds to two atoms of the graphene unit cell.

The interaction of these energy spectrums demonstrates the linear dispersion between energy and wave vector. The Fermi level runs between the dispersion cones near the Dirac's points (Fig. 3. 1_e). The *K* and *K'* points corresponding to the unit cell are independent, and the other may be calculated by using the vectors *b'* and *b''*. The **BZ** performed by the reconstruction of real hexagonal lattice into reciprocal lattice implies a transformation into space of two states for electron per atom (Wallace, 1947). Each *C*-atom of single unit cell proves to be bonded with the nearest atoms of the opposite sub-lattice.

The low-energy spectrum demonstrating the linear dispersion relation between energy and wave vector resembles the low-energy spectrum for the Dirac's mass-less fermions with ½ spin. It points to the existence of antiparticles according to the charge-conjugation symmetry principle of quantum electro-dynamics. The

positive and negative energies of these relativistic particles followed from the changes of spin sign are described in the Dirac equation by different components of the same wave function. The similar situation may be recognised in graphene as a direct consequence of crystal symmetry and quantum mechanical interaction of two sub-lattices **A** and **B**. Furthermore, the moving electrons interacting with the periodic potential of crystal lattice give rise to the new quasi-particles. While losing their own masses, these particles acquire the charges. Formation of quasi-particles contributed by both sub-lattices should be expressed by different components of the same wave function ("spinor"). The energies of these charge carriers obey the linear dependence on wave vector that is different from parabolic dispersion relation characteristic of many materials.

For this reason, graphene behaviour in chemical transformations is expected to be very different in comparison with a majority of condensed matters.

3. 3 Routes to graphene synthesis

Although several routes to graphene synthesis have been proposed, there is a great challenge for the development of computer controlled processes leading to scale-up and low cost industrial production. Synthesis is one of the main immediate tasks for graphene manufacturing. Several approaches have been developed (Table 1, Appendix 2).

(1) – mechanical splitting by using cleavage of foliated graphite. The first experience involves the use of "scotch tape" to peel from crystalline graphite (Novoselov et al., 2004, 2005, 2007; Geim and Novoselov, 2007). This method was later developed (Bunch et al., 2005; Schniepp et al., 2006; Stolyarova et al., 2007; Ritter and Lyding, 2008).

(2) – chemical exfoliation by attachment of appropriate organic group to graphite oxides surfaces resulted in graphene oxide. Chemical conversion in water by removal of oxygen groups result in negatively charged graphene sheets under electrostatic repulsion. The processing is developed and results in high yield production (Stankovich et al., 2006, 2007; Niyogi et al., 2006; Li D. et al., 2008; Eda et al., 2008; Wang S. et al., 2010).

(3) – organic synthesis by chemical vapor deposition (CVD) on metal surfaces and self-assembly while decomposition of aromatic or aliphatic hydrocarbons. A grown layer can be doped during deposition by adding impurities

either to the gas phase or to metallic substrates. The concentration of impurity determines the properties and epitaxial growth rate. The films grown from gas or liquid may be succeeded to the substrate structure. The added dopants which are able to diffuse into the growing layer from other layers are admitted. Liquid phase epitaxy (LPE) produces the crystal layer from the hot-melt adhesive. Molecular beam epitaxy (MBE) uses condensation of evaporated particles on the solids (Oshima and Nagashima, 1997; Gamo et al., 1997; Ueta et al., 2004; N'Diaye et al., 2006; Marchini et al., 2007; Makarenko et al., 2007; Coraux et al., 2008; Hofrichter et al., 2010).

(4) – epitaxial growth on the solid surfaces by using different techniques. The advanced synthesis is approved for *SiC* surfaces by means of thermal decomposition and *Si*-sublimation (Muehlhoff et al., 1986; Forbeaux et al., 1998, 1999; Hass et al., 2006, 2008; Mattaush and Pankratov, 2007; Rutter et al., 2007; Varchon et al., 2007; Hiebel et al., 2008). Another technique is realised through a segregation of interstitial doping carbon (Starr et al., 2006).

3. 4 Epitaxial graphene

Epitaxial growth results in mono-crystalline films on a supporting top-level without structural rearrangement. Two contrast approaches result in large graphene layers suitable for further fabrication. Few-layered patterns can be grown via chemical deposition on transition metals surface by using pyrolysis operations. Another mechanism is performed by thermal or chemical decomposition leading to carbide derived carbon. Excess of carbon is left on the surface since the sublimation rates of removed atoms are higher. In this way, the carbon layer is formed with the retention of the original structure of substrate.

Epitaxial graphene is grown via decomposition of substrate converted into carbide derived carbon (CDC). Carbon is formed by selective extraction of the metal or metalloid atoms from the proper precursor. Since the sublimation rate of removed pieces is higher against carbon, CDC excess is left on the surface. Then, the carbon layer is formed with the retention of the initial structure. Among the materials of ionic, covalent and metallic bonds, the carbide group is systematically used as a supporting substrate for epitaxial processes. Due to the large crystals with an atomically flat surface of extremely low defects being available, silicon carbide (*SiC*) group crystallised in cubic, hexagonal or rhombohedral systems emerges to be

the best precursor for graphene of the higher quality. Intended assemblies stacked in different order result in the variable novel qualities with successive growth. The approximation degree to graphene identity increases as a thickness progress.

From the variable carbides only covalent silicon carbide (*SiC*) is extensively used with a view to graphene formation. The first flakes of epitaxial graphene were formed while simple annealing as the "floating" pieces. The small patches strongly bonded to substrate were azimuthally disordered while preventing a homogeneous monolayer. The roughness and disorder are succeeded to substrate.

The other carbide groups, e.g. the salt-like carbides composed of the alkali metals (Na_2C_2, K_2C_2), the alkaline earth metals (CaC_2, SrC_2) and also *Al*, *Ga*, etc. of ionic bonds, proved to be dangerous and not suitable for processing because of their explosiveness while interacting with the external environment. The transition metal carbides including the *Fe, Co* and *Ni* carbides and the interstitial compounds constituted of the small *C*-particles fitting for the octahedral interstices in a metal lattice are of very high refractory and chemical inertness (Ettmayer and Lengauer, 1994). A majority of metallic carbides are of cubic symmetry which is not coherent with graphene hexagonal structure.

On the surfaces of transition metals the epitaxial graphene films are grown by chemical vapor deposition (CVD). This advanced technique based on catalytic effects was developed by means of exposing the metallic surfaces to hydrocarbon gas or liquid at an elevated temperature (Oshima and Nagashima, 1997; Gamo et al., 1997; Ueta et al., 2004; Starr et al., 2006; N'Diaye et al., 2006; Makarenko et al., 2007; Marchini et al., 2007; Coraux et al., 2008; Sutter P. et al., 2008). Decomposition of hydrocarbons on exposed metals resulted in graphene with high defects in density (Starr et al., 2006). Catalytic reactions with benzene and ethylene revealed big mismatches and moiré patterns (Coraux et al., 2008). Only experience on the *Ru, Os, Re* surfaces was comparable with growth on *SiC* substrate because of high structural coherency with graphene (Marchini et al., 2007; Sutter P. et al., 2008). The main disadvantage of the transition metals lies in removal of the metallic moieties.

3. 4. 1 Growth of carbide derived carbon

The epitaxial growth of carbide derived carbon (CDC) performs the synchronous events leading to carbon excess transformed into graphene (Hass et al., 2006, 2008;

Rutter et al., 2007; Varchon et al., 2007; Hiebel et al., 2008; Tzalenchuck et al., 2010). The first graphene flakes on the different *SiC* surfaces were formed while annealing at the range T = 850 – 1400°C under UHV conditions (Forbeaux et al., 1998, 1999).

In early studies, the graphitisation was presumed due to the commensurate alignment of graphene moiré patterns on an unreconstructed *SiC* surface. Decomposition of *SiC* is accompanied with the silicon depletion, carbon oxidation and graphitisation. The small *C*-flakes were free oriented and connected into a homogeneous film. This layer by layer growth leads to the single graphene's sheet. The domain sizes became much bigger. A roughness and disorder are reduced (Forbeaux et al., 1998, 1999). The first plane called "buffer" acts as an intermediate zone between the substrate and the upper layers. On the bottom the significant disorder does exist, whereas the genuine graphene is formed on the top. The metallic properties of graphene were revealed on the *Si*-face surface where the strongest interaction was also found. For the *C*-face the semi-conducting properties and weaker interaction were recognised (Hass et al., 2006, 2008; Rutter et al., 2007; Hiebel et al., 2008).

As a result, it was proposed that graphene is loosely bonded to the surface by the Van der Waals forces as 2D structure (Forbeaux et al., 1998, 1999). On the (0001) surface the growth proceeds at 850°C on the (3×3) surface reconstruction. The further annealing was implemented on the $(\sqrt{3} \times \sqrt{3})R30°$ reconstruction at around 1050°C. The system evolves through the $(6\sqrt{3} \times 6\sqrt{3})R30°$ reconstruction and then graphene on the (1×1) reconstruction is formed. The growth on the *C*-face occurs on the (2×2) reconstructed surface at 1050°C. Graphene was initially found on the (1×1) *SiC* $(000\bar{1})$ surface while forming the $(\sqrt{3} \times \sqrt{3})R30°$ reconstruction (Berger et al., 2004, 2006; Hass et al., 2006, 2008), whereas the $(6\sqrt{3} \times 6\sqrt{3})R30°$ reconstruction was not observed (Hiebel et al., 2008; Hass et al., 2006, 2008). Recently ab initio calculations (Varchon et al., 2007; Mattaush and Pankratov, 2007) predicted the self-assembled monolayer buffering the subsequent graphene sheets and *Si*-face substrate of $(\sqrt{3} \times \sqrt{3})R30°$ reconstruction. Because of the stronger interaction with substrate, the small patches keep a fixed position and cannot be freely oriented, which prevents homogeneous monolayer growth. However, graphene

on the $(000\bar{1})$ surface proved sometimes to be of high quality (Hass et al., 2006, 2008).

Substrate and interface quality are of crucial challenges. The consensus from recent experiments by many investigators is that $\left(6\sqrt{3}\times 6\sqrt{3}\right)R30°$ reconstruction proved to be the best structural precursor for graphene (Hass et al., 2006, 2008; Kim S. et al., 2008; Magaud et al., 2009). For the well-grounded simulation, one should use the $\left(6\sqrt{3}\times 6\sqrt{3}\right)R30°$ reconstruction corresponding to the (13 × 13) unit cell. However, this model is too complicated for calculation. Furthermore, the novel large scale pattern of covalent bonding between *C*-atoms and *Si*-atoms on the 4H-*SiC* (0001) surface showed that the $\left(6\sqrt{3}\times 6\sqrt{3}\right)R30°$ reconstruction splits into the matched domains of the $\left(\sqrt{3}\times\sqrt{3}\right)R30°$ reconstruction (Kim S. et al., 2008). Some investigations allowed to be concluded that graphene layers may be grown on the carbon rich interface including *Si*-atoms (Hass et al., 2006, 2008).

Another route is based on surface conversion due to *SiC* decomposition resulting from halogenations. The chemical etching on the *SiC* surface is performed by many complicated reactions of gas-surface interaction, which have been extensively studied in recent years (Winters, 1983; Sugiura et al., 1986; Flowers et al., 1995; Yih et al., 1997; Wang J. et al., 1998; Scofield et al., 2000; Edwards et al., 2000; Kim B. et al., 2002; Jiang L. et al., 2003; Gou et al., 2007; Batisse et al., 2010). The experimental and theoretical studies of *Si – F* interaction provide the fundamental knowledge of mechanism by which SiF_x species are produced on the *Si*-terminated layer. Fluorine etching via the SiF_x intermediate is the advanced way to SiF_4 formation and *Si*-atoms removal. There are many routes in terms of how the *F*-atoms are bonded to the *Si*-face substrate. It is mainly SiF_4 that desorbs from the surface. The first study involving energetic atomic *F* on the *SiC* surface by means of molecular dynamic methods showed that transition from deposition of *F*-atoms to etching takes place under energy more than 10 eV. The exploration was concentrated on the uptake of energetic atomic *F* on the surface, the etching and yield rates for *Si*- and *C*-atoms on substrate, modification of surface structure, composition and the final product. However, the etching mechanisms are still poorly understood. The incident atomic quantities were defined in terms of fluence measured in units of one monolayer (ML). The uptake of *F*-atoms deposited on the surface is a function of incident energy and fluence. The threshold fluence

increases with energy. For the initial state, the coverage sharply increases independently on energy. The steady state coverage is defined when coverage of *F*-atoms remains constant and a balance between deposition and etching is established. The etching rate for *C* is less than that for *Si*. It sharply increases with increasing incident energy, whereas *F* and F_2 cluster quantities decrease. Corresponding to the theoretical and experimental investigations, the main trends of gas-surface interaction on *SiC* surface under fluorine attack are found as follows:

- the surface modification is strongly sensitive to the incident energy;
- the *F*-atoms penetrate deeply into the bulk and react with *Si*-atoms successively while adding each other beneath the surface and forming the interface;
- the incident energetic *F*-atoms are deposited in interfacial layer in form of *SiF*, SiF_2 and SiF_3 groups while ejecting from the *SiC* surface as SiF_4;
- the interfacial layer consists of many clusters of *C*, *Si*, *F*, F_2 ejected from *SiC*;
- the initial uptake of incident *F*-atoms increases independently on energy because of saturation the dangling bonds arising from the surface;
- the balance between the deposited and the etched atoms is established;
- the yield of ejected CF_x clusters is too small every time.

3. 4. 2 Chemical vapor deposition

Epitaxial growth on the surfaces of transition metals and metal carbides is interpreted as a self-organisation running through the decomposition of aromatic and aliphatic hydrocarbons under high temperatures (Oshima and Nagashima, 1997; Gamo et al., 1997; Ueta et al., 2004; Starr et al., 2006; N'Diaye et al., 2006; Makarenko et al., 2007; Marchini et al., 2007; Coraux et al., 2008; Sutter P. et al., 2008). The advanced technique was developed due to the catalytic effects while exposing the solids to hydrocarbon gases. The experiments carried out for the metals in the hexagonal system demonstrated the structural coherency with graphene. The advanced technique based on the catalytic effects was developed by means of exposing the metallic surfaces to hydrocarbon gas at an elevated temperature (Page and Brenner, 1991; Musgrave et al., 1991; Chang X. et al., 1993; McIntyre et al., 1994; Foley et al., 1998; Hersam et al., 1999; Lauhon and Ho, 2000).

These experiments showed that graphene on metallic substrates may be more easily synthesised through the thermal decomposition of hydrocarbon than by using the surface segregation of *C*-atoms from the bulk. Thus, *C* growth on the thoroughly

cleaned *Ni (111)* surface resulted from dehydrogenation of ethylene at T > 600°C (Gamo et al., 1997). The atomic structure revealed that one of two *C*-atoms occupies the top site of a metal substrate unit cell. The second atom is located at the *fcc* lattice. At T = 1000 – 1300°K graphene resulted from the thermal decomposition of ethylene on the *Pt (111)* with high density of defects (Starr et al., 2006). The collision of methane molecules resulted in extensive domains completely covering the *Pt (111)* surface (Ueta et al., 2004). Decomposition of benzene and ethylene formed graphene on the smooth *Ir (111)* surfaces at T = 1600 – 1800°K (N'Diaye et al., 2006; Makarenko et al., 2007; Coraux et al., 2008). The growth on the hexagonal *Ru, Os, Re* resulted in high quality graphene because of its structural coherence with the substrate surface (Sutter P. et al., 2008). The commensurate lattice of graphene structural coherency with substrate was shown (Coraux et al., 2008).

Epitaxial graphene grown on transition metal surfaces was comparable with the best quality sheets formed on the *SiC* surfaces. This was confirmed by the sufficient segregates adsorbed from the interstitial carbon in bulk on the (0001) *Ru* under cooling from 1150°C to 825°C (Marchini et al., 2007; Sutter P. et al., 2008). The first layer strongly interacts with the substrate and plays the role of a buffer supporting the second layer. The latter may be easily decoupled and transferred to another substrate. However, the surface processes on *SiC* and metallic substrates are different. Sublimation on the H-*SiC* occurs at the range of T = 1250 – 1450°C when the small multilayer nuclei start to appear. For the *Ru* (0001), arrays of nuclei grown to macroscopic domains occur at T = 850°C (Sutter P. et al., 2008).

The topical problem of graphene compatibility with the other metallic materials exists nowadays only in an embryo state. Thus, the calculations using the density functional theory were performed for the gold atoms and dimers on the surface of graphene (Varns and Strange, 2008). It was revealed that the gold-gold interaction is considerably stronger than the gold-graphene interaction. Therefore, it is hardly possible to achieve the uniform coverage over graphene template. At the same time, the gold nano-particles dispersion on the graphene sheets indicated good gold stability (Muszynski et al., 2008). The metal-graphene composites were derived from drying aqueous dispersions of platinum on graphene surfaces (Si and Samulski, 2008). Platinum particles were adhered to graphene by the chemical method

involving the reduction of metal precursors. The graphene sheets were incorporated into *Ge* and *GaN* by using the catalytic *Au* nano-particles (Sutter E. et al., 2007).

3. 5 Graphene in many-layered systems

The new graphene sheets are able to be grown on the *Si*-face substrate even if this surface is already covered with the first graphene film. Decomposition and *Si*-sublimation lead to the carbon excess and strong covalent bonds with the substrate. The electronic properties are rapidly changed as a number of layers are enlarged. Graphene monolayer (ML), bi-layer (BL) and subsequent few-layer (FL) patterns should be performed as the different 2D crystals, because their properties are different and each graphene layer is thermodynamically independent.

The first step to many-layered graphene construction concerns the self-organisation processes owing to the *SiC* substrate decomposition, old bonds breaking, *Si* depletion and *C* accumulation in the interfacial layer. The intermediate buffer covalently bonded with the substrate keeps some precursor properties along with the novel signs of graphene.

The subsequent carbon layers are formed by using the CVD. The best precursor would be the relevant structure of six carbon atoms arranged into the hexagonal ring, likewise the benzene molecule (Fig. 3. 2) (McDuell, 1982).

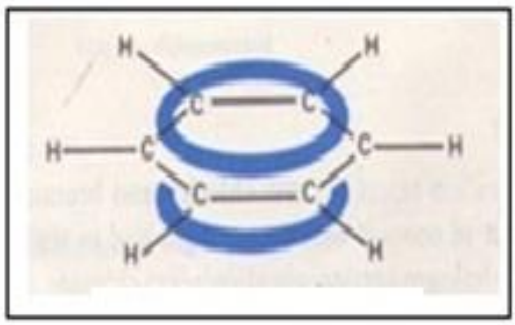

Figure 3. 2. Planar ring of the benzene molecule; a negative charge above and below the ring is shown in blue (McDuell, 1982).

For this atomic structure, each carbon atom is hybridised and forms three sp^2 hybrid orbitals. One of these orbitals on each carbon atom overlaps with the 1*s* orbital of hydrogen atom and the other two sp^2 orbitals overlap with sp^2 orbitals of other carbon atoms. It forms a planar hexagonal framework with one *p* orbital on each carbon atom unused at right angles to the ring. These remaining *p* orbitals are

overlapped and form the ring of negative charge above and below the benzene ring. The lengths of $C - C$ single and double bonds are 0.154 nm and 0.132 nm respectively, likewise graphene. So far as graphene is a giant aromatic molecule, the second and subsequent layers can be easily formed by using benzene-like aromatic hydrocarbon.

The molecules of aromatic halogen groups from six carbon atoms, where each carbon atom is bonded with the additional halogen atom, e.g. *Cl*, *Br* or *J*, may be considered as the best precursor for the few-layered graphene. These molecules brought into contact with the buffer are destroyed (Fig. 3. 3).

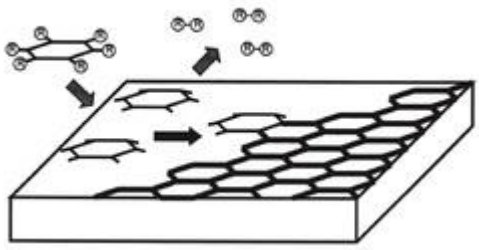

Figure 3. 3. Growth of the graphene layer by decomposition of organic halogen (Bronikowski and Manohara, 2008).

The carbon bonds are weak and easily broken under reasonable temperature. The substituent groups are detached from the carbon atoms as a volatile phase and escape into ambient. The rest of the *C*-atoms of the hexagonal ring are adsorbed on the underlay, encounter carbon atoms and create a new sheet (Bronikowski and Manohara, 2008).

3. 6 Industrial tasks

Graphene quality in combination with other solids will depend on the composition and structure of adjoining matters, their lattice coherence and commensuration, geometric arrangement of grown many-layered assemblies. Therefore, graphene mutability emerges as a key factor for both synthesis and fabrication.

A capability to produce the scale-up and uniform graphene of high quality is the main challenge for up-dated manufacturing (Berger et al., 2004, 2006; Ohta et al., 2006; Kim S. et al., 2008; Tzalenchuck et al., 2010; Wang S. et al., 2010; Presser et al., 2011; Xu et al., 2011; Novoselov et al., 2012). Because of the limitation of the exfoliation technique in regard to the scientific area, the industrial aims require the advanced development of epitaxial processes. This is the only

proper way to produce homogeneous films on a large scale of high quality and low cost. The production is reproducible by growth of one substance on the top of another so both materials have the same structural orientation. Such highly ordered carbon structures are referred to as epitaxial graphene.

The manufacturing of epitaxial graphene is advanced by means of two contrast mechanisms. Few graphene layers can be grown via chemical deposition on transition metals or carbides by using pyrolysis of hydrocarbon. Another mechanism is performed by controlled growth of the carbide derived carbon under thermal or chemical decomposition with partial material removal. Carbon is formed by selective extraction of metal or metalloid atoms. Since the sublimation rate of removed atoms is higher than that of carbon, excessive carbon is left on the surface. In this way, the carbon layer is formed by inward growth, usually with the retention of the original structure of the precursor. Rearrangement of the crystalline structure into highly ordered carbon occurs due to the self-organisation transformation.

Because the large crystals with an atomically flat surface of extremely low defects are available, silicon carbide (*SiC*) emerges as the best precursor for graphene of a higher quality. The carbide thermal decomposition is produced either in inert atmospheres or in the ultra-high vacuum (UHV). The atmospheric argon (*Ar*) environment requires the higher temperatures (1500°C – 2000°C) for *Si*-atoms to overcome the *Ar* pressure. In the case of UHV, graphene quality is lower than that grown at higher temperature. It requires the stable vacuum conditions to avoid any roughness. This technique is not compatible with some supporting structures.

For the large substrate areas the rates of silicon evaporation are held near its thermal equilibrium (Sprinkle et al., 2010; Heer et al., 2011). The process relies on the interplay between two driving mechanisms. For the initial CDC, the physical conditions, such as temperature and sublimation rate, are of great importance. Uncontrolled evaporation of silicon produces a poor graphene quality. The structure of CDC also depends on the temperature. At lower temperatures, such as 600°C, there is no significant increase in the crystallinity. At around 1000°C there is a constant increase in structural order starting with disordered amorphous carbon to dominated graphitic lattice. At higher temperatures the complementary reorganisation promotes the carbon atoms into highly ordered graphene sheets.

Both mechanisms depend on the initial surface termination. Epitaxial processes on the *Si* and on the *C* terminated surfaces are evolved to be very different

(Presser et al., 2011). Material on the *Si*-face usually has only one layer. No more than five layers may be arranged at once. The exposition of the layers is arranged in the Bernal stacking order. That is, half of the atoms lie directly over the centre of a hexagon in the lower sheet. The other stacking gives the different electronic properties. On the *C*-face graphene is typically multi-layered from 5 to about 100 layers. The *C*-face performs several layers grown, that it retains the essential feature of a freestanding graphene. The most important feature is that the layers are not Bernal stacked. The successive layers prefer to be rotated with respect to each other. The material behaves like a stack of independent decoupled layers.

Epitaxial growth via chemical decomposition by halogen compounds maintains the original shape and volume of the carbide precursor referred to as a conformal transformation. The CDC formed by selective substrate etching is possible for different carbides and halogens. Halogenations, particularly chlorination, became the key chemical methods for large-scale production. Fluorination proved to be more aggressive, either producing fluorocarbons or leading to the disintegration of *SiC*. Different methods of dry etching applied for chemical conversion are nowadays substituted by the wet etching providing the lower surface damages. For halogenated carbides, a high control over the resulting amorphous porous carbon structure is possible by the changing of synthesis conditions and carbide precursor. The treatment temperature and the halogen-carbide ratio turned into the most important key factors. In the low temperature range, below 600°C, there is no CDC formation because of the preferable aryl halides. At moderate temperatures, between 600 – 1000°C, both halides and free carbon can be observed. Under temperature as high as 1200°C or more solid carbon is the only stable product. The halogen species must be present at an excess to produce carbon without residual solids even at high temperatures. With an increased halogen-carbide ratio, the onset of carbon formation and maximum carbon yield are produced. There is an optimum value for halogen-carbide ratio, corresponding to a large range of pure carbon as the only stable product. The maximum yield of carbon can be observed at moderate temperatures for moderate halogen-carbide ratios.

The other key aspects of epitaxial growth are concerned with structural anisotropy of CDC succeeding all the substrate properties. The surface chemistry standards are not accepted for the different compounds with the same topmost atoms.

Therefore, the epitaxial growth of graphene multilayer occurs to be chemically functionalised.

Epitaxial growth and integration with the other materials proved to be of great industrial task. The moving electrons confined into 2D dimension determine graphene mutability in the different external environments. Graphene alteration evolving under interaction with the supporting matters is turned into the immediate task for advanced manufacture. Through this interaction the new properties are revealed. Any practical application requires a proper adjustment of graphene with the other solids. This is why the new composite assemblies in the alternating combinations are designed and studied, including the submitted investigation, with the subject of substrate induced interaction. The new material is made up of the few layers stacked one on top of the other that each layer is electronically independent. Two joint layers reveal the spectrum of freestanding graphene, whereas the subsequent layers add new qualities. However, no more than 10 sheets keep graphene identification. A multilayer of different numbers may be used as a building block for the graphene based system.

3. 7 Application of graphene

Graphene is the first 2D atomic crystal available for different technological aims due to its variety from electronic to mechanical supreme properties. A large number of material characteristics, such as mechanical stiffness, strength and elastic, electric and thermal conductivity, taken in their combination, means that graphene could replace other materials used for modern technology (Novoselov et al., 2005; Geim and Novoselov, 2007; Morozov et al., 2008; Seyller et al., 2008; Nair et al., 2010; Wang S. et al., 2010; Zhang et al., 2010; Heer et al., 2011; Kuroda et al., 2011; Presser et al., 2011).

Many graphene parameters are able to reach theoretically predicted limits. For instance, electron mobility under room temperature, optical absorption, intrinsic strength and conductivity, ability to sustain extremely high electric density, complete impermeability to any gases and chemical functionalisation exceeded the values measured for any other materials. However, the majority of these properties were found only in high quality samples produced in a laboratory by mechanical exfoliation. By using other methods, the different characteristics may be applicable for specific aims.

Numerous merits in the same material mean a great versatility of graphene application in various combinations of its useful properties. If these properties are transferred into particular applications, graphene will become really competitive to replace the existing benchmarks of materials (Novoselov et al., 2012). This suggests that graphene's full power may be realised through the innovations specifically designed for future prospects. This opportunity might be provided with the development of novel high technologies intended for such aims as flexible electronics, photonics, energy generation, medicine and other applications.

In the near future, the planar graphene is unlikely to be used for high performance of electronic systems because of the band gap absence. However, the other less stringent situations are developed by using the available graphene grades. Graphene has outstanding mechanical flexibility and chemical durability – very important qualities for flexible electronic devices (Bae et al., 2010). Conductive transparent coatings are widely applicable in production of touch screen displays, electronic paper and organic light emitting diodes. The endurance of electrodes in touch panels produced from graphene exceeds any other currently used materials. Electronic paper requires very small bending radius that is easily achieved by graphene. The uniform absorption is also beneficial for colour electronic papers.

Graphene moving electrons like 2D massless particles lead to significant absorption for incident light energy. Mono- and bi-layer graphene planes become absolutely transparent when optical energy value is smaller than the double Fermi level. These properties might be used for many photonic applications (Li D. et al., 2008). Graphene photo-detectors are the most actively developed photonic devices used in a wide spectrum from ultraviolet to infrared. In comparison with the other applicable materials (*In, Ga, As* or *Ge*), the high carrier mobility in graphene enables the ultrafast bandwidth operations (Meric et al., 2008; Xia et al., 2009). For modulation intensity by transmitting light the saturable absorbers are usually used. Graphene adsorbs a significant amount of photons. As a result, it reaches saturation under lower intensity of spectral range as against the ordinary semiconductors. Graphene saturable absorbers can also be applicable in semiconductor laser technology while producing a mode-locked laser for simple operations in spectroscopy, material micro-machining and medicine. Ultrafast carrier relaxation time, controllable modulation, high threshold and thermal conductivity and wide spectral range tenability emerge as the other benefits of graphene absorbers

(Zhang et al., 2010; Xu et al., 2011). Efficiently renewable technology for energy generation and storage focused at solar cells can use graphene as either the active medium or the transparent electrodes. In commercially-used lithium-ion batteries the cathodes are frequently damaged because of poor electrical conductivity. Graphene would be applied not only as advanced filler increasing electrical conductivity. It also gives the novel core-shell type of these composite structures (Yang et al., 2010). Besides, the high thermal conductivity enables the significant heat within the battery systems to be overcome. In conjunction with carbon nano-tubes and fullerenes C_{60}, graphene increases the battery charge capacity. Owing to high intrinsic electric conductivity, accessible pore structure, resistance for oxidative processes and temperature stability, graphene might be super capacitor intended for energy storage (Stoller et al., 2008). Graphene nano-sheets might be used in platinum catalysts for fuel cells. Due to the strong interaction between *Pt*-atoms and graphene, activity in methanol fuel cells should be increased (Yoo et al., 2009).

Due to the combination of mechanical, electronic and chemical properties, graphene proved to be very attractive for different composite materials as a reinforcement component. Because of very high inertness graphene is able to contribute to gas and moisture protection using a corrosion barrier against water and oxygen diffusion. Protective conformal layer is grown directly on almost any metal surface. In addition, a composite matrix might provide a number of applications beneficial for excellent mechanical reinforcement, such as temperature operating, antistatic behaviour, electromagnetic shielding, lightning strike protection and improvement of compressive strength (Young et al., 2012). Graphene large surface area, chemical purity and easy functionalisation provide suitability for sensor, metrology and bio-applications. The unique combination of thinness, conductivity and penetration properties provides excellent opportunity for drug delivery in regenerative medicine (Nair et al., 2010; Nayak et al., 2011; Sanchez et al., 2012). As a result of a large surface area and delocalised π electrons, graphene derivatives can solubilise anticancer molecules so that they are like delivery vehicles for drug distribution by means of membrane barrier penetration. However, before graphene application, manufacture and final use in the medical field, one should clarify its bio-distribution, compatibility and chronic toxicity functions.

The current graphene market is driven by requirements of special industrial operations (Novoselov et al., 2012). Graphene flakes produced by chemical

exfoliation in liquid are used for composite reinforcement, coating, transparent layers, energy storage, conductive paints/inks, bio-applications, etc. Chemical exfoliation in liquid phase is based on splitting of graphite or graphite oxide exposed into solvent with added surfactant (Hernandez et al., 2008; Blake et al., 2008; Coleman et al., 2011). A surface tension in initial solution results in the increase of graphite total area. Proceeding treatment by using sonication leads to graphite split into small platelets and significant fraction of nano-flakes. The resulting suspension is further enriched through centrifugation. After treatment the final product is disposed at almost any desired surface and reduced to graphene state. These graphene grades are evaluated for numerous applications (Segal, 2009), e.g. printing electronics, electromagnetic shielding, heat dissipating super capacitors, barrier coating and so on. Uniform graphene films are nowadays grown by chemical vapor deposition (CVD) on metal surface. The production of square metres is already available and used in many applications (Li X. et al., 2009; Bae et al., 2010). Graphene growth on thin metallic surface needs an effective control over sizes, number and crystalline orientation of produced layers. The major drawback is that the ready product should be transferred onto another substrate suitable for intended application. This transfer procedure proves as usual to be much more complicated as against graphene growth itself. The transfer processes should be improved to minimise graphene damages. The CVD processes are too expensive because of large energy consumption and problem with removal of metallic substrate particles. These films are suitable for transparent conductive coating, touch screen and other components of low performance electronics. Some applications relying on the double, triple and thicker layers of conformal growth on metallic substrate without transfer are used as a barrier against corrosion. Planar graphene grades suitable for high-performance flexible electronics, sensory and metrology standard, high-frequency transistors, etc. are produced via carbide derived carbon (CDC) generation. Silicon carbide (*SiC*) of different poly-types and top-level terminations was experimentally approved to be the best precursor for graphene of very high quality grown by sublimation of the *Si*-atoms leaving the surface (Forbeaux et al., 1998, 1999; Berger et al., 2004, 2006; Ohta et al., 2006; Virojanadara et al., 2008). However, due to the growth at high temperature and deficit of useful *SiC* wafers for a large graphene area, this route is limited for wide application. The further explorations are also required to overcome graphene defects and unwanted doping

succeeding to substrate induced interaction. The general graphene manufacture is developed depending on industrial demands. One can see the different modes of graphene production are appropriate to its application. According to purposeful destination, only planar graphene of the best quality might be currently used for electronic devices of high performance. The limited areas of consumption are supplied with the middling quality, which is too far from theoretical prediction for a pure graphene. As a means of steady progress in science, the permanent search for capabilities needs to be advanced for the highest graphene performance.

Chapter 4 Surface engineering of *SiC* substrates

4. 1 Introduction

This section is devoted to thermal and chemical transformations resulted in epitaxial graphene on the 4H-*SiC* substrate surface. At least two general circumstances should be taken into consideration for the intended surface conversion. First of all, it concerns the proper precursor for epitaxial growth. Then, the appropriate technique is required for the implementation.

A large group of carbon materials derived from carbide precursors known as the carbide derived carbons (CDC) is transformed via physical or chemical processes from amorphous carbon into highly ordered structures, e.g. crystalline graphite, carbon nano-tubes or graphene (Presser et al., 2011). The CDCs were derived from many precursors (*SiC*, *TiC*, Mo_2C, *VC*, etc.) by using a variety of conditions that lead to a broad range of useful properties.

The carbon structures resulting from the removal of metal atoms from the carbides depend on the synthesis methods, applied temperature, pressure and choice of carbide precursor. Most studies are focused on the thermal and chemical decomposition of *SiC* substrate (Muehlhoff et al., 1986; Forbeaux et al., 1998, 1999; Hass et al., 2006, 2008; Rutter et al., 2007; Hiebel et al., 2008). Graphene growth from other carbide precursors has not been studied in detail. The chemical extraction of metal atoms via thermal/hydrothermal treatment, vacuum decomposition and halogenations are the most common reactions leading to highly ordered carbon formation.

The thermal decomposition in vacuum or in inert atmospheres enables carbides to be transformed into carbon due to incongruent melting and evaporation of the constituting elements. This is because the melting point of carbon exceeds the melting points of most metals. The local oxidation and *C* excess under thermal excitation are produced either by high current density (Avouris et al., 1997, 1998) or while annealing (Forbeaux et al., 1998, 1999; Hass et al., 2006, 2008; Rutter et al., 2007). In any case, the old bonds are broken. The reconstruction of *SiC* substrate structure takes place accompanied with the surface atomic rearrangement and graphitisation.

The selective abstraction of metal atoms from carbides by means of chemical treatment using halogenations is carried out at temperatures around 200°C and ambient pressure. Both gaseous phase and solid carbon are produced as follows:

$$MC(s) + 2A_2(g) \rightarrow MA_4(g) + C(s)$$

where *M* is *Si, Ti, Zr* and *A* is a gaseous halogen *(F_2 , Cl_2 , Br_2 , I_2).* The halogen containing etchants (e.g. *HCl* or *HF*) are used as well. Fluorination with F_2 is found to be a very aggressive process, offering a low temperature synthesis (120°C) leading to either the disintegration of *SiC* substrate or fluorocarbon formation. Chemical decomposition with the selective material removal resulted from halogenation was under thorough experimental exploration (Presser et al., 2011). This revealed some evident advantages as against the other approaches. For example, it is preferable because allows to solve the problem of unwanted contaminations during the removal of decomposition products. Furthermore, the rate-determining operations using *HF/SiC* ratio can ensure the controllable surface conversion. Therefore, this case of wet chemical decomposition in electrochemical *HF* system has been chosen for the current research.

Another approach to surface modification is based on the technique of material deposition. A molecule containing carbon atoms attached to substituent groups is put on the exposed substrate surfaces. Brought into contact with the solid surfaces, these molecules are decomposed under catalytic effects. The substituent groups are detached and escape in a volatile phase. The carbon atoms encounter while forming *C*-layer. The aromatic compounds arranged into the hexagonal rings added with the gaseous halogen radicals would be the proper precursor for this technique (Olander and Larsson, 2004; Bronikowski and Manohara, 2008).

The advanced methods of scanning probe microscopy lithography (SPML) enable the synchronous surface effects of different origin to be generated. The high resolution mapping and spectroscopy combined with the STM and AFM lithography emerge as a unique tool for nano-scaled fabrications and characteristics of interface quality. The lithographic technique is divided into three categories: surface modification (1), material deposition (2) and material removal (3). The different energy sources including thermal, mechanical, electrochemical, etc. supply these transformations. Modification of the surface may involve the processes of local oxidation (LO) on the solids introduced by the SPM coated tips or current density.

The tips and substrates should be conductive and substrates should form stable oxides. By moving the biased tips in contact or non-contact mode close to the solid surfaces, a high electric field is induced while forming the ionisation of water molecule from the ambient interface between cathode (tip) and anode (substrate). The produced OH^- ions provide the oxidant for electrochemical reaction. As the vertical drift enhances, the OH^- ions react with ad-atoms of substrate to form localised oxides (Avouris et al., 1997, 1998; Tseng et al., 2005; Sugimoto et al., 2005, 2007, 2008).

4. 2 *SiC* conversion by thermal decomposition

Epitaxial growth of graphene by thermal decomposition of *SiC* substrate is a promising way to large-scale and low-cost production, because this carbide precursor is the only carbide which is performed by available large single crystals without surface defects. This procedure requires stable vacuum conditions, heating either in inert atmospheres at ambient pressure, or extremely low oxygen partial pressures.

There are several limits for this processing. Factually, the optimal graphene domains can be realised only on atomically flat *SiC* surface, free from any defects. However, *SiC* surface on atomic level is characterised by many steps and terraces. It is a serious problem because graphene nucleation starts just at these terraces. Also, the numerous nano-structural pits and caps are performed at temperature below 1200°C associated with the point defects on *SiC* surface. The thicker layers usually exhibit many wrinkles. Some operations exist for treatment to remove these defects a priory graphene synthesis. A chemical etching and mechanical polishing are commonly useful to a certain degree but not sufficient for ideal flatness. From a structural point of view, the top-most surfaces should be thoroughly selected and prepared for the proper basal graphene layer evolving under close interaction with the supporting framework. This layer known as a buffer is intermediate isolating substrate from the subsequent *C*-layers. The specific honeycomb lattice is formed within the buffer layer while defining the graphene properties. This is why the perfect interfacial layer plays a crucial role in the FLG growth as a whole.

One more requirement of great importance concerns a regulation of graphene growth because graphene shows a decay of properties with increasing number of layers. Thus, one should choose suitable annealing conditions, the heating rate or

time/temperature to minimise excess carbon. The *Si*-face top level has a slower growth rate and allows a better control over the number of layers.

4. 3 Chemical modifications of *SiC* surfaces

Chemical mechanism of epitaxial growth on *SiC* support, as usual for the surface processes, is hidden away owing to intervening reactions running via interface. Since the surface reactions are of irreversible character, only the initial reactants and target products are definite, whereas the interim products are estimated by computational proceeding or hypothetical guesses. Surface conversion and epitaxial growth of *C*-films perform a succession of interim products and structural reconstructions that are concealed behind the interfacial events (Gates, 1992). The serious requirements exist for the basal layer, i.e. interface between substrate and subsequent *C*-films. The interface quality is determined by structure of *SiC* poly-type (1), periodicity of unit cell (2), top-level termination (3), geometrical commensuration of adjacent layers (4) and stacking order between crystalline lattices of initial and final products (5). The bonds and position of *C*-atoms in the geometrically correct adjustment determine the best interface quality and subsequent arrangement of multilayer. The coordinates of all carbon atoms should be calculated with a view to the proper connexion of all consistent layers.

4. 3. 1 Material removal from *SiC* surfaces

After initial dehydrogenation and activation of *SiC* surface –

$$[SiC - H] + X \rightarrow SiC + HX \quad (1)$$

where *X* is *F, Cl or Br* (Olander and Larsson, 2004), a catalytic mechanism is launched for synchronous processes of interaction and local oxidation as follows:

$$Si^{4+}\, C^{4-\,(L)} + 4[H^{+}\,(OH)^{-}]^{(S)} \rightarrow Si(OH)_4 + [C^{4-} - 4H^{+}] \quad (2)$$

$$(OH)^{-} \rightarrow O^{2-} + H^{+} + vacancy \quad (3)$$

$$Si(OH)_4 + [C^{4-} - 4H^{+}] \rightarrow SiO_2 + C + 2H_2 + 2H_2O \quad (4)$$

While running under humidity in an aqueous ambient, the reaction (2) involves a disintegration of OH^{-} group (3). The O^{2-} ions are captured into *SiC* lattice while forming SiO_2 (4) and vacancy site in interface. The oxidation state of carbon atoms is enlarged since its electrons are taken away by the protons while restoring the

electrochemical balance. A new vacancy is filled with oxidised *C*-atom. The endothermic character of this reaction was revealed for both terminations. The specific enthalpies for the initial and final truncated blocks were calculated. The value of $\Delta H = +\ 704$ kJmol^{-1} and endothermic effect are attributed to high energy for old bonds breaking at the range of T = 850 – 1400°C. The reaction of local oxidation was experimentally promoted by lithography technique (SPML) producing the OH^- ions to form localised oxides controlled by applied bias, set current, number of pulses, humidity, tip/sample distance, etc. (Tseng et al., 2005).

The surface modification under oxidation is enforced by addition of atomic *F* added in diluted *HF* solution. The experimental and theoretical studies of *Si – F* interaction provide an advanced experience for chemical modification on the *Si*-terminated surfaces in form of SiF_4 removal (Winters, 1983; Winters and Houle, 1983; Houle, 1986; Coburn, 1986, 1994; Garrison and Goddard, 1987; Wu and Carter, 1991; Flowers et al., 1995; Yih et al., 1997; Wang J. et al., 1998; Scofield et al., 2000; Edwards et al., 2000; Kim B. et al., 2002; Jiang L. et al., 2003; Chang and Coburn, 2003; Gou et al., 2007; Batisse et al., 2010).

Fluorine dry etching is performed as follows:

$$Si^{4+}C^{4-} + 2F_2 \rightarrow C^0 + SiF_4\uparrow \qquad (5)$$

In case of wet etching, the intervening reactions running through the interface resulted in local oxidation. The transition is schematically viewed as follows:

$$Si^{4+}C^{4-} + 4HF \rightarrow C^0 + SiF_4\uparrow + 2H_2\uparrow \qquad (6)$$

The generalised transition (5) is interpreted through few proposed interim products. Surface rearrangement in the moist ambience is expressed by reaction (6). Oxidised *C*-atoms are realised while electrochemical reaction growing the interfacial layer. The driving mechanism for graphene ring formation is ensured with promotion effects and sp^2 hybridisation.

4. 3. 2 Material deposition

The generally known operations with pyrolysis proceeding from hydrocarbon decomposition on exposed catalytic surface are applicable for the upper *C*-layer epitaxial growth. The aromatic hydrocarbons were found to be the proper precursor for material deposition on the solid surface resulting in graphene layers. The

molecules of aromatic halogen groups also contain carbon hexagonal ring, each one bonded with the additional halogen atoms, e.g. *F, Cl, Br, J.* These compounds are already arranged like the atomic structure of graphene. From the available reactants the aromatic halogen benzenes group structurally coherent for graphene occurs as a better relevance. The hexahalogenated benzenes corresponding to $C_6Cl_{(6-n)}Br_{(n)}$, $C_6Cl_{(6-n)}I_{(n)}$, $C_6Br_{(6-n)}I_{(n)}$ solid solutions are put forward for further consideration. These compounds are crystallised either in the monoclinic or triclinic space system. The first case isostructural to the hexachlorobenzene (C_6Cl_6) or chlorocarbon is more common and appropriate to crystallographic disorder. The planar molecules form *Cl⋯Cl* contacts and also π⋯π stacking interactions.

When the crystals are mechanically compressed, the dislocations take place leading to weakness of the bonds (Reddy et al., 2006). The bending related to the *Cl⋯Cl* interactions is weaker in comparison with the stronger π⋯π stacking interactions. C_6Cl_6 is soluble in benzene while making the bonds very weak. Its boiling point is around 323 – 326°C. The crystals readily participate in nucleophilic substitution resulting in carbocations.

Coming into contact with the catalytic surfaces, these molecules are decomposed because the *C*-bonds are weak enough to be easily broken at the low temperature T = 25 – 300°C (Srinivasan and Parsons, 1998). The activation barrier is approximately close to zero. It points to the spontaneous reaction as follows:

$$6C + C_6Cl_6 \rightarrow 6[C - C] + 3Cl_2\uparrow \qquad (7)$$

4. 4 *Si – F* interaction under fluorine attack

Although there are a lot of routes how the *F*-atoms are bonded to the *Si*-face substrate, it is mainly SiF_4 that desorbs from surface.

4. 4. 1 Interaction in the fluorosilane layer

By means of photo emission it was found that a fluorine etching results in fluorosilane layer formation of 10 – 20 *Å* thickness with high concentration of *SiF*, SiF_2 and SiF_3. The final rate determining step forms the product SiF_4 from atomic *F* and SiF_3 still bonded to other atoms. For the *n*-doped substrate the reaction rate is 2.5 times faster than for the intrinsic silicon and the fluorosilane layer is thinner. For the *p*-doped type the rate is 0.8 times slower but the SiF_x layer is thicker.

The adsorption of fluorine on the silicon surfaces was ab initio electronic structure calculated (Wu and Carter, 1991). In the course of the successive addition of atomic fluorine to the topmost *Si*-atoms, it was found that a build-up of 2-6 layers of fluorinated silicon should be formed before the start of the etching process. The interaction with fluorine on the *Si* (100) - (2×1) surface revealed that the *F*-atoms initially attack the *Si*-dimer dangling bonds of the first monolayer or alone pair of electrons. This process proved to be non-activated and its exothermic effect is 5.5 – 6.5 eV. After saturation of dangling bonds the surface is covered with the *SiF* group only. The second step and forming the SiF_2 group requires a breaking of *Si – Si* bond that costs of 2.1 eV, equal to dimer energy. The third *F*-atom addition leads to formation of *SiF* and SiF_2 groups covering the surface. The adjacent of SiF_2 group have the huge nearest neighbour repulsions. Therefore, SiF_2 is predicted to be less favourable on the surface due to repulsive interactions, and the etching of *Si*-atoms occurs more quickly against the *SiF* group. It seems to be easy for *F*-atoms to be attached to the dangling bonds on the *Si*-terminating surfaces and form SiF_x, where X = 1, 2 and 3. The final rate determining step results in the product SiF_4 formed from *F*-atom and SiF_3 group still bonded to substrate.

The quantum-mechanical calculations (Garrison and Goddard, 1987) showed that the *Si – Si* bond is attacked by *F*-radical to form SiF_4 according to the scheme of rate-determining transition shown as follows:

$$F + F_3Si - SiH_3 \rightarrow SiF_4 + SiH_3$$

The transition state has the *F – Si* distance of 2.35 $\dot{A}$ and activation barrier of 1.0 ± 0.2 eV. Since the reaction is highly exothermic any distortion will tend to weaken the *Si – Si* bond and the value of activation energy should be lower. This low barrier is owing to the fact that the attacking *F*-atom is a radical. In the transition state the electron from *Si – Si* bond is accepted and the SiF_3 group is transferred to radical. It also easily explains the difference of the etching rates between the *n*-doped and *p*-doped crystals. As for the *n*-doping, there is a high electron density for promotion. In the case of the F^- ion the process would be slower.

4. 4. 2 Atomic *F* uptake on *SiC*

Although the study of gas-surface interaction is extensive, the probable mechanisms of fluorine etching on *SiC* surface are still poorly understood (Batisse et al., 2010;

Presser et al., 2011). The former experiments were recently supported by the advanced molecular dynamic simulation resulting in preferential etching of *Si*-atoms and *C*-rich interfacial layer (Gou et al., 2007). The exploration was focused on surface modification under uptake of atomic *F*, the yield and rates of *Si* and *C* etching from substrate and composition of the final products. The structure of modified surface proved to be strongly sensitive to the incident energy. Increased energy for one order resulted in enlargement of interfacial layer thickness by more than two times.

Carbon rich interface was formed because *Si – C* bonds are broken and crystalline structure does not exist anymore. Subsequent *F*-atoms penetrated into the bulk, reacted with *Si*-atoms while breaking the *C*-atoms bonds and forming volatile product. As a result, the *Si*-atoms were preferably removed, whereas *C*-rich interfacial layer was formed. The total yield of SiF_x ejected from the surface was much higher than CF_x. For incident energy, less than 10 eV the main etch product SiF_4 is only dominant followed by SiF_2 and *SiF* under higher energy. The clusters *SiF*, SiF_2, SiF_3, SiF_4, CF_2 occur in interface. Also, $Si_xC_yF_z$ products were found among the interfacial clusters.

Thus, the complicated mechanism of *F* interaction on *SiC* surface was found including the numerous interim products. The *C*-films of best quality were recently produced by experimental formation on the *SiC* surface at low T = 120 – 130°C. The new films were rearranged themselves to form a nano-structured carbon of sp^2 hybridisation (Batisse et al., 2010).

4. 5 Carbon growth on *SiC* substrate

Carbon is one of the most promising for the development of materials with controlled properties. It can be produced by many different methods. One of the most versatile in terms of a variety of structures is selective etching of carbides. Since the metal atoms are extracted layer by layer, atomic control of the carbon structures can be achieved. Carbon produced by this method is called carbide derived carbon (CDC). Numerous families of materials derived from carbide precursors are transformed into pure carbon via physical (thermal decomposition) or chemical (halogenation) processes. Structurally, CDC family includes a large group of materials from fully amorphous to highly ordered carbon. Any known structures – graphene, nano-tubes, diamond or porous amorphous networks – can be synthesised.

4. 5. 1 CDC synthesis routes

The structure resulting from removal of the metal or metalloid depends on applied temperature, pressure and choice of carbide precursor. Studies of binary carbides with different grain sizes show the possibility of low temperature formation.

Thermodynamic analysis shows the possibility of CDC synthesis from almost any carbide under appropriate T – P parameters and etchant. The cornerstone of all current developments is a relationship between the carbide structure, synthesis conditions and the resulting properties. The most experiments were obtained on *SiC* (Yushin et al., 2006, Presser et al., 2011). A better understanding of graphene formation during high temperature vacuum decomposition of *SiC* is achieved because the single crystals are now available with extremely low defect concentrations.

Several chemical and physical processes can be used for CDC synthesis. Thermal decomposition in a vacuum or in high temperature inert atmospheres transforms carbides into carbon due to incongruent melting of carbide and evaporation of the carbide forming elements, as the melting point of carbon exceeds that of most metals. The potential of vacuum decomposition to synthesise high purity epitaxial graphitic carbon was demonstrated. Hydrothermal treatment is another way for reactive chemical removal of metal or metalloid atoms from the carbide network. To produce CDC, hot water at typical temperatures in the range of 200 – 1000°C and pressures of up to hundreds MPa should be provided. Thermodynamic calculations by using Gibbs potential for a number of metal carbides under hydrothermal conditions were carried out for system $MC - H_2O$ with *M = Si, Ti, Ta, Nb, W* or *B* (Jacobson et al., 1995). The thermodynamic analysis indicated the main products of reaction: *MOx*, CH_4, CO_2, *CO* and H_2. The chemical extractions of *M*-atoms via halogens are the most common reactions leading to the carbon formation. The carbon formation by means of selective carbide etching is possible for many carbides and different halogens leading to reaction:

$$MC(s) + 2A_2(g) \rightarrow MA_4(g) + C(s)$$

where *M = Si, Ti* or *Zr*; *A = F, Cl* or *Br*. MA_4 is a gaseous reaction product. Selective extraction of *M*-atoms from the carbide lattice was carried out at elevated temperatures above 200°C and ambient pressures for many of carbides. The thermodynamic simulations for interactions of a variety of carbides with different

halogens such as *F*, *Cl* and *Br* and halogen containing gases such as *HF* and *HCl* confirmed the possibility for CDC formation. For halogenated carbides, a high level of control over the resulting amorphous porous carbon structure is possible by changing the carbide precursors and synthesis conditions.

Chlorination became one of the key synthetic methods for large-scale production. Chlorination is the most economic and scalable method for CDC synthesis. Chlorination of *SiC* was the first experiment producing CDC (Hutchins, 1918). By exposing hot silicon carbide to dry chlorine gas, the formation of silicon tetrachloride and residual carbon was observed as follows:

$$SiC(s) + 2Cl_2(g) \rightarrow SiCl_4(g) + C(s)$$

Many investigations were carried out for chlorination of *SiC*. The multiplicity of carbon structures from amorphous carbon to diamond were found (Welz et al., 2006). The chlorination required high temperature of 900°C to produce $SiCl_4$ instead of CCl_4. The treatment temperature and the halogen-carbide ratio are the most important factors of thermodynamics.

For CDC formation, three different temperature intervals can be determined (Dash et al., 2005; Presser et al., 2011). Under a temperature below 400°C no CDC is predicted because CCl_4 is preferable. Under a moderate temperature of 400 – 600°C, both CCl_4 and carbon are formed. Under a temperature regime of 600°C and higher the solid carbon is the only stable product. Under lower temperatures there is no significant increase in the carbon crystallinity. Under higher temperatures, graphene sheets and ribbons are formed. It is also evident from calculation that the halogen species must be present in excess to produce carbon without residual solids even at 1200°C. With increased halogen-carbide ratio, the maximum carbon yield was found.

4. 5. 2 Fluorination

Fluorination is proposed as another way for halogenations to facilitate carbon synthesis. It results because the volatile SiF_4 is easily evaporated from the *C*-atoms (Fracassi and d'Agostino, 1992). Thermodynamic studies are required to determine the synthesis temperatures, carbide structure and carbide-fluorine ratio to avoid the fluorinated carbon formation. Fluorination is not a chemical process easily produced by different routes. The electrochemical reactions in terms of the liquid

agents need a very high concentration of *HF* for a rather low reaction yield (Matsuo et al., 1998; Abe, 2000). Therefore, gaseous fluorination using the pure fluorine or plasma is preferable. Non-fluorinated CDC was described in the case of XeF_2 etching under low temperature of 120°C (Batisse et al., 2010). However, the dry methods commonly result in ion induced damage on the etched surface undesirable for the device operations. The wet etching substituting the dry method results in low damage characteristics. This is why the electrochemical methods providing the homogeneous surface have a better potential for the fabrication.

Fluorination with F_2 or with a milder agent was shown to etch a large number of carbides (Al_4C_3, B_4C, CaC_2, Cr_3C_2, Fe_3C, SiC, ThC_2, TiC, WC). For ternary carbides, more complex reaction equations must be written. Direct fluorination of SiC was found to be very aggressive, as against an alternative chlorination (Yushin et al., 2006). The etching of *Si*-atoms leads to steady surface layer containing the high concentrations of SiF, SiF_2 and SiF_3. It predominates that SiF_4 evaporates as the volatile rate determining phase. This process produces fluorocarbons from carbides and leads to the disintegration of SiC thin films (Presser et al., 2011).

Thus, a halogen can be successfully promoted for the CDC synthesis at the variable rates. In particularly, there is a great dependence on the physical conditions, carbide precursor and halogen structures. While using the different oxidising routes by halogen treatment the novel surface properties for the future rewards are produced (Abe, 2000; Shin and Song, 2002; Zinovev et al., 2004).

The electrochemical transformation of carbides under *HF* electrolyte based on another oxidising scheme promises much for the pure CDC. It enables production of a high structural homogeneity of a resulting surface and avoids the side products of contamination. Due to the fact that oxidation state of *F* in *HF* molecule $= -1$, as against the atomic or molecular fluorine, where oxidation state of $F = 0$, the carbon oxidation resulted after *Si – F* interaction runs via the *H*-atoms, which escape in gaseous phase:

$$SiC + 4HF \rightarrow SiF_4\uparrow + C + 2H_2\uparrow$$

These processes are not yet understood well and should be thoroughly studied.

4. 5. 3 Graphene by *SiC* decomposition

Along with amorphous carbon and graphite like structures many other carbon nanostructures were observed during CDC process. Formation of well-ordered graphene by halogenations showed that graphene growth on carbides is achieved in various environments. Crystalline carbon evolves at higher temperatures.

Graphene is the product of *SiC* vacuum decomposition or heating in inert gas atmospheres (Forbeaux et al., 1998, 1999; Zinovev et al., 2004; Berger et al., 2004, 2006; Rollings et al., 2006; Yushin et al., 2006; Hass et al., 2006, 2008; Heer et al., 2011; Presser et al., 2011). The temperature of graphene formation in CDC seems to be strongly dependent on the initial carbide, its purity, presence of catalyst particles and selected halogen. In a recent study, it was shown that the charge carrier type and concentration of epitaxial graphene may be controlled by the substrate. Optimal graphene growth may be observed only for atomically flat and defect free surfaces. The *SiC* wafers etching, prior to synthesis is a possible route to remove surface defects. The *SiC* of *C*-face termination shows that graphene is often distorted by nano-caps. Control over graphene growth is important because graphene multi-layers show decay with increasing number of layers approaching the properties of graphite bulk.

Thus, one should adjust the heating rate or time/temperature to minimise excess of carbon formation during heating and choose suitable annealing conditions. The *Si*-face has a slower growth rate and allows a better control over the number of layers. The initial stage of graphene layer formation at terrace steps is characterised by step bunching of two *SiC* bi-layers. Also, substrate orientation is important. As step erosion continues, graphene films are formed promoted by enhanced carbon mobility at high temperatures around 1200°C. For the *Si*-face termination, *SiC* is firstly reconstructed to form a so-called “buffer” layer with a carbon density close to that of graphene monolayer and close interactions with the *SiC* substrate. Layer **1** will then be formed on top of the buffer layer. The buffer layer provides some isolation from the substrate while giving rise to the well-known honeycomb-like structure. Subsequent graphene layers will then be formed as the *SiC* decomposition progresses (Presser et al., 2011).

Graphene formation was described for the doped (*n*-type and *p*-type) and semi-insulating silicon carbide (Rutter et al., 2007; Cambaz et al., 2008; Ni et al., 2008; Yang et al., 2010). Graphene attached to *SiC* does not necessarily show the

same properties as exfoliated and suspended samples. As a consequence of the interaction between graphene and carbide substrate, the electron mobility is lower by an order of magnitude. Graphene growth from the other carbide precursors is possible, even at the temperatures lower than for the graphene from silicon carbide. However, it has not been studied yet.

4. 6 Capability for surface modification

The SPM applications within the main scanning technologies on the basis of STM and AFM techniques enable the universal operations involving the material removal and material deposition under different mechanism and energy sources. Surface conversion by the SPM-based nanolithography (SPML), which has progressed since the 1980s, offers a wide spectrum of methods for material modification (McIntyre et al., 1994; Hersam et al., 1999; Hla et al., 2000; Oyabu et al., 2003, 2006; Morita et al., 2004; Tseng et al., 2005; Nishi et al., 2006; Katano et al., 2007). Along with the conventional SPML based on the AFM, STM and other advanced techniques, the universal operations for surface modifications are developed. The composite reactant decomposition, thermo induced and electric induced transformations, self-assemblage processes, mechanical scratching, chemical etching, galvanisation and electrochemical reactions are promoted under variable driving mechanism. The principles of mechanical chemistry allow the different manoeuvres by removing unwanted pieces and position of the new ones. The material decomposition and removal by using the AFM has been employed in terms of current induced local oxidation (Avouris et al., 1997, 1998). Under high current densities the electrochemical processes with the complementary REDOX effects are stimulated. A high electric field close to the surface between cathode (tip) and anode (substrate) results in ionisation of electrolytic molecules while providing the oxidants for the electrochemical reactions. As the vertical drift enhances the anions are collected close to the substrate which acts as anode electrode. While aiding decomposition by chemical etching in *HF* solution the activated *Si*-atoms on the surface react with anions to form an oxidised carbon (Michler et al., 2004). The AFM tip under negative bias is capable of etching a graphite surface and carbon nano-tubes (Kim D. et al., 2003). Both tip and substrate should be conductive and form stable oxides. The surfaces need to be regularly cleaned from oxides.

With a view to material deposition many useful experiences were implemented by using the STM technique. The tip is employed as an emission source of atoms or nano-particles delivered to the target surface controlled by the adjoining pulse duration and voltage. The threshold voltage of a few volts is changed in dependence on the tip and the sample material, the distance and configuration of the tip/target space and the polarities. The stable transfer results are usually reached by means of the tip negative polarity. Also, the STM-based modification is adjusted for gaseous precursor decomposition and electrochemical reactions in electrolytes. By means of applying the cathode and anode potentials, the different mechanisms of reaction were roused. A controllable conversion on some semiconductor surfaces was carried out by the STM in the presence of *HF* solution (Nagahara et al., 1990; Ye et al., 1995). Meanwhile, the new opportunities for surface modification were developed known as the Dip Pen Nanolithography (DPN). This is a lithography technique; the tips transferring the molecules or atoms make up the patterned substrate surfaces. The AFM tip with a chemical compound acts as a "pen" while writing the nano-scale patterns on a surface. This direct write technique offers high resolution for the molecular “inks” on a variety of metals, semiconductors and other functionalised surfaces. The molecular inks are usually composed of small molecules coated on a tip and delivered through a water meniscus. The liquid inks can be any soluble material under deposition conditions determined by variables of temperature, humidity, tip/substrate interaction and the physics-chemical relevance of the liquid and the substrate. The narrow gap between tip and surface behaves as a tiny capillary that condenses water from the air. This tiny water meniscus is used as a nano-metre sized electrochemical cell in which metal salts can be dissolved and delivered to the surface for localised chemical reactions with precise control of position. The only pre-condition is required that the reaction products should be insoluble in the transport medium. Thus, the advanced SPMN techniques are based on the contamination of the tip apex with the transferred chemical composition delivered through “pick and place” mechanism in precise mechanical contact with the worked-out surfaces. The last success with lateral and vertical atom-by-atom manipulations reopened a new capability for sophisticated patterning of desired structures. In the course of intended modification the active pieces contaminating the tip apex enable the substrate particles to be inserted and substituted. During the short-range chemical interaction the unwanted atoms are withdrawn from the surface.

Chapter 5 Theoretical basis

5. 1 Introduction

The only theory given by quantum mechanics is available for all branches of nanotechnology. Theoretical and computational explorations of nano-structures are concerned with the laws of quantum theory proper for engineering, device construction, mechanical fabrication, catalytic industry, medicine, biology, etc. (Schommers, 2007).

Quantum mechanics provides the possibility of calculating the atomic nuclei-electrons systems in any situation and thus predicting the properties of materials governed by the behaviour of electrons. Almost all the material properties are in dependence on the total energies of atom aggregates determined by computations. Therefore, it would be pertinent to review the general theoretical postulates concerning the relevant concepts and ideas used and developed in undertaken research. The following essay is composed on the basis of well-known fundamental works (Payne et al., 1992; Koch W. and Holthausen, 2001; Levine, 2002, 2009; Segall et al., 2002; Martin R., 2005; Kohanoff, 2006).

More than 80 years ago Heisenberg and Schrodinger introduced the mathematical formalism of quantum theory. However, the interpretation of its states remains controversial. Many problematic questions have arisen. For instance, how much can one know about the state of a system? What is the most probable interpretation for the nature of wave function? What constitute and reflect our measurements? Although similar questions are extensively discussed, the quantum theory has already proved its own capacity while providing, in practice, good understanding of a wide variety of phenomena confirmed by proof of principles experiments. The success in nanotechnology may result in the further development of theoretical approaches and methods.

5. 2 Approaches to the prediction of electronic structures

The fundamental laws of quantum mechanics state that any system of interacting electrons and nuclei is characterised by the special wave function that comprises the whole information about the system (Atkins, 1998; Levine, 2002, 2009; Kohanoff, 2006). All the properties may be expressed in terms of this wave function $\boldsymbol{\psi}$ defined

by the time-independent Schrodinger equation. For the general case the particle of mass $\boldsymbol{m}$ moving in three dimension space with energy $\boldsymbol{E}$ may be described by the full equation: $\hat{\boldsymbol{H}}\boldsymbol{\psi} = \boldsymbol{E}\boldsymbol{\psi}$. If the wave function has the value $\boldsymbol{\psi}$ at point $\boldsymbol{r}$, the probability of particle finding is proportional to $|\boldsymbol{\psi}|^2\boldsymbol{dr}$, where $\boldsymbol{dr} = \boldsymbol{dxdydz}$. The wave function $\boldsymbol{\psi}$ depends on all nuclear and electronic coordinates. Because of the large difference in mass between electrons and nuclei, the electronic and nuclear motions might be separated. For these reasons, the full wave function is represented as the product of nuclear and electronic wave functions. This approximation is known as the Born-Oppenheimer approximation.

Useful information concerning all properties of a system rests upon correct interpretation of electronic structure in terms of the wave function. The properties defined by electronic structure fall into two categories: determined by electronic ground state - (1) and by excited states - (2). One of the crucial problems is to find the ground state of inhomogeneous system containing $\boldsymbol{N}$ interacting electrons and consequently determine the total energy, band structure, density of states, phase transition between structures, transition state, etc.

The key issue for analysing the structure of matter is to solve the electronic Schrodinger equation for the system of $\boldsymbol{N}$ interacting electrons in the Coulomb's field generated by atomic nuclei:

$$\hat{H}_e \Phi_n(R,r) = \varepsilon_n(R)\Phi_n(R,r)$$

Where: $\Phi_n(R,r)$ is the eigenfunction of electronic Hamiltonian operator $\hat{H}_e$, $\varepsilon_n(R)$ is its eigenvalue (Kohanoff, 2006). Solving this equation means making the electronic structure calculation. The electronic Hamiltonian operator $\boldsymbol{H_e}$ plays the special role in quantum mechanics. It corresponds to the sum of operators for kinetic and potential energies of electrons. For the full Schrodinger equation the wave function $\boldsymbol{\psi}$ is an eigenfunction different for each eigenvalue $\boldsymbol{E}$ (energy). The electronic structure calculations imply finding the eigenvalues $\boldsymbol{\varepsilon_n}$ and eigenfunctions $\boldsymbol{\Phi_n}$ of the electronic Hamiltonian operator $\hat{H}_e$:

$$\hat{H}_e = -\frac{\hbar^2}{2m}\sum_{i=1}^{N}\nabla_i^2 - e^2\sum_{I=1}^{P}\sum_{i=1}^{N}\frac{Z_I}{|R_I - r_i|} + \frac{e^2}{2}\sum_{i=1}^{N}\sum_{j\neq i}^{N}\frac{1}{|r_i - r_j|}$$

The first term corresponds to the electron kinetic energy; the second term is the electron-nuclear interaction; the third term is the electron-electron Coulomb's

repulsion. N – number of electrons, P – number of nuclei, Z_I – charge of nucleus I, R_I – coordinates of nucleus I, r_i – coordinates of electron i (Kohanoff, 2006).

In principle, every system may be described by the Schrodinger equation. But in practice, only few cases, such as hydrogen atoms or H_2 molecules, may be completely solved. The fact is that the electrons cannot be treated as the individual point-like entities because the electron in some region influences the behaviour of all the other electrons in the other regions. This is why the quantum many-body problems arose. In the many-electron system the wave functions cannot be the simple product of wave functions for individual electrons. As to the many-body system, the main problem concerns the effects of the electron-electron interaction. The probability of electron finding at $\boldsymbol{r}$ depends on the location of other electrons. This phenomenon known as **correlation** means that the many-body function depends on several coordinates. The Schrodinger equation cannot be easily decoupled into the set of equations because there are $3(P+N)$ coupled degrees of freedom. This is the reason why one needs to resort to the approximations. The first is the adiabatic one separating the motion of nuclei and electrons (Born and Oppenheimer, 1927).

There are great ambitions to study properties regardless of approximations and free parameters. The relevant approach is known as **ab initio**. This approach indicates that the calculations are carried out on **the first principles** from the fundamental physical laws (Payne et al., 1992). It means that the calculations do not use any empirical data but only molecular Hamiltonian corresponding to the ion specifications. For the practical aims the system of electron interactions is usually reworked into another system where interactions are expressed in terms of $\boldsymbol{V_{eff}}$, *i.e.* some effective potential acting on independent electrons. Factually, the problem is solved by means of the transformation of full $\boldsymbol{N}$-body equation into $\boldsymbol{N}$ single-body equations:

$$\hat{H}\psi_n = \left(-\frac{\hbar^2}{2m}\nabla_i^2 + V_{ext} + V_{eff} \right)\psi_n = \varepsilon_i \psi_n .$$

ψ_n is n^{th} one-electron wave function, $\boldsymbol{V_{ext}}$ - external potential of the nuclei, $\boldsymbol{V_{eff}}$ is the effective potential where electron interaction is "hidden" (Segall et al., 2002).

The majority of **ab initio** methods are applicable only to the simple systems of few atoms, whereas their capacity for a real system is extremely limited. In the very beginning, the basic assumption was that many-electron wave functions may be considered as a simple product of one-electron orbitals. For the early approach $\boldsymbol{V_{eff}}$

was introduced to be the average Coulomb potential between the electrons. The simplest approach known as the Hartree's approximation treats the electrons as distinguishable particles (Hartree, 1928). This approach is not realistic because it corresponds to the completely uncorrelated system where the two-body interaction assumes a continuous distribution of charge. This approach does not take into account the exchange energy contribution dictated by Pauli's principle.

The next step of approximation is associated with the Hartree-Fock (HF) method that introduces the exchange energy contribution (Slater, 1928; Fock, 1930). The HF potential is non-local and takes the total wave function to be anti-symmetric upon exchange of any two electrons. The anti-symmetry character of wave function of many-electron system produces the separation of electrons with the same spin that reduces the Coulomb energy for the value of **exchange energy**. This reduction is referred to as the HF approximation that includes the exchange energy but neglects the correlation energy. The difference between total many-body energy $\boldsymbol{E_{tot}}$ and the $\boldsymbol{E_{HF}}$ value is called the **correlation energy**. The HF wave function enables us most of the total energy calculation. However, the separation of energy into different contributions – direct Coulomb, exchange and correlation energies – may be in general case different from the admitted methods and depends on the framework. The significant achievement by Hartree and Fock concerns the atomic orbitals and molecular orbitals based on the equation: $\hat{F}\phi_i = \varepsilon_i\phi_i$, where $\hat{F}$ is the Fock operator. Each spatial orbital ϕ_i is the function of three spatial coordinates of single electron; ε_i is the energy of orbital ***i***. The variational wave function is the product of the best possible orbitals and called the Hartree-Fock wave function. The most convenient way to express the HF orbitals is the linear combinations of functions called in this case **basis functions**. The set of these functions is referred to as the complete set. The Hartree-Fock wave functions were calculated for the ground state of first atoms of the periodic system. In general, the many-body wave functions cannot be written as the anti-symmetrised product of one-electron orbitals.

In summary, the total energy of many-body electronic system may be separated into different contributions: $\boldsymbol{E = T_R + V_{ext} + E_H + E_{XC}}$ (Kohanoff, 2006), where $\boldsymbol{T_R}$ is the non-interacting kinetic energy, $\boldsymbol{V_{ext}}$ – the interaction of electrons with external fields, e.g. atomic nuclei. The third term $\boldsymbol{E_H}$ is known as the classical electron-electron interaction or Hartree term. The last term is the exchange-

correlation energy $\boldsymbol{E_{XC}} = \boldsymbol{E_X} + \boldsymbol{E_C}$. The calculation of the correlation hole, i.e. the part resulting from the deduction of the exchange depletion, is the great challenge. While the exchange energy contribution is well-determined, the correlation energy contribution is not available as to exact calculation. The approaches for correlation energy calculation were developed within the limits of density functional theory. Also, the first principles application was refined during the last years. Recently, it was relevant for the system only of few atoms. Nowadays, the new methods are applicable to the system of many hundreds and even thousands of atoms, e.g. the total energy pseudo-potential methods (Phillips, 1958; Yin and Cohen, 1982), molecular dynamics (Car and Parrinello, 1985), conjugate gradient (Teter et al., 1989; Gillian, 1989) and others. These methods enable the quantum mechanical simulations for very large systems.

5. 3 Density functional theory

Since the end of the 1920s, the contrast approach has been simultaneously developed giving rise to the density functional theory (DFT) (Koch and Holthausen, 2001). It was based on the initial works of L. H. Thomas and E. Fermi, who proposed the prescription for electronic system energy calculation in terms of electronic density (Thomas L., 1927; Fermi, 1928).

The theoretical ground was initially formulated by the Hohenberg-Kohn theorem (Hohenberg and Kohn, 1964). This theorem put forward the crucial basis for the DFT. The main idea was that the total energy for system of electrons in external potential is the unique functional of ground state density. This approach does not concern a multidimensional many-body wave function. Instead, the energy is expressed in terms of the electron density. The DFT corresponds to the alternative form of first principles application: (1) – the energy for total system of electrons and nuclei is the unique functional of electron probability density; (2) – the variational minimum of energy is exactly equivalent to the ground state energy; (3) – the ground state properties may be calculated from the electron density.

The total energy of system, including exchange and correlation contributions, is considered as the unique functional of electronic density. The minimum value of total energy functional is the ground state energy of system. The density yielding this minimum value is exact single-particle ground state density. The energy and all other

properties of ground state system **(E_{GS})** are determined by the ground state probability density – $\rho(x, y, z)$, corresponding to:

$$E_{GS} = E[\rho(r)] = \int dr V_{ext}(r)\rho(r) + F[\rho(r)]$$

where $F[\rho(r)]$ is the **universal functional** of electron charge density $\rho(r)$, that defines the total energy of electronic system (Segall et al., 2002). The functional minimum is the ground state energy of system. The Hohenberg-Kohn theorem is unable to calculate E_{GS} because of impossibility to determine ρ without the ground state electronic wave function. Therefore, the functional F cannot be found. Also, the exact form of this functional is unknown.

In practice, the DFT application is based on the Kohn-Sham method (KS), where the problem of interacting electrons in external potential is mapped onto a problem of non-interacting electrons in effective local potential. Corresponding to the KS method the many-body problem is solved in terms of the equivalent set of self-consistent one-electron equations (Kohn and Sham, 1965). Thus, the DFT ideas were put on the solid mathematical ground. The expression for the KS-equation has a view:

$$\left[-\frac{\hbar^2}{2m}\nabla^2 + V_{ext}(r) + e^2\int\frac{\rho(r')}{|r-r'|}dr' + V_{XC}(r)\right]\psi_i(r) = \varepsilon_i\psi_i(r)$$

where V_{ext} is the static total electron-ion potential, the third term is the Hartree potential, ψ_i is the wave function of electronic state i, ε_i is the KS eigenvalue. $V_{XC}(r)$ is exchange correlation potential formally defined by the functional derivative

$V_{XC}(r) = \frac{\delta E_{XC}[\rho(r)]}{\delta\rho(r)}$ (Payne et al., 1992). The equations are solved via iterative operations up to self-consistent achievement as the result of the many-electron system of interacting electrons projected onto the system of non-interacting electrons moving in the effective potential induced by the other electrons.

The energy universal functional $E_{XC}[\rho]$ is independent of V_{ext} and can define the exchange-correlation potential, energy and density for exact ground state. Nevertheless, the E_{XC} exact dependence on $\rho(r)$ is unknown (Segall et al., 2002). Besides, the whole sum of the single part KS eigenvalues does not correspond to the overestimated. The main limitation of the DFT is that the exchange-correlation energy is the functional of density and explicitly unknown. At the same time, in

order that the approximation is reliable, both terms $\boldsymbol{E_X}$ and $\boldsymbol{E_C}$ should be treated consistently.

The several groups of valid approximations are accepted in the DFT in dependence on the chosen approaches to the problem of electron-electron interaction effects. The local density approximation (LDA) is one of the most used that considers the electron exchange-correlation energy ($\boldsymbol{E_{XC}}$) as the function of electron density. It is based on the Hohenberg-Kohn theorem. The appropriate method introduced by Kohn and Sham is aimed to express the $\boldsymbol{E_{XC}}$ in terms of the electron density from the knowledge of the exchange-correlation energy per particle, $\boldsymbol{\varepsilon_{XC}}$, of the homogeneous electron gas. Every infinitesimal element of density $\boldsymbol{\rho(r)dr}$ has the exchange-correlation density equivalent to the density $\boldsymbol{\rho = \rho(r)}$ of electron gas:

$$E_{XC}^{LDA} = \int dr\rho(r) \in_{XC} (\rho(r)),$$

$\in_{XC} (\rho)$ is the exchange-correlation energy per electron in the uniform electron gas of density ρ (Segall et al., 2002).

The LDA assumes that $\boldsymbol{E_{XC}}$ functional is local and ignores spatial variations in the electronic density field. According to the approximation, three regions might be distinguished in atoms and molecules: (1) – a region near the nuclei, where electronic density is high and the approximation is satisfactory; (2) – the main body of charge distribution, where the varieties of electronic density $\rho(r)$ is relatively slow; $\in_{XC} (\rho)$ is expected to be satisfactory as well; (3) – the surface of atoms and molecules overlapping regions, where the approximation is not valid, though in large atoms this region is not very important. For metals, alloys and small-gap semi-conductors a good representation of exchange-correlation effects are expected (Kohanoff, 2006).

Thus, the LDA considers the exchange-correlation energy functional $\boldsymbol{E_{XC}[\rho]}$ to be local because the exchange electron energy at any point of system is the function of electron density at that point only. At every point the per-electron $\boldsymbol{XC}$ energy is equal to the per-electron exchange energy of a homogeneous electron gas. The universal functional $\boldsymbol{E_{XC}}$ is the sum of a correlation functional and an exchange functional. This is one of the achievements of the LDA that both energy contributions are treated in the same limits of locally homogeneous system. As a whole, in the DFT context, $\boldsymbol{E_{XC}}$ might be determined as the difference between the total energy and the sum of Coulomb energies. Although the functional is not known,

it should give the different effect as against the E_{HF} value. The LDA successful performance, particularly in total-energy calculations, is attributed to the correct sum rule for the exchange-correlation hole. The extension to spin-polarised system proposes the local spin density approximation replacing the E_{XC} by the spin-polarised expression (Payne et al., 1992; Kohanoff, 2006). The generalised gradient approximation (GGA) is valid for densities that vary slowly in space. This approximation is often used together with the LDA for one or several parameter values. The GGA enables calculations to be improved for binding energy, dissociation energy, especially for hydrogen-containing systems (e.g. water and ice), bond lengths and angles. There is some improvement of information as regards the gap energy and lattice constants of noble metals (Kohanoff, 2006). The possible errors can arise from the gradient contribution to the correlation energy. The gradient expansion may be easily violated for one or more conditions. Therefore, this approximation should be applied very carefully (Gross and Dreizler, 1981; Perdew, 1985). On the basis of the GGA, a number of modified models of gradient expansion were carried out, for example, the BLYP functional (Becke, 1986, 1988).

5. 4 Periodic structures

Crystalline solids are built of a periodic array of atoms or atom groups and constructed by infinitive repetition of identical combinations of atoms called **the basis** (Kittel, 2005; Kohanoff, 2006). The set of mathematical points to which the basis is attached constitutes **the lattice**. In three dimensions space the lattice is defined by three translation vectors: a_1, a_2, a_3. As a result, the crystal looks from the point r absolutely the same as from every point of translation r. An imaginary parallelepiped containing one unit of the repeating by translation pattern is called **the unit cell**. A primitive unit cell is formed by straight lines joining neighbouring lattice points and characterised by the primitive translation vectors a_i appropriate to the crystal axes. Another way of determining a primitive cell resulted in the Wigner-Seitz cell (Payne et al., 1992; Atkins, 1998; Segall et al., 2002).

A crystal is proved to be invariant under translation $T = u_1a_1 + u_2a_2 + u_3a_3$, where u_1, u_2, u_3 are integers. The local properties are also invariant under T. Such periodicity is relevant for Fourier analysis related to the Fourier components of electron density. The Fourier space includes the concept of reciprocal lattice, where primitive vectors b_1, b_2, b_3 are defined by the relation: $a_ib_j = 2\pi\delta_{ij}$. Points in the

reciprocal lattice are mapped by means of primitive vectors as follows: $\boldsymbol{G = v_1 b_1 + v_2 b_2 + v_3 b_3}$, where $\boldsymbol{v_1, v_2, v_3}$ are integers and $\boldsymbol{G}$ is reciprocal lattice vector (Segall et al., 2002). The Wigner-Seitz primitive cell in the reciprocal lattice called **the first Brillouin zone (BZ)** is of great importance for the geometrical interpretation of diffraction phenomena. The waves incoming from the origin point are scattered and diffracted on the phase boundary characterised by particular class of vectors $\boldsymbol{k}$ such that the phase factor $\boldsymbol{\exp(ika_i) = 1}$. Thus, the wave function is in phase for all the periodic replicas of the unit cell. Arising from the origin and terminated on the surface of the **BZ** the waves should be diffracted by the crystals (Kittel, 2005). Introduction of the energy cut-off into the plane-wave continuum produces the finite basis set. Factually, a finite number of plane wave functions are used as energy cut-off.

For the crystalline systems the Bloch's theorem is applied (Payne et al., 1992; Kohanoff, 2006). This theorem states that in the periodic potential each wave function of electron can be expressed as the product of the imaginary factor arising from the translation symmetry (cell-periodic part) and the function with the same periodicity of potential (wavelike part): $\boldsymbol{\psi_i(r) = \exp(ikr)\, f_i(r)}$. The cell-periodic part can be expanded through the discrete set of plane waves, i.e. the waves of constant frequency whose fronts (surfaces of constant phase) are infinite parallel planes of constant amplitude normal to the phase velocity vector. The phase vectors of plane wave correspond to the reciprocal lattice vectors $\boldsymbol{G}$. The plane waves are commensurate with the super-cell. Each wave function expanded via discrete plane-wave basis set is expressed as a sum of plane waves (Payne et al., 1992):

$$f_i(r) = \sum_G C_{i,G} \exp[iG \cdot r], \qquad \psi_i(r) = \sum_G C_{i,k+G} \exp[i(k+G) \cdot r],$$

where $C_{i,G}$ and $C_{i,k+G}$ are the expansion coefficients. The number of $\boldsymbol{G}$-vectors and the number of $\boldsymbol{k}$-vectors should be infinite. Each of these corresponds to the solution for $\boldsymbol{\psi_i}$. However, if the $\boldsymbol{k}$ points are situated very close to each other, the change of ψ_i with $\boldsymbol{k}$ may be neglected. The Bloch's theorem states that there is no necessity to determine electronic wave function everywhere in space. It would be sufficient to have the solution in the unit cell. The calculation problem for infinite number of wave functions is changed with calculating for finite number appropriate to definite number of $\boldsymbol{k}$ points. Therefore, the problem of $\boldsymbol{k}$ point sampling is of great

importance. The density of allowed ***k*** points is proportional to the volume of the solid. However, the electronic states occur only at ***k*** points under the boundary conditions of the **BZ**. Thus, it is possible to represent the electronic wave functions over the region around ***k*** space by means of the wave functions at single ***k*** point. As a result, only a finite number of ***k*** points are necessary to determine the total energy of the solid with the calculating of the electronic potential. This method is especially appropriate for the electronic potential approximation and the total energy calculation for insulators and semiconductors. The errors are reduced by the denser set of ***k*** points.

Many systems are not periodic, and so one need to construct what is known as a **super-cell**. This is essentially a large unit cell, repeated periodically in space, but containing the "spacer" region to separate the region of interest from its periodic images. By using super-cells the advantage of Bloch's theorem can be used even for non-periodic systems. In this case the super-cell should be approximated to the original system.

5. 5 Determination of electronic structure

In general case, the wave function for ***N***-electron system is multi-determinant (Levine, 2002, 2009; Kittel, 2005; Kohanoff, 2006). As for the particular system, the expanding function includes the Slater determinants including the occupied and unoccupied orbitals of the HF Hamiltonian. This function can be expressed in the form of linear combination of the Slater determinants:

$$\Phi(x_1 \dots \dots x_N) = C_0\Phi_{\mathrm{HF}}(x_1 \dots \dots x_N) + \sum_{i=1}^{ND} C_i\Phi_i\,(x_1 \dots \dots x_N)$$

$\boldsymbol{\Phi_{HF}}$ is the Hartree-Fock solution for ground state; $\boldsymbol{C_i}$ are the expansion coefficients to minimise the total energy; and $\boldsymbol{\Phi_i}$ are the additional determinants corresponding to the excited states (Kohanoff, 2006). The ground state term corresponds to the ***N*** electrons occupying the energetically lowest spin orbitals. The very different types of excited configuration exist and define the number of determinants. Consequently, the one-electron wave functions are expanded in a set given by the possible ways of ***N*** electrons settling in molecular orbital (MO). With a view to accurate representation, MO should be expressed as a linear combination called **basis set**.

Different types of basis set were proposed with a view to electronic structure determination. Independent on the particular approach to the electronic structures,

the mathematical representation of the one-electron orbital is of great importance. The methods take into account the expanding one-electron wave functions derived from the time-independent Schrodinger equations and defined by the energy eigenvalues that form a discrete set or continuum.

The plane wave basis set (PW) is a general approach to solution of differential equations applied for the condensed phases when the wave functions are defined by a phase factor and a periodic part of solids. Appropriate basis set is composed by sets of plane waves down to cut-off wavelength. The plane waves are eigenfunctions of the Schrodinger equation with constant external potential. It provides the basis set for description of bands for many materials.

In practice, the plane wave basis sets are used in the combination with effective core potential, or pseudo potential. The pseudo potential approximation (PA) is intertwined with the PW basis set that allows the calculations with a feasible number of plane waves. The fact is that in condensed periodic matter the electronic wave functions are expanded in terms of a discrete set of plane waves. The PA enables the electronic wave functions to be expanded by means of much lesser number of plane waves. The main idea is to replace the real potential with the effective potential within the core area of radius $\boldsymbol{r_c}$. Many of the nodes of atomic states lie in the "core region" close to the nucleus. The wave functions in this region are relatively unchanging, regardless of the chemical environment of the atom, and many of the lower energy states are localised in this region. In the PA the electrons whose wave functions are localised in the core region are removed and replaced with the effective potential. In combination with the nuclear coulomb potential, it is called the pseudo potential. Outside the core region the wave functions are unchanged.

The plane waves describe the valence charge density because the core electrons are concentrated around the atomic nuclei where density gradient is very high and not easily described. The valence orbital eigenvalues should be the same as in all the electronic calculations for the atom. This combined approach of plane wave basis set together with core pseudo potential is usually noted as a PWP (or PSPW) calculation. The combination of pseudo potentials and fast Fourier transforms allow using plane wave basis set in reciprocal space and avoiding the numerous solutions for electronic wave function (Payne et al., 1992; Segall et al., 2002).

Chapter 6 Simulation and computational design of CDC systems

6. 1 Introduction

The composite CDC systems are thereby designed on different surfaces of 4H-*SiC* precursor to reveal the epitaxial graphene mutability under substrate induced interaction during gradual growth. Many-layered graphene assemblies designed on the supporting solids are grown under substrate induced interaction that every new layer adds the novel properties (Forbeaux et al., 1998, 1999; Berger et al., 2004, 2006; Hass et al., 2006, 2008; Hiebel et al., 2008). The first *C*-plane acts like intermediate buffering the interaction between substrate and subsequent layers. This is the basal layer formed under strong substrate influence and deprived of the freestanding graphene quality. The following carbon sheets can be grown through the interfacial layer that relaxes substrate induced interaction. Two jointed *C*-levels reveal mixed properties under dominant graphene identity. Only since the fourth level the freestanding graphene qualities are found out. However, these properties fade as a multisystem growth approaches the 3D structure of graphite. Therefore, foliated graphene patterns evolving on the solid substrates reveal a very sensitive mutability depending on substrate framework, number and arrangement of successive layers. At every stage of gradual growth, a multilayer demonstrates the novel properties and may be used as a ready building block for intended device. Graphene of bi-layer and few-layer patterns are of special significance due to composite electronic structure formed under mixed influence.

The epitaxial carbide derived carbon (CDC) patterns grown on *SiC* surface are of great dependence on structural coherency with the supporting framework. The perfect films are formed by means of ordinary annealing of proper precursor at an elevated temperature more than 1000°C. Decomposition and selective material sublimation result in self-organisation of *C* excess into graphene rings. Due to the strong interaction the covalent bonds are formed while transforming a basal monolayer into intermediate. The typical graphene properties are evidently suppressed. Instead, there are the electron doping on the interface top, a significant disorder, unique transport abilities and catalytic effects (Gamo et al., 1997; Ueta et al., 2004; Gall et al., 2004) predetermining the upper layer growth. The second layer provides the independent properties approximately appropriate for the

freestanding graphene. The distinctions between the layers are defined by interactions between graphene and support. Therefore, the initial search for proper substrate becomes an immediate aim.

6. 2 *SiC* precursor structures

The α-*SiC* modification crystallised in high temperature is divided into the hexagonal H-*SiC* and the rhombohedral R-*SiC* systems. The *β*-*SiC* modification of cubic symmetry 3C-*SiC* is formed at the lower temperature. These poly-types are different in dependence on bi-layer stacking order (Starke, 2009). Silicon carbide is a semiconductor of rather wide gap around 2.36 - 3.23 eV depending on the poly-types. Crystalline lattice comprises *Si*- and *C*-atoms alternatively bonded in tetrahedral coordination (Fig. 6. 1).

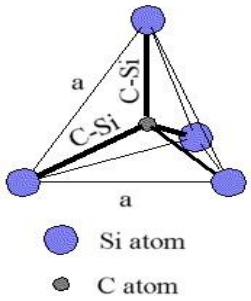

Figure 6. 1. *C*-atom in the tetragonal structure of neighbouring *Si*-atoms.

Two or three identically oriented bi-layers are stacked in different order and constitute the slabs (Fig. 6. 2).

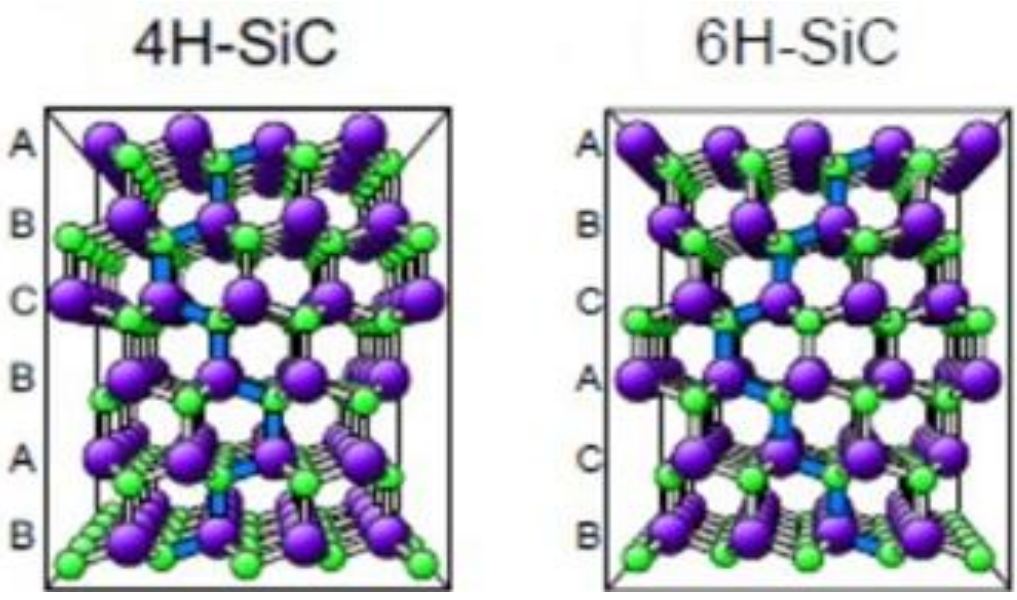

Figure 6. 2. Bi-layer stacking for hexagonal symmetry (Starke, 2009).

The poly-type comprising two slabs of two identically oriented bi-layers is referred to as 4H-*SiC*. The 6H-*SiC* poly-type comprises two slabs of three identically oriented *SiC* bi-layers. The poly-types of hexagonal lattice symmetry are especially stable because of the periodicity arranged along *c*-axis. This hexagonal type used for many researches is divided into the *Si*-face (0001) and the *C*-face $(000\bar{1})$ surfaces. Both surfaces exhibit the different atomic reconstructions of unit cell: (1×1), (2×2), (3×3), $\left(\sqrt{3}\times\sqrt{3}\right)R30°$ and $\left(6\sqrt{3}\times 6\sqrt{3}\right)R30°$. The $\left(\sqrt{3}\times\sqrt{3}\right)R30°$ reconstruction is usually used for computational study. The distance between two neighbour bi-layer planes is 2.52 $\dot{A}$. The bond length between the nearest atoms is 1.89 $\dot{A}$. The distance between the nearest two *Si*- (or *C*-) atoms in *SiC* is 3.078 $\dot{A}$.

The systematic study was undertaken to reveal the electronic characteristics in dependence on taken reconstructions and surface terminations. The electronic structures of 4H-*SiC* substrate grown by the subsequent *C*-layers were calculated for different combinations of substrate unit cell reconstructions, top-level terminations and crystalline lattice commensurations. The number of slabs and bi-layers was determined by convergence of total energy that stopped as the bulk increase. The upper vacuum gap is held of 15 $\dot{A}$. On the bottom layer, the *C*-atoms are saturated with hydrogen. The atoms are always kept relaxed. The electronic structures were calculated for the alternating combinations of substrate unit cells and surface terminations.

The simulation was intended as the stepwise succession of consistent layers including the interfacial monolayer (ML) grown on the supporting substrate. The initial $\left(\sqrt{3}\times\sqrt{3}\right)R30°$ and (3×3) reconstructions divided into *Si*-face and *C*-face terminations were taken as the starting points for further trails. At every step of computation, the results were compared with each other in order to elucidate the electronic structures of evolving multilayer. Each subsequent layer gives the rise of difference. This is why the substrate's proper choice is of crucial importance for the interface and multilayer as a whole.

6. 3 Models of interfacial layer

The geometrical adjustments of the substrate and carbon over-layers were carried out for the different modes of lattice commensuration and stacking order of overlapped layers (Fig. 6. 3). In order to avoid the unwanted mismatches between the

(0001) - $(\sqrt{3} \times \sqrt{3})R30°$ and (3×3) substrate surfaces and the first *C* monolayer, the admissible stretch between *C* – *C* atoms was held not more than 8% by analogy with the previous investigations (Mattaush and Pankratov, 2007; Varchon et al., 2007). The admissible length for *C* – *C* bonds in graphene of 1.539 *Å* was calculated by taking into account the nearest distance between two *Si*- (or *C*-) atoms of 3.078 *Å* in substrate. According to the calculated model, the basic matrix of interfacial layer is placed at the distance of 2.0 *Å* for *Si*-face termination (1.66 *Å* for *C*-face) acceptable for the covalent bonds and performed by the hexagonal rings with permissible bond length. Thus, every adjustable four unit cells of graphene are set up in the (0001) - $(\sqrt{3} \times \sqrt{3})R30°$ unit cell of substrate (Fig. 6. 3_a, b).

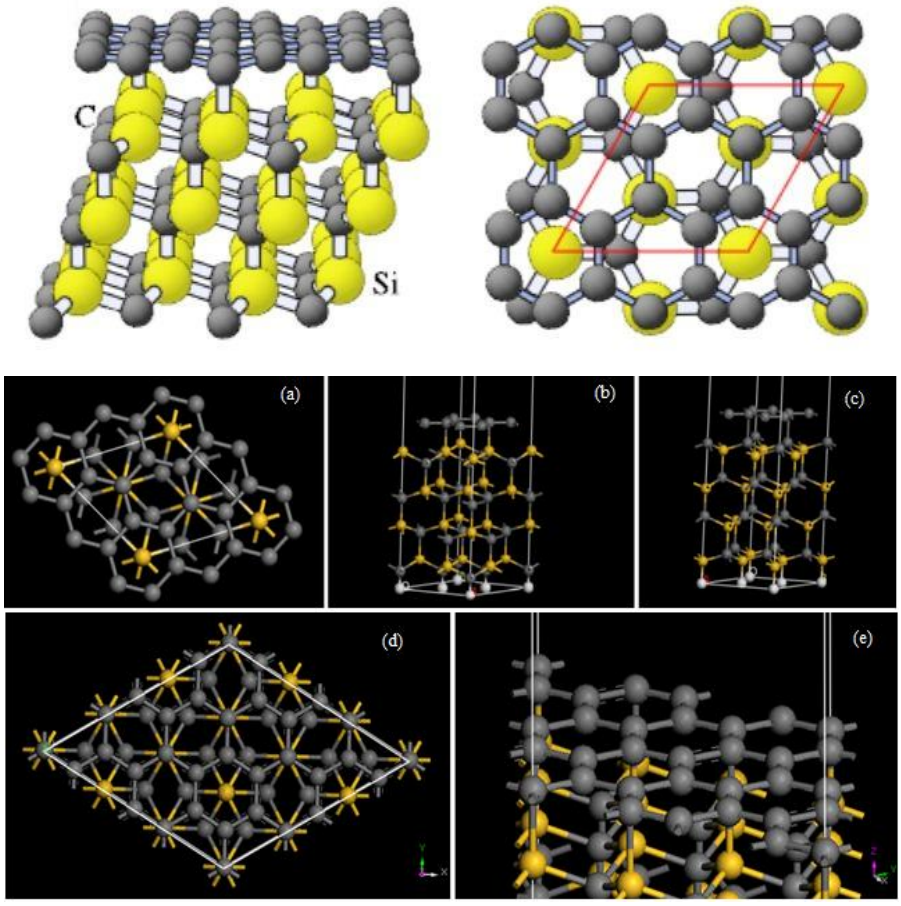

Figure 6. 3. Modelling for basal 2D *C* monolayer on the *Si*-face and *C*-face surfaces.
Top: first *C* monolayer on the *Si*-face surface (Mattausch and Pankratov, 2007);
(a) - (b): first *C* monolayer on the (0001) - $(\sqrt{3} \times \sqrt{3})R30°$ surface;
(c): first *C* monolayer on the $(000\bar{1})$ - $(\sqrt{3} \times \sqrt{3})R30°$ surface;
(d) - (e): first *C* monolayer on the (0001) - (3×3) surface.

The central *Si*-atoms of unit cell are bonded with two *C*-atoms that correspond to the opposite sub-lattices of graphene ring. The unsaturated dangling bonds rise upward from *Si*-atoms located in the lattice corners. Six of eight *C*-atoms for four graphene unit cells are relaxed upward as well. Some graphene rings are not bonded with the substrate. The same principle is kept for the interfacial layer on the $(000\bar{1})$ - $\left(\sqrt{3}\times\sqrt{3}\right)R30°$ surface (Fig. 6. 3_c). The interface on the (0001) - (3×3) surface (Fig. 6. 3_d, e) is arranged with twelve graphene unit cells corresponding to this reconstruction. Two *C*-atoms of opposite triangles in regular graphene rings compensate six dangling bonds arising from nine terminating *Si*-atoms. Three dangling bonds are left unsaturated. These regular rings are bonded by means of two *C*-atoms of the opposite sub-lattices. The other rings hover on uncompensated *Si*-atoms. The lattice mismatch between *SiC* of (0001) - $\left(\sqrt{3}\times\sqrt{3}\right)R30°$ unit cell and graphene requires some distortion in graphene lattice. The proper $C-C$ bond length in graphene may be calculated as follows: $2Lsin30° + L = 3.078\ A$. Therefore, $L = 1.539\ A$ is the permissible $C-C$ bond length in graphene, taking into account that the nearest distance between two *Si* (or *C*) atoms in substrate is equal to 3.078 *A*. Thus, the coordinates of every *C*-atom constituting four graphene unit cells on the *SiC* substrate of (0001) - $\left(\sqrt{3}\times\sqrt{3}\right)R30°$ unit cell should be calculated while taking into consideration a priori known coordinates for two central *Si*-atoms of the (0001) - $\left(\sqrt{3}\times\sqrt{3}\right)R30°$ unit cell (Fig. 6. 4).

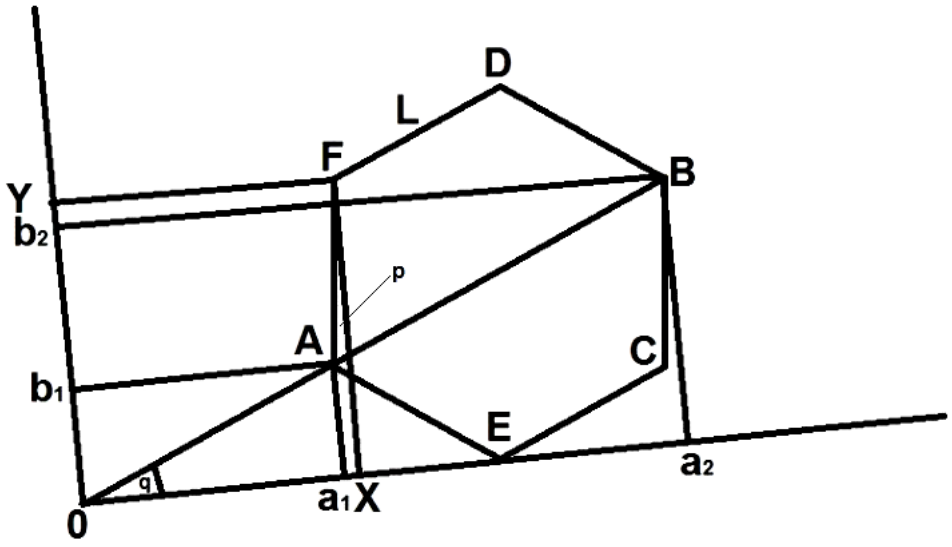

Figure 6. 4. Arrangement of graphene ring on the *SiC* (0001) - $\left(\sqrt{3}\times\sqrt{3}\right)R30°$ unit cell. **A** and **B** atoms correspond to *Si*-atoms of substrate.

The coordinates for *C*-atoms and geometrically proper arrangement of graphene unit cells are calculated by means of the individual algorithm. For example, let us find the coordinates for *C*-atom **F** (Fig. 6. 4).

$$2L = \sqrt{(a_2 - a_1)^2 + (b_2 - b_1)^2} \quad (1)$$

$X - a_1 = L\sin p$; $Y - b_1 = L\cos p$;

$X = L\sin p + a_1$

$$Y = L\cos p + b_1 \quad (2)$$

$p = 30° - q$; p is AFX angle.

Furthermore: $\frac{a_2 - a_1}{2L} = \cos(30° - p)$; $\frac{b_2 - b_1}{2L} = \sin(30° - p)$;

$$\cos(30° - p) = \frac{\sin p + \sqrt{3}\cos p}{2};\ \sin(30° - p) = \frac{\cos p - \sqrt{3}\sin p}{2} \quad (3)$$

And we have: $\frac{a_2 - a_1}{L} = \sqrt{3}\cos p + \sin p$; $\frac{b_2 - b_1}{L} = \cos p - \sqrt{3}\sin p$ (4)

As a result: $\sin p = \frac{a_2 - a_1}{L} - \sqrt{3}\cos p$ and $\frac{b_2 - b_1}{L} = 4\cos p - \frac{\sqrt{3}(a_2 - a_1)}{L}$ (5)

Therefore: $\cos p = \frac{b_2 - b_1 + \sqrt{3}(a_2 - a_1)}{4L}$; $\sin p = \frac{a_2 - a_1 + \sqrt{3}(b_1 - b_2)}{4L}$ (6)

Finally, it is possible to have *X* and *Y* coordinates for *C*-atom **F**:

$$X = a_1 + \frac{a_2 - a_1 + \sqrt{3}(b_1 - b_2)}{4};\quad Y = b_1 + \frac{b_2 - b_1 + \sqrt{3}(a_2 - a_1)}{4} \quad (7)$$

By this principle the coordinates for eight atoms of four unit cells are determined.

6. 4 Design of composite interfacial structures

The other models of interface used in some earlier works are designed either by placing the additional atomic surface layers between the bulk and multilayer graphene film (Hass et al., 2006, 2008; Magaud et al., 2009) or through the adsorption of *C*-rings loosely adopted by substrate lattice.

The additional atoms placed over the bulk lead to the several sets (Fig. 6. 5). It means that about 1/3 of interface should be represented by *Si*-atoms. Three calculated interface models are determined as follows: "*Si*-up" model (b), "*Si*-down" model (c) and "*C*-adatom" model (d) (Hass et al., 2006, 2008). Graphene epitaxial growth is realised through the intermediate layer along the boundary between bulk and new film. The interfacial layer is extending rather deeply into the bulk structure. The relaxed *SiC* bi-layer is covered with a dense carbon layer partially containing the *Si*-atoms separating the upper graphene sheet. The carbon concentration is approximately twice more than in *SiC* bi-layer. The average distance between

Si-ad-atoms and first graphene layer is 2.32 $\dot{A}$. The different constructions formed via interface were simulated and calculated.

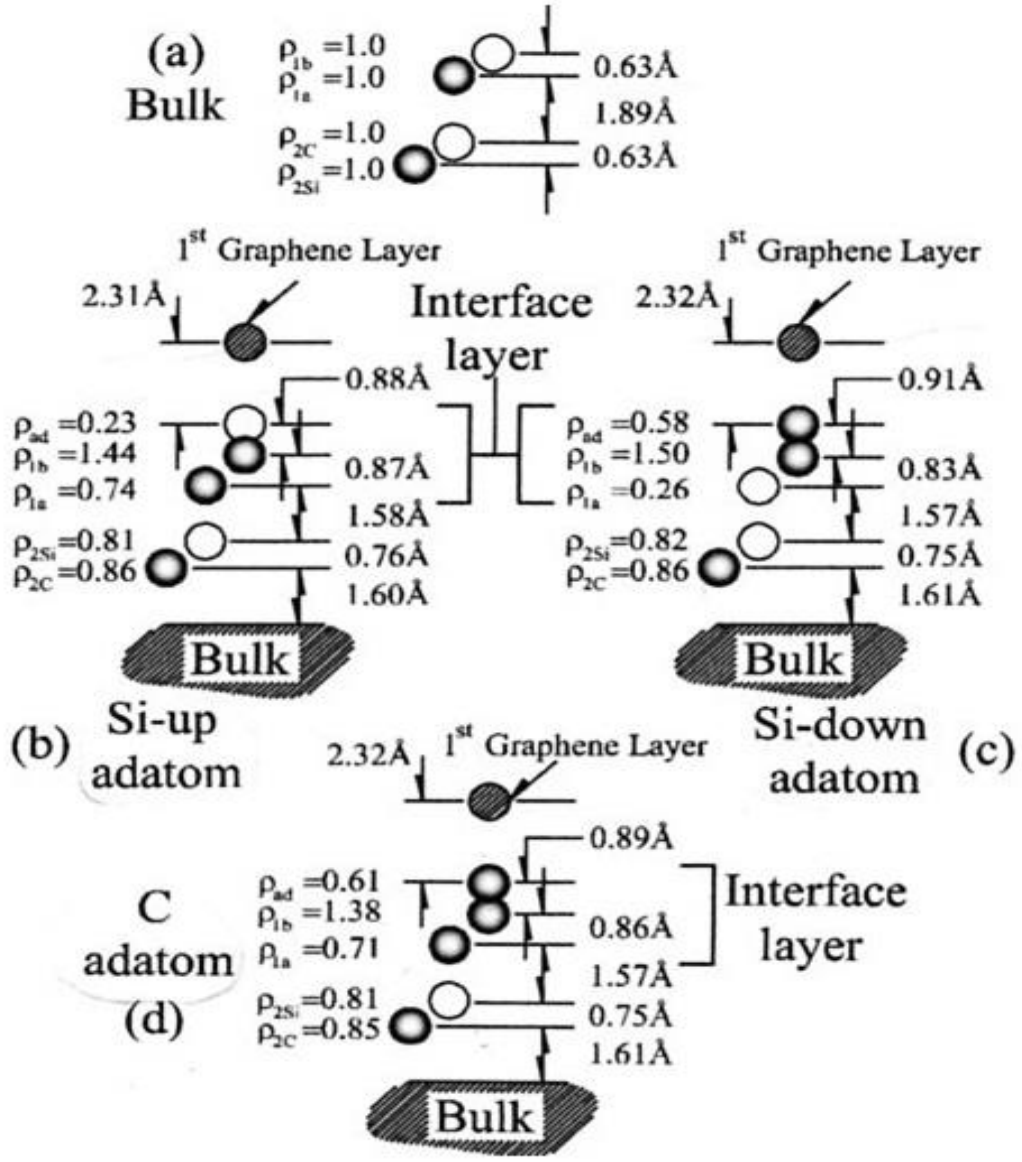

Figure 6. 5. Three models for graphene / SiC (0001) interface (Hass et al., 2006, 2008).

Concentration of carbon atoms in "*Si*-up" interface on the (0001) - $(\sqrt{3} \times \sqrt{3})R30°$ was held to be approximately twice more compared with *SiC* bi-layer in bulk. The interface width and the bond distance for the "*Si*-up" case are bigger than for the "*Si*-down" on the $(000\bar{1})$ - $(\sqrt{3} \times \sqrt{3})R30°$, where the lower part of interfacial layer prolongs the bulk structure. Hence, the carbon layer on the *Si*-face is less tightly bonded than film grown on the *C*-face substrate. The *Si*-atoms

in interface are saturated for both depicted cases. However, from the two coupled atoms of graphene unit cell only one atom is covalently bonded and relaxed towards the interface ad-atom. Each second one is unsaturated. As it was previously noted, the bond lengths should be different and it is the most evident explanation for a roughness of graphene-like layer.

6. 5 Second CDC plane modelling

A multilayer on the solids is grown under strong interaction with the supporting framework until a layer number runs to graphite 3D crystal. The multilayer growth is defined by geometrical arrangement and stacking order of the constituent *C*-planes. The layers may be joined by means of the Bernal (*AB*) stacking order, likewise the graphite structure (Mattaush and Pankratov, 2007; Varchon et al., 2007; Magaud et al., 2009). In the graphite-type *AB* stacking order the second layer has a weak bonding at the distance of 3. 5 $\dot{A}$. It implies the interlayer distance acceptable for the Van der Waals forces. Bonding of graphene layers is similar to the graphitic bulk with the same inter-planar distances (Fig. 6. 6).

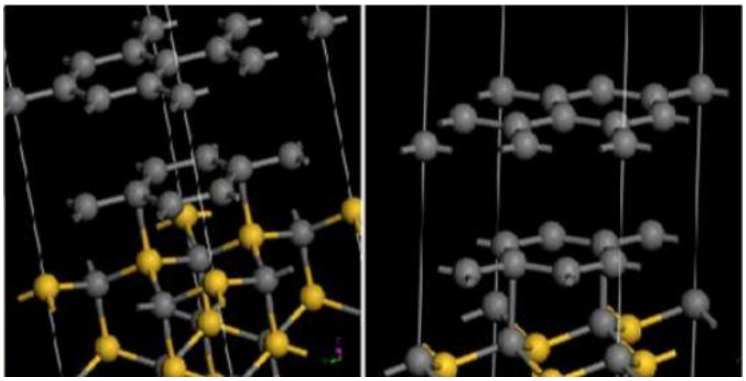

Figure 6. 6. CDC bi-layer on the (0001) - $\left(\sqrt{3}\times\sqrt{3}\right)R30°$ and on the $(000\bar{1})$ - $\left(\sqrt{3}\times\sqrt{3}\right)R30°$ surfaces.

Under epitaxial growth the new properties may be induced in the graphene multilayer by using the different arrangement of layers. Modifications of stacking order are changed from the conventional *AB* order to the *AA* and *AC* or another arrangement produced by arbitrary or combined rotation of *C*-planes (Andres et al., 2008; Hibino et al., 2009). The *C*-layers in designed model over the (0001) - $\left(\sqrt{3}\times\sqrt{3}\right)R30°$ substrate surface are located by analogy with graphite

structure in the Bernal stacking order and placed at the distance of 3.5 *Å* acceptable for the Van der Waals forces.

The second layer is performed by alternating rows of *C*-rings, where every three atoms of the single triangle are bonded with the interfacial layer. These rings are arranged that in every second ring of alternating rows the fourth atom is located over unsaturated dangling bond of "lonely" *Si*-atom arising from the corners of substrate unit cell. Thus, the second layer is simulated so that three atoms of lattice triangle are connected with the underlay, whereas the fourth hovers over uncompensated *Si*-atom. The subordinate rings comprise only three bonded atoms. As a result, graphene unit cells joined together prove to be connected with the fixed coordinates of *Si*-atoms. The whole number of free dangling bonds decreases as the thickness of multilayer is grown. Therefore, the bonds get weaker, whereas the subsequent layers become electronically independent. The second layer on the (0001) - (3×3) support (Fig. 6. 7) is arranged in such a way that three *C*-atoms of each ring are connected with the interfacial atoms. The fourth atom hovers over the "lonely" *Si*-atoms. Two *C*-dangling bonds are unsaturated.

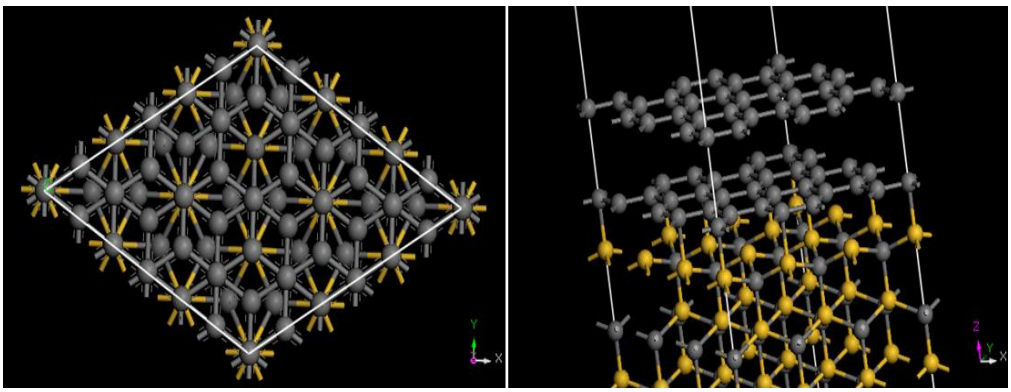

Figure 6. 7. Modelling for the bi-layer on the (0001) - (3×3) surface.

Which and when the novel properties should occur as a progressive growth? Does the second carbon layer have the properties of the freestanding graphene? How far do the subsequent layers avoid the properties of substrate and buffer? All these relevant questions can be partly answered by further calculations.

Chapter 7 Determination of electronic states

7. 1 Introduction

The electronic structures of composite CDC systems simulated on alternative 4H-*SiC* substrates have been explored by using the CASTEP code within the DFT first principles (Segall et al., 2002; Clark et al., 2005). Mutability and divergence of states under substrate induced interaction are revealed to be inherited from the initial precursor diversities and structural arrangements of systems.

Simulation and determination of electronic properties based only on the fundamental physical laws without support by approximations and free parameters are referred to as "the first principles" approach (Payne et al., 1992; Levine, 2009). Elaborated to apply within density functional theory (DFT), this approach is transformed for the calculations on the first principles landscape and the PWP (plane wave pseudopotential) concept using plane-wave basis set, effective core pseudopotential, fast Fourier transforms and some other ingredients. All these ingredients are combined into the single method to describe electron behaviour in the large systems (Car and Parrinello, 1985; Payne et al., 1992). Only the valence electrons are treated because the most physical properties of material depend on these electrons. Effective interaction between the valence electrons and the ionic cores is described by using the effective pseudo potential for any type of atoms. The key components of PWP including fast Fourier transforms and factors for minimisation of total energy enable the computation of electron structures for the large systems in a ground state.

The similar approach as a precursor for the CASTEP code was used. This programme is elaborated to predict the electronic properties of matter as follows (Segall et al., 2002; Clark et al., 2005):

- total energies (forces, stresses, elastic constants);
- electronic structure including electronic charge, potential, band structure, DOS;
- geometry optimisation, i.e. atomic positions, cell parameters, external pressure;
- molecular dynamics;
- search of reaction pathways and transition states;
- optical spectra, phonon spectra, electric field response, etc.

This programme is based on Bloch's theorem applicable for the periodic solids. It states that in periodic structure each electronic wave function is spread

under control of cell-periodic factor. Another regulation is affected due to the phase factor expanding through the plane waves. The wave functions in periodic structure are spread via basis set that means a discrete system of plane wave vectors. The system involves the plane waves of small kinetic energy less than particular value for free electron known as an energy cut-off E_c . The smaller E_c, the smaller basis set and the faster calculations. Along with the plane wave basis set the pseudopotential application essentially reduces the calculations in terms of a much smaller number of plane waves. However, the very truncated basis set leads to the error in total energy values. Therefore, the set should be enlarged up to the converged total energy. The CASTEP code for the total energy, geometry optimisation, band structures and DOS determination was used (Payne et al., 1992; Segall et al., 2002). The plane wave basis set cut-off of 310 eV and MP grid size for SCF calculation of $5 \times 5 \times 1$ were taken as the convergence test results. The generalised gradient approximation (GGA) functional for the exchange-correlation terms was used. The ultra-soft pseudo potential represented for the reciprocal space was applied. As against experiment, the computational tests can be interrupted for access into evolving process. The results were compared in order to elucidate the gradual electronic mutability at every step of computation during multilayer stepwise growth.

7. 2 Electronic structure of 4H-*SiC* substrate

The electronic structures for passivated surfaces of (3×3) reconstruction proved to be very similar for both (0001) and $(000\bar{1})$ terminations (Fig. 7. 1_1- 4). For passivated surfaces of $\left(\sqrt{3} \times \sqrt{3}\right)R30°$ reconstruction the structures were also identical for different terminations (Fig. 7. 1_5-8). These reconstructions display a rather wide gap of 2.58 eV for both terminations. The Fermi levels located near the valence bands correspond to the values of 0.9 eV and 2.7 eV for (3×3) and $\left(\sqrt{3} \times \sqrt{3}\right)R30°$ unit cells respectively. After hydrogen removal the band diagrams demonstrate appreciable differences enforced for both reconstructions and terminations. The considerable distinctions between electronic structures for the (0001) and the $(000\bar{1})$ terminations concern both reconstructions (Fig. 7. 2 and 7. 3). The gap state diagrams for the (0001) termination of the (3×3) and $\left(\sqrt{3} \times \sqrt{3}\right)R30°$ unit cells comprise the transitional band including half-filled level occupied with unpaired electron (Fig. 7. 3_1, 3). The band is separated by this half-filled level into two narrow

sub-bands. The lower one is filled and the upper one is empty. The Fermi level of 1.52 eV (1.01 eV for (3×3) reconstruction) is located inside this band.

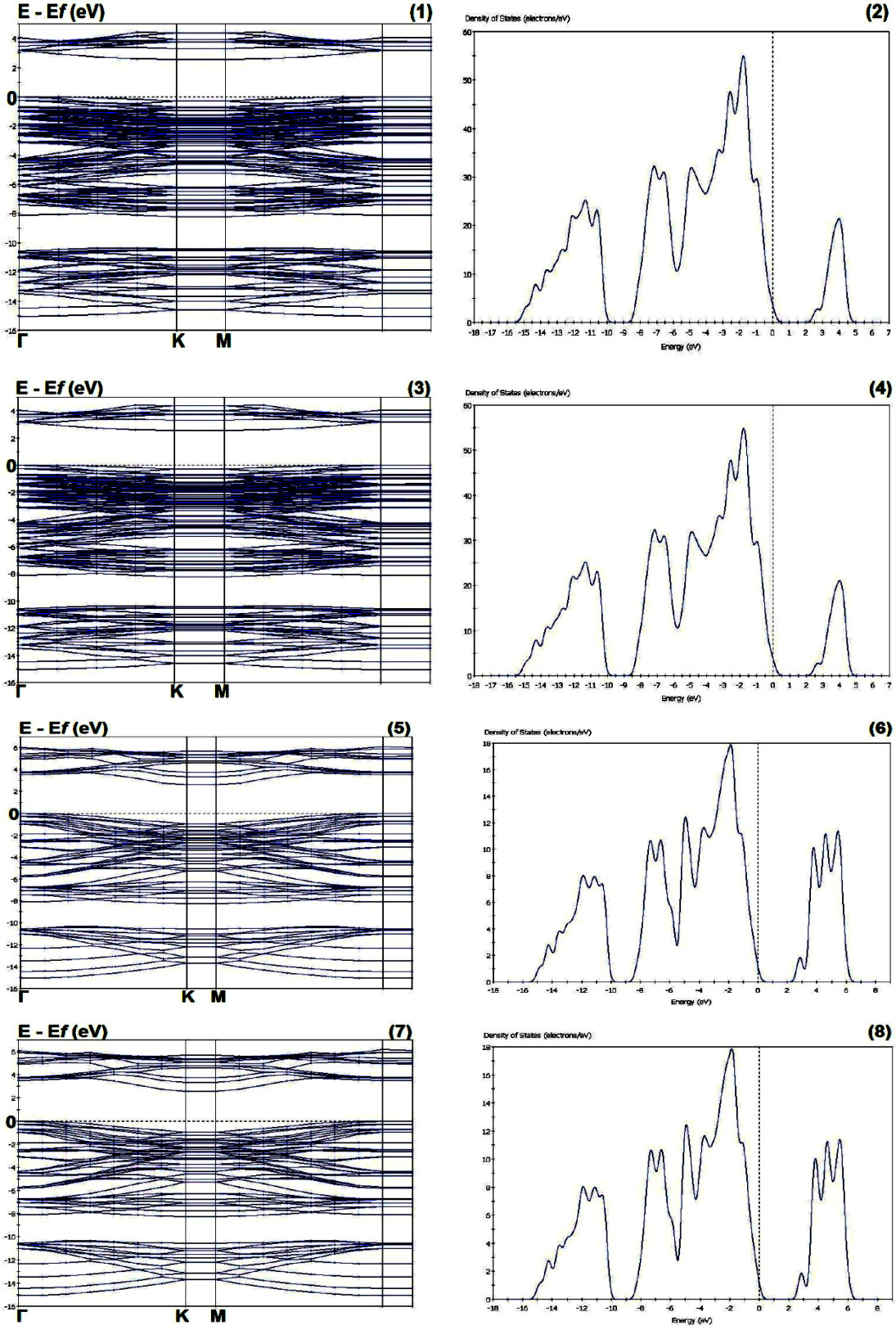

Figure 7. 1. Band structures and DOS for passivated 4H-*SiC* substrate surfaces:
(1-4) - (0001)/(000$\bar{1}$) - (3×3) surfaces; (5-8) - (0001)/(000$\bar{1}$) - $\left(\sqrt{3}\times\sqrt{3}\right)R30°$surfaces.

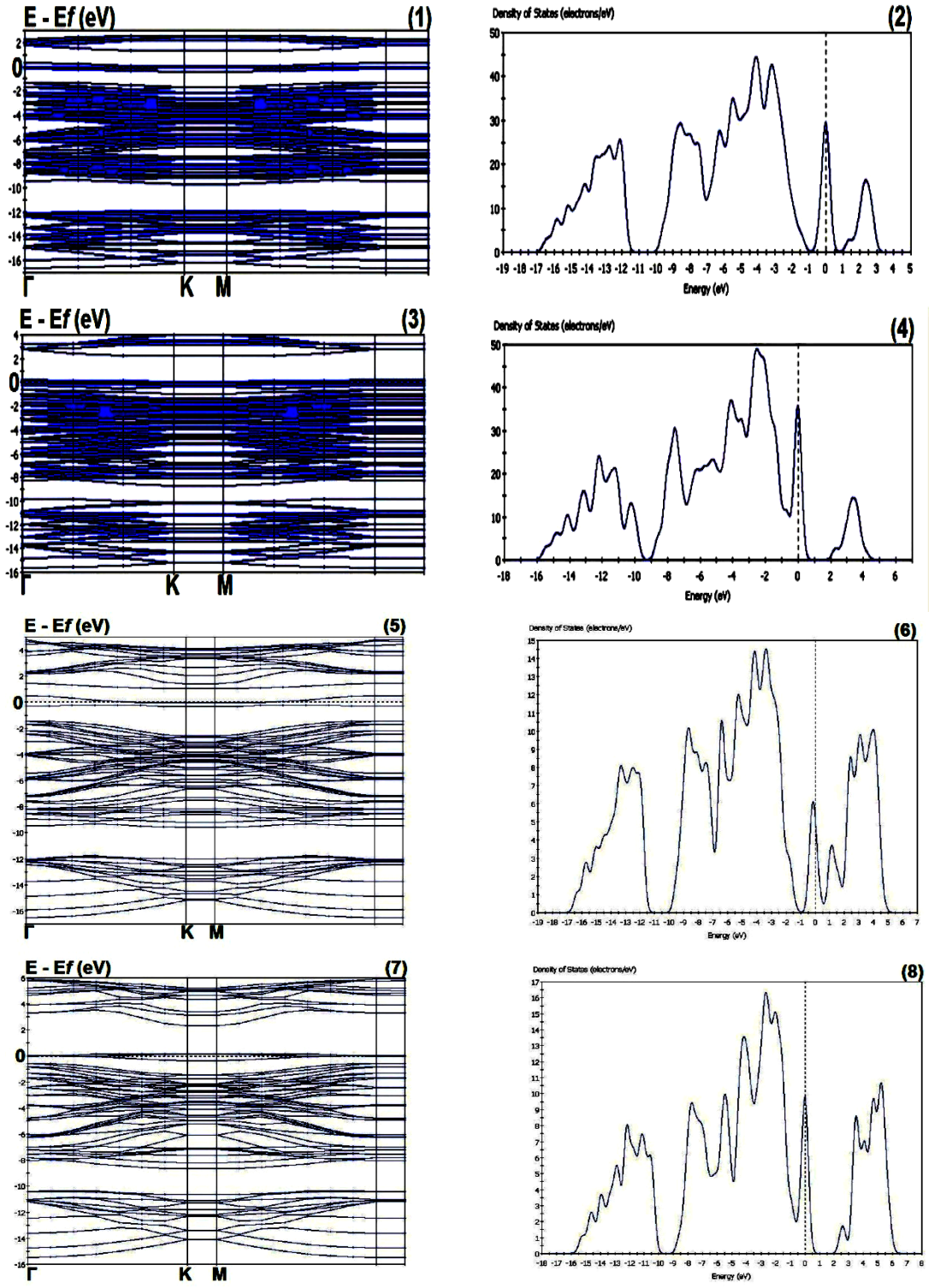

Figure 7. 2. Band structures and DOS for non-passivated 4H-*SiC* substrate surfaces:
(1-2) - (0001) - (3×3) surface; (3-4) - $(000\bar{1})$ - (3×3) surface;
(5-6) - (0001) - $\left(\sqrt{3}\times\sqrt{3}\right)R30°$ surface; (7-8) - $(000\bar{1})$ - $\left(\sqrt{3}\times\sqrt{3}\right)R30°$ surface.

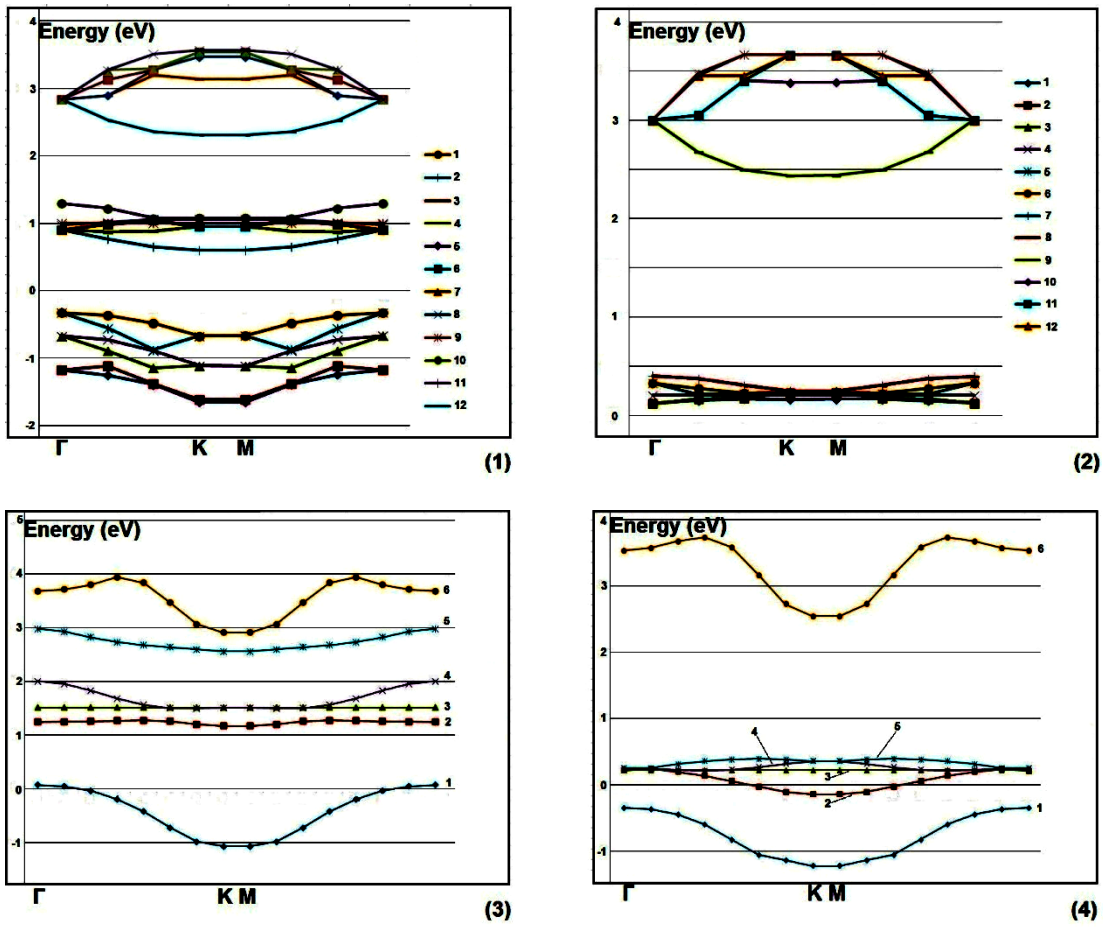

Figure 7. 3. Gap states for non-passivated 4H-*SiC* substrate surfaces.
(3×3) reconstruction: (1) - (0001) surface; (2) - $(000\bar{1})$ surface;
$\left(\sqrt{3}\times\sqrt{3}\right)R30°$ reconstruction: (3) - (0001) surface; (4) - $(000\bar{1})$ surface.

The band structure calculated for (0001) substrate surface of $\left(\sqrt{3}\times\sqrt{3}\right)R30°$ reconstruction (Fig. 7. 3_3) is interpreted by using the former experimental data (Johansson et al., 1996; Northrup and Neugebauer, 1998). The half-filled level (4) is found to be running along the Fermi level (3) and located 1.43 eV above the maximum of level (1) corresponding to the valence band maximum. The filled level (2) experimentally confirmed (Johansson et al., 1996) was identified 1.1 eV above the valence band maximum, just below the Fermi level. The empty level (5) is located 1.05 eV above the Fermi level and displaced towards the conduction band.

In the band structures for $(000\bar{1})$ termination of both reconstructions (Fig. 7. 3_2, 4), the transitional band is moved to the valence band. In the gap state diagram for $(000\bar{1})$ substrate surface of $\left(\sqrt{3}\times\sqrt{3}\right)R30°$ reconstruction (Fig. 7. 3_4) the Fermi level of 0.2 eV runs through this transitional band and the endpoints of half-filled level (4) are located 0.56 eV above the maximum of level (1)

corresponding to the valence band maximum. Its centre is 0.14 eV above the Fermi level (3). The level (2) with centre located 0.2 eV above the valence band maximum and 0.36 eV below the Fermi level was found to be filled. The level (5) with maximum located 2.15 eV below the minimum of level (6) (the conduction band minimum) was identified to be empty. By analogy the similar transitional bands consisting of the filled, half-filled and empty levels including the Fermi level were found for the substrates of (3×3) reconstruction (Fig. 7. 3_1, 2).

7. 3 Electronic state of interfacial layer

The electronic structure of interface as a consequence of the first *C*-layer – substrate interaction succeeds to the substrate alterations. Therefore, the main distinctions concern the substrate reconstructions enforced by the surface terminations. For both polar *Si*-face and *C*-face terminations of $\left(\sqrt{3}\times\sqrt{3}\right)R30°$ reconstruction (Fig. 7. 4) the half-filled level is placed in different positions to band gap of 1.734 eV and 1.630 eV pinned by the Fermi level of 3.692 eV and 1.828 eV respectively.

During the interface formation on (0001) - $\left(\sqrt{3}\times\sqrt{3}\right)R30°$ substrate surface, the half-filled level (3) and the coupled Fermi level (5) are located in the conduction band, likewise the *n*-type semiconductor (Fig. 7. 4_5). The maximum of filled level (2) corresponds to the valence band maximum. The minimum of empty level (4) meeting with the half-filled level (3) corresponds to the conduction band minimum. For the interface layer on $(000\bar{1})$ - $\left(\sqrt{3}\times\sqrt{3}\right)R30°$ substrate surface (Fig. 7. 4_6) the half-filled level (4) pinned by the Fermi level (3) are significantly closer to the valence band, likewise the *p*-type semiconductor. They are located 0.62 eV above the maximum of level (2) corresponding to the valence band maximum and about 1.7 eV below the minimum of level (5) corresponding to the conduction band minimum. The level (2) is filled and the level (5) is empty. This difference explains why the interfacial layer on *Si*-face termination represents the metallic property, whereas on *C*-face termination it behaves like the semiconductor (Hass et al., 2006, 2008; Hiebel et al., 2008). For both cases the interfacial layers perform intermediates devoid of the freestanding graphene features.

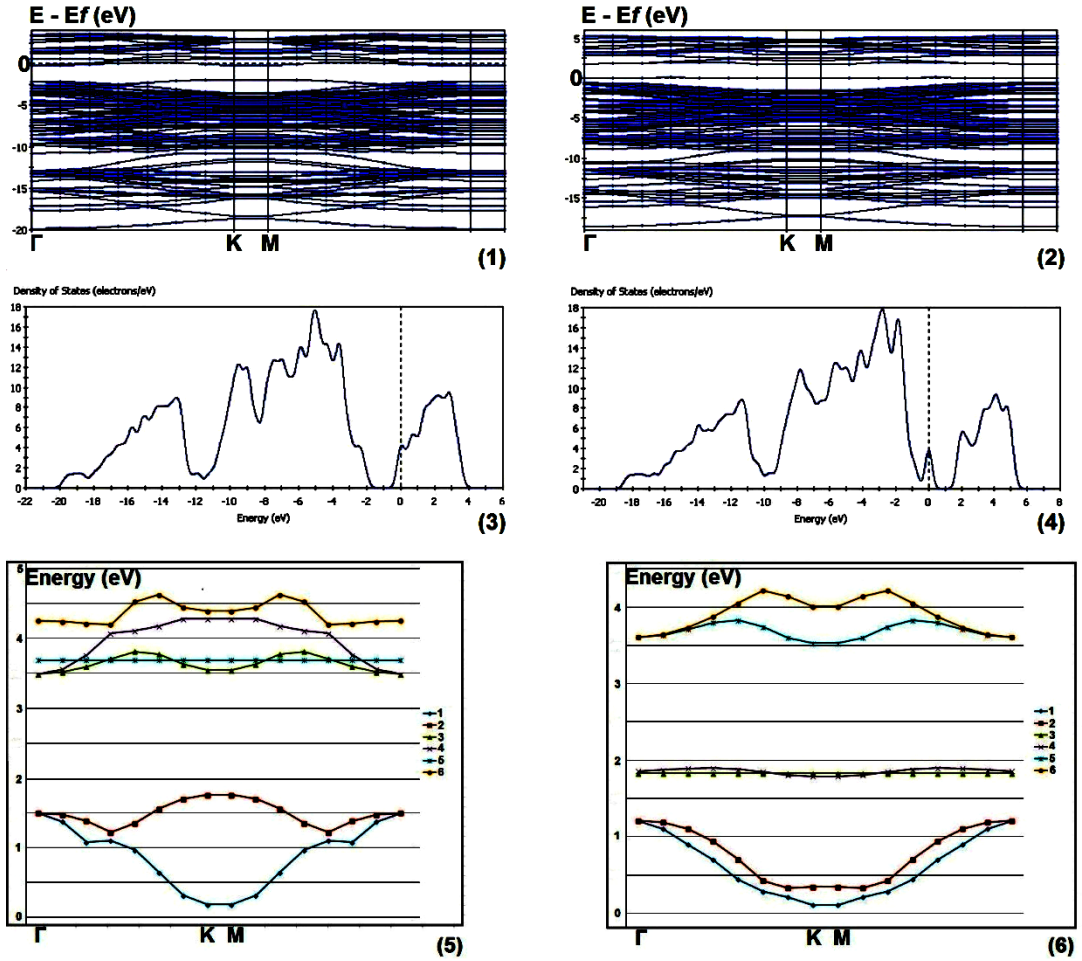

Figure 7. 4. Band structures, DOS and Gap states for the monolayer on 4H-*SiC* $(\sqrt{3}\times\sqrt{3})R30°$ substrate surface reconstruction: (1, 3, 5) - (0001) termination; (2, 4, 6) - $(000\bar{1})$ termination.

Both terminations of the (3×3) reconstruction display the complicated band states (Fig. 7. 5), which are essentially different as against the structures on the $(\sqrt{3}\times\sqrt{3})R30°$ reconstruction. The main distinction of band structure and DOS configurations on the (0001) substrate surface is found owing to the transitional half-filled level (3) in the vicinity of the Fermi level (4) of 2.745 eV (Fig. 7. 5_5). Together with the supporting filled level (2) and the upper empty levels (5) and (6) this intermediate band is located in touch with the conduction band separated from the valence band by the very small gap of 0.4 eV with the trend to be closed. The maximum of valence band corresponds to the maximum of filled level (1). All these levels meet together in the *K* and *M* points. The converged (2) and (3) levels are moved from the conduction band in the *Γ* point. The empty (5) and (6) levels join together in the same point.

For the $(000\bar{1})$ - (3×3) substrate surface (Fig. 7. 5_6) the transitional band includes the half-filled level (4) pinned by the Fermi level of 2.323 eV (3). This couple meets with the filled level (2) and empty level (5) in the *K* and *M* points. This case differs from the above-mentioned one since the transitional (2), (4) and (5) levels are located inside the gap. Also, the levels (2) and (5) diverge in the *Γ* point, whereas the levels (4) and (5) meet there. Due to the transitional band existence and convergence of band spectrum in the *Γ* point the interfacial layers of both terminations have a considerable specification, which supports the experimental data that the (3×3) reconstruction is not the proper precursor for graphene formation replaced by the $\left(\sqrt{3} \times \sqrt{3}\right)R30°$ as an annealing progress (Forbeaux et al., 1998, 1999).

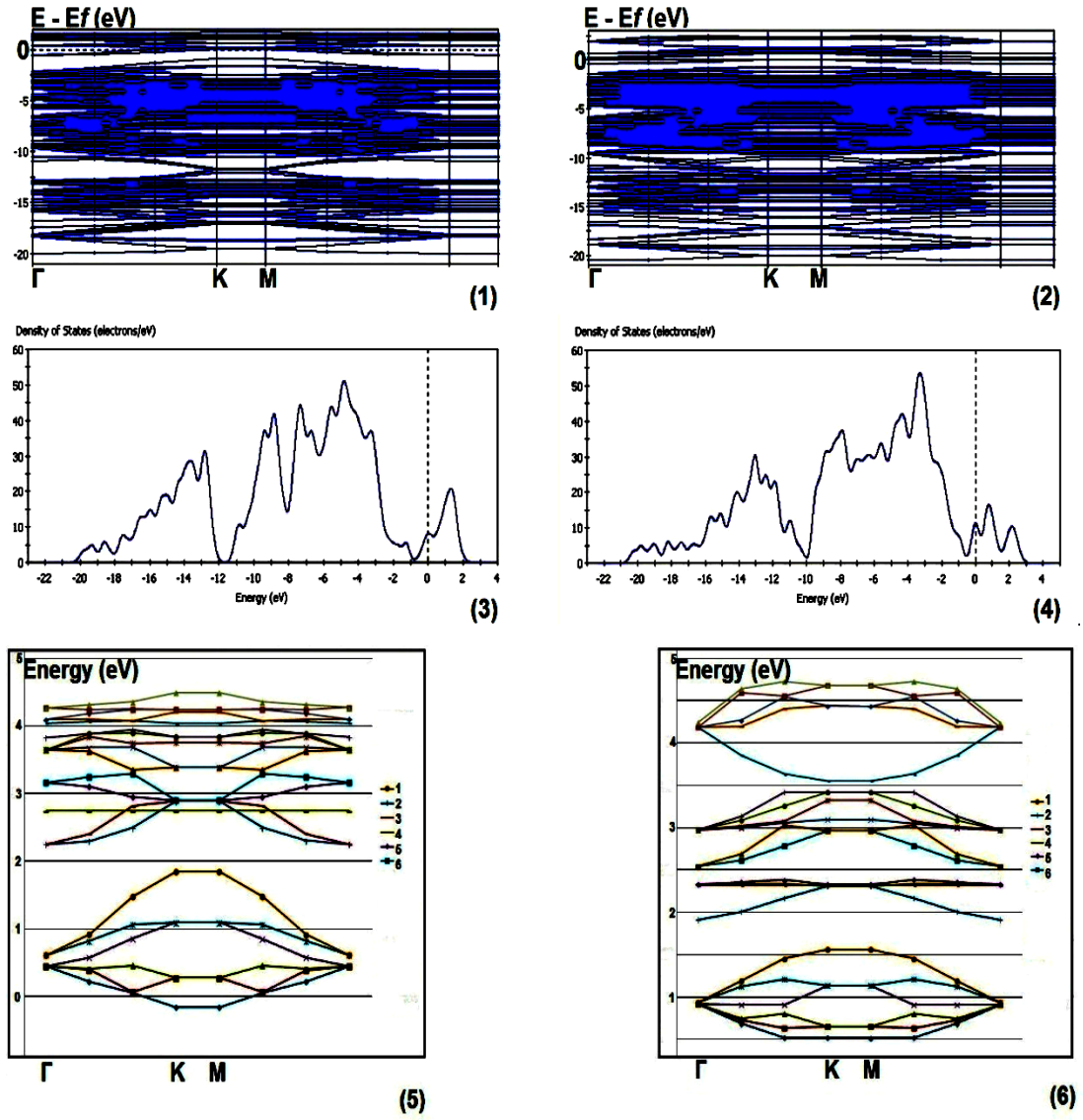

Figure 7. 5. Band structures, DOS and Gap states for the monolayer on 4H-*SiC* (3×3) substrate surface reconstruction: (1, 3, 5) - (0001) termination; (2, 4, 6) - $(000\bar{1})$ termination.

7. 4 Bi-layer's electronic structure

The BL electronic structures were calculated for the Bernal stacking order while arranging the second graphene layer at the distance of 3.5 *A* from the first one acceptable for the Van der Waals forces. These forces are very poorly operated by the DFT leading to some complications and uncertain results (Clark et al., 2005). For instance, the band gaps revealed at the DOS diagrams (Fig. 7. 6) trend to be closed.

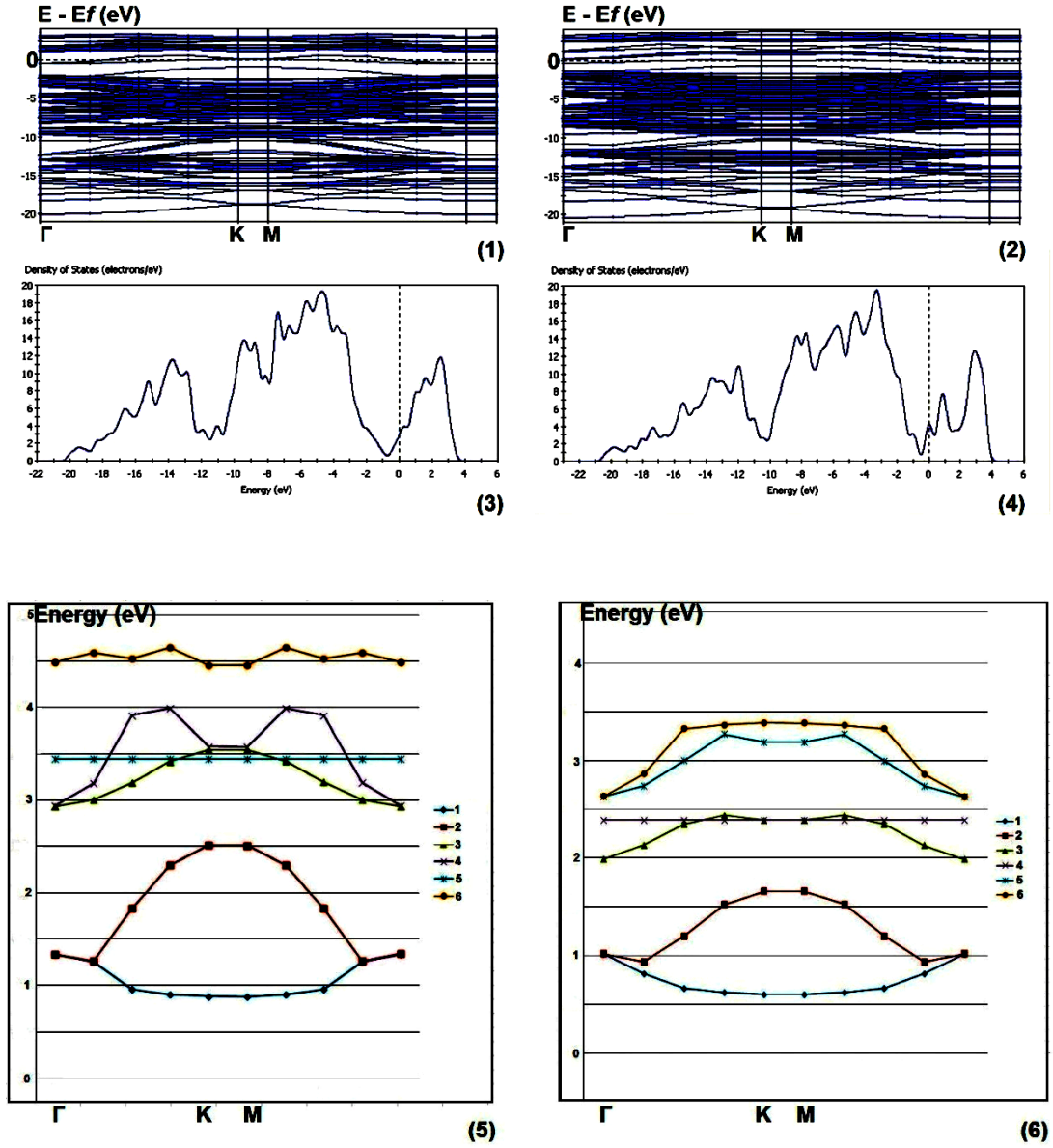

Figure 7. 6. Band structures, DOS and Gap states for the bi-layer on 4H-*SiC* $(\sqrt{3} \times \sqrt{3})R30°$ substrate surface reconstruction: (1, 3, 5) - (0001) termination; (2, 4, 6) - $(000\bar{1})$ termination.

At the same time the very intricate pictures of meetings and divergences in *K*, *M* and *Γ* points take place for both *Si*-face and *C*-face terminations that require special analysis to elucidate the gap states around the Fermi level. For the second layer the effect owing to interaction with substrate fades as against the interface. Therefore, the electronic structures for both terminations are essentially like each other.

The BL on (0001) - $\left(\sqrt{3}\times\sqrt{3}\right)R30°$ substrate reveals the narrow transitional band together with the Fermi level separating the valence and conduction bands. For this electronic structure the half-filled level (3) touches the Fermi level (4) and meets the empty level (5) in *Γ*, *K* and *M* points at once (Fig. 7. 6_5). The locations in *Γ* point corresponding to their minimums are 0.5 eV below the Fermi level and 0.1 eV above the Fermi level in *K* and *M* points. The maximum of level (5) is located 0.46 eV below the minimum of level (6), which corresponds to the conduction band minimum. The locations in *Γ* point are 0.42 eV above the maximum of filled level (2) corresponding to the valence band maximum.

The similar transitional band exists for the $(000\bar{1})$ - $\left(\sqrt{3}\times\sqrt{3}\right)R30°$ surface (Fig. 7. 6_6). The half-filled level (3) and the Fermi level (4) form this transitional band. Its maximum is 0.2 eV below the minimums of levels (5) and (6) corresponding to the conduction band minimum. Its minimum is 0.3 eV above the maximum of level (2) corresponding to the valence band maximum. This transitional band does not meet with the levels (2), (5) and (6).

The results of simulation show that the dependence on support effects fades while the intended bi-layer is gradually grown. As the distances between alternating layers are increased the interaction with substrate reduces. Every following layer becomes electronically independent of substrate. It was noted that the band gap has trends to be zero only after the thickness of foliated structure exceeds the fourth planes (Zhou et al., 2007, 2008). The resembling images of the above-mentioned band structures are also distinguished by comparison, particularly for both terminations of same unit cell $\left(\sqrt{3}\times\sqrt{3}\right)R30°$ reconstruction. The narrow transitional band coupled with the Fermi level in the middle of the gap is the main characteristic of both structures. At the distance of 3.5 $\dot{A}$ acceptable for the Van der Waals forces both *Si*-face and *C*-face terminations of the $\left(\sqrt{3}\times\sqrt{3}\right)R30°$ reconstruction exhibit very negligible distinctions because of remoteness from substrate.

The band states and DOS diagrams calculated for the (3×3) unit cell reconstruction of both terminations showed similarity as regards the closure of all gaps (Fig. 7. 7).

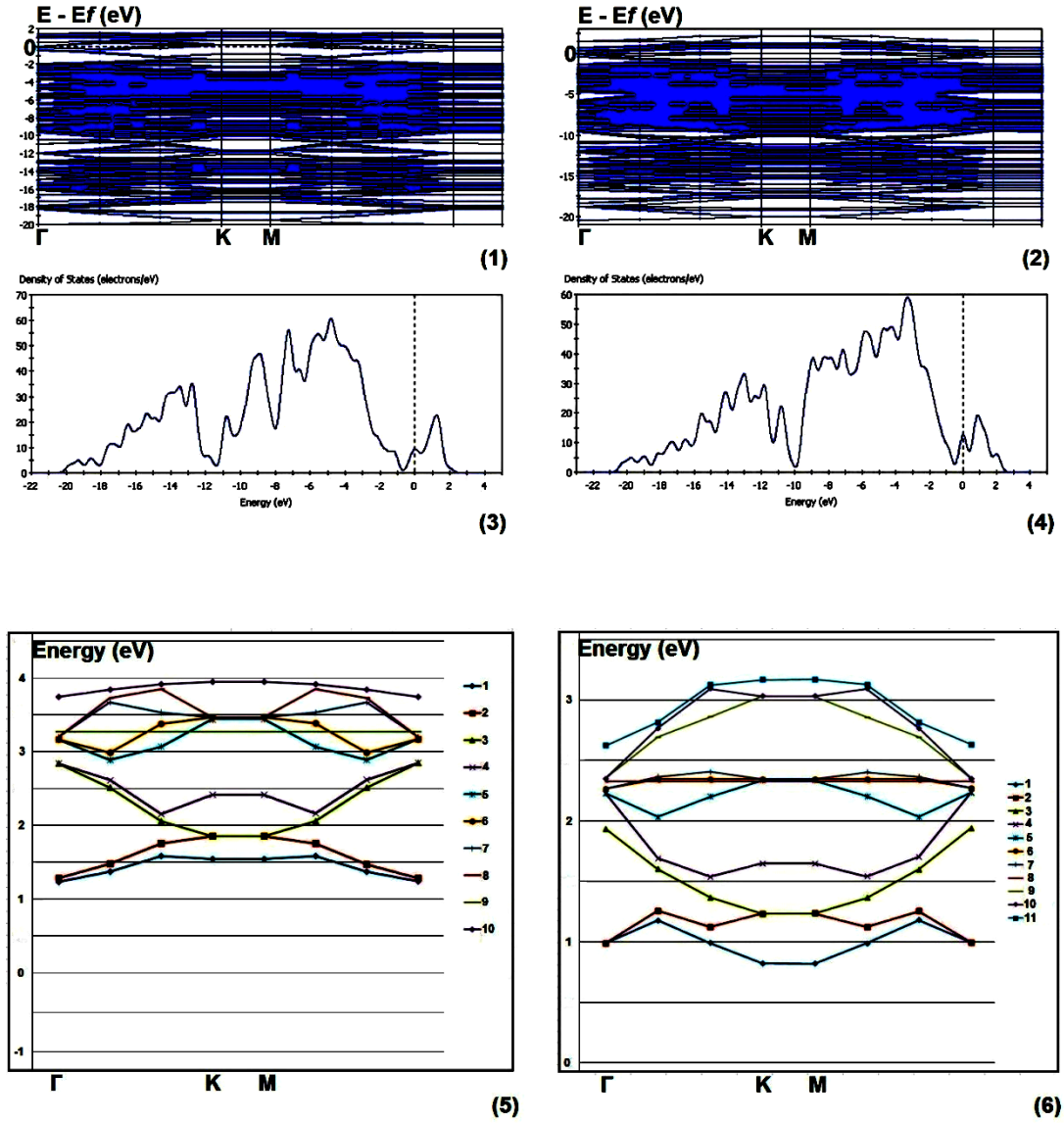

Figure 7. 7. Band structures, DOS and Gap states for the bi-layer on 4H-*SiC* (3×3) substrate surface reconstruction: (1, 3, 5) - (0001) termination; (2, 4, 6) - (000$\bar{1}$) termination.

On the (0001) surface the half-filled level (6) runs along the Fermi level (9) with minimum located 0.3 eV below. They form the transitional sub-band including the filled level (5) and the empty levels (7) and (8). The levels (5), (6), (7) and (8) meet together in the *Γ, K* and *M* points (Fig. 7. 7_5). Their locations in *Γ* point are 0.1 eV below the Fermi level. Their locations in *K* and *M* points are 0.2 eV above the Fermi level. The maximums of levels (3) and (4) correspond to the valence band

maximum. For the BL on $(000\bar{1})$ - (3×3) substrate (Fig. 7. 7_6) the half-filled level (6) passes through the Fermi level (8), and meets with the filled level (5) and the empty level (7) in *Γ*, *K* and *M* points. The locations in *Γ* point corresponding to the minimum of level (6) are 0.06 eV below the Fermi level. The locations in *K* and *M* points coincide with the Fermi level. All these transitional levels for both (0001) and $(000\bar{1})$ terminations meet in *Γ* point. Therefore, the BLs on (3×3) reconstruction do not reveal any similarity with graphene formation. The gap states for both terminations are of a very intriguing configuration. The essential distinction was performed due to the convergence of all transitional band levels in the vicinity of the Fermi level in *Γ* point that is forbidden for graphene. It is in good agreement with the experiment that graphene is not crystallised on the (3 × 3) reconstruction formed via transformation on the (0001) surface of $\left(\sqrt{3}\times\sqrt{3}\right)R30°$ reconstruction as the best graphene precursor (Forbeaux et al., 1998, 1999).

7. 5 Divergence of multi-layer

The mutability of the FLG (few-layer graphene) structures is interpreted via electronic state evolution as its propagation from the substrate to target bi-layer. At the beginning, the passivated (0001) and $(000\bar{1})$ surfaces of both $\left(\sqrt{3}\times\sqrt{3}\right)R30°$ and (3×3) reconstructions were trailed with a view to initial recognition (Fig. 7. 1). As for the same reconstruction, the band structures and DOS showed the wide gaps of 2.58 eV were completely identical for both polar surfaces.

After substrate surface dehydrogenation the cardinally changed situation occurs (Fig. 7. 2). The transitional bands separating gaps prove to be the main features found for all the calculated modifications at different energy levels. This band is traced by the Fermi level together with the half-filled level occupied by the last unpaired electron. It is separated into two narrow sub-bands: the lower one is filled and the upper one is empty. The structure calculated for the (0001) - $\left(\sqrt{3}\times\sqrt{3}\right)R30°$ surface is in good agreement with the experimental data (Johansson et al., 1996; Northrup and Neugebauer, 1998). The half-filled level and the Fermi level are emplaced above the valence band maximum (Fig. 7. 3_3). The filled level is located under the half-filled and the Fermi levels, but above the valence band maximum. The nearest empty level is displaced towards the conduction band. For the $(000\bar{1})$ - $\left(\sqrt{3}\times\sqrt{3}\right)R30°$ surface (Fig. 7. 3_4) the half-filled level coupled

with the Fermi level are closely moved to the valence band. The very similar configurations in vicinity of the Fermi level are revealed for the (3×3) reconstruction (Fig. 7. 3_1, 2). Therefore, the transitional band including the filled, half-filled and empty levels adjoined to the Fermi level is characteristic of dehydrogenised substrate modifications. Nevertheless, the different dispositions with regard to the bands and gaps on the (0001) and $(000\bar{1})$ surfaces predetermine the different pathways during superimposed processes (growth).

At close distance of 2.0 $\dot{A}$ (or less) acceptable for covalent bonds the first deposited *C*-layer succeeds to underlying mutability. Under strong interaction the substrate diversity is transformed into the interface. The modified transitional bands inherited from supporting substrate are found on both polar surfaces of the $\left(\sqrt{3}\times\sqrt{3}\right)R30°$ reconstruction (Fig. 7. 4_5, 6). The half-filled level and the Fermi level are recognised near the opposite edges of wide gaps. This couple separates the empty level and the filled level and touches the conduction and valence bands in different cases. On the (0001) surface the system looks like the *n*-type semiconductor as against the *p*-type on the $(000\bar{1})$ surface. The tendency to be closed in the *K*-*M* points of the **BZ** might be attributed to graphene influence. However, this tendency is very hardly identified because of substrate influence. The same effect is dominant for the (3×3) reconstruction (Fig 7. 5_5, 6), where the bands are separated with maximal gap of 0.4 eV. The band of half-filled, filled and empty levels adjoined in the *K*-*M* points stretches towards the conduction band. Thus, the interface layers demonstrate the intermediate properties of buffer, as it was experimentally shown (Forbeaux et al., 1998, 1999; Hass et al., 2006, 2008).

As a consequence of total remoteness of 5.5 $\dot{A}$ from substrate the renewed electronic patterns result in the Van der Waals forces and weak interaction in the enlarged bi-layer thickness. The former contrast fades between the polar surfaces but enforced as to both reconstructions. For the (0001) - $\left(\sqrt{3}\times\sqrt{3}\right)R30°$ support the half-filled level joint with the Fermi level and the empty level separate the two tiny gaps (Fig. 7. 6_5). These levels meet together in the *K*-*M* points below the minimum of conduction band. Their crossing in the Γ point occurs above the maximum of valence band. For the $(000\bar{1})$ surface, we have two gaps of 0.2 eV and 0.3 eV. The empty level moves towards the conduction band (Fig. 7. 6_6).

Both bi-layers for the polar surfaces of (3×3) reconstruction display the gap closure (Fig. 7. 7_5, 6). The half-filled level in the vicinity of the Fermi level meets with the filled level and the empty level in the *K*, *M* and *Γ* points at once. This band is connected together with the conduction band and the valence band. Although the tendency of closure in *K*-*M* points, *Γ* point occurs as the main location where the conduction and the valence bands are crossing. It is a satisfactory explanation why graphene was experimentally failed on the (3×3) reconstruction, produced only by the transformation via the $(\sqrt{3} \times \sqrt{3})R30°$ reconstruction (Forbeaux et al., 1998, 1999).

7. 6 Distance between CDC planes

Because of the DFT poor operations with the Van der Waals forces (Clark et al., 2005) the bi-layer electronic structures were revised as the functions of separation between two CDC layers grown on the (0001) - $(\sqrt{3} \times \sqrt{3})R30°$ substrate surface (Fig. 7. 8). As for the separation of 0.35 nm, the shorter distance of 0.25 nm does not make any essential differences (Fig. 7. 8_1, 2). Only the half-filled level (3) and the empty level (4) of transitional band are divergent near the *K* – *M* points and joint to the Fermi level (5) in the *Γ* point. As a result, the gap between the transitional band and the conduction band (6) turns into the narrow slot. The lower gap between the transitional band and the valence band (2) gets wider. As an approach to the combined Van der Waals and covalent interaction at the distance, for example, 0.17 nm between CDC planes, the resulting gap state demonstrates a completely new band structure (Fig. 7. 8_3). For this band structure the inherited transitional band closes the lower gap. Thus, the new valence band is created. The band gap between this new valence band and conduction band gets narrower, but still exists. For the distances of 0.16 nm and 0.15 nm between CDC planes this band gap is closed in the *K* – *M* points (Fig. 7. 8_4, 5). At the same time, in the *Γ* point the divergence does take place. Thus, the resulting band structures become approximating to the electronic structure for the freestanding graphene (Fig. 3. 1_e). However, there is noticeable difference because of the inherited transitional band existence. It is explained by the substrate influence. One can see (Fig. 7. 8_4, 5) that the Fermi level passes not strictly through the *K* – *M* points of meeting for the valence and conduction bands, but slightly lower. Furthermore, the empty level is located in the area of divergence for the valence and conduction bands. This is why the resulting

band structures (Fig. 7. 8_4, 5) differ from the electronic structure for the freestanding graphene because of the substrate induced interaction.

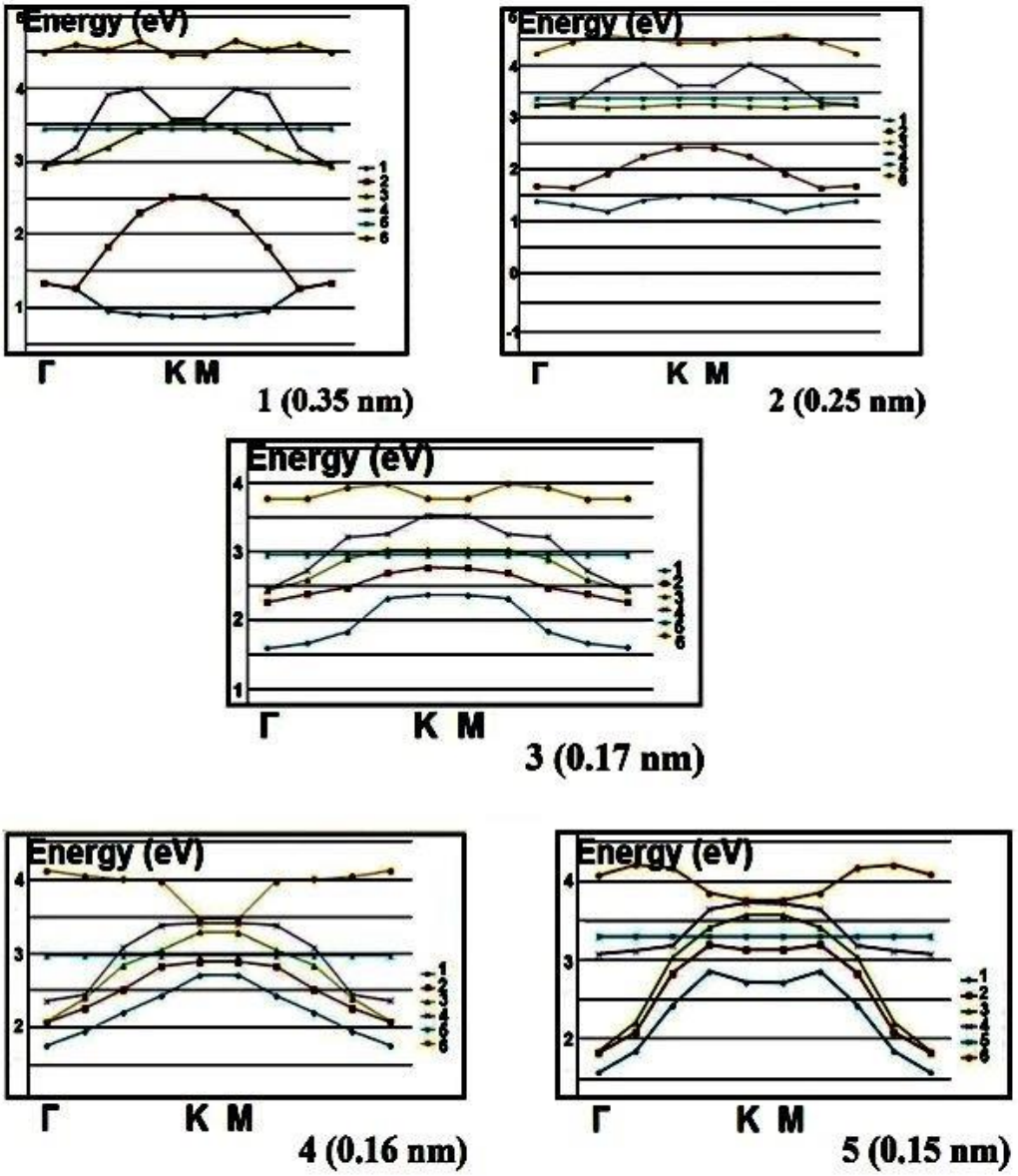

Fugure 7. 8. Gap states for the alternating distances between *C*-planes of bi-layer grown on the 4H-*SiC* (0001) - $\left(\sqrt{3}\times\sqrt{3}\right)R30°$ substrate surface.

7. 7 Computation results

The electronic properties of the graphene multilayer change rapidly. A multilayer is grown under effective interaction with the supporting framework while a layer number run to graphite 3D crystal. The unique substrate alternatives pre-determine every time different pathways of intended growth. Our first experience of gap-

engineering showed that the interaction with solids enables the regulation of the multi-layer properties by using the alternating substrates, number of interlaying planes, their stacking orders and distances between them.

A gradual transformation of two consistent *C*-layers was trailed under permanent geometric disposition. Therefore, all the possible deviations might be attributed to the substrate induced interaction. An initial divergence starts since the substrate dehydrogenisation. This mutability is transferred into the interfacial layer imitating the *n*-type and *p*-type structures. The buffering carbon planes succeeding to substrate alteration have nothing in common with the freestanding graphene. This layer shows the intermediate quality grown under uncompensated substrate dangling bonds. The influence of interaction fades as a multilayer thickness increases. Further multilayer growth is defined by geometrical arrangement and stacking order.

At the second plane, the new electronic states are revealed via mixed properties. The structure grown on the 4H-*SiC* (0001) - $\left(\sqrt{3}\times\sqrt{3}\right)R30°$ substrate surface involves the dominant graphene identification. The general conduction and valence bands trend to meet in *K* – *M* points while diverging towards the **BZ** centre. In other words, the characteristics of graphene are becoming more evident (Geim and MacDonald, 2007). Meanwhile, the substrate induced influences are interfering by means of the transitional band. The pure graphene properties might be in anticipation only as the thickness of the foliated structure exceeds the four CDC planes (Zhou et al., 2007, 2008).

Chapter 8 Surface conversion under *HF* impact

8. 1 Introduction

Chemical transformations on the 4H-*SiC* (0001) - $(\sqrt{3} \times \sqrt{3})R30°$ substrate surface are simulated under *HF* impact with a view to perfect CDC interface in anticipation of epitaxial graphene growth. To reveal reaction dynamics and feasibility the successive stages of *Si – F* interaction are analysed on the basis of transition state theory (TST).

In the course of CDC growth a many-atomic system of 4H-*SiC* substrate is transformed by the rearrangement of nuclear configurations from the starting point to the final product while running through the regular array of transition states and interim products. The initial ideas of transition state theory (TST) introduce the basic concepts of chemical kinetics to explain the rates of elementary transformation. It also refers to an activation complex theory and theory of absolute reaction rates. The TST assumes a special type of equilibrium between reactants and activated complexes when the minimal energy is required for the beginning of chemical reaction. Activation energy is also defined as the height of potential energy separating reactants and products.

The TST development is based on the variable configurations of potential energy surface (PES). The PES is described in terms of the potential energy function $U(q_\alpha)$, where q_α indicates the nuclei coordinates of reactant molecules. For every configuration the value *U* is defined by the nuclei coordinates. The maximum of potential energy *U* will fall as the atoms rearrange and reach the products. The geometric parameters, such as bond length, bond angle or other non-geometrical approximations are used as the reaction coordinates. This is recognised as the most important characteristic of molecular geometry (Levine, 2002, 2009). The fast reaction path along the gradient of potential energy is advanced as the geometric parameters change from one or more reactants to one or more products.

The relevant points and curves on the PES connecting the reactants and the product (Fig. 8. 1_a) are appropriate for the path of minimum potential energy (MEP). The sets of atomic configurations running along the MEP determine the intrinsic reaction coordinate (IRC). The local minimums on the MEP correspond to the reactants, products, reaction interim products and intermediates. The cluster of atoms corresponding to the region of maximum on the MEP is called the activated

complex (Fig. 8. 1_b). This maximum along the MEP is a saddle point. The energy value of this saddle point corresponds to the activation barrier as a typical characteristic of transition state. The difference of energy values between the reactant and the transition state is the activation energy value.

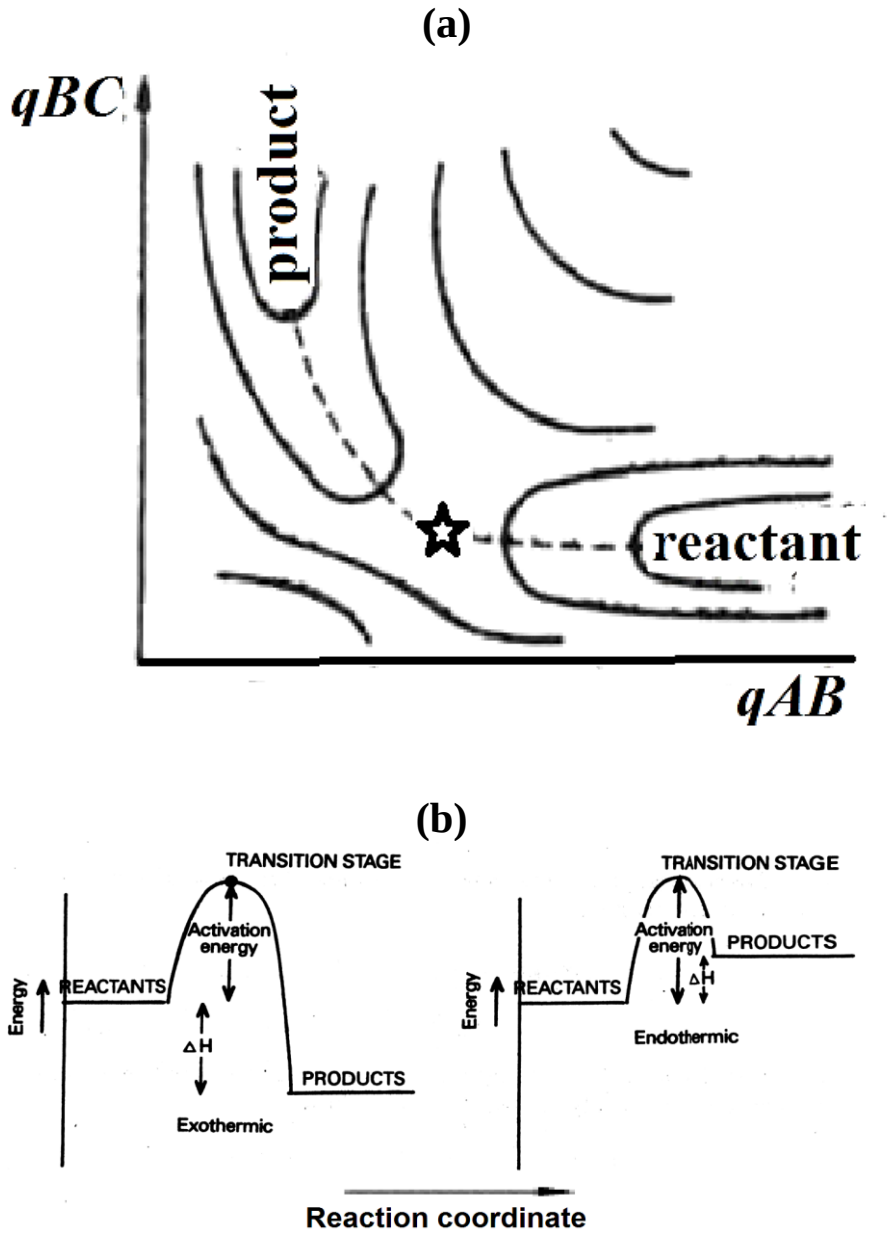

Figure 8. 1. Energy profile along the reaction coordinates.
(a) – Potential energy surface (for reaction AB+C = BC+A);
Dotted line – the path of minimum potential energy (MEP);
Star point – the transition state located on the MEP.
(b) – Both minima of reactant and product; the maximal point corresponds to activation energy value for rate-determining transition state.

The search of transition state requires the proper data of reactant and product. The PES concept is a basis for the TST development. For the transition state finding, one should calculate the potential energy surface, determine the main saddle point on the MEP pathway and connect it with the minimum points of the starting and the final states. Reactant molecules in the TST follow a unique path that connects the reactant basin and the product basin. The highest point on this path is the saddle point of the highest order. This is the point of highest energy along the reaction path. Such a state is not a stable molecule. This is the state when old bonds are broken and new bonds are created, i.e. the only transition from reactants to products.

There are some ways to locate transition state for chemical reactions. The CASTEP methods require the structural and energetic snapshots for every step of reaction progress. The principles work as follows: a collection of intermediate sets of configurations is created by interpolation of nuclear coordinates from the starting to the final states. If the interpolation is carried out along the straight line that connects reactants and products, the method is called the Linear Synchronous Transit (LST). If the interpolation is carried out along the parabola that connects reactants and products, the method is called the Quadratic Synchronous Transit (QST). Both mutual methods are used in combination for structural and energetic snapshots at every step of a designed process.

8. 2 *Si – F* interaction on (0001) - $(\sqrt{3} \times \sqrt{3})R30^{o}$ surface

The optimal CDC patterns are designed for development by means of 4H-*SiC* substrate surface transformation under heating and wet etching in electrolytic system. These electrochemical operations are most suitable to avoid the undesirable damages of surface and its contamination by the possible side products. As it was shown before, these conditions are necessary for perfect graphene. The foliated carbon layers evolving under interaction with the carbide substrate are developed through the successive surface conversion. The etching operations under *HF* impact are intended for the beginning stage. The 4H-*SiC* (0001) - $(\sqrt{3} \times \sqrt{3})R30°$ unit cell is taken as a starting point to be the most proper precursor for graphene. The reactions of surface conversion run through the break of *Si – C* bonds, oxidation of the *C*-atoms, whereas the *Si*-atoms escape in the form of volatile SiF_4.

The general trends of *Si – F* interaction are taken into account. The fluorine is able to penetrate deeply into the bulk successively while forming the interface.

Interfacial layer consists of *C, Si, F, F_2,* etc. clusters under steady state balance. The *F*-atoms form *SiF, SiF_2* and *SiF_3* components while ejecting from the *SiC* surface in the form of volatile *SiF_4*. The yield of ejected *CF_x* is very small.

These processes running in the interface via intermediate *SiF_x* groups are not differentiated for the most suitable site. As to the beginning, the free dangling bonds directed towards the *HF* molecule can make easy saturation with the *SiF* groups due to the strong difference of electro-negativities. All the following *F*-atoms should search the suitable sites for *Si – C* bonds breaking and *Si*-atoms removal. Atomic control for selectivity is the main complexity of *HF* etching. To understand the conversion mechanism a systematic monitoring is required for the stepwise *SiF_x* formation. The best indexes for reaction progress are supplied by two energetic barriers. The barrier from reactant (BR) also known as activation energy is the difference between transition state and reactant energy values. The barrier from product (BP) is found as the difference between transition state and product energy values. The difference between both barriers defines the energy of reaction (ER).

The surface modification by means of material removal via chemical *Si – F* interaction is carried out for the 4H-*SiC* (0001) - $(\sqrt{3} \times \sqrt{3})R30°$ substrate surface. The explored super cell comprises 48 *Si*- and *C*-atoms forming 8 *SiC* bi-layers. The number of bi-layers was determined by the converging of total energy as the super cell enlarges. The alternation of bi-layers is arranged so that the top surface with one central *Si*-atom is emplaced over the adjacent surface with two central *Si*-atoms. The *C*-atoms on the bottom of super cell are saturated with hydrogen. The vacuum gap of 15 $\dot{A}$ over the top surface is held to be filled with *HF* molecules to attack the *Si*-atoms. Each *HF* molecule is turned with *F*-atom downward to *SiC* surface. All the atoms of super cell are kept fixed at their original position during calculation. Only the *Si*-atom and *C*-atom of *Si – C* bond together with the *H*-atom and *F*-atom of *HF* molecule interacting with these *Si*-atom and *C*-atom are unfixed.

The operations of surface modification by *HF* etching were firstly probated by a simultaneous attack of four *HF* molecules on the central *Si*-atom of top level to remove this atom in form of *SiF_4* volatile product. This experience proved to be unsuccessful because very energetically high intermediates resulted instead of transition states. Therefore, for the subsequent trial, we needed to use different tactics of manipulation by analogy with the former experience (Garrison and Goddard, 1987; Wu and Carter, 1991) of *F*-atom attack on silicon surface by proceeding in

turns. This means that the transition states should have been found for each *F*-atom separately.

8. 2. 1 *SiF* and SiF_2 groups formation

The characteristics of stepwise addition for the *SiF* group on the 1st *SiC* bi-layer of *Si*-face support are shown (Fig. *S* 1) (index **"*S*"** is used for Supporting Materials, Appendix 1). The *SiF* group involving the first three *F*-atoms was easily set up by means of the risen upward dangling bonds from terminating *Si*-atoms. The addition of initial two *F*-atoms on the 1st and 2nd steps has the exothermic effect comparable with the *Si – F* bond strength (Table 2, Appendix 2). The very low activation barrier (BR) implies the spontaneous process. The activation barriers are gradually increased. The values for energies of transition state are decreased. The third step is found to have a weak endothermic effect running under the increasing activation energy and low barrier from product.

The attack by subsequent three *F*-atoms forming the SiF_2 group on this surface requires the regular *Si – C* bonds breaking (Fig. *S* 2). The SiF_2 group formation corresponds to the lower energy of reactant and product (Table 2, Appendix 2). The energies of reactions are increased. The energies of transition states are decreased, whereas the activation barriers are considerably increased. These trends are enforced with each following *F*-atom. The strong endothermic effect is defined by energies of reactions increasing considerably as against the *SiF* group. The high activation energy and the low barrier from product are appropriate for this step.

The *SiF* and SiF_2 groups formations take place through the different routes to transition states (Fig. *S* 3, 4). The *SiF* group is formed through the saturation of free dangling bonds on the terminating substrate surface. The formations of subsequent SiF_2 group cost much more energy spent for the *Si – C* bonds breaking. These bonds are located on the different sides of *Si*-atoms. The oxidised *C*-atoms are released and their electrons are taken into the interface to form a gaseous H_2.

8. 2. 2 SiF_3 group formation

The SiF_3 group starts to be formed from the 7th *F*-atom (Table 2, Appendix 2). The 7th *F*-atom is joined by complicated pathway through the several interim products (Fig. *S* 5). The consistent approximations via the transition states are shown

(Fig. *S* 6). These transition states separate the above-mentioned four interim products and the resulting state is finally found. All the interim products are in turn performed as new reactants for the succeeding operations repeated several times until the final product is reached. In the beginning of these operations, the energy of reaction values decreasing does occur after the first transition state (Table 2, Appendix 2). This exothermic effect is enforced as the *F*-atoms addition takes place. It is defined by the difference between the barrier from reactant (activation energy) and barrier from product. Both values are initially held at the high level. Then, they decrease on the final step 7_5. The tendency for alternating of transition state energy values and its location is kept traced (Fig. *S* 7). The transition state energy values prolong the general decreasing trend. The search for new location for the stepwise replacement of transition states may also be seen (Fig. *S* 7). The following 8^{th} *F*-atom addition avoids any interim products as it immediately passes through the relevant transition state (Fig. *S* 8, 9). While creating in turn the next SiF_3 cluster, it breaks the next *Si – C* bond. The energies of reactant and product continue to decrease (Table 2, Appendix 2). The energy of transition state falls as well while locating in the moderate position. The activation energy increases to the level of first transition state for the previous 7^{th} *F*-atom. This value is partly compensated by the value of barrier from product. It results in the high energy of reaction and endothermic effect for this addition step. The subsequent growth for the 9^{th} *F*-atom adding one more SiF_3 cluster passes through the unusual interim product separating two contrary transition states (Fig. *S* 10, 11). Both states are appropriate for the moderate endothermic effect under equal energy of reaction values (Table 2, Appendix 2). The special feature of this step is owing to the extraordinary increase of activation energy determined for the second transition state. This activation energy value is almost three times bigger than the former maximal values. The barrier from product proved to be unusually increased as well. Therefore, the insignificant energy of reaction value decreasing was found. The location of transition state was moved from the high to middle position.

8. 2. 3 SiF_4 group formation

The 10^{th} *F*-atom is added to create first cluster of SiF_4 group while the energies of reactant, product and transition state proceed to come down (Table 2, Appendix 2). The relevant difference of reactant and product energy values determines the energy

of reaction on the same level as before. However, this transition state is accompanied by the lowering of barrier from reactant and especially barrier from product. Its location is found for increasing path coordinate.

Since the first *C*-atom is finally released after SiF_4 removal (Fig. *S* 12, 13), the energetic characteristics are essentially changed. The next *F*-atom forming the second SiF_4 cluster is added while passing through the two transition states separating interim product (Fig. *S* 14, 15). The energies of reactant, product and transition state increase for the first time as against the former trends. It results in the low value of barrier from reactant under negligible decreasing of barrier from product. As a consequence, the first transition state occurs under small exothermic effect. The second transition state differs by the increasing of endothermic effect due to the difference between both energy barriers (Table 2, Appendix 2). The final transition state is found under increasing path coordinate.

The last SiF_4 cluster is formed while passing through the two transition states separating the reactant and product from the interim product (Fig. *S* 16, 17). Both transition states are found for the increasing energy of reactant and product values. These values are negligibly different from the energy of reactant and product values for the *SiF* group formation. The high value for barrier from product and the low value for barrier from reactant result in the exothermic effect for the first transition state. The second transition state occurring in the same energy range differs by the lowering barrier from product. It proves to be the reason for endothermic effect. All the *Si*-atoms escape in the form of volatile SiF_4 product and the first *SiC* bi-layer of substrate is destroyed. The released *C*-atoms are accumulated in the interface.

8. 3 Penetrating *HF* etching on the deeper bi-layers

After destruction of the upper *SiC* bi-layer the penetrating conversion process is put forward on the new disclosed 4H-*SiC* (0001) - $(\sqrt{3} \times \sqrt{3})R30°$ substrate surfaces.

8. 3. 1 Destruction of the second *SiC* bi-layer

For the starting point the energies of reactant, product, transition state and other values are determined and continuously changed (Table 3, Appendix 2). The initial *SiF* group is emplaced via stepwise transition states evolving from the exothermic regime of starting low barrier from reactant (BR) and high barrier from product (BP) values to the endothermic regime due to the mutual exchange between both barriers.

The 13th *F*-atom attacks the *Si*-atom while occupying the first free dangling bond. The following 14th and 15th transition states mean the completing of the *SiF* group (Fig. *S* 18). As a result, each of the terminating *Si*-atoms loses one bond with *C*-atom while adjoining with *F*-atom.

The following SiF_2 group is created via the 12 successive transition states separating the interim products concerned with the 16th, 17th and 18th *F*-atoms addition. These atoms start to react from the minimal activation and reaction energy values. These values increase at the end of process. The successive interim products alternate while changing each other until the proper site is found. Every regular attack results in the increasing number of SiF_2 clusters and the next *Si – C* bond breaking (Fig. *S* 19, 20, 21).

At the beginning of SiF_2 group formation, the 16th *F*-atom attacks the unit cell and three interim products change each other. The final proper site results from the fourth transition state found for the one of central *Si*-atom (Fig. *S* 19). The corner *Si*-atoms create the SiF_2 cluster after the mostly hard search by means of the 17th *F*-atom via six transition states (Fig. *S* 20). The second central atom is occupied after the 18th fluorine attack through the one interim product and two transition states (Fig. *S* 21). Subsequently, the SiF_2 group is created. It costs the endothermic effect and increase of both barriers energy values.

The same ways of penetrating for *Si – F* interaction are found for the SiF_3 group. As the whole of this group runs via six transition states corresponding to two interim products produced by the 19th *F*-atom and one interim product produced by the 21st *F*-atom (Fig. *S* 22, 23, 24). Three transition states, during the 19th fluorine attack, are found to reach the proper position. It starts from the lowering activation energy value in slightly exothermic conditions. The 20th and 21st *F*-atoms take the different energies for adjoining with the *Si*-atoms. These atoms are connected under local differences for both barriers and energy of reaction values. The abrupt increase of activation and reaction energy values in endothermic regime occurs during the addition of the 21st *F*-atom.

As for the completing SiF_4 group, the following *F*-atoms are advanced to the final target under increasing the total energy values and decreasing the BR and BP values. The final SiF_4 group is formed without any interim products while running via three transition states (Fig. *S* 25, 26, 27). Minimal energy is spent to remove the first *Si*-atom by the addition of 22nd *F*-atom. Due to the decrease of barrier from

product values the 23rd and 24th *F*-atoms are added in endothermic regime. As a result, the volatile phase escapes and three *C*-atoms are oxidised while losing the last bonds with *Si*-atoms. The locations of TS describe the loop (Fig. *S* 28). Finally, the location of TS returns to the initial position for the *SiF* group, i.e. starting point.

Thus, the long trials were undertaken for the SiF_2 and SiF_3 groups. The easiest search of transition states under *Si – F* interaction occurs for the *SiF* and SiF_4 groups. These groups avoid any interim products because only few choices for direct bonds are available. For the SiF_2 and SiF_3 groups many possibilities stipulate the long search for proper sites for possible bonds. These groups are formed via numerous interim products. Each SiF_x group (besides SiF_4) is formed while decreasing the total energy and increasing the activation energy values. The activation and reaction energies increase at the end of these groups completion. The highest activation energy is reached with the SiF_3 group.

8. 3. 2 Destruction of the third *SiC* bi-layer

The third *SiC* bi-layer is broken under increasing energy values as a proceeding *HF* penetration (Table 4, Appendix 2). Again, as before, the locations of TS describe the loop (Fig. *S* 29) and returns to the initial position for the *SiF* group, i.e. starting point.

In contrast to the former case, the transition states were found for the successive row of SiF_x groups through the relatively increasing total energy values. The geometric pattern for exposed unit cell repeats the configuration of surface level. It means that the reworked bi-layer is arranged with the only central *Si*-atom. The other two *Si*-atoms are located on the sides of unit cell.

The starting *SiF* group resulted from the exothermic regime under very low value of activation energy found for the 25th *F*-atom addition to the central *Si*-atom (Fig. *S* 30, 31, 32). As the reaction continues both barriers from reactant and product values decrease. The energy of reaction values gradually fall to zero while the BR value exceeds the BP value.

The following SiF_2 group (Fig. *S* 33, 34, 35) starts to evolve under very low BR and negative BP values. Therefore, from the 28th *F*-atom the energy of reaction corresponds to endothermic value. Then, the BR value gradually increases. The 29th and 30th *F*-atoms provide the positive energy of reaction value for the group as a whole.

The SiF_3 group (Fig. *S* 36, 37, 38) is formed in endothermic conditions under variable relation between both barriers values. The 31st and 32nd *F*-atoms are added under very low BR value, but considerably higher than BP value. The average endothermic effects are held for the SiF_3 group as the BR and BP values abruptly increase for the 33rd *F*-atom addition.

The last SiF_4 group (Fig. *S* 39, 40, 41) starts to be formed from the 34th *F*-atom with the unusual situation of negative and extremely low BP value. It results in the very high endothermic effect to release the first, central, *Si*-atom even for the low BR value. The two other *Si*-atoms escape under increase of both barriers values. Both energies of reactant and product values eventually return to the initial state.

As against the upper bi-layers, all the SiF_x groups of the 3rd bi-layer are formed on the higher energy level. The release of oxidised carbon atoms reveals the simple way of decomposition advanced through the minimal number of interim products. Two opposite opportunities are found for the maximal endothermic effects of reactions. The first case is stipulated by the extremely negative BP values, e.g. for the 28th, 32nd and 34th *F*-atoms addition. Another endothermic effect is stipulated by the high BR values, e.g. for the 33th *F*-atom addition. At the final stage, the gradual SiF_4 removal results in the successive loss of last electrons from the oxidised *C*-atoms released and accumulated in the unit cell. The SiF_4 removal and release of oxidised *C*-atoms start under the low BR values increasing to the final steps as well as the BP values. The exothermic effects are attributed to the escape process.

8. 4 Progress of the CDC reactions

The designed model for chemical conversion of *SiC* substrate under *Si – F* interaction involves the poly-stage process resulting in the old *Si – C* bonds breaking, escape of SiF_4 volatile phase and accumulation of *C*-atoms segregated after oxidation. To release the carbide derived carbon via *SiC* decomposition the stepwise *HF* attack should penetrate the bulk.

The *Si – F* interaction was traced by means of transition states finding. This process moves forward through the successive interim products in dependence on the unit cell configurations, depth of penetration and way to proper site for transition state. As the reaction stages change each other the new interim products are created under different energy values. One can see essential energy distinctions for different levels and moving SiF_x groups forward (Fig. 8. 2).

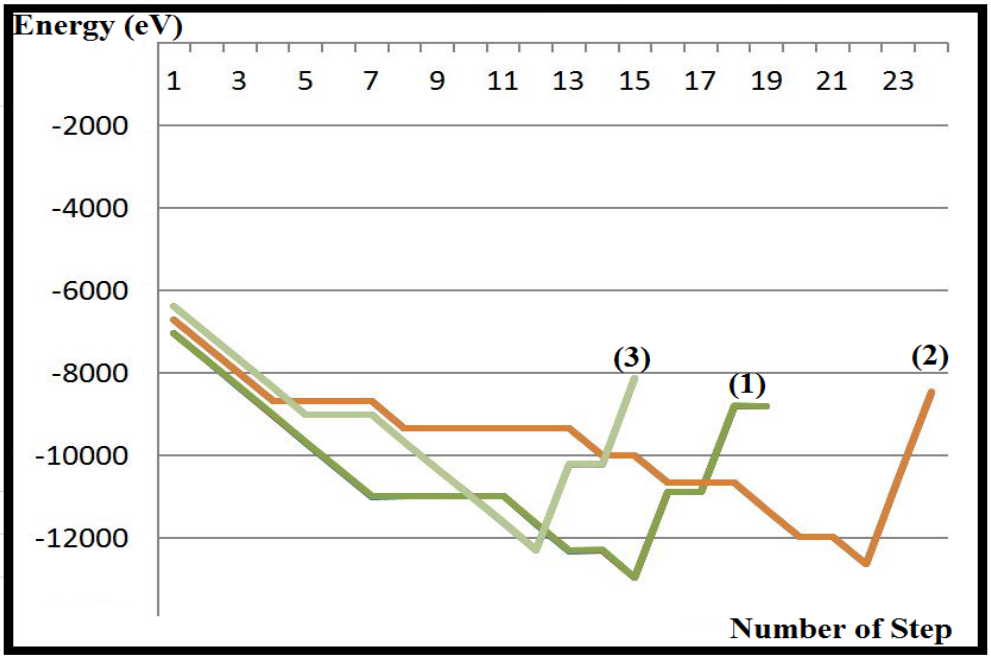

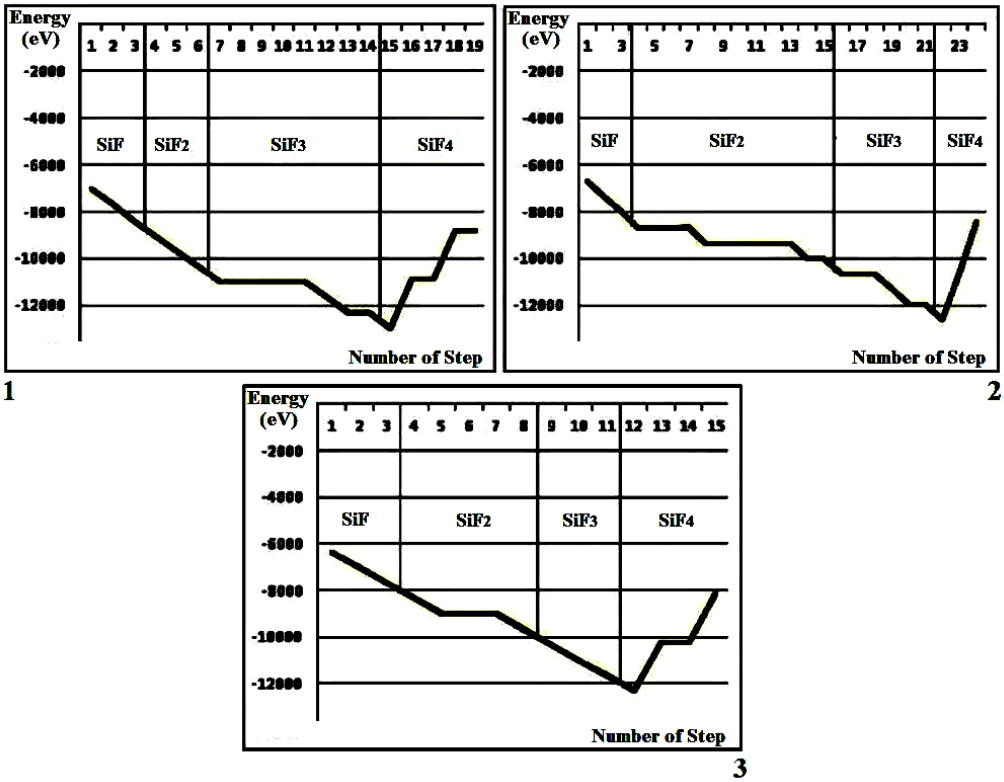

Figure 8. 2. Energies of reactant, product and TS values diagrams for different *SiC* bi-layers as the reaction propagation from *SiF* group towards SiF_4 group;
(1), (2), (3) – numbers of bi-layers.

The whole reaction proved to be expanded through the alternating number of interim products and transition states. The unit cells with the only one central *Si*-atom (1st and 3rd bi-layers) differ by the less number of interim products. As a

penetration is advanced into the substrate bulk the total energies of reactants, products and transition states values gradually increase with the depth. The SiF_x groups go forward under decrease of transition state energy values while returning every time to the initial states during SiF_4 removal.

The main indicative indexes, namely BR, BP and ER are the characteristics of penetration progress. The maximal energies of reaction and activation are spent for the 1st bi-layer and exceed the values spent for the deeper bi-layers (Table 5, Appendix 2). The biggest energy contrasts are also found for the 1st bi-layer. The minimal energies of reaction and activation values are found for the *SiF* groups. The maximal values found for the SiF_2 and SiF_3 groups decrease as the SiF_4 volatile product escapes. The CDC progress is pushed on via the BR, BP and ER as the values of expended energies gradually increase from the *SiF* groups and return to the initial conditions while the SiF_4 volatile product escapes.

The initial *SiF* group of the 1st bi-layer is formed during the saturation of dangling bonds (Fig. 8. 3). The first *C*-atom bonds are broken. This is the case when the BR corresponds to the lower energy level as against the BP. It results in the exothermic effect. Only the third *F*-atom is added under the equal energy values for both barriers. The trend for BR values increasing is the characteristic of SiF_2 group, whereas the energy values for barrier from product decrease. It results in the energy of reaction values increasing. In contradistinction to the previous groups, the SiF_3 group starts to form from transition state search. The starting 7th *F*-atom passes over four interim products. The separating transition states are found in the region of activation energy values approximately equal to the barrier from product values. By means of several recalculations the final transition state is found corresponding to the very small values for both barriers. This defines the energy of reaction value negative and close to zero. After the first SiF_3 cluster, the dynamics of *F*-atoms additions is dramatically changed. The next SiF_3 clusters are formed while the increasing activation energy values which outstrip the barrier from product values. As a result, the energy of reaction values increase to the endothermic level. The SiF_3 group are completed under impulsive increasing of energy values for both barriers. The SiF_4 group is released under the increasing reactant, product and TS energy values. Both barriers abruptly decrease.

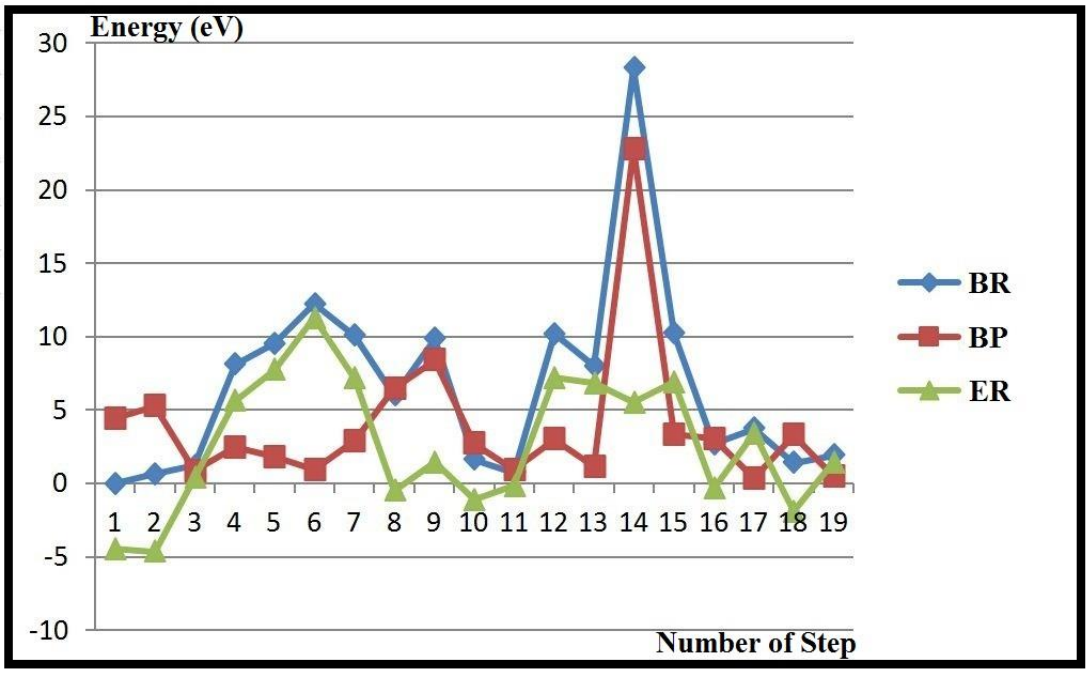

Figure 8. 3. BR, BP and ER values alterations for 1st *SiC* bi-layer.

The advanced *HF* impact on the 2nd bi-layer is shown in Fig. 8. 4.

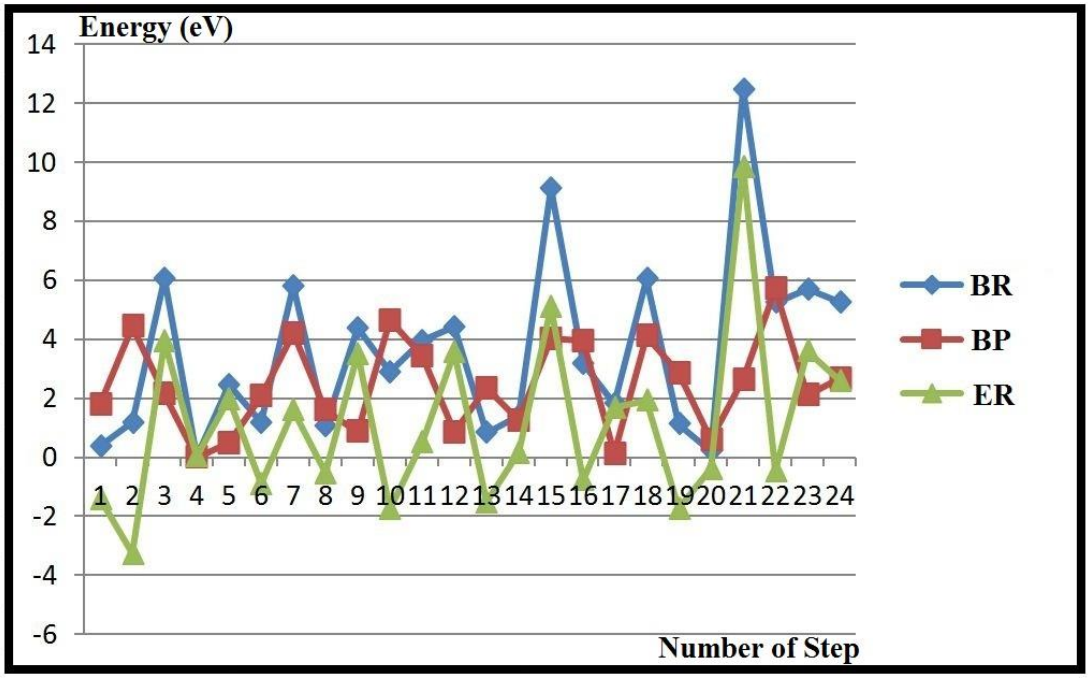

Figure 8. 4. BR, BP and ER values alterations for 2nd *SiC* bi-layer.

The exclusive order of transition states is attributed to particular configuration of unit cell. The initial *SiF* group is created via stepwise stages from the exothermic conditions towards the endothermic conditions due to the changes of

both barriers values. The following SiF_2 group is created through the 12 interim products. The alternation of both BR and BP values trends to the endothermic effects increasing. The tendency for maximal BR and ER values increasing occurs at the end of SiF_3 group formation. The final SiF_4 group starts to form from the strong decrease of BR value. This leads to the local exothermic effect (Fig. 8. 4). The third bi-layer is transformed via quite different dynamics (Fig. 8. 5).

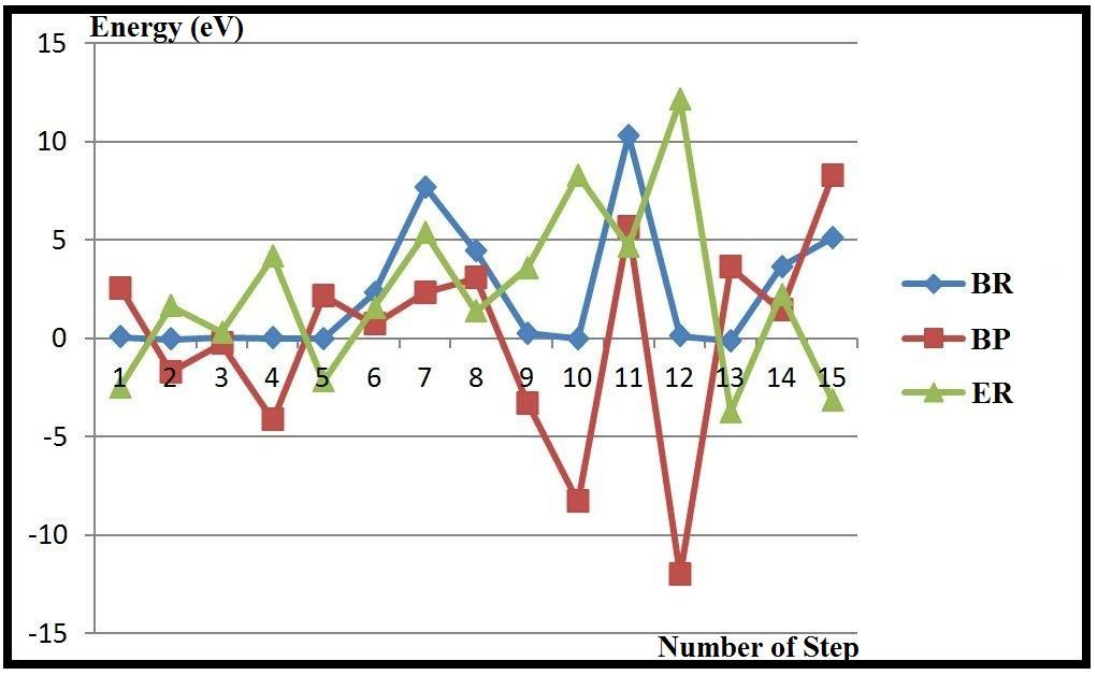

Figure 8. 5. BR, BP and ER values alterations for 3rd *SiC* bi-layer.

The BR values gradually increase by the end of process. As a result, the energy of reaction values are kept at the high level and become lower by the end of process. Along with the essential distinctions some recurrent features are the characteristics of different levels. The successive creation of SiF_x groups and structural transformation are developed via the gradual old bonds breaking and material removal. The beginning of *SiF* groups is easily set up by using the dangling bonds rising upward from the top-most *Si*-atoms. The SiF_2 groups require high energy for the original ring structure breaking within *SiC* bi-layers and partly *C*-atoms oxidation. The final SiF_3 groups are created during culmination stage under abrupt increase of both barrier values. The sudden burst of activation energy foregoes to the final stage, *i.e.* the last *Si – C* bonds breaking. As a material selective removal, *C*-atoms are completely released.

Chapter 9 Stable epitaxial graphene via 4H-*SiC* chemical conversion

9. 1 Introduction

A final discussion about the hidden meaning of driving forces and physical conditions for graphene epitaxial fabrication is performed on the basis of the transition state theory (TST). The concept of transition state is very important in many theories for the rate of chemical reactions. It starts with the TST that explains the rates of elementary transformation. It is also referred to as the activated complex theory, which introduced basic concepts in chemical kinetics. This theory was also developed as "activated complex theory", "absolute rate theory" and "theory of absolute reaction rates". The TST assumes a special type of equilibrium between reactants and activated complexes. It is the minimum energy required for chemical reaction. Activation energy may also be defined as the height of the potential barrier separating two minima on the MEP for reactants and products. The transition state of chemical reaction is a particular nuclei configuration corresponding to the highest energy along this reaction coordinates.

The search of the rate-determining transition state is a very labour intensive operation carried out in different ways. The basic recipe of optimisation is to identify the reaction mode and maximise the energy along this mode while minimising energy in all other directions (Sugimoto et al., 2005, 2007, 2008). At every entire path between reactant and product, one should overcome the highest activation complex. The activation complex is defined as the assembly of atoms corresponding to an arbitrary small region of intermediate structures while the old bonds are broken and new bonds are created. The activation complex is the subject studied via the reaction kinetics. Chemical kinetics studying the rates of chemical processes yields the information about the reaction mechanism and transition states as the rate determining step. The main factors that influence the reaction rate include:

- the physical state of the reactants;
- the concentrations of the reactants;
- the temperature at which the reaction takes place;
- whether any catalysts are present in the reaction.

The physical state of a reactant (solid, liquid or gas) is a very important factor for the rate. Concentration is very important because the molecules must collide to react. By increasing the amount of one or more reactants, these collisions happen more often, increasing the reaction rate. Temperature usually has a major effect on the rate. Molecules at a higher temperature have more thermal energy. A catalyst that remains chemically unchanged accelerates the rate of a chemical reaction by providing a different reaction mechanism, which occurs with the lower activation energy.

Before the development of TST, the Arrhenius law was introduced as follows:

$$k = Ae^{-E_a/(k_B T)} \quad (1)$$

where K – rate constant, k_B – Boltzmann constant, T – Kelvin temperature, E_a – activation energy and A – pre-exponential factor.

The Arrhenius equation gives the energy values for reaction barriers while determining the dependence of the rate constant K on the absolute temperature T and activation energy E_a. The plot of $ln\ K$ against $1/T$ is found to be expressed as a straight line for many reactions. The main Arrhenius parameters – the pre-exponential factor A and activation energy E_a define the intercept and the slope of this line. Thus, the TST is used primarily to understand qualitatively how chemical reactions take place and explains the rates of elementary chemical transformations.

9. 2 Transition state as a rate determining factor

The Arrhenius law is used for kinetic analysis of many elementary reactions under different rates. The calculated model of SiC conversion and release of oxidised CDC after SiF_4 removal is carried out as follows:

$$SiC + 4HF \rightarrow SiF_4 \uparrow + 2H_2 \uparrow + C$$

This process is considered as four stages, namely SiF, SiF_2, SiF_3 and SiF_4 formations. SiF_4 is evaporated as a volatile product. Its boiling point is $-86℃$.

The surface of $(\sqrt{3} \times \sqrt{3})R30°$ reconstruction comprises three SiC molecules for each unit cell. It means that every stage can be performed in

terms of identical reactions. Thus, for the first stage of each unit cell there are three similar reactions:

$$SiC^{-4} + H^{+1}F \rightarrow SiF + H^{0} + C^{-3}$$

Despite this fact, the DFT first principles calculations give for each *SiC* molecule (i.e. for each *SiF* cluster or for each reaction) the special values of activation energy E_a. According to the Arrhenius law, the constants $K(T)$ defined for ground state and the rates of identical reactions proved to be quite different. However, in reality these reactions are realised simultaneously and their rates should be equal. This argument is the starting point for calculated data. The final goal is to determine the conditions when the reaction rates would be equal.

With this objective in mind, let us consider two reactions that are different for the pre-exponential factor *A* and for the activation energy E_a. The Arrhenius equation for the first and for the second reactions gives: $K_1(T) = A(1) \cdot \exp(-\frac{E_a(1)}{k_b T})$ and $K_2(T) = A(2) \cdot \exp(-\frac{E_a(2)}{k_b T})$. The next expression is correct for the general case:

$$\frac{K_1(T)}{K_2(T)} = A(1) \cdot \exp(-\frac{E_a(1)}{k_b T}) / A(2) \cdot \exp(-\frac{E_a(2)}{k_b T}) \qquad (2)$$

For both reactions of identical nature we have: $A(1) = A(2)$ and

$$\frac{K_1(T)}{K_2(T)} = \exp(-\frac{E_a(1)}{k_b T}) / \exp(-\frac{E_a(2)}{k_b T}) \qquad (3)$$

therefore:

$$ln\frac{K_1(T)}{K_2(T)} = \frac{E_a(2) - E_a(1)}{k_b T} \qquad (4)$$

It means that: $ln\frac{K_1(T)}{K_2(T)} \rightarrow 0$, if $T \rightarrow \infty$. In other words, $K_1(T)$ trends to be equal $K_2(T)$ under T increasing.

9. 2. 1 Calculations

As for the particular model of *Si – F* interaction, the identical reactions of successive *SiC* decomposition are proposed for the calculation in pairs for each SiF_x group of each *SiC* bi-layer unit cell. By analogy with the above-mentioned example, each SiF_x group of each *SiC* bi-layer unit cell is considered in pairs. That is to say, we have two

same reactions for different SiF_x clusters (three SiF_x clusters for each SiF_x group) of each *SiC* bi-layer unit cell carried out under equal rates. Thus, at least three pairs should be considered. Two significant trials shown below explain the way of calculating the rate constant ratio in dependence on temperature. The first case considers the *Si – F* interaction that avoids any interim products. For each three pairs the consequence (3) from Arrhenius law (1) gives the expression:

$$ln\frac{K_1(T)}{K_2(T)} = \frac{E_a(2) - E_a(1)}{k_b T}$$

Thus, the dependence of $ln\frac{K_1(T)}{K_2(T)}$ on T calculated for the *SiF* group of the first *SiC* bi-layer unit cell results as follows:

Pair 1: $E_a(1) = -0.03401;\ E_a(2) = 0.62739$

$0.62739 + 0.03401 = 0.6614;\quad 0.6614/8.6173324\times10^5 = 7675.23$

$$ln\frac{K_1(T)}{K_2(T)} = \frac{7675.23}{T}$$

Pair 2: $E_a(1) = 0.62739;\ E_a(2) = 1.21069$

$1.21069 - 0.62739 = 0.5833;\quad 0.5833/8.6173324\times10^5 = 6768.916$

$$ln\frac{K_1(T)}{K_2(T)} = 6768.916/T$$

Pair 3: $E_a(1) = -0.03401;\ E_a(2) = 1.21069$

$1.21069 + 0.03401 = 1.2447;\quad 1.2447/8.6173324\times10^5 = 14444.15$

$$ln\frac{K_1(T)}{K_2(T)} = 14444.15/T$$

The second case considers the *Si – F* interactions when the numerous pair calculations for interim products should be taken into consideration. While running around many pair combinations, only two pairs are employed. Just the maximal and minimal differences of activation energy values are taken into consideration. Thus, the dependence of $ln\frac{K_1(T)}{K_2(T)}$ on T calculated for the SiF_4 group of the third *SiC* bi-layer unit cell results as follows:

Pair 1: $E_a(1) = -0.12887$ eV; $E_a(2) = 0.10588$ eV

$0.10588 + 0.12887 = 0.23475;\ 0.23475/8.6173324\times10^5 = 2724.161$

$$ln\frac{K_1(T)}{K_2(T)} = 2724.161/T$$

Pair 2: $E_a(1) = -0.12887$ eV; $E_a(2) = 5.11026$ eV

5.11026 + 0.12887 = 5.23913; 5.23913/8.6173324×10^5 = 60797.59

$$ln\frac{K_1(T)}{K_2(T)} = 60797.59/\ T$$

The pairs for dependence $ln\frac{K_1(T)}{K_2(T)}$ on T are performed (Table 6, Appendix 2).

Figure 9. 1 performs the above-calculated graphs.

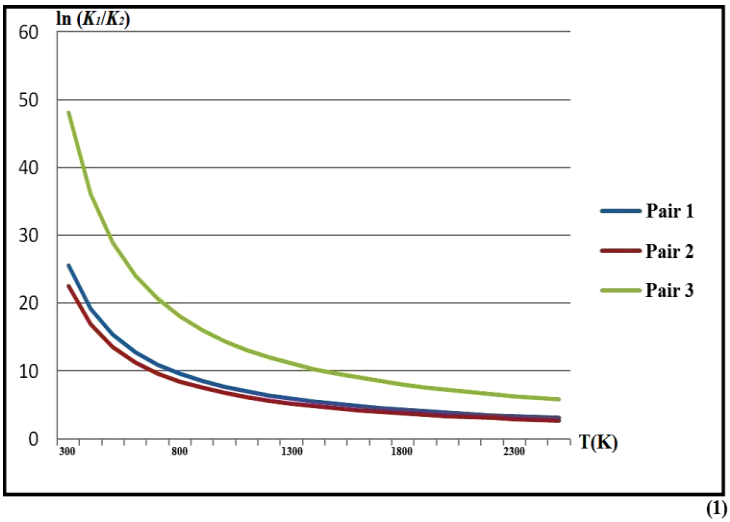

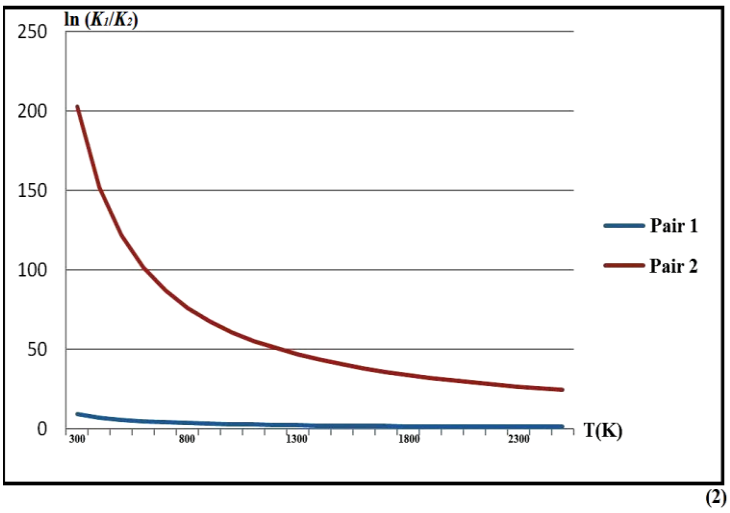

Figure 9. 1. Logarithm of rate constants ratio versus temperature:
(1) – 1st, 2nd and 3rd pairs for *SiF* group of first *SiC* bi-layer;
(2) – 1st and 2nd pairs for SiF_4 group of third *SiC* bi-layer.

The higher the temperature, the closer these graphs become. The limits for $ln\frac{K_1(T)}{K_2(T)}$ are converged as the temperature enlargement. Eventually, all these graphs converge in zero. It means that $\frac{K_1(T)}{K_2(T)}$ = 1 for each pair of reactions and the reaction rates trend to be equal. Thus, the optimal reaction conditions are reached.

Similar convergences were also revealed for all the SiF_x groups of each *SiC* bi-layer unit cell (Fig. *S* 42, 43, 44). For each case the curve declivity is gently sloping from $1800°K$, whereas a curvature does not exceed 4 – 5% for every 100°. It means that the reaction rates have a tendency to be equal for the T-interval of 1500 – $2000°K$. The best convergence is found for the *SiF* group of the 1st and 3rd bi-layers and for the SiF_4 group of the 2nd bi-layer. The worst convergence is found for the SiF_3 group of the 1st bi-layer.

The Arrhenius equation and subsequent calculations enable the kinetic interpretation for available data of transition states and activation energy values to estimate the temperature conditions for the real CDC production. The process of *Si – F* interaction to release the oxidised carbon in designed model under hydrofluoric acid treatment in the ambient conditions requires heating at least up to 1500°C. This result is in good agreement with experimental data of graphene epitaxial growth by simple annealing in the UHV or in the inert gas environment (Hass et al., 2006, 2008; Sprinkle et al., 2010; Heer et al., 2011; Presser et al., 2011). The physical conditions and dependence of graphene quality on temperature may be essentially changed by the catalytic effects of metals mixed with carbide substrate. The effect of metal catalysts is not significant at temperatures below 700°C, but at higher temperatures the catalysts strongly increase the graphitisation degree (Yushin et al., 2006).

9. 3 Promotion for transformation into highly ordered graphene structure

Surface modification running under material removal by *HF* etching results in *C*-atoms (amorphous carbon) that are to be turned into graphene lattice. This transformation implies the special quantum mechanical process known as "promotion" interpreted as follows. The electronic formula of *C*-atom is performed as $2s^2 2p_x^1 2p_y^1$. It suggests that this atom is capable of forming only two bonds rather than four. This deficiency is overcome by "promotion", which means the excitation

of an electron to an orbital of higher energy. In carbon the promotion of $2s$ electron to $2p$ electron leads to the configuration from $2s^2 2p_x^1 2p_y^1$ to $2s^1 2p_x^1 2p_y^1 2p_z^1$, with four unpaired electrons in separate orbitals. That is, the promoted electron leaves an occupied $2s$ orbital and occupies a vacant $2p$ orbital. These four electrons form the pairs with four electrons in orbitals provided by four other *C*-atoms (Atkins, 1998).

The description of the bonding in graphene layer is still incomplete because of the presence of one σ bond of one type (formed with $2s$ orbital) and two σ bonds (formed with $2p$ orbitals) of distinctly different character. This problem is overcome by realising that the electron density distribution in the promoted atom is equivalent to the electron density in which each electron occupies a hybrid orbital formed by the interference between $2s$ and $2p$ orbitals. The origin of this hybridisation can be appreciated by thinking of the three atomic orbitals, which are waves centred on a nucleus, as being like ripples spreading from a single point on the surface of a lake. These waves interfere constructively and destructively in different regions and give rise to three new shapes. The angles between axes of the hybrid orbitals $= 120°$. Because each hybrid is built from one s orbital and two p orbitals, it is called sp^2 hybrid orbital. Thus, each *C*-atom in graphene plane contains three sp^2 hybrid orbitals. Each sp^2 hybrid orbital consists of one s one p_x and one p_y orbitals. They form three σ bonds. The fourth p_z orbital is perpendicular to form π bond (Atkins, 1998).

With a view to graphene formation resulting from *HF* etching of substrate, eight amorphous *C*-atoms released after decomposition of three *SiC* bi-layers are accepted as a reactant for promotion into graphene. The final product of promotion comprises four graphene unit cells forming the hexagonal ring of crystalline honeycomb lattice. Two *C*-atoms of the opposite sub-lattices saturate free dangling bonds arisen from the 4H-*SiC* (0001) - $(\sqrt{3} \times \sqrt{3})R30^{o}$ unit cell. Each from the rest of the six *C*-atoms possesses a free dangling bond directed upward.

Calculation of promotion events revealed a stepwise transformation (Tables 7 and 8, Appendix 2) from the initial reactant to the final product. This development passes through many interim products and transition states as the system is transformed from amorphous carbon into highly ordered graphene structure (Fig. *S* 45). Two different sequences are performed as a promotion development. In the first stage of development process the two top-most *Si*-atoms of the

4H-*SiC* (0001) - $(\sqrt{3} \times \sqrt{3})R30^{o}$ substrate unit cell are bonded via free dangling bonds with the *C*-atoms connected with the other *C*-atoms of overlay. The resulting interim products (Fig. *S* 46; 1 – 21) and transition states (Fig. *S* 47; 1 – 20) are advanced to search the proper arrangements of constituting atoms. In the majority of cases, the energy of reactant values are higher than the relevant energy of product values. The BR values are usually less than BP values. Therefore, the process is mainly developed in the exothermal regime (Fig. 9. 2). As a result, by the 21st step all the *C*-atoms are bonded in the preliminary disposition prepared for the promotion.

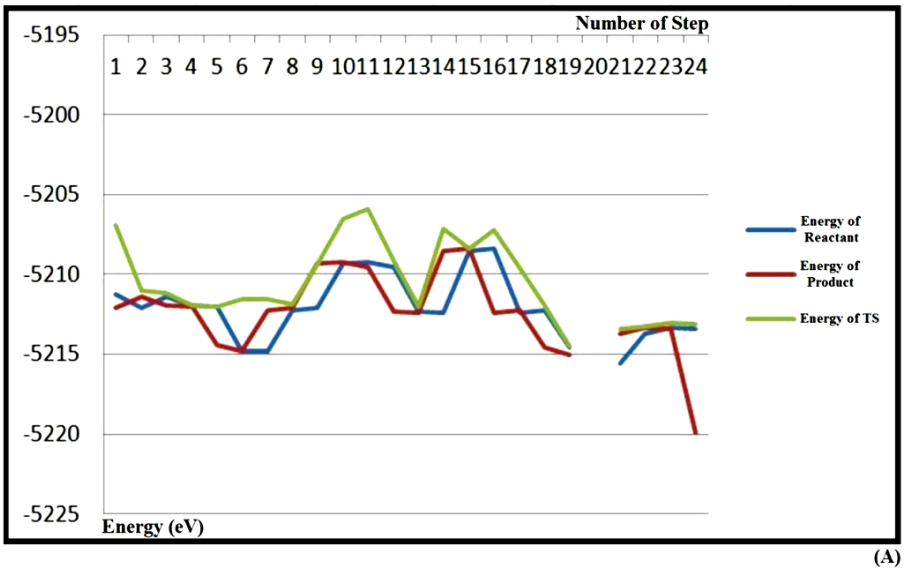

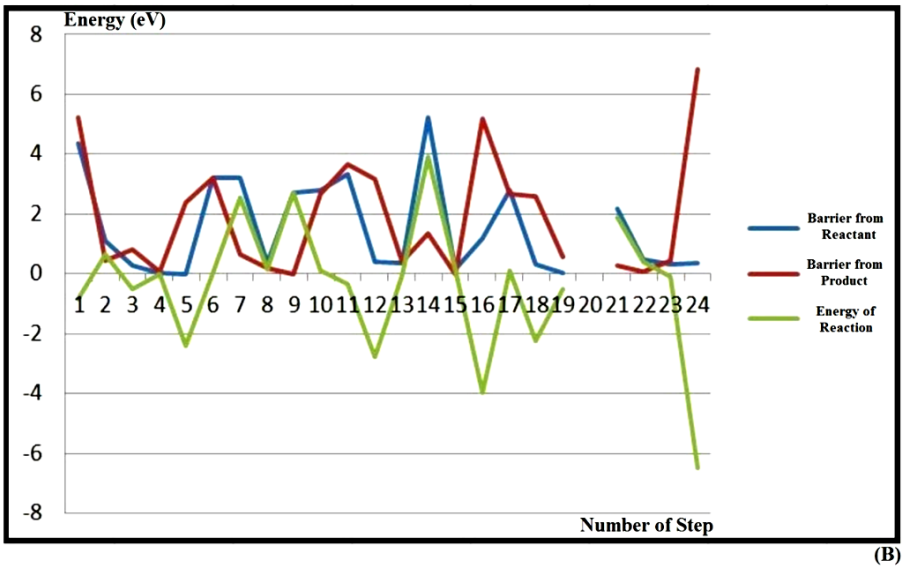

Figure 9. 2. Energy distributions and values for transformation of amorphous carbon into highly ordered graphene structure (see the next page for details).

In the second stage of the development process the proceeding sequence involves the interim products and transition states, approached turn by turn until the final product is reached (Fig. *S* 46, 47; 22 – 25). The transformation is propagated under convergent energy of transition state values appropriate for the variable energy of reactant and product values (Fig. 9. 2_A). At the beginning of this stage, the endothermic effects occur because the values of products energies for the first time exceed the values of reactants energies. This beginning step corresponds to the highest energy of reaction and BR values of the second stage (Fig. 9. 2_B). All these values apply even for the subsequent interim products. By the last transition state the energy values are dramatically changed. Whereas the BR value trends to zero, the BP value is abruptly increased. The resulting target product loses its own energy and the intended graphene structure is created.

There are couple of crucial situations along the generalised extension of promotion events. First of all, it is revealed due to the sudden break between both found sequences. After the 20^{th} transition state the changes for energetic parameter values occur around the suspended 21^{st} step. It is accompanied by the increasing energy of reaction and BR values. The most acceptable interpretation for these critical occurrences is concerned with the promotion effects that require the additional energy. The break within the graphs in the 21^{st} step is provoked by the change of electronic configuration of *C*-atoms from $2s^2 2p^2$ to $2s^1 2p^3$ because of the transformation of initial reactant into final product. After the 20^{th} transition state the 21^{st} interim product results. Its energy value is -5215.055 eV. This 21^{st} interim product should be transformed through the 21^{st} transition state into the 22^{nd} interim product. However, at this stage the change of electronic configuration for *C*-atoms of overlay and transformation of amorphous carbon into highly ordered graphene structure takes place. Because of the essential difference between these structural arrangements the computation operations have not revealed any transition state for this step. Instead, the 21^{st} interim product is transformed through the intermediate into another modification of -5215.608 eV that is energetically lower and more stable. In turn, this modification is transformed through the 22^{nd} transition state into the 22^{nd} interim product. This stage results in the change of electronic configuration and the increase of energy value for 22^{nd} interim product, because *p* electrons are energetically higher than *s* electrons. Another crucial situation is related to the final transition when the energy of product and energy of reaction values abruptly fall.

These changes most probably correspond to the carbon crystalline rearrangement into the plane 2D structure. Furthermore, for both sequences the transition state locations are found under different path coordinates, but they are abruptly increased after the suspended 21st step (Fig. *S* 48).

By analogy with the above-mentioned experiences, one should make the calculation for the transformation of amorphous carbon into highly ordered graphene structure by using the Arrhenius equation. While running around many pair combinations, just two pairs are employed. Only the maximal and minimal differences of activation energy values are taken into consideration (Fig. 9. 3). The dependences of $ln\frac{K_1(T)}{K_2(T)}$ on T calculated for this transformation result:

$$\textbf{Pair 1}: E_a(1) = 0.35688 \text{ eV};\ E_a(2) = 0.36038 \text{ eV}$$

$$0.36038 - 0.35688 = 0.0035;\ 0.0035/8.6173324\times10^5 = 40.62$$

$$ln\frac{K_1(T)}{K_2(T)} = \frac{40.62}{T}$$

$$\textbf{Pair 2}: E_a(1) = -0.02963 \text{ eV};\ E_a(2) = 5.23979 \text{ eV}$$

$$5.23979 + 0.02963 = 5.26942;\ 5.26942/8.6173324\times10^5 = 61149.09$$

$$ln\frac{K_1(T)}{K_2(T)} = \frac{61149.09}{T}$$

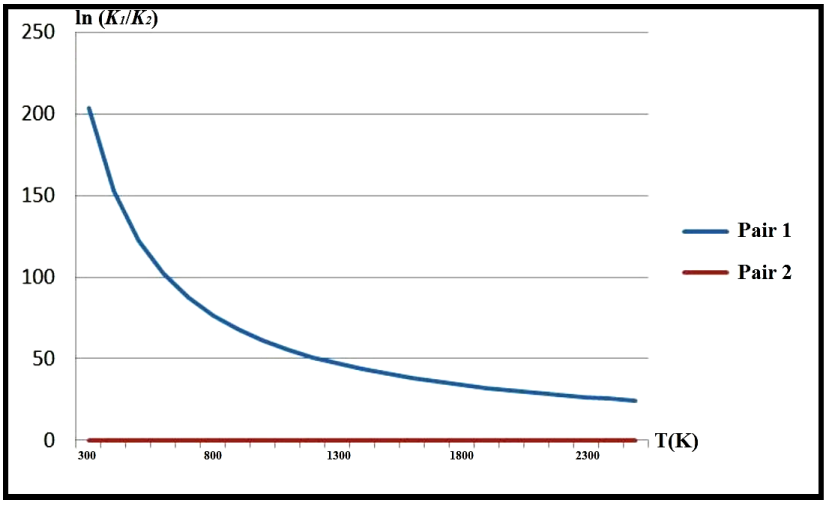

Figure 9. 3. Logarithm of rate constants ratio versus temperature for transformation of amorphous carbon into highly ordered graphene structure. The process occurs at around 2000°K.

Thus, the transformation of amorphous carbon into highly ordered graphene structure passes through the two stages. The first one is promotion and the second one is hybridisation. As explained previously, promotion is transfer of electron from *s* state into *p* state. In other words, it is transfer from the $2s^2 2p^2$ configuration of two unpaired electrons into the $2s^1 2p^3$ configuration of four unpaired electrons. In accordance with quantum mechanical theory, *p* electrons have higher energy than *s* electrons. Therefore, promotion requiring energy supply is endothermic process. In our diagram (Fig. 9. 2), one can see that the break from step 20 to step 22 is the only interval where the energy of reaction considerably changes its values from negative to positive. That is, in the product corresponding to step 20 the *C*-atoms still have $2s^2 2p^2$ configuration, whereas in the reactant corresponding to step 22 the *C*-atoms already have $2s^1 2p^3$ configuration. The effect of hybridisation takes place at the last step of the whole process, where the energy of reaction value dramatically falls. The last interim product is transformed into the crystal graphene monolayer, where all the bonds between *C*-atoms are equal and sp^2 hybridised.

9. 4 Experimental validation

A capability to produce the scale-up and uniform graphene of high quality is the main challenge for updated manufacturing. Since the limitation of exfoliation technique for scientific area, the industrial aims require the advanced development of epitaxial processes. This is the only appropriate way that promises homogeneous films of large scale at low cost. The production is reproducible by growth of one substance on the top of another so both materials have the same structural orientation. Such carbon structures are referred to as epitaxial graphene.

The manufacturing of epitaxial graphene is advanced by means of two contrast mechanisms. Few graphene layers can be grown via chemical deposition on transition metals or carbides by using pyrolysis of carbon gasses. Another mechanism is performed by controlled growth of carbide derived carbon under thermal or chemical decomposition with partly material removal. Carbon is formed by selective extraction of the metal or metalloid atoms. Since the sublimation rate of removed atoms is higher than that of carbon, excess carbon is left on the surface. In this way, the carbon layer is formed by inward growth, usually with the retention of the original structure of the precursor rearranged itself into graphene. Due to the fact that large crystals with an atomically flat surface of extremely low defects are

available, silicon carbide (*SiC*) emerges to be the best precursor for graphene of the higher quality. The carbide thermal decomposition is produced either in inert atmospheres or in the ultra-high vacuum (UHV). The atmospheric argon (*Ar*) environment requires the higher temperatures (1500°C – 2000°C) for the *Si*-atoms. In the case of UHV graphene quality is lower than that grown at higher temperature. It requires the stable vacuum conditions to avoid any roughness.

Both mechanisms depend on the initial surface termination. Epitaxial processes on the *Si*- and the *C*-terminated surfaces are very different under evolution (Presser et al., 2011). Material on the *Si*-face has no more than five layers arranged at once. The exposition of the layers is arranged in the Bernal stacking order. That is, half of the atoms lie directly over the centre of a hexagon in the lower sheet. The other stacking gives the different electronic properties. On the *C*-face, graphene is typically multi-layered from five to about 100 layers. The *C*-face performs several layers grown and retains the essential features of freestanding graphene. The most important feature is that the layers are not Bernal stacked. The successive layers prefer to be rotated with respect to each other. The material behaves like a stack of independent decoupled layers. Nevertheless, the electronic structure proves to be the same as in the case of freestanding graphene.

Epitaxial growth via chemical decomposition by halogen compounds maintains the original shape and volume of the carbide precursor referred to as a conformal transformation. The CDC formed by selective substrate etching is possible for different carbides and halogens. Halogenation, particularly chlorination, has become the key chemical methods for large-scale production. Fluorination proved to be more aggressive, either producing fluorocarbons or leading to the disintegration of *SiC*. Different methods of dry etching applied for chemical conversion is nowadays substituted by the wet etching providing the lower surface damages. For halogenated carbides, a high control over the resulting amorphous porous carbon structure is possible by changing the synthesis conditions and carbide precursor. The treatment temperature and the halogen-carbide ratio are the most crucial factors.

In the low temperature range, below 600°C, there is no CDC formation because of the preferable aryl halides. At moderate temperatures between 600 – 1000°C both halides and free carbon can be observed. Under temperature as high as 1200°C or more, the solid carbon is the only stable product. The halogen species must be present in excess to produce carbon without residual solids even at

high temperatures. With an increased halogen to carbide ratio the maximum carbon yield is produced.

There is an optimal value for halogen-carbide ratio corresponding to a large range of pure carbon as the only stable product. The maximum yield of carbon can be observed at moderate temperatures for moderate halogen to carbide ratios.

The activation energies are calculated in dependence on temperature (Chen L. et al., 2003; Presser et al., 2011). Thus, the value of E_a = 144 kJ/mol is reported for *SiC* at 900 – 1000°C. For the chlorination of *TiC*, the activation energy = 50 kJ/mol is found in the range between 400 – 800°C. The activation energy = 92 kJ mol^{-1} is found for fluorination in the range of 300 – 900°C. For *ZrC* chlorination, there is a large decrease in E_a = from 62 kJ/mol (450 – 650°C) to 10 kJ/mol (650 – 950°C). E_a for *WC* = 153 kJ/mol (600 – 750°C) and 42 kJ/mol (750 – 980°C). The decrease in activation energy is explained by the linear kinetics at higher temperatures.

With a view to proof of principle experiment, the intended epitaxial graphene growth requires the heating and mechanical vibrations supplied by the SPM operations. The AFM capabilities provide the most effective mechanisms for material decomposition and removal. The rearrangements of terminating atoms are designed after the *HF* treatment in the high electric field. By applying the negative and positive biased tip, the different mechanisms are possible under control by the applied bias, set current, humidity and moisture, number of pulses, duration time, tip/sample properties and distance. Close to surface an enlarged current density between cathode and anode launches ionisation in electrolyte. The electrochemical processes in the tip/surface gap are employed by the REDOX effects. During the short range interaction the unwanted atoms are withdrawn. The transferred pieces occupy the free vacancies. In the case of verified experiment, the negatively biased tip performs the cathode polarisation potential, whereas the sample surface takes part as the anodic potential. The old bonds are broken as the vertical drift of electrolyte components is enhanced. The anions are driven away from the tip region. The sample surface serves as anode accumulating the energetic *F*-ions. Due to the strong electro-negativity difference the dipper layers are reworked under massive fluorine attack.

The mechanism of graphene epitaxial growth might be approved as follows. The chemical decomposition is evolved in terms of two complementary stages. First of all, the CDC should be produced by means of self-organisation on the

4H-*SiC* (0001) - $(\sqrt{3} \times \sqrt{3})R30^{o}$ surface dipped into the *HF* electrolyte. In dependence on incident energy from the relevant source, the exited *F*-atoms penetrate deeply into substrate bulk. The thickness of the $Si_xC_yF_z$ interfacial layer is initially grown as the incident energy increases. While losing the old bonds the *Si*-atoms are ejected in the form of SiF_4 volatile phase. The oxidised *C*-atoms transfer their electrons to four protons (H^+). The steady balance between deposited and etched atoms should be controlled by rate determining transition states to avoid the CF_x clusters yield. The progress and credibility of carbide derived carbon are estimated by rate determining transition states for *Si – F* interaction by using the concept of potential energy surface (PES) and minimum energy path (MEP). The best indicators for reaction progress are supplied by two critical indexes – barrier from reactant (BR) and barrier from product (BP). The former, known as activation energy, is a difference between transition state and energy of reactant values. The latter is found as a difference between transition state and energy of product values. A difference between both barriers defines the energy of reaction (ER) and thermal effect.

At the second stage of self-organisation, the promotion and hybridisation are implemented under high temperature conditions. Eight amorphous *C*-atoms are accepted as reactant. Computation of promotion revealed a stepwise transformation implemented through many interim products and transition states. The final product comprises four graphene unit cells. Promotion is transfer of electron from *s* state into *p* state. In accordance with quantum theory, *p* electrons have higher energy than *s* electrons. It means that the transfer into $2s^1 2p^3$ configuration is endothermic process. The effect of hybridisation takes place in the last step of whole process.

As a summary, the original pathway for carbide derived carbon patterns approximated to highly ordered graphene structure is designed via stepwise processing on *SiC* substrate converted by *HF* etching. A subject of innovation consists in the novelty of approach to the complicated system evolving under multiplex interaction induced by substrate precondition, on the one hand, and the external environment, on the other. Two mutual driving mechanisms responsible for the intended graphene-based system are considered on the molecular geometry principles with the object of reaction progress. Simultaneously, the electronic promotion and sp^2 hybridisation are put forward to form 2D graphene like plane from the amorphous carbon.

Chapter 10 Conclusions

After recent graphene discovery, extensive investigations and expanding knowledge have showed that many unique theoretically predicted properties of this material strongly depend on the fabrication methods and combinations with other condensed matters (Berger et al., 2004, 2006; Hass et al., 2006, 2008; Rollings et al., 2006; Yushin et al., 2006; Stankovich et al., 2006, 2007; Stolyarova et al., 2007; Morozov et al., 2008; Seyller et al., 2008; Hibino et al., 2009; Magaud et al., 2009; Batisse et al., 2010; Presser et al., 2011).

Initially produced by simple mechanical exfoliation, graphene of high crystalline purity is still required and produced for laboratory aims. However, this method of synthesis is not adequate for the industrial demands. Also, it should be taken into account that any industrial application requires a proper adjustment with the other supporting materials, because it results in change of graphene's properties. This unusual ability for alteration stipulated the advanced explorations for special industrial progress and required the design of a novel methodology for epitaxial graphene fabrication. The controllable epitaxial graphene growth on the solid substrates proved to be the most effective method for manufacturing production of proper quality suitable for high-performance nanotechnology (Heer et al., 2011; Kuroda et al., 2011; Novoselov et al., 2012).

Therefore, the present research was elaborated via interaction design of the alternating graphene compositions evolving under substrate induced interaction. The purposeful models of epitaxial growth have been simulated for the advanced fabrication under directed control over interaction tendencies as a key factor of mutability. With a view to this goal, two successive planes of carbide derived carbon (CDC) were simulated on the alternating 4H-*SiC* frameworks different for unit cell reconstructions and terminations. Calculation by using DFT first principles enables us to reveal the different electronic structures changeable as epitaxial growth. Due to the strong covalent bonds, the first deposited monolayer needs to adapt itself to framework. Diversity of electronic structures found for substrate modifications is transferred forward into an interfacial monolayer. The interface diversity was propagated towards the target bi-layer under dominant graphene identification. The characteristics of freestanding graphene have been recognised for the (0001) - $\left(\sqrt{3}\times\sqrt{3}\right)R30°$ unit cell. The original method for the fabrication of novel

graphene-composite assemblies in electrochemical (*HF*) system by decomposition of 4H-*SiC* substrate via *Si – F* interaction, selective material removal, carbon oxidation, CDC formation and transformation of amorphous carbon into highly ordered graphene structure was elaborated to avoid the possible defects and contaminations.

10. 1 General results

This research expounds the results of elaboration in accordance with a conventional scheme taken for the usual scientific work. The results of the investigation were expanded into nine chapters consisting of several thematic sections, conclusions and a list of references.

The introduction includes subject, destination and topical justification of the research focused on general factors of graphene mutability in the external environment. The aim and objectives of the investigation were formulated on the basis of the available graphene database, advancements and applications. The exceptional adaptation to any support and intercalation was interpreted as a consequence of exclusive electronic structure. Therefore, this ability for alteration emerges as the principal regulator of epitaxial processes mostly preferable for graphene engineering. The methodological approach to study is based on the simulation and computation of graphene electronic diversity evolving under different circumstances of epitaxial growth.

Chapters 2 and 3 perform the literature review about general problems of nano-material compilations and, in particular, nano-scaled graphene manufacture. The topical prerequisites and the roadmap for modern molecular compilation, general branches, approaches, methods and tools, nano-scaled materials, building blocks and precise manufacture, including diamond mechanical synthesis and graphene fabrication, arose before advanced nano-science problems. The multidisciplinary aspects of atomically precise manufacture are disclosed via the updated approaches and methods for molecular compilation, the strategy of self-assembly and direct positional assembly, modern nano-materials, including carbon group, their applications and productions. The advanced operations for surface conversion, procedures and tools applied for diamond and graphene fabrication are considered.

Chapter 4 examines available routes of surface chemistry for graphene epitaxial growth. Two contrasting approaches to reproductive carbon are considered through the material deposition by CVD on the solid surface under catalytic effects

and material removal via carbide chemical decomposition and CDC formation. The interfacial layer evolves via selective substrate removal resulting from wet *HF* etching. The dissociated *HF* solution penetrates deeply into the truncated bulk. Due to the electrochemical mechanism, the *F*-atoms are concentrated near the substrate surface while reworking bi-layer by bi-layer according to the scheme:

$$Si^{+4}C^{-4} + 4H^{+1}F^{-1} \rightarrow Si^{+4}F_4^{-1}\uparrow + C^0 + 2H_2{}^0\uparrow$$

The wet etching operation could result in the lower interface contamination. The superimposed planes might be formed by analogy with pyrolysis processes by using chlorocarbon decomposition as follows:

$$6C + C_6Cl_6 \rightarrow 6[C - C] + 3Cl_2\uparrow$$

General approaches to the calculation of many-body structures and preferable principles for solution of electron problems are considered in Chapter 5.

In Chapter 6, graphene epitaxial growth is simulated under strong interaction with a supporting framework to reveal CDC mutability succeeding to the substrate heterogeneity of different reconstructions and terminations. The compatibility with the external environment defines a huge advantage for graphene epitaxial growth on the solid surfaces. From the supporting materials of ionic, covalent and metallic bonds, the silicon carbide of hexagonal symmetry (4H-*SiC*) is especially chosen for systematic study due to its high chemical affinity to graphene. Therefore, two $(\sqrt{3} \times \sqrt{3})R30°$ and (3×3) unit cells of both *Si*-face and *C*-face terminations are taken as an initial point to reveal and trace the mutability trends under substrate induced interaction. These surfaces are used as a basis for the further simulation. The first deposited *C*-layer is emplaced on the (0001) - $(\sqrt{3} \times \sqrt{3})R30°$ surface at the distances acceptable for strong covalent bonds. With a view to elastic commensuration of adjacent crystalline lattices, a little flattened *C*-monolayer is located above a slightly warped substrate surface. The geometric model is arranged in such a way that one of three *C*-atoms of opposite graphene triangles is connected with one of two central *Si*-atoms of substrate. Therefore, four graphene unit cells correspond to one substrate unit cell. The remaining four bonds of ring and two more are unsaturated. They are directed upward to the subsequent layer. On the (0001) - (3 × 3) surface the interface is performed with twelve unit cells, while

compensating six dangling bonds of terminating *Si*-atoms. Three dangling bonds are left unsaturated.

The intended models are elaborated as composite assemblies evolving under substrate induced interaction. The *SiC* surfaces of variable unit cell reconstructions and terminations with grown CDC planes arranged in the standard Bernal stacking order are acceptable for the covalent and Van der Waals forces. The few-layered graphene assemblies are designed under weak substrate induced interaction accessible through the Van der Waals forces. The novel patterns of dominant graphene identity are simulated. The subsequent planes are exposed so that the conjugate atoms of the opposite triangles are hovered. One of these atoms is systematically close to the "lonely" *Si*-atom of the substrate. At least three dangling bonds arising from every ring are uncompensated.

The results of electronic structures as regards evolving assemblies are shown in Chapter 7. The electronic diversity found for the substrate structures is transferred forward into the interfacial monolayer devoid of graphene identification. Only a few negligible distinctions for both unit cells of the same reconstructions are recognised for passivated substrates. However, after depassivation these polar surfaces proved to be strongly different. For the (0001) termination of both reconstructions the transitional sub-band has been found. The half-filled level and the Fermi level are located in the gap divided into small parts. On the $(000\bar{1})$ termination the similar sub-band is stretched towards the valence band separated from the conduction band with the wide gap. The basal *C*-monolayer grown in direct contact with the substrate surface is adapted to the unit underneath. Therefore, the substrate divergence is succeeded and enforced by the basal *C*-monolayer at the close distances from the supporting levels. The new system "substrate – monolayer" gains the mixed qualities. For the (0001) termination of both reconstructions the transitional sub-bands, including the Fermi level inherited from substrate, are displaced into the conduction band. For the $(000\bar{1})$ termination the transitional sub-bands are modified and stretched towards the valence band. As a result, the electronic structures become likewise the *n*-type and the *p*-type semiconductors for the *Si*-face and *C*-face terminations respectively. Thus, the initial mutability of the supporting framework is transferred into the buffer diversity. Graphene self-identity is sub-pressed by substrate induced interaction. The gap energy level dispersion is enforced and diverged. All the structures are devoid of pure graphene features.

As a consequence of total remoteness from the framework, the graphene BL electronic structures result from the weak substrate induced interaction in the enlarged thickness. The former contrast of the polar surfaces fades but is enforced between both reconstructions. The structures on the $(\sqrt{3} \times \sqrt{3})R30°$ reconstruction are grown with dominant graphene signs. Band gap is closed in Dirac's *K* points while expanding towards the **BZ** centre. The Fermi level runs along the $\Gamma - K$ line. For the (3×3) reconstruction the Γ point occurs as the main location where the conduction and valence bands are crossing. It is a good explanation why graphene is experimentally failed on the (3×3) reconstruction.

Thus, the band energy dispersion for the gap-engineering aims is regulated via the chosen substrate modification and geometrical disposition of constituting units. By using the total combination of these factors the different qualities and degree of proximity to freestanding graphene are reached for the alternating systems.

Computation details for CDC progress via *Si – F* interaction and analysis of wet etching processes is supplied in Chapter 8. The 4H-*SiC* (0001) - $(\sqrt{3} \times \sqrt{3})R30°$ surface conversion is subjected to computation of CDC epitaxial growth under fluorinations. Dynamics of *Si – F* interaction is analysed through the transition state, reaction, BR and BP energy values. The stepwise new *Si – F* bonds are simulated and the total energy values increase as the *HF* flow penetrates through the substrate bi-layers into the bulk. This process is expanded through the number of interim products and transition states. The *SiF*, SiF_2, SiF_3 and SiF_4 groups evolve under irreversible structural transformations. The initial *F*-atoms for every *SiF* group are usually bonded under exothermic effect while saturating the free dangling bonds. The last *F*-atoms are added under abrupt increase of activation and reaction energy values. The most endothermic effect is found for the SiF_2 groups, i.e. beginning for destruction of *SiC* structure. The non-rhythmic dynamics via numerous interim products and transition states leading to the high activation complex are related to the SiF_3 groups and total collapse of the old bonds with substrate. The transition states for the SiF_4 groups are realised when both barriers from reactant and product values are abruptly decreased. The maximal energy values correspond to the surface unit cell and fall with the depth.

The general discussion in Chapter 9 is subjected to the hidden processes and operations resulting in graphene growth via 4H-*SiC* chemical conversion. First of all it is concerned with kinetics and physical conditions calculated on the basis of the

Arrhenius equation. The driving mechanism for promotion from amorphous carbon into highly ordered graphene structure is shown. The concepts of potential energy surface (PES) and minimum energy path (MEP) are used. The rate determining activation barriers calculated in ground state are applied for the real models to estimate the reaction rates in dependence on temperature. By using the Arrhenius equation the equal rate constants are defined at temperature as high as 1500°C and more.

For good understanding of promotion from CDC into highly ordered graphene structure, this self-organisation mechanism is investigated through the DFT first principles calculations. Surface modification running under material removal by *HF* etching results in the excess of *C*-atoms that are intended to be turned into a graphene lattice. With a view to promotion for graphene, eight amorphous *C*-atoms are accepted as the reactant. The final product comprises four graphene unit cells. Computation of promotion revealed a stepwise transformation implemented from initial reactant to final product through about 25 interim products and 25 transition states. The transformation of amorphous carbon into highly ordered graphene structure passes through two stages. The first one is promotion and the second one is hybridisation. Promotion is the transfer of an electron from *s* state into *p* state, i.e. from $2s^2 2p^2$ ($2s^2 2p_x^1 2p_y^1$) configuration into $2s^1 2p^3$ ($2s^1 2p_x^1 2p_y^1 2p_z^1$) configuration. The $2s^1 2p^3$ state has four unpaired electrons. In accordance with quantum theory, *p* electrons have higher energy than *s* electrons. Therefore, the transfer from $2s^2 2p^2$ state into $2s^1 2p^3$ state is an endothermic process. The effect of hybridisation takes place in the last step of the whole process which is strongly exothermic.

In summary, the different aspects of graphene diversity are revealed to be the basis for a novel methodology aimed at directed control over carbide derived carbon patterns. The heterogeneous assemblies of variable proximity to freestanding graphene result from adaptation to substrate induced interaction. As a result, at least three groups of factors for graphene regulation are significant during purposeful design and assembly engineering. The first group of factors (1) is concerned with combination of the alternating materials in variable composites. The second group of factors (2) is related to structural arrangement, distance and number of stacked *C*-layers. Finally, the external environment and conditions of epitaxial growth result in chemically functionalised graphene (3).

The compositional control represents the most significant influence in terms of supporting carbide materials coherent with the hexagonal structure of graphene. The structural arrangement of alternating planes proved to be another crucial factor for graphene composite quality. In particular, it was proved that under strong covalent bonds the interfacial CDC succeeds to substrate mutability, whereas graphene identity is revealed only for a many-layered system.

The novel pathway for fabrication of the graphene-composite assemblies in an electrochemical (*HF*) system is simulated in anticipation of the high graphene quality. The synchronous processes of 4H-*SiC* substrate decomposition via *Si – F* interaction, selective material removal, carbon oxidation, CDC formation via volatile H_2 and SiF_4 escape and transformation of amorphous carbon into highly ordered graphene structure are proposed to avoid the possible damage to and contamination of the buffer layer. The key-factors of advanced fluorination driving to CDC are discovered by using the transition state theory that enables the discovery of reaction dynamics and feasibility.

The reaction and activation energy values of the irreversible electrochemical process are changed in accordance with the unit cell configuration and depth of the reworked substrate. Energy values of transition states increase as the *Si – F* interaction penetrates into the bulk structure and decrease as the SiF_x groups are created in the unit cell. Activation energy values increase as the old bonds are broken. By using the Arrhenius equation a huge dispersion of activation energy values carried out for the *Si – F* interaction in ground state is recalculated for the real CDC formation. They are recurrent in temperature conditions of 1800 – 2000°K. The mechanism for experimental CDC transformation into highly ordered graphene structure is disclosed in terms of a prolonged row of transition states and interim products in anticipation of the promotion effect and sp^2 hybridisation.

10. 2 Future research directions

Among the most significant results of the present research, the novel methodological approach for directed control over the intended properties during the epitaxial CDC fabrication has been elaborated based on the graphene mutability factors under interaction with the surrounding medium.

The general contributions are advanced via the interaction design of composite systems developed by using graphene's capacity for adaptation to the

external environment. The many-layered graphene composite system properties depending on design features and fabrication methods are considered as a subject for updated manufacturing aims. The methodological innovations are elaborated via the diversity of many-layered assemblies evolving under substrate induced interaction, structural compatibility of composite units and chemical conversion of the initial precursor. The structural arrangements and electronic properties of the composite systems are resulted from the coherent commensuration with a particular substrate, interaction between the adjacent layers and the fabrication method in dependence on external environment. The tendencies of controllable graphene mutability emerge as the crucial factor for the most reproducible epitaxial graphene films. Directed control over graphene mutability and adaptation to the surrounding medium proved to be a key requirement for graphene efficient utilisation and gap-state engineering (Yishin et al., 2006; Zhou et al., 2007; Seyller et al., 2008; Batisse et al., 2010; Kuroda et al., 2011; Presser et al., 2011; Novoselov et al., 2012). Some severe topical questions may also be explored by using interaction with another precursor, a different design of the interfacial layer, structural arrangement in terms of variable stacking order, number and distance between *C*-planes.

There are many aspects concerning directed graphene fabrication by using the recognised mutability tendencies. The variable substrate modifications are of paramount importance for designed systems. With a view to the verification of substrate induced interaction, different composite systems were simulated. The substrate alternating reconstructions, polarity of terminations, commensuration and number of layers, their stacking order and distances between constituting units have been taken into consideration as the main regulators. The significant diversity of 4H-*SiC* precursor is revealed for structural modifications after dehydrogenation. The first buffering *C*-plane reinforces the difference between composite systems of different terminations and reconstructions. The distinctive feature resulted from the substrate impact is kept as the transitional band of different locations within the band gap around the Fermi level. The *n*-type interface structure is the exclusive characteristic of basal layer formed on the *Si*-face unit cell, whereas the *p*-type is found for the *C*-face unit cell. The identity of freestanding graphene is revealed only for the second *C*-plane grown on the *Si*-face substrate via *n*-type interface.

Taking into account the interrelation between *n*-type interface and meeting in Dirac's points of the **BZ** for the second *C*-layer, one can see that *n*-type interface

predetermines the freestanding graphene growth. In other words, a proximity to freestanding graphene in a composite building block depends on the *n*-type interface structure. This observation is of great importance for the design of directed graphene properties in combination with other solid materials. This is why various doping supplements to the supporting framework and intermediate layers should be explored as the perspective regulators of epitaxial fabrication. Only *n*-type interface is conducive to freestanding graphene signs.

Two driving mechanisms have been employed as the most responsible for graphene epitaxial growth via the 4H-*SiC* (0001) - $(\sqrt{3} \times \sqrt{3})R30°$ substrate surface conversion. Initially the transformations result in precursor decomposition, CDC formation and the escape of volatile phases. To avoid the unwanted roughness and possible contamination in interface the electrochemical system has been simulated to ensure the slow and regular etching process in *HF* electrolyte. The gradual destruction of the old bonds, selective material removal and oxidation of the residual *C*-atoms are confirmed via finding of the successive transition states and relevant energetic barriers. Another difficult problem consists in search of well-grounded causation between scattering transition state values and structural destruction of *SiC* precursor. The presence of regular transition states means the reaction feasibility and progress. The decomposition processes have been traced as the successive *Si – F* interaction penetrates deeper into the bulk, whereas the carbon atoms are accumulated on the surface. Simultaneously, the oxidised carbon is involved in the self-organisation process, resulting in a highly ordered graphene structure. By analogy with the CDC fabrication the complementary promotion mechanism is deciphered via a long succession of transition states and interim products interrupted before the change of electron configuration and sp^2 hybridisation.

The dispersion of rate-determining activation energy values enables us to estimate the real temperatures of conversion and promotion by using the Arrhenius equation. The results corresponding to an interval of T = 1500 – 2000^{o}C for both synchronous processes are in good agreement with the experiments (Presser et al., 2011). Taking into account these values, it would be extremely justified to elaborate the catalytic system to reduce the energy consumption and decrease temperature conditions. The catalytic additives, by using *Au - Pd - Pt* nanoparticles, would facilitate the process of substrate destruction, local oxidation, CDC formation and

transformation into highly ordered graphene structure (Haruta, 2001; Hoffmann et al., 2001; Meusel et al., 2001; Giorgi et al., 2002).

The major severe tasks arising from the investigation that was undertaken concern the experimental support to the elaborated principles of the novel methodology. Thus, both synchronous driving mechanisms of epitaxial graphene growth require practical verification. The stable EG should be implemented via surface conversion in an electrochemical system by using the SPM nano-lithography techniques (Avouris et al., 1997, 1998; Hla et al., 2000; Oyabu et al., 2003, 2006; Tseng et al., 2005). The $Si - C$ bonds of substrate terminating levels are broken with the tip-induced electrochemical effects (Michler et al., 2004). Under relevant conditions the electrochemical flows are produced in the tip-surface space. As the vertical drift enhances, the *F*-atoms are driven away from the tip region, towards the sample surface. Because of the strong electro-negativity difference between *F*- and *Si*-atoms the new volatile SiF_4 groups escape under a massive fluorine attack.

REFERENCES

Abe, T. **(**2000), The electrochemical fluorination as a locomotive for the development of fluorine chemistry. J. Fluor. Chem. 105, 181.

Adachi, S., Capper, P., Kasap, S. and Willoughby, A. (2009), Properties of semiconductor alloys. Wiley, 422.

Akamine, S., Barrett, R. C. and Quate, C. F. (1990), Improved Atomic Force Microscope images using microcantilevers with sharp tips. Appl. Phys. Lett. 57, 316.

Albrecht, T. R., Akamine, S., Carver, T. E. and Quate, C. F. (1990), Microfabrication of cantilever styli for the Atomic Force Microscope. J. Vac. Sci. Technol. A 8, 3386.

Allis, D. G. and Drexler, K. E. (2005), Design and analysis of a molecular tool for carbon transfer in mechanosynthesis. J. Comput. Theor. Nanosci. 2, 45.

Andres, P. L., Ramirez, R. and Verges, J. A. (2008), Strong covalent bonding between two graphene layers. Phys. Rev. B 77, 045403.

Aono, M., Kobayashi, A., Grey, F., Uchida, H. and Huang, D. H. (1993), Tip-sample interactions in the Scanning Tunneling Microscope for atomic-scale structure fabrication. J. Appl. Phys. 32, 1470.

Atkins, P. W. (1998), Physical Chemistry. Oxford University Press.

Avouris, Ph. (1995), Manipulation of matter at the atomic and molecular levels. Acc. Chem. Res. 28, 95.

Avouris, Ph., Hertel, T. and Martel, R. (1997), Atomic Force Microscope tip-induced local oxidation of silicon: Kinetics, mechanism, and nanofabrication. Appl. Phys. Lett. 71, 2, 285.

Avouris, Ph., Martel, R., Hertel, T. and Sandstrom, R. (1998), AFM tip induced and current local oxidation of silicon and metals. App. Phys. A 66, S659.

Badia, A., Cuccia, L., Demers, L., Morin, F. and Lennox, R. B. (1997), Structure and dynamics in alkanethiolate monolayers self-assembled on gold nanoparticles. J. Am. Chem. Soc. 119, 2682.

Bae, S. et al. (2010), Roll-to-roll production of 30-inch graphene films for transparent electrodes. Nature Nanotech. 5, 574.

Bartels, L., Meyer, G. and Rieder, K. H. (1997), Basic steps of lateral manipulation of single atoms and diatomic clusters. Phys. Rev. Lett. 79, 4, 697.

Barth, C. and Reichling, M. (2001), Imaging the atomic arrangements on the high-temperature reconstructed alpha-Al_2O_3 (0001) surface. Nature 414, 6859, 54.

Batisse, N., Guerin, K., Dubois, M., Hamwi, A., Spinelle, L. and Tomasella, E. (2010), Fluorination of silicon carbide thin films using pure F_2 gas or XeF_2. Thin Solid Films 518, 6746.

Baumer, M., Frank, M., Kuhnemuth, R., Heemeier, M., Stempel, S. and Freund, H. J. (2000), Metal particles on oxide surfaces: Structure and adsorption behaviour. Stud. Surf. Sci. Catal. 130, 311.

Becke, A. D. (1986), Density functional calculations of molecular-bond energies. J. Chem. Phys. 84, 4524.

Becke, A. D. (1988), Density-functional exchange-energy approximation with correct asymptotic behavior. Phys. Rev. A 38, 3098.

Becker, R. S., Golovchenko, J. A. and Swartzentruber, B. S. (1987), Atomic scale surface modification using a Tunneling Microscope. Nature 325, 419.

Berger, C., Song, Z., Li, T., Li, X., Ogbazghi, A. Y., Feng, R., Dai, Z., Marchenkov, A. N., Conrad, E. H., First, P. N. and Heer, W. A. **(**2004), Ultrathin epitaxial graphite: 2D electron gas properties and a route toward graphene-based nanoelectronics. J. Phys. Chem. B 108, 19912.

Berger, C., Song, Z., Li, X., Wu, X., Brown, N., Naud, C., Mayou, D., Li, T., Hass, J., Marchenkov, A. N., Conrad, E. H., First, P. N. and Heer, W. A. (2006), Electronic confinement and coherence in patterned epitaxial graphene. Science 312, 1191.

Binnig, G., Quate, C. F. and Gerber, Ch. (1986), Atomic Force Microscope. Phys. Rev. Lett. 56, 930.

Blake, P. et al. (2008), Graphene-based liquid crystal device. Nano Lett. 8, 1704.
Blunt, M. O., Martin, C. P., Ahola-Tuomi, M., Pauliac-Vaujour, E., Sharp, P., Nativo, P., Brust, M. and Moriarty, P. J. (2007), Coerced mechanical coarsening of nanoparticle assemblies. Nature Nanotechnology 2, 167.
Boccuzzi, F., Chiorino, A., Tsubota, S. and Haruta, M. (1996), IR study of CO oxidation and scrambling at room temperature over gold supported on ZnO and TiO_2. J. Phys. Chem. 100, 3625.
Born, M. and Oppenheimer, J. R. (1927), On the quantum theory of molecules. Ann. Physik 84, 458.
Bovin, J. O., Huber, T., Balmes, O., Malm, J. O. and Karlsson, G. (2000), A New view on chemistry of solids in solution cryo energy-filtered Transmission Electron Microscopy. Chem. Eur. J. 6, 129.
Bradley, J. S. (1994), In: Clusters and colloids: From theory to applications. Schmid, G. ed. New York: VCH, 459.
Brenner, D. W., Sinnott, S. B., Harrison, J. A. and Shenderova, O. A. (1996), Simulated engineering of nanostructures. Nanotechnology 7, 161.
Bronikowski, M. and Manohara, H. (2008), Fabricating large-area of single-layer graphene by CVD. NASA's Jet Propulsion Lab.
Brust, M., Walker, M., Bethell, D., Schiffrin, D. J. and Whyman, R. (1994), Synthesis of thiol derivatised gold nanoparticles in a 2-phase liquid-liquid system. J. Chem. Soc., 801.
Bunch, J. S., Yaish, Y., Brink, M., Bolotin, K. and McEuen, P. L. (2005), Coulomb oscillations and Hall effect in quasi-2D graphite. Nano Lett. 5, 287.
Cambaz, Z. G., Yushin, G., Osswald, S., Mochalin, Y. and Gogotsi, Y. (2008), Noncatalytic synthesis of nanotubes, graphene and graphite on SiC. Carbon 46, 6, 841.
Car, R. and Parrinello, M. (1985), Unified approach for molecular dynamics and Density Functional Theory. Phys. Rev. Lett. 55, 22, 2471.
Chang, J. P. and Coburn, J. W. (2003), Plasma-surface interactions. J. Vac. Sci. Tech. A 21, 145.
Chang, X. Y., Perry, M., Peploski, J., Thompson, D. L. and Raff, L. M. (1993), Theoretical studies of hydrogen-abstraction reactions from diamond and diamond-like surfaces. J. Chem. Phys. 99, 6, 4748.
Chen, C. J. (1993), Introduction to Scanning Tunneling Microscope. Oxford Univ. Press.
Chen, L., Behlau, G., Gogotsi, Y. and McNallan, M. J. (2003), Carbide derived carbon (CDC) coatings for Tyranno ZMI SiC Fibers. Ceramic Eng. Sci. Proc. 24, 57.
Chithrani, B. D., Ghazani, A. A. and Chan, W. C. W. (2006), Determining the size and shape dependence of gold nanoparticle uptake into mammalian cells. Nano. Lett. 6, 662.
Clark, S. J., Segall, M. D., Pickard, C. J., Hasnip, P. J., Probert, M. I. J., Refson, K. and Payne, M. C. (2005), First principles methods using CASTEP. Z. Kristallogr. 220, 567.
Coburn, J. W. (1986), Summary Abstract: Diagnostics in plasma processing. J. Vac. Sci. Tech. A 4, 1830.
Coburn, J. W. (1994), Role of ions in reactive ion etching. J. Vac. Sci. Tech. A 12, 1417.
Coleman, J. N. et al. (2011), Two-dimensional nanosheets produced by liquid exfoliation of layered materials. Science 331, 568.
Coraux, J., N'Diaye, A. T., Busse, C. and Michely, T. (2008), Structural coherency of graphene on Ir (111). Nano Lett. 8, 2, 565.
Corey, E. J. (1967), General methods for the construction of complex molecules. Pure and App. Chemistry 14, 1, 19.
Corey, E. J. (1971), Centenary lecture. Computer-assisted analysis of complex synthetic problems. Quart. Rev. Chem. Soc. 25, 455.
Corey, E. J. (1988), Retrosynthetic thinking – essentials and examples. Chem. Soc. Rev. 17, 111.
Corey, E. J. (1990), The logic of chemical synthesis: Multistep synthesis of complex carbogenic molecules. Nobel Lecture, December 8.
Corey, E. J. and Wipke, W. T. (1969), Computer-assisted design of complex organic syntheses. Science 166, 178.

Corey, E. J. and Cheng, X. M. (1989), The logic of chemical synthesis. J. Wiley and Sons, Inc., N-Y.

Corey, E. J., Ohno, M., Vatakencherry, P. A. and Mitra, R. W. (1961), Total synthesis of d, l-longifolene. J. Am. Chem. Soc. 83, 1251.

Corey, E. J., Katzenellenbogen, J. A., Gilman, N. W., Roman, S. A. and Erickson, B. W. (1968), Stereospecific total synthesis of the dl-C_{18} cecropia juvenile hormone. J. Am. Chem. Soc. 90, 5618.

Corey, E. J., Wipke, W. T., Cramer, R. D. and Howe, W. J. (1972), Techniques for perception by a computer of synthetically significant structural features in complex molecules. J. Am. Chem. Soc. 94, 431.

Corey, E. J., Long, A. K. and Rubenstein, S. D. (1985), Computer-assisted analysis in organic synthesis. Science 228, 408.

Dash, R. K., Yushin, G. and Gogotsi, Y. **(**2005), Synthesis, structure and porosity analysis of microporous and mesoporous carbon derived from zirconium carbide. Microporous and Mesoporous Mater., 86, 50.

Deppert, K., Magnusson, M. H. L., Samuelson, L., Malm, J. O., Svensson, C. and Bovin, J. O. (1998), Size-selected nanocrystals of III–V semiconductor materials by the aerotaxy method. J. Aerosol Sci. 29, 737.

Drexler, K. E. (1981), Molecular engineering: An approach to the development of general capabilities for molecular manipulation. Proc. Natl. Acad. Sci. (USA) 78, 5275.

Drexler, K. E. (1991), Molecular tip arrays for imaging and nanofabrication. J. Vac. Sci. Technol. B 9, 1394.

Drexler, K. E. (1992), Nanosystems: Molecular machinery. John Wiley and Sons, N-Y.

Drexler, K. E. (1994), Molecular nanomachines: Physical principles and implementation strategies. Ann. Rev. Biophys. Biomol. Struct. 23, 377.

Drexler, K. E. and Foster, J. S. (1990), Synthetic tips. Nature 343, 600.

Dujardin, G., Mayne, A., Robert, O., Rose, F., Joachim, C. and Tang, H. (1998), Vertical manipulation of individual atoms by a direct STM tip-surface contact on Ge (111). Phys. Rev. Lett. 80, 3085.

Eda, G., Fanchini, G. and Chhowalla, M. (2008), Large-area ultrathin films of reduced graphene oxide as a transparent and flexible electronic material. Nature Nanotechnology 3, 270.

Edwards, N. V., Jarrendahl, K., Aspnes, D. E., Robbie, K., Powell, G. D., Cobet, C., Esser, N., Richter, W. and Madsen, L. D. (2000), Real-time assessment of selected surface preparation regimens for 4H-SiC surfaces using spectroscopic ellipsometry. Surf. Sci. 464, L703.

Eigler, D. M. and Schweizer, E. K. (1990), Positioning single atoms with a Scanning Tunnelling Microscope. Nature 344, 524.

Erlandsson, R., McClelland, G. M., Mate, C. M. and Chiang, S. (1988), Atomic Force Microscopy using optical interferometry. J. Vac. Sci. Technol. A 6, 266.

Ettmayer, P. and Lengauer, W. (1994), Carbides: Transition metal solid state chemistry. New York: Wiley, Encyclopedia of Inorganic Chemistry, 519.

Faraday, M. **(**1857), Experimental relations of gold (and other metals) to light. Philos. Trans. R. Soc. London 147, 145.

Farrell, H. H. and Levinson, M. (1985), Scanning Tunneling Microscope as a structure-modifying tool**.** Phys. Rev. B 31, 3593.

Fermi, E. (1928), Statistical method of investigating electrons in atoms. Z. Phys. 48, 73.

Feynman, R. (1959), There is plenty of room at the bottom. American Physical Society meeting, Caltech.

Flowers, M. C., Dartnell, N. J., Greef, R., Zhut, J., Blackburn, A. and Zhu, J. (1995), Reactive ion etching of silicon carbide (Si_xC_{1-x})**.** Vacuum 46, 4, 349.

Fock, V. (1930), Näherungsmethode zur Lösung des quantenmechanischen Mehrkörper problems. Z. Phys. 61, 126.

Foley, E. T., Kam, A. F., Lyding, J. W. and Avouris, P. H. (1998), Cryogenic UHV-STM study of hydrogen and deuterium desorption from Si (100). Phys. Rev. Lett. 80, 6, 1336.

Forbeaux, I., Themlin, J. M. and Debever, J. M. (1998), Heteroepitaxial graphite on 6H-SiC (0001): Interface formation through conduction-band electronic structure. Phys. Rev. B 58, 24, 16396.
Forbeaux, I., Themlin, J. M. and Debever, J. M. (1999), High-temperature graphitisation of the 6H-SiC (0001). Surf. Sci. 442, 9.
Foster, J. S. and Frommer, J. E. (1988), Imaging of liquid crystals using a Tunnelling Microscope. Nature 333, 542.
Fracassi, F. and d'Agostino, R. (1992), Chemistry of titanium dry etching in fluorinated and chlorinated gases. Pure Appl. Chem. Vol. 64, 5, 703.
Freitag, M. (2008), Graphene: Nanoelectronics goes flat out. Nature Nanotechnology 3, 8, 455.
Freitas, R. A. Jr., Allis, D. G. and Merkle, R. C. (2007), Horizontal Ge-substituted polymantane-based C_2 dimer placement tooltip motifs for diamond mechanosynthesis. J. Comput. Theor. Nanosci. 4, 3, 433.
Gacoin, T., Malier, L. and Boilot, J. P. (1997), New transparent chalcogenide materials using a sol-gel process. Chem. Mater. 9, 1502.
Gall, N. R., Rutkov, E. V. and Tontegode, A. Ya. (2004), Interaction of silver atoms with iridium and with a two-dimensional graphite film on iridium: Adsorption, desorption, and dissolution. Phys. Solid State 46, 2, 371.
Galletto, P., Brevet, P. F., Girault, H. H., Antoine, R. and Broyer, M. (1999), Enhancement of the second harmonic response by adsorbates on gold colloids: The effect of aggregation. J. Phys. Chem. B 103, 8706.
Gamo, Y., Nagashima, A., Wakabayashi, M., Terai, M. and Oshima, C. (1997), Atomic structure of monolayer graphite formed on Ni (111). Surf. Sci. 374, 61.
Garrison, B. and Goddard, W. A. (1987), Reaction mechanism for fluorine etching of silicon. Phys. Rev. B Condens Matter, 36, 18, 9805.
Gates, B. C. (1992), Catalytic Chemistry. NY Chichester: Wiley, 406.
Geim, A. K. and MacDonald, A. (2007), Graphene: Exploring carbon flatland. Am. Int. Phys., Physics Today, 35.
Geim, A. K. and Novoselov, K. S. (2007), The rise of graphene. Nature Matter 6, 183.
General Chemistry (2007), Chapter 11 (Dutton Ph.), Chemical bonding II, Prentice Hall.
Giessibl, F. J. (1995), Atomic resolution of the silicon (111) - (7×7) surface by Atomic Force Microscopy. Science 267, 5194, 68.
Gillian, M. J. (1989), Calculation of the vacancy formation energy in aluminium. J. Phys. Condens. Matter 1, 689.
Giorgi, J. B., Schroeder, T., Baumer, M. and Freund, H. J. (2002), Study of CO adsorption on crystalline-silica-supported palladium particles. Surf. Sci. Lett. 498, L71.
Gleiter, H. (1989), Nanocrystalline materials. Prog. Mater. Sci. 33, 223.
Goldman, A. and Nishioka, M. (2007), Spin transport through multilayer graphene. Appl. Phys. Lett. 90, 252505.
Gomer, R. (1986), Possible mechanisms of atom transfer in Scanning Tunnelling Microscopy. IBM J. Res. Dev. 30, 428.
Gou, F., Chen, L. Z. T., Meng, C. and Qian, Q. (2007), Molecular dynamics simulations of reactive etching of SiC by energetic fluorine. Appl. Phys. A 88, 385.
Grabar, K. C., Freeman, R. G., Hommer, M. B. and Natan, M. J. (1995), Preparation and characterisation monolayers. Anal. Chem. 67, 735.
Gross, E. K. U. and Dreizler, R. M. (1981), Gradient expansion of the Coulomb exchange energy. Zeitschrift für Physik A, Atoms and Nuclei, Volume 302, 2, 103.
Guczi, L., Horvath, D., Paszti, Z., Toth, L., Horvath, Z. E., Karacs, A. and Peto, G. (2000), Modelling gold nanoparticles: Morphology, electron structure and catalytic activity in CO oxidation. J. Phys. Chem. B 104, 3183.
Hahn, J. R. and Ho, W. (2001), Oxidation of a single carbon monoxide molecule manipulated and induced with a Scanning Tunneling Microscope. Phys. Rev. Lett. 87, 16, 166102-1.
Halperin, W. P. (1986), Quantum size effects in metal particles. Rev. Mod. Phys. 58, 533.

Hartree, D. R. (1928), The wave mechanics of an atom with a non-Coulomb central field. Proc. Cambridge Phil. Soc. 24, 89.

Haruta, M. (1997), Size- and support-dependency in the catalysis of gold. Catal. Today 36, 153.

Haruta, M. (2001), The IUVSTA Workshop on Nanoparticles, University of Birmingham.

Haruta, M., Yamada, N., Kobayashi, T. and Iijima, S. (1989), Gold catalysts prepared by coprecipitation for low-temperature oxidation of hydrogen and of carbon monoxide. J. Catal. 115, 2, 301.

Haruta, M., Tsubota, S., Kobayashi, T., Kageyama, H., Genet, M. J. and Delmon, B. (1993), Low-temperature oxidation of CO over gold supported on TiO_2, Fe_2O_3, Co_3O_4. J. Catal. 144, 175.

Hass, J., Feng, R., Li, T., Li, X., Zong, Z., Heer, W. A., First, P. N., Conrad, E. H., Jeffrey, C. A. and Berger, C. (2006), Highly ordered graphene for two dimensional electronics. Appl. Phys. Lett. 89, 143106.

Hass, J., Millán-Otoya, J. E., First, P. N. and Conrad, E. H. (2008), Interface structure of epitaxial graphene grown on 4H-SiC (0001). Phys. Rev. B 78, 205424.

Hayashi, T., Tanaka, K. and Haruta, M. (1996), Selective vapor-phase epoxidation of propylene over Au/TiO_2 catalysts in the presence of oxygen and hydrogen. Journal of Catalysis, 178, 2, 566.

Heer, W. A., Berger, C., Ruan, M., Sprinkle, M., Li, X., Hu, Y., Zhang, B., Hankinson, J. and Conrad, E. H. (2011), Large area and structured epitaxial graphene produced by confinement controlled sublimation of silicon carbide. PNAS 108, 41.

Herman, A. (1997), Towards mechanosynthesis of diamondoid structures. I. Quantum-chemical molecular dynamics simulations of sila-adamantane synthesis on a hydrogenated Si (111) surface with the STM. Nanotechnology 8, 132.

Herman, A. (1999), Towards mechanosynthesis of diamondoid structures. II. Quantum-chemical molecular dynamics simulations of mechanosynthesis on a hydrogenated Si (111) surface with the STM. Modelling Simul. Mater. Sci. Eng. 7, 43.

Hernandez, Y. et al. (2008), High-yield production of graphene by liquid-phase exfoliation of graphite. Nature Nanotechnol. 3, 563.

Hersam, M. C., Abeln, G. C. and Lyding, J. W. (1999), Approach for efficiently locating and electrically contacting nanostructures fabricated via UHV-STM lithography on Si (100). Microelectronic Engineering 47, 1, 235.

Hibino, H., Kageshima, H., Kotsugi, M., Maeda, F., Guo, F. Z. and Watanabe, Y. (2009), Dependence of electronic properties of epitaxial few-layer graphene on the number of layers investigated by photoelectron emission microscopy. Phys. Rev. B 79.

Hiebel, F., Mallet, P., Varchon, F., Magaud, L. and Veuillen, J. Y. (2008), Graphene-substrate interaction on 6H-SiC $(000\bar{1})$: A Scanning Tunneling Microscopy study. Phys. Rev. B 78, 153412.

Higgins, R. J. (1997), An economical process for manufacturing of nano-sized powders based on microemulsion-mediated synthesis. In Proc. of the Joint NSF-NIST Conf. on Nanoparticles.

Hill, T., Mozaffari-Afshar, M., Schmidt, J., Risse, T., Stempel, S. M., Heemeier, M. and Freund, H. J. (1998), Influence of CO adsorption on the magnetism of small co-particles deposited on Al_2O_3. Chem. Phys. Lett. 292, 524.

Hill, T., Mozaffari-Afshar, M., Schmidt, J., Risse, T. and Freund, H. J. (1999), Changes in the magnetism of small supported cobalt particles during the oxidation process observed by ferromagnetic resonance. Surf. Sci. 429, 246.

Hla, S. W., Bartels, L., Meyer, G. and Rieder, K. H. (2000), Inducing all steps of a chemical reaction with the Scanning Tunneling Microscope tip: Towards single molecule engineering. Phys. Rev. Let. 85, 13, 2777.

Hla, S. W. and Rieder, K. H. (2002), Engineering of single molecules with a Scanning Tunneling Microscope tip. Superlattices and Microstructures 31, 63.

Hla, S. W. and Rieder, K. H. (2003), STM control of chemical reactions: Single molecule synthesis. Ann. Rev. Phys. Chem. 54, 307.

Hoffmann, J., Meusel, I., Hartmann, J., Libuda, J. and Freund, H. J. (2001), Reaction kinetics on heterogeneous model catalysts. J. Catal. 204, 378.
Hofrichter, J., Szafranek, B. N., Otto, M., Echtermeyer, T. J., Baus, M., Majerus, A., Geringer, V., Ramsteiner, M. and Kurz, H. (2010), Synthesis of graphene on silicon dioxide by a solid carbon source. Nano Letter 10, 36.
Hohenberg, P. and Kohn, W. (1964), Inhomogeneous electron gas**.** Phys. Rev. 136, B864.
Horvath, D., Toth, L. and Guczi, L. (2000), Gold nanoparticles: Effect of treatment on structure and catalytic activity of Au/Fe_2O_3 catalyst prepared by co-precipitation. Catalysis Letters 67, 117.
Houle, F. A. (1986), A reinvestigation of the etch products of silicon and XeF_2: Doping and pressure effects**.** J. Appl. Phys. 60, 3018.
Huang, D. and Yamamoto, Y. (1997), Physical mechanism of hydrogen deposition from a Scanning Tunneling Microscopy tip. Appl. Phys. A 64, 419.
Huang, H. H., Seet, C. S., Xu, G. Q. and Hrbek, J. A. (1994), Hydrogen adsorption on sulfur and nitrogen covered Ru (001) surfaces. Surface Science 319, 3, 344.
Hutchins, O. (1918), Method for the production of silicon tetrachloride. US Patent 1, 271, 713.
Ishizuka, H., Tano, T., Torigoe, K., Esumi, K. and Meguro, K. (1992), Preparation of monodispersed colloidal gold by reduction of $AuCl^{-}_{4}$ - cationic surfactant complexes. Colloids and Surfaces 63, 3-4, 337.
Jacobson, N. S., Gogotsi, Y. G. and Yoshimura, M. (1995), Thermodynamic and experimental study of carbon formation on carbides under hydrothermal conditions. J. Mater. Chem. 5, 595.
Jiang, L., Cheung, R., Hassan, M., Harris, A., Burdess, J., Zoman, C. and Mechregany, M. (2003), Fabrication of SiC microelectromechanical systems using one-step dry etching. J. Vac. Sci. Technol. B 21, 2998.
Jiang, W., Kim, B. Y. S., Rutka, J. T. and Chan, W. C. W. (2008), Nanoparticle-mediated cellular response is size-dependent. Nature Nanotech. 3, 145.
Johansson, L. I., Owman, F. and Martensson, P. (1996), High-resolution core-level study of 6H-SiC (0001). Phys. Rev. B 53, 13793.
Jung, T. A., Schlittler, R. R., Gimzewski, J. K., Tang, H. and Joachim, C. (1996), Controlled room-temperature positioning of individual molecules: Molecular flexure and motion. Science 271, No. 5246, 181.
Kamimoto, Y., Okuda, T., Fujii, H., Yoshioka, K., Fukazawa, Y. and Ono, I. (1998), In thesis: Advanced nanostructures from vapour 98, ESF, Uppsala, Sweden.
Kantorovich, L. N. (2002), Quantum theory of energy dissipation in Non-contact Atomic Force Microscopy in Markovian approximation. Surf. Sc. 521, 117.
Kantorovich, L. N. and Trevethan, T. (2004), General theory of microscopic dynamical response in Surface Probe Microscopy: From imaging to dissipation. Phys. Rev. Let. PRL, 93, 236102.
Katano, S., Kim, Y., Hori, M., Trenary, M. and Kawai, M. (2007), Reversible control of hydrogenation of a single molecule. Science 316, 1883.
Katsnelson, M. I. (2007), Graphene: Carbon in two dimensions. Materials Today 10, 20.
Kiely, C. J., Fink, J., Brust, M., Bethell, D. and Schiffrin, D. J. (1998), Spontaneous ordering of bimodal ensembles of nanoscopic gold clusters. Nature 396, 444.
Kim, B., Kong, S. M. and Lee, B. T. (2002), Modeling SiC etching in C_2F_6/O_2 inductively coupled plasma using neural networks. J. Vac. Sci. Technol. A 20, 146.
Kim, D. H., Koo, J. Y. and Kim, J. J. (2003), Cutting of multiwalled carbon nanotubes by a negative voltage tip of an Atomic Force Microscope: A possible mechanism. Phys. Rev. B 68, 113406.
Kim, S., Ihm, J., Choi, H. J. and Son, Y. W. (2008), Origin of anomalous electronic structures of epitaxial graphene on silicon carbide. Phys. Rev. Lett. 100, 17, 176802.
King, D. A. and Woodruff, D. P. (1997), Growth and properties of ultrathin epitaxial layers. In "The Chemical Physics of Solid Surface" Vol. 8, Elsevier, Amsterdam.
Kittel, Ch. (2005), Introduction to Solid State Physics. John Wiley and Sons, Inc.

Koch, C. C. (1989), Materials synthesis by mechanical alloying. Annual Review of Materials Science 19, 121.
Koch, W. and Holthausen, M. C. (2001), A chemist's guide to Density Functional Theory. WILEY-VCH ISBN: 3-527-30422-3.
Kohanoff, J. (2006), Electronic structure calculations for solids and molecules. Cambridge University Press.
Kohn, W. and Sham, L. (1965), Self-consistent equations including exchange and correlation effects. Phys. Rev. 14, A1133.
Kung, H. H. and Ko, E. I. (1996), Preparation of oxide catalysts and catalyst supports – a review of recent advances. Chem. Eng. J. 64, 203.
Kuroda, M., Tersoff, J., Newns, D. M. and Martyna, G. J. (2011), Conductance through multilayer graphene films. Nano Lett. 11, 9, 3629.
Kyprianidou-Leodidou, T., Caseri, W. and Suter, U. W. **(**1994), Size variation of PbS particles in high-refractive-index nanocomposites. J. Phys. Chem. 98, 8992.
Landau, L. D. (1937), Zur Theorie der Phasenumwandlungen II. Phys. Z. Sowjetunion 11, 26.
Lauhon, L. J. and Ho, W. (2000), Single-molecule chemistry and vibrational spectroscopy: Pyridine and benzene on Cu (001). J. Phys. Chem. 104, 2463.
Lee, H. J. and Ho, W. (1999), Single-bond formation and characterisation with a Scanning Tunneling Microscope. Science 286, 5445, 1719.
Leslie-Pelecky, D. L. and Rieke, R. D. (1996), Magnetic properties of nanostructured materials. Chem. Mater. 8, 8, 1770.
Levine, I. N. (2002), Physical Chemistry. McGraw Hill Com. NY.
Levine, I. N. (2009), Quantum Chemistry. Pearson Education Inc. NY.
Li, D., Muller, M. B., Gilje, S., Kaner, R. B. and Wallace, G. G. (2008), Processable aqueous dispersions of graphene nanosheets. Nature Nanotechnology 3, 101.
Li, X. S. et al. (2009), Large-area synthesis of high-quality and uniform graphene films on copper foils. Science 324, 1312.
Loppacher, Ch., Bammerlin, M., Guggisberg, M., Schär, S., Bennewitz, R., Baratoff, A., Meyer, E. and Güntherodt, H. J. (2000), Dynamic Force Microscopy of copper surfaces. Atomic resolution and distance dependence of tip-sample interaction and tunneling current. Phys. Rev. B 62, 16944.
Lyding, J. W., Shen, T. C., Hubacek, J. S., Tucker, J. R. and Abeln, G. C. (1994), Nanoscale patterning and oxidation of H-passivated Si (100) - (2×1) surfaces with an ultrahigh vacuum Scanning Tunnelling Microscope. Appl. Phys. Lett. 64, 2010.
Lyding, J. W., Hess, K., Abeln, G. C., Thompson, D. S., Moore, J. S., Hersam, M. C., Foley, E. T., Lee, J., Chen, Z., Hwang, S. T., Choi, H., Avouris, P. H. and Kizilyalli, I. C. (1998), UHV-STM nanofabrication and hydrogen/deuterium desorption from silicon surfaces: Implications for CMOS technology. App. Surf. Sc. 130-132, 221.
Lyo, I. W. and Avouris, Ph. (1991), Field-induced nanometer to atomic-scale manipulation of silicon surfaces with the STM**.** Science 253, 173.
Magaud, L., Hiebel, F., Varchon, F., Mallet, P. and Veuillen, J. Y. (2009), Graphene on the C-terminated SiC $(000\bar{1})$ surface: An ab initio study. Phys. Rev. B 79, 161405.
Magnusson, M. H., Deppert, K., Malm, J. O., Bovin, J. O. and Samuelson, L. (1999), Gold nanoparticles: Production, reshaping and thermal charging. J. Nanoparticle Res. 1, 243.
Magnusson, M. H., Deppert, K. and Malm, J. O. (2000), Single-crystalline tungsten nanoparticles produced by thermal decomposition of tungsten hexacarbonyl. J. Mater. Res. 15, 1564.
Makarenko, I. V., Titkov, A. N., Waqar, Z., Dumas, Ph., Rutkov, E. V. and Gall, N. R. (2007), Structural properties of a monolayer graphite film on the Ir (111) surface. Phys. Solid State 49, 2, 371.
Mann, D. J., Peng, J., Freitas, R. A. J. and Merkle, R. C. (2004), Theoretical analysis of diamond mechanosynthesis. Part II: C_2 mediated growth of diamond C (110) surface via Si/Ge-triadamantane dimer placement tools. J. Comput. Theor. Nanosci. 1, 71.

Marchini, S., Gunther, S. and Wintterlin, J. (2007), Scanning Tunneling Microscopy of graphene on Ru (0001). J. Phys. Rev. B 76, 075429.
Martin, Y., Williams, C. C. and Wickramasinghe, H. K. (1988), Scanning Microscopy. Appl. Phys. Let. 52, 244.
Martin, C. P., Blunt, M. O. and Moriarty, P. (2004), Nanoparticle networks on silicon: Self-organised or disorganised? Nano Lett. 4, 12, 2389.
Martin, C. P., Blunt, M. O., Pauliac-Vaujour, E., Stannard, A., Moriarty, P., Vancea, I. and Thiele, U. (2007), Controlling pattern formation in nanoparticle assemblies via directed solvent dewetting. Physical Review Letters 99, 11.
Martin, R. M. (2005), Electronic structure, basic theory and practical methods. Cambridge University Press.
Matsuo, Y., Segawa, M., Mitani, J. and Sugie, Y. (1998), Electrochemical fluorination of graphite in 47% HF aqueous solution**.** J. Fluorine Chem. 87, 145.
Mattaush, A. and Pankratov, O. (2007), Ab initio study of graphene on SiC. Phys. Rev. Lett. 99, 076802.
Maxwell, J. C. (1867- 68), On the dynamical theory of gases. Phil. Trans. Roy. Soc. London.
McIntyre, B. J., Salmeron, M. and Somorjai, G. A. (1994), Nanocatalysis by the tip of a Scanning Tunneling Microscope operating inside a reactor cell. Science 265, 1415.
McDuell, G. R. (1982), A-Level Chemistry: Course Companion. Charles Letts Books Ltd.
Meric, I., Han, M. Y., Young, A. F., Ozyilmaz, B., Kim, Ph. and Shepard, K. L. (2008), Current saturation in zero-bandgap, top-gated graphene field-effect transistors. Nature Nanotechnology 3, 654.
Merkle, R. C. (1993), Molecular manufacturing: Adding positional control to chemical synthesis. http://www.zyvex.com/nanotech/CDAarticle.html
Merkle, R. C. (1997), A proposed 'metabolism' for a hydrocarbon assembler. Nanotechnology 8, 149.
Merkle, R. C. (2000), Molecular building blocks and development strategies for molecular nanotechnology. Nanotechnology 11, 89.
Merkle, R. C. and Freitas, R. A. J. (2003), Theoretical analysis of a carbon-carbon dimer placement tool for diamond mechanosynthesis. J. Nanosci. Nanotechnol. 3, 319.
Mermin, N. D. (1968), Crystalline order in two dimensions. Phys. Rev. 176, 250.
Meusel, I., Hoffmann, J., Hartmann, J., Heemeier, M., Baumer, M., Libuda, J. and Freund, H. J. (2001), The interaction of oxygen with alumina-supported palladium particles. Catal. Lett. 71, 5.
Meyer, G. and Amer, N. M. (1988), Novel optical approach to Atomic Force Microscopy. Appl. Phys. Lett. 53, 1045.
Meyer, G., Neu, B. and Rieder, K. H. (1995), Controlled lateral manipulation of single molecules with the STM. Appl. Phys. A 60, 343.
Meyer, G. and Rieder, K. H. (1997), Controlled manipulation of single atoms and small molecules with the Scanning Tunneling Microscope. Surf. Sci. 377-379, 1087.
Miao, F., Wijeratne, S., Zhang, Y., Coskun, U. C., Bao, W. and Lau, C. N. (2007), Phase coherent transport in graphene quantum billiards. Science 317, 1530.
Michler, J., Gassilloud, R., Gasser, P., Santinacci, L. and Schmuki, P. (2004), Defect-free AFM scratching at the Si/SiO_2 interface. Electrochem. Solid State Lett. 7, A 41.
Miller, M. S. and Drexler, K. E. (1988), Markets and computation. In: The Ecology of Computation, Elsevier Pub.
Moriarty, P., Ma, Y. R., Upward, M. D. and Beton, P. H. (1998), Translation, rotation and removal of C_{60} on Si (100) - (2×1) using anisotropic molecular manipulation. Surf. Sc. 407, 27.
Morita, S., Sugimoto, Y., Oyabu, N., Nishi, R., Custance, O., Sugawara, Y. and Abe, M. (2004), Atom-selective imaging and mechanical atom manipulation using the Non-contact Atomic Force Microscope. J. Electron Microsc. (Tokyo) 53, 2, 163.
Morozov, S. V., Novoselov, K. S., Katsnelson, M. I., Schedin, F., Elias, D. S., Jaszczak, J. A. and Geim, A. K. (2008), Giant intrinsic carrier mobilities in graphene and its bilayer**.** Phys. Rev. Lett. 100, 016602.

Mozaffari-Afshar, M., Risse, T., Freund, H. J., Barth, C. and Reichling, M. (2001), In thesis: The 31st IUVSTA Workshop on Nanoparticles, University of Birmingham.
Muehlhoff, L., Bozack, M. J., Choyke, W. J. and Yates, J. T. Jr. (1986), Comparative oxidation studies of SiC (000$\bar{1}$) and SiC (0001) surfaces. J. Appl. Phys. 60, 7, 2558.
Muller, W. T., Klein, D. L., Lee, T., Clarke, J., McEuen, P. L. and Schultz, P. G. (1995), A strategy for the chemical synthesis of nanostructures. Science 268, 272.
Murray, C. B., Norris, D. J. and Bawendi, M. G. (1993), Synthesis and characterisation of nearly monodisperse CdE (E = sulfur, selenium, tellurium) semiconductor nanocrystallites. J. Am. Chem. Soc. 115, 8706.
Musgrave, C. B., Perry, J. K., Merkle, R. C. and Goddard, W. (1991), Theoretical studies of a hydrogen abstraction tool for nanotechnology. Nanotechnology 2, 187.
Muszynski, R., Seger, B. and Kamat, P. V. (2008), Decorating graphene sheets with gold nanoparticles. J. Phys. Chem. C, 112, 14, 5263.
Nagahara, L. A., Thundat, T. and Lindsay, S. M. (1990), Nanolithography on semiconductor surfaces under an etching solution. Appl. Phys. Lett. 57, 270.
Nair, R. R., Blake, P., Blake, J. R., Zan, R., Anissimova, S., Bangert, U., Golovanov, A. P., Morozov, S. V., Latychevskaia, T., Geim, A. K. and Novoselov, K. S. (2010), Graphene as a transparent conductive support for studying biological molecules by Transmission Electron Microscopy. Appl. Phys. Lett. 97, 153102.
Nayak, T. R. et al. (2011), Graphene for controlled and accelerated osteogenic differentiation of human mesenchymal stem cells. ACS Nano 5, 4670.
N'Diaye, A. T., Bleikamp, S., Feibelman, P. J. and Michely, T. (2006), Two-dimensional Ir cluster lattice on a graphene moiré on Ir (111). Phys. Rev. Lett. 97, 215501.
Ni, Z., Wang, Y., Yu, T. and Shen, Z. (2008), Raman Spectroscopy and imaging of graphene. Nano Res. 1, 273.
Nishi, R., Miyagawa, D., Seino, Y., Yi, I. and Morita, S. **(**2006), Non-contact Atomic Force Microscopy study of atomic manipulation on an insulator surface by nanoindentation. Nanotech. 17, S142.
Niyogi, S., Bekyarova, E., Itkis, M. E., McWilliams, J. L., Hamon, M. A. and Haddon, R. C. (2006), Solution properties of graphite and graphene. J. Am. Chem. Soc. 128, 24, 7720.
Northrup, J. E. and Neugebauer, J. (1998), Possibility of a Mott-Hubbard ground state for the SiC (0001) surface. Phys. Rev. B 57, R4230.
Novoselov, K. S., Geim, A. K., Morozov, S. V., Jiang, D., Zhang, Y., Dubonos, S. V., Grigorieva, I. V. and Firsov, A. A. (2004), Electric field effect in atomically thin carbon films. Science 306, 666.
Novoselov, K. S., Geim, A. K., Morozov, S. V., Jiang, D., Katsnelson, M. I., Grigorieva, I. V., Dubonos, S. V. and Firsov, A. A. (2005), Two-dimensional gas of massless Dirac fermions in graphene. Nature 438, 10, 197.
Novoselov, K. S., Jiang, Z., Zhang, Y., Morozov, S. V., Stormer, H. L., Zeitler, U., Maan, J. C., Boebinger, G. S., Kim, P. and Geim, A. K. (2007), Room-temperature quantum Hall effect in graphene. Science 315, 5817, 1379.
Novoselov, K. S., Falko, V. I., Colombo, L., Gellert, P. R., Schwab, M. G. and Kim, K. (2012), A roadmap for graphene. Nature 490, No. 7419, 192.
Ohta, T., Bostwick, A., Seyller, T., Horn, K. and Rotenberg, E. (2006), Controlling the electronic structure of bilayer graphene. Science 313, 951.
Olander, J. and Larsson, K. M. E. (2004), An ab initio study of 4H-SiC (0001) and (000$\bar{1}$) surface processes at experimental temperatures. Thin solid films 458, 191.
Orisaka, S., Minobe, T., Uchihashi, T., Sugawara, Y. and Morita, S. (1999), The atomic resolution imaging of metallic Ag (111) surface by Non-contact Atomic Force Microscope. Appl. Surf. Science 140, 243.
Oshima, C. and Nagashima, A. (1997), Ultra-thin epitaxial films of graphite and hexagonal boron nitride on solid surfaces. J. Phys. Condens. Matt. 9, 1.
Ostwald, W. (1907), Colloid-Zeitschrift 1, 291.
Ostwald, W. (1915), Colloids - „World of neglected dimensions". In Itroduction to Theoretical and Applied Colloidal chemistry, NY: Wiley and Sons 1917.

Oyabu, N., Custance, O., Yi, I., Sugawara, Y. and Morita, S. (2003), Mechanical vertical manipulation of selected single atoms by soft nanoindentation using near Contact Atomic Force Microscopy. Phys. Rev. Lett. 90, 176102.

Oyabu, N., Pou, P., Sugimoto, Y., Jelinek, P., Abe, M., Morita, S., Perez, R. and Custance, O. (2006), Single atomic contact adhesion and dissipation in Dynamic Force Microscopy. Phys. Rev. Lett. 96, 10, 106101.

Page, M. and Brenner, D. W. (1991), Hydrogen abstraction from a diamond surface: Ab initio quantum chemical study using constrained isobutane as a model. J. Am. Chem. Soc. 113, 3270.

Pauliac-Vaujour, E. and Moriarty, Ph. (2007), Meniscus-mediated organisation of colloidal nanoparticles. J. Phys. Chem. C, 111, 16255.

Payne, M. C., Teter, M. P., Allan, D. C., Arias, T. A. and Joannopoulos, J. D. (1992), Iterative minimisation techniques for ab initio total energy calculations: Molecular dynamics and conjugate gradients. Rev. Mod. Phys. 64, 4, 1945.

Peierls, R. E. (1935), Quelques properties typiques des corpses solides. Ann. I. H. Poincare 5, 177.

Peng, J., Freitas, R. A. J. and Merkle, R. C. (2004), Theoretical analysis of diamond mechanosynthesis. Part I. Stability of C_2 mediated growth of nanocrystalline diamond C (110) surface. J. Comput. Theor. Nanosci. 1, 62.

Peng, J., Freitas, R. A. J., Merkle, R. C., Von Ehr, J. R., Randall, J. N. and Skidmore, G. D. (2006), Theoretical analysis of diamond mechanosynthesis. Part III. Positional C_2 deposition on diamond C (110) surface using Si/Ge/Sn-based dimer placement tools. J. Comput. Theor. Nanosci. 3, 28.

Perdew,`J. P. (1985), Accurate Density Functional for the Energy: Real-space cutoff of the gradient expansion for the exchange hole. Phys. Rev. Lett. 55, 16, 1665.

Phillips, J. C. (1958), Energy band interpolation scheme based on a pseudopotential. Phys. Rev. 112, 685.

Pisana, S., Lazzeri, M., Casiraghi, C., Novoselov, K. S., Geim, A. K., Ferrari, A. C. and Mauri, F. (2007), Breakdown of the adiabatic Born-Oppenheimer approximation in graphene. Nature Mater. 6, 198.

Presser, V., Heon, M. and Gogotsi, Y. **(**2011), Carbide derived carbons from porous networks to nanotubes and graphene. Advanced Functional Materials 21, 5, 810.

Reddy, C. M., Kirchner, M. T., Gundakaram, R. C., Padmanabhan, K. A. and Desiraju, G. R. (2006), Isostructurality, polymorphism and mechanical properties of some hexahalogenated benzenes. Chemistry - A European Journal 12, 8, 2222.

Reichling, M. and Barth, C. **(**1999), Scanning force imaging of atomic size defects on the CaF_2 (111) surface**.** Phys. Rev. Lett. 83, 4, 768.

Ricca, A., Bauschlicher, C. W., Kang, J. K. and Musgrave, C. B. (1999), Hydrogen abstraction from a diamond (111) surface in an uniform electric field. Surf. Sc. 429, 199.

Ritter, K. A. and Lyding, J. W. (2008), Characterisation of nanometer-sized, mechanically exfoliated graphene on the H-passivated Si (100) surface using Scanning Tunneling Microscopy. Nanotechnology 19, 015704.

Rollings, E., Gweon, G. H., Zhou, S. Y., Mun, B. S., McChesney, J. L., Hussain, B. S., Fedorov, A. V., First, P. N., Heer, W. A. and Lanzara, A. (2006), Synthesis and characterisation of atomically thin graphite films on a silicon carbide substrate**.** J. Phys. Chem. Solids 67, 2172.

Rosch, N. and Pacchioni, G. (1994), Electronic structure of metal clusters and cluster compounds. In: Clusters and Colloids: From theory to applications. VCH, Weinheim, 5.

Rutter, G. M., Guisinger, N. P., Crain, J. N., Jarvis, E. A. A., Stiles, M. D., Li, T., First, P. N. and Stroscio J. A. (2007), Imaging the interface of epitaxial graphene with silicon carbide via Scanning Tunneling Microscopy**.** Phys. Rev. B 76, 235416.

Salling, C. T. and Lagally, M. G. (1994), Fabrication of atomic-scale structures on Si (001) surfaces. Science 265, 502.

Sanchez, V. C., Jachak, A., Hurt, R. H. and Kane, A. B. (2012), Biological interactions of graphene-family nanomaterials: An interdisciplinary review. Chem. Res. Tox. 25, 15.

Sankaran, V., Yue, J., Cahen, R. E., Schrock, R. R. and Silbey, R. J. (1993), Synthesis of zinc sulfide clusters and zinc particles within microphase-separated domains of organometallic block copolymers. Chem. Mater. 5, 1133.

Sarid, D. (1991), Scanning Force Microscopy with applications to electric, magnetic and atomic forces. Oxford University Press, New York.

Saunders, M. and Jarret, R. M. (1986), A new method for molecular mechanics. J. Comp. Chem. 7, 578.

Schmid, G. (1992), Large clusters and colloids. Metals in the embryonic state. Chem. Rev. 92, 1709.

Schmid, G. **(**1994), Clusters and colloids. From theory to application. VCH Verlagsgesellschaft, Weinheim, 546.

Schniepp, H. C. et al. **(**2006), Functionalised single graphene sheets derived from splitting graphite oxide. J. Phys. Chem. B 110**,** 8535.

Schommers, W. (2007), Basic quantum theory for nanoscience. J. Comp. Theor. Nanosci. 4, 992.

Scofield, J. D., Ganguly, B. N. and Bletzinger, P. (2000), Investigation of dilute SF_6 discharges for application to SiC reactive ion etching. J. Vac. Sci. Technol. A 18, 2175.

Segal, M. (2009), Selling graphene by the ton. Nature Nanotechnol. 4, 612.

Segall, M. D., Lindan, P. J. D., Probert, M. J., Pickard, C. J., Hasnip, P. J., Clark, S. J. and Payne, M. C. (2002), First-principles simulation: Ideas, illustrations and the CASTEP code. J. Phys. Condens. Matter 14, 2717.

Seyller, T., Bostwick, A., Emtsev, K. V., Horn, K., Ley, L., McChesney, J. L., Ohta, T., Riley, J. D., Rotenberg, E. and Speck, F. (2008), Epitaxial graphene: A new material. Phys. Stat. Sol. 245, 7, 1436.

Shin, M. W. and Song, J. G. (2002), Study on the photoelectrochemical etching process of semiconducting 6H-SiC wafer. Materials Science and Engineering B 95, 191.

Shipway, A. N., Katz, E. and Willner, I. (2000), Nanoparticle arrays on surfaces for electronic, optical and sensoric applications. J. Phys. Chem. 1, 18.

Shluger, A. L., Kantorovich, L. N., Livshits, A. I. and Gillan, M. J. (1997), Ionic and electronic processes at ionic surfaces induced by Atomic Force Microscope tips. Phys. Rev. B, 56, 15332.

Si, Y. and Samulski, E. (2008), Synthesis of water soluble graphene. Nano Lett. 8, 6, 1679.

Siegel, R. W. (1991), Cluster-assembled nanophase materials**.** Ann. Rev. Mater. Sci. 21, 559.

Siepmann, P., Martin, Ch. P., Vancea, I., Moriarty, Ph. J. and Krasnogor, N. **(**2007), A genetic algorithm approach to probing the evolution of self-organised nanostructured systems. Nano Lett 7, 7, 1985.

Slater, J. C. (1928), The self-consistent field and the structure of atoms. Physical Review 32, 339.

Sprinkle, M., Ruan, M., Hu, Y., Hankinson, J., Rubio-Roy, M., Zhang, B., Wu, X., Berger, C. and Heer, W. A. (2010), Scalable templated growth of graphene nanoribbons on SiC. Nature Nanotechnology 5, 727.

Srinivasan, E., Yang, H. and Parsons, G. N. (1996), Ab initio studies of hydrogen abstraction reactions of silicon hydrides. J. Chem. Phys. 105, 13, 5467.

Srinivasan, E. and Parsons, G. N. (1998), Hydrogen abstraction kinetics and crystallisation in low temperature plasma deposition of silicon. Appl. Phys. Lett. 72, 456.

Stankovich, S., Dikin, D. A., Dommett, G. H. A., Kohlhaas, K. A., Zimney, E. J., Stach, E. A., Piner, R. D., Nguyen, S. T. and Ruoff, R. S. (2006), Graphene-based composite materials. Nature 442, 20, 282.

Stankovich, S., Dikin, D. A., Piner, R. D., Kohlhaas, K. A., Kleinhammes, A., Jia, Y., Wu, Y., Nguyen, S. T. and Ruoff, R. S. (2007), Synthesis of graphene-based nanosheets via chemical reduction of exfoliated graphite oxide. Carbon 45, 7, 1558.

Starke, U. (2009), Non-basal plane SiC surfaces: Anisotropic structures and low-dimensional electron systems. Phys. Stat. Sol. B, 246, 7, 1569.
Starr, D. E., Pazhetnov, E. M., Stadnichenko, A. I., Boronin, A. I. and Shaikhutdinov, S. K. (2006), Carbon films grown on Pt (111) as supports for model gold catalysts. Surf. Sci. 600, 2688.
Stipe, B. C., Rezaei, M. A. and Ho, W. (1997), Site-specific displacement of Si-adatoms on Si (111) - (7×7). Phys. Rev. Lett. 79, 22, 4397.
Stipe, B. C., Rezaei, M. A. and Ho, W. (1998), Inducing and viewing the rotational motion of a single molecule. Science 279, 5358, 1907.
Stoller, M. D., Park, S. J., Zhu, Y. W., An, J. H. and Ruoff, R. S. (2008), Graphene-based ultracapacitors. Nano Lett. 8, 3498.
Stolyarova, E., Rim, K. T., Ryu, S., Maultzsch, J., Kim, Ph., Brus, L. E., Heinz, T. F., Hybertsen, M. S. and Flynn, G. W. (2007), High-resolution STM imaging of mesoscopic graphene sheets on an insulating surface. PNAS 104, 22, 9209.
Strocio, J. A. and Eigler, D. M. (1991), Atomic and molecular manipulation with the Scanning Tunneling Microscope. Science 254, 1319.
Stroscio, J. A. and Celotta, R. J. (2004), Controlling the dynamics of a single atom in lateral atom manipulation. Science 306, 242.
Sugahara, S., Hosaka, K. and Matsumura, M. (1998), Hydrogen-induced abstraction mechanism of surface methyl groups in atomic-layer-epitaxy of germanium. App. Surf. Sc. 130-132, 327.
Sugawara, Y., Ohta, M., Ueyama, H. and Morita, S. (1995), Defect motion on an InP (110) surface observed with Non-contact AFM. Science 270, 1646.
Sugimoto, Y., Abe, M., Hirayama, S., Oyabu, N., Custance, O. and Morita, S. (2005), Atom inlays performed at room temperature using Atomic Force Microscopy. Nat. Mater. 4, 2, 156.
Sugimoto, Y., Jelinek, P., Pou, P., Abe, M., Morita, S., Perez, R. and Custance, O. (2007), Mechanism for room-temperature single-atom lateral manipulations on semiconductors using Dynamic Force Microscopy. Phys. Rev. Lett. 98, 106104.
Sugimoto, Y., Pou, P., Custance, O., Jelinek, P., Abe, M., Perez, R. and Morita, S. (2008), Complex patterning by vertical interchange atom manipulation using Atomic Force Microscope. Science 322, 413.
Sugiura, J., Lu, W. J., Cadien, K. C. and Steckl, A. J. (1986), Reactive ion etching of SiC thin films using fluorinated gases. J. Vac. Sci. Technol. B 4, 349.
Sun, S. H., Murray, C. B., Weller, D., Folks, L. and Moser, A. (2000), Monodisperse FePt nanoparticles and ferromagnetic FePt nanocrystal superlattices. Science 287, 1989.
Sunstrom, J. E., Moser, W. R. and Marshik-Guerts, B. (1996), General route to nanocrystalline oxides by hydrodynamic cavitation. Chem. Mater. 8, 2061.
Suslick, K. S., Hyeon, T. and Fang, F. (1996), Nanostructured materials generated by high-intensity ultrasound: Sonochemical synthesis and catalytic studies. Chem. Mater. 8, 2172.
Sutter, E., Sutter, P., Calarco, R., Stoica, T. and Meijers, R. (2007), Assembly of ordered carbon shells on GaN nanowires. Appl. Phys. Lett. 90, 093118.
Sutter, P. W., Flege, J. I. and Sutter, E. A. (2008), Epitaxial graphene on ruthenium. Nature Materials 7, 406.
Taniguchi, N. (1974), On the basic concept of nano-technology. Proc. Intl. Conf. Prod. Eng. Tokyo, Part II, Japan Society of Precision Engineering.
Temelso, B., Sherrill, C. D., Merkle, R. C. and Freitas, R. A. J. (2006), High-level ab initio studies of hydrogen abstraction from prototype hydrocarbon systems. J. Phys. Chem. A 110, 11160.
Temelso, B., Sherrill, C. D., Merkle, R. C. and Freitas, R. A. J. (2007), Ab initio thermochemistry of the hydrogenation of hydrocarbon radicals using silicon, germanium, tin and lead substituted methane and isobutane. J. Phys. Chem. A 111, 35 8677.
Teranishi, T. and Miyake, M. (1998), Size control of palladium nanoparticles and their crystal structures. Chem. Mater 10, 594.

Teranishi, T., Kiyokawa, I. and Miyake, M. (1998), Synthesis of monodisperse gold nanoparticles using linear polymers as protective agents**.** Adv. Mater. 10, 8, 596.

Teranishi, T., Haga, M., Shiozawa, Y. and Miyake, M. (2000), Self-organisation of Au nanoparticles protected by 2, 6-bis (1'- (8-thiooctyl) benzimidazol-2-yl) pyridine. J. Am. Chem. Soc. 122, 17, 4237.

Teranishi, T., Hasegawa, S., Shimuzu, T. and Miyake, M. (2001), Heat-induced size evolution of gold nanoparticles in solid state. Adv. Mater. 13, 1699.

Teranishi, T., Sugawara, A., Shimizu, T. and Miyake, M. (2002), Planar array of 1D gold nanoparticles on ridge-and-valley structured carbon. J. Am. Chem. Soc. 124.

Teter, M. P., Payne, M. C. and Allan, D. C. (1989), Solution of Schrödinger's equation for large systems**.** Phys. Rev. B 40, 12255.

Thirstrup, C., Sakurai, M., Nakayama, T. and Aono, M. (1998), Atomic scale modifications of hydrogen-terminated silicon (2×1) and (3×1) (001) surfaces by Scanning Tunneling Microscope. Surf. Science 411, 203.

Thomas, J. M. (1988), Colloidall metals: Past, present and future. Pure and Appl. Chem. 60, 1517.

Thomas, L. H. **(**1927), The calculation of atomic fields. Proc. Cambridge Phil. Soc. 23, 542.

Trevethan, T., Kantorovich, L., Polesel-Maris, J. and Gauthier, S. (2007), Is atomic-scale dissipation in NC-AFM real? Investigation using virtual Atomic Force Microscopy. Nanotechnology 18, 084017.

Trevethan, T., Kantorovich, L., Polesel-Maris, J., Gauthier, S. and Shluger, A. (2007), Multiscale model of the manipulation of single atoms on insulating surfaces using an Atomic Force Microscope tip. Phys. Rev. B 76, 0851414.

Tseng, A. A., Notargiacomo, A. and Chen, T. P. (2005), Nanofabrication by Scanning Probe Microscopy lithography. J. Vac. Sci. Technol. B 23, 3, 877.

Turkevich, J. (1985), Colloidal gold. Part I**.** Gold Bulletin 18, 86.

Tzalenchuck, A., Lara-Avila, S., Kalaboukhov, A., Paolillo, S., Syvajarvi, M., Yakimova, R., Kazakova, O., Janssen, T. J. B. M., Falko, V. and Kubatkin, S. (2010), Towards a quantum resistance standard based on epitaxial graphene. Nature Nanotech. 5, 186.

Ueta, H., Saida, M., Nakai, C., Yamada, Y., Sasaki, M. and Yamamoto, S. (2004), Highly oriented monolayer graphite formation on Pt (111) by a supersonic methane beam. Surf. Sci. 560**,** 183.

Van Rheenen, P. R., McKelvey, M. J. and Glaunsinger, W. S. (1987), Synthesis and characterisation of small platinum particles formed by the chemical reduction of chloroplatinic acid. J. Solid State Chem. 67, 151.

Varchon, F., Feng, R., Hass, J., Li, X., Nguyen, B. N., Naud, C., Mallet, P., Veuillen, J. Y., Berger, C., Conrad, E. H. and Magaud, L. (2007), Electronic structure of epitaxial graphene layers on SiC: Effect of the substrate. Phys. Rev. Lett. 99, 126805.

Varns, R. and Strange, P. (2008), Stability of gold atoms and dimers adsorbed on graphene. J. Phys. Conden. Matter 20, 22, 225005.

Virojanadara, C., Syväjarvi, M., Yakimova, R., Johansson, L. I., Zakharov, A. A. and Balasubramanian, T. (2008), Homogeneous large-area graphene layer growth on 6H-SiC (0001). Phys. Rev. B 78, 245403.

Walch, S. P. and Merkle, R. C. (1998), Theoretical studies of diamond mechanosynthesis reactions. Nanotechnology 9, 285.

Wallace, P. R. (1947), The band theory of graphite**.** Phys. Rev. 71, 9, 622.

Wang, C. C., Zhang, Z. and Ying, J. Y. (1997), Photocatalytic decomposition of halogenated organics over nanocrystalline titania. Nanostructured Mater. 9, 583.

Wang, J. J., Lambers, E. S., Pearton, S. J., Ostling, M., Zetterling, C. M., Grow, J. M. and Ren, F. (1998), High rate etching of SiC and SiCN in NF_3 inductively coupled plasmas. Solid State Electron 42, 743.

Wang, R., Yang, J., Zheng, Z., Carducci, M. D., Jiao, J. and Seraphin, S. (2001), Dendron-controlled nucleation and growth of gold nanoparticles. Angew. Chem. Int. Ed. 40, 549.

Wang, D., Rogach, A. L. and Caruso, F. (2002), Semiconductor quantum dot-labeled microsphere bioconjugates prepared by stepwise self-assembly. Nano Lett. 2, 857.
Wang, S., Ang, P. K., Wang, Z., Tang, A. L. L., Thong, J. T. L. and Loh, K. P. (2010), High mobility, printable and solution-processed graphene electronics. Nano Lett. 10, 92.
Welz, S., McNallan, M. J. and Gogotsi, Y. (2006), Carbon structures in silicon carbide derived carbon. Journal of Materials Processing Technology 179, 1-3, 11.
Winters, H. F. (1983), Etch products from the reaction of XeF_2 with SiO_2, Si_3N_4, SiC, and Si in the presence of ion bombardment. J. Vac. Sci. Tech. B 1, 927.
Winters, H. F. and Houle, F. A. (1983), Gaseous products from the reaction of XeF_2 with silicon. J. Appl. Phys. 54, 1218.
Wu, Ch. J. and Carter, E. A. (1991), Mechanistic predictions for fluorine etching of Si (100). J. Am. Chem. Soc. 113, 9061.
Xia, F. N., Mueller, T., Lin, Y. M., Valdes-Garcia, A. and Avouris, P. (2009), Ultrafast graphene photodetector. Nature Nanotechnol. 4, 839.
Xu, J. L., Li, X. L., He, J. L., Hao, X. P., Wu, Y. Z., Yang, Y. and Yang, K. J. (2011), Performance of large-area few-layer graphene saturable absorber in femtosecond bulk laser. Appl. Phys. Lett. 99, 261107.
Yang, R., Huang, Q. S., Chen, X. L., Zhang, G. Y. and Gao, H. J. (2010), Substrate doping effects on Raman spectrum of epitaxial graphene on SiC. J. Appl. Phys. 107, 034305/1.
Ye, J. H., Perez-Murano, F., Barniol, N., Abadal, G. and Aymerich, X. (1995), Nanoscale modification of H-terminated n-Si (100) surfaces in aqueous solutions with an in Situ Electrochemical Scanning Tunneling Microscope. J. Phys. Chem. 99, 49, 17650.
Yih, P. H., Saxena, V. and Steckl, A. (1997), A review of SiC reactive ion etching in fluorinated plasmas**.** Phys. Stat. Solid. B 202, 605.
Yin, M. T. and Cohen, M. L. (1982), Theory of ab initio pseudopotential calculations. Phys. Rev. B 25, 7403.
Ying, J. Y. and Sun, T. (1997), Research needs assessment on nanostructured catalysts**.** J. of Electroceramics 1, 219.
Yoo, E., Okata, T., Akita, T., Kohyama, M., Nakamura, J. and Honma, I. (2009), Enhanced electrocatalytic activity of Pt subnanoclusters on graphene nanosheet surface. Nano Lett. 9, 2255.
Young, R. J., Kinloch, I. A., Gong, L. and Novoselov, K. S. (2012), The mechanics of graphene nanocomposites: A review. Compos. Sci. Technol. 72, 1459.
Yuan, Y., Fendler, J. and Cabasso, I. (1992), Photoelectron transfer mediated by size-quantised CdS particles in polymer-blend membranes. Chem. Mater. 4, 2, 312.
Yushin, G., Nikitin, A. and Gogotsi Y. (2006), Carbide derived carbon. In Carbon Nanomaterials (Ed: Y. Gogotsi), CRC Taylor and Francis.
Zareie, M. H., Ma, H., Reed, B. W., Jen, A. K. Y. and Sarikaya, M. (2003), Controlled assembly of conducting monomers for molecular electronics. Nano Lett. 3, 2, 139, 142.
Zavitsas, A. A. and Chatgilialoglu, Ch. (1995), Energies of activation. The paradigm of hydrogen abstractions by radicals**.** J. Am. Chem. Soc. 117, 10645.
Zhang, H., Tang, D., Knize, R. J., Zhao, L., Bao, Q. and Loh, K. P. (2010), Graphene mode locked, wavelength-tunable, dissipative soliton fiber laser. Appl. Phys. Lett. 96, 11, 111112.
Zhou, S. Y., Gweon, G. H., Fedorov, A. V., First, P. N., Heer, W. A., Lee, D. H., Guinea, F., Castro Neto, A. H. and Lanzara, A**.** (2007), Substrate induced band gap opening in epitaxial graphene**.** Nature Materials, 6, 770.
Zhou, S. Y., Siegel, D. A., Fedorov, A. V. and Lanzara, A. (2008), Metal to insulator transition in epitaxial graphene induced by molecular doping. Phys. Rev. Lett. 101, 086402.
Zinovev, A. V., Elam, J. W., Moore, J. F., Hryn, J. N., Auciello, O., Carlisle, J. A. and Pellin, M. J. (2004), Coating of SiC surface by thin carbon films using the carbide derived carbon process. Thin Solid Films 469-470, 1.
Zsigmondy, R. (1914), Colloids and the Ultramicroscope. J.Wiley and Sons, NY.

Appendix I

Supporting Information for the Carbide Derived Carbon Produced on the 4H-*SiC* (0001) - $\left(\sqrt{3} \times \sqrt{3}\right)R30°$ Substrate Surface by Means of *HF* Etching and Transformation of Amorphous Carbon into Highly Ordered Graphene Structure

Section 1

In this section the supplementary materials for the reaction $SiC + 4HF = SiF_4\uparrow + 2H_2\uparrow + C$ presented in Chapter 8 are placed. In these explanatory illustrations the serial old $Si - C$ bonds breakings and new SiF_x groups formations are shown. SiF_4 escapes as a volatile product and carbon is oxidised by protons. The sequence of figures are arranged as HF penetration involving the (0001) - $\left(\sqrt{3} \times \sqrt{3}\right)R30°$ unit cell from 1st to 3rd SiC bi-layers.

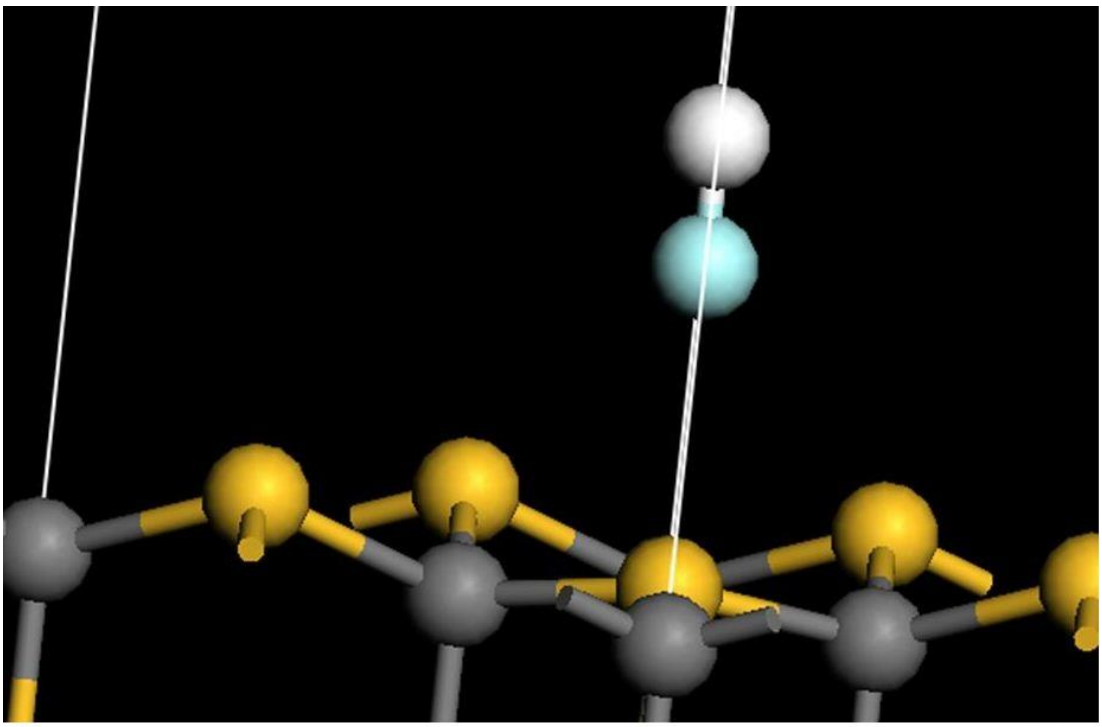

RE 1

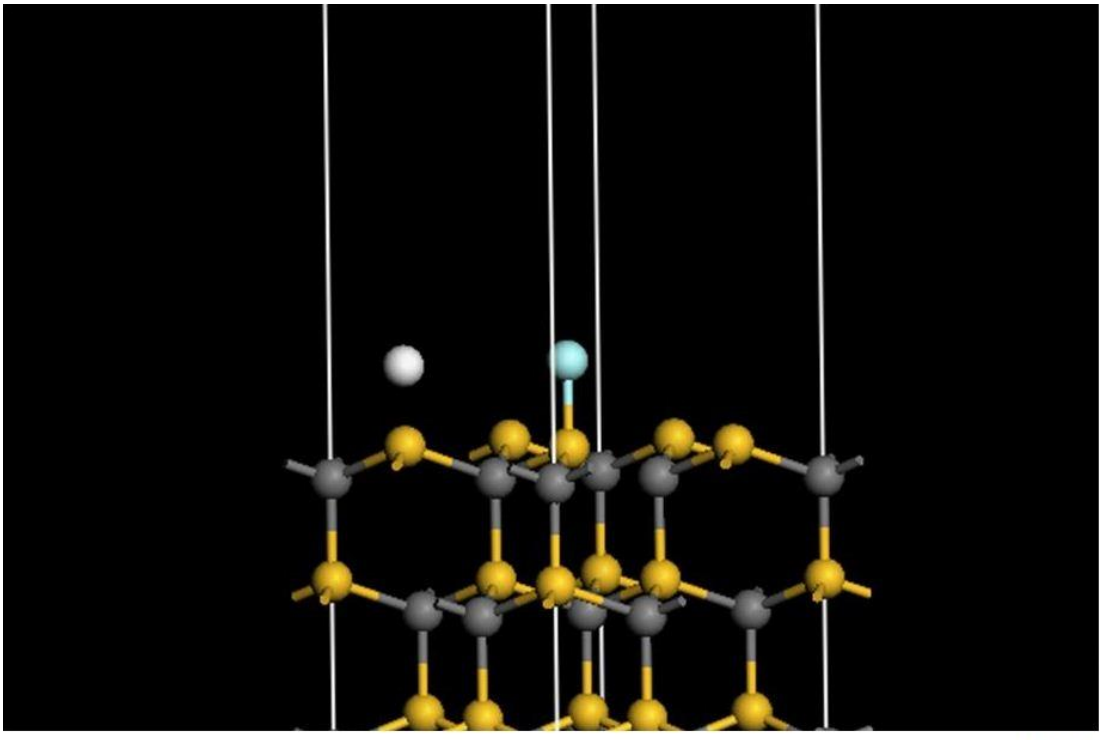

PR 1

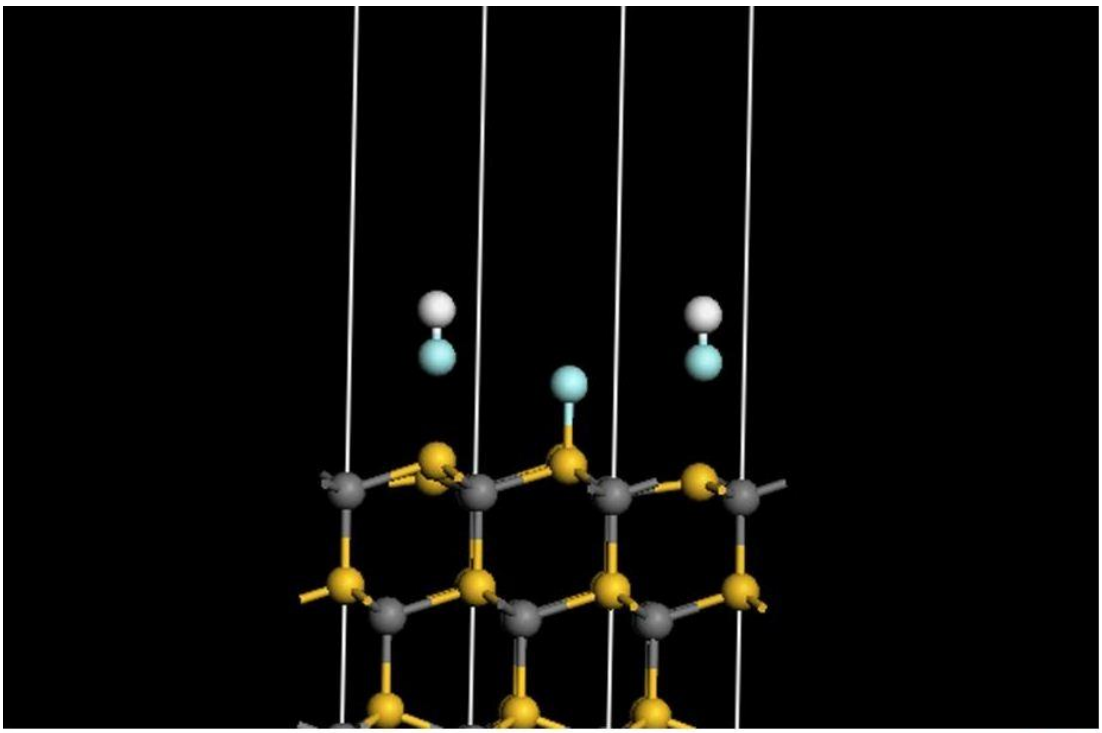

RE 2

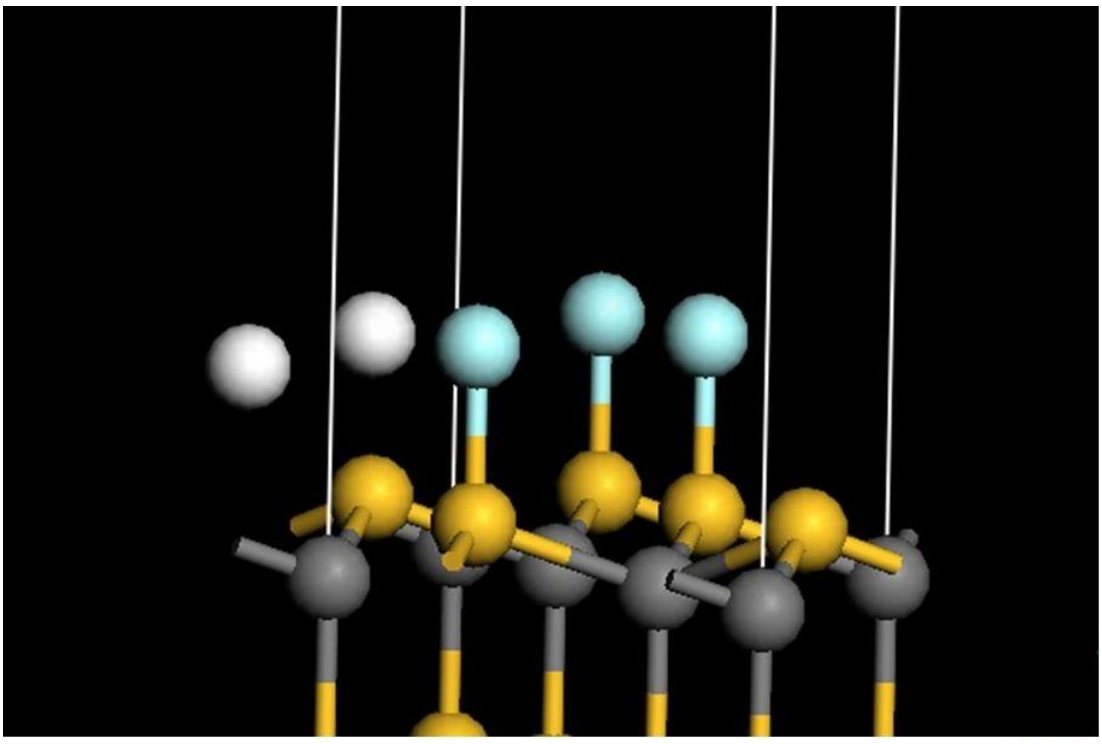

PR 2

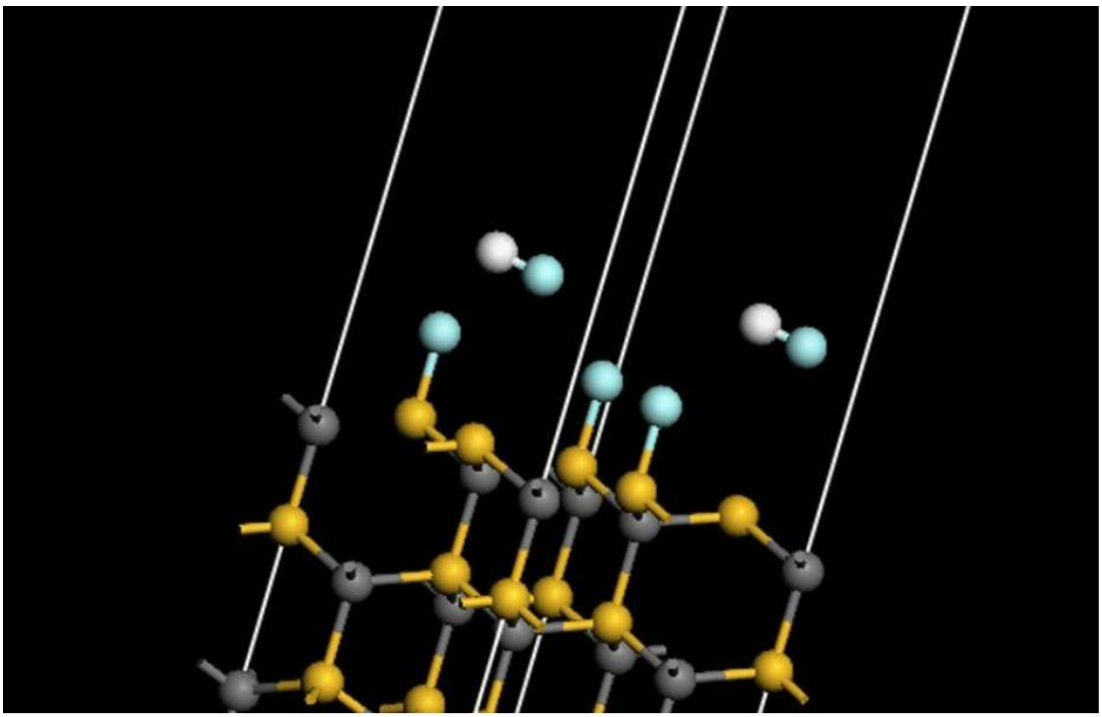

RE 3

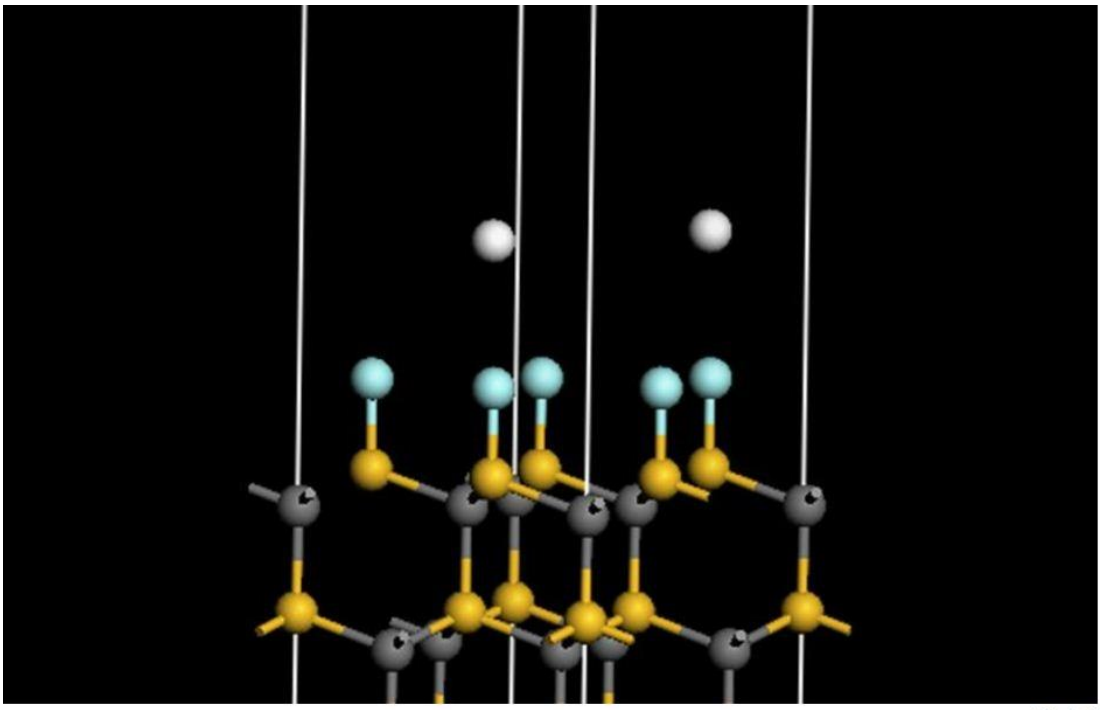

PR 3

Figure *S* 1. Fluorine attack on the 1st *SiC* bi-layer of 4H-*SiC* (0001) - $\left(\sqrt{3}\times\sqrt{3}\right)R30°$ substrate surface forming *SiF* group is demonstrated. RE – reactants, PR – products. The 1st, 2nd and 3rd *F*-atoms are added. The *Si* – *F* interaction by using free dangling bonds arisen from the topmost *Si*-atoms (yellow) of substrate is shown. The bonds arisen from the *C*-atoms (grey) are saturated. *C*-atoms are oxidised from -4 to -3. *F*-atoms (blue) are connected in the *SiF* clusters. The reduced *H*-atoms (white) while connecting with the reduced *H*-atoms of the next (neighbour) unit cell escape as a volatile phase.

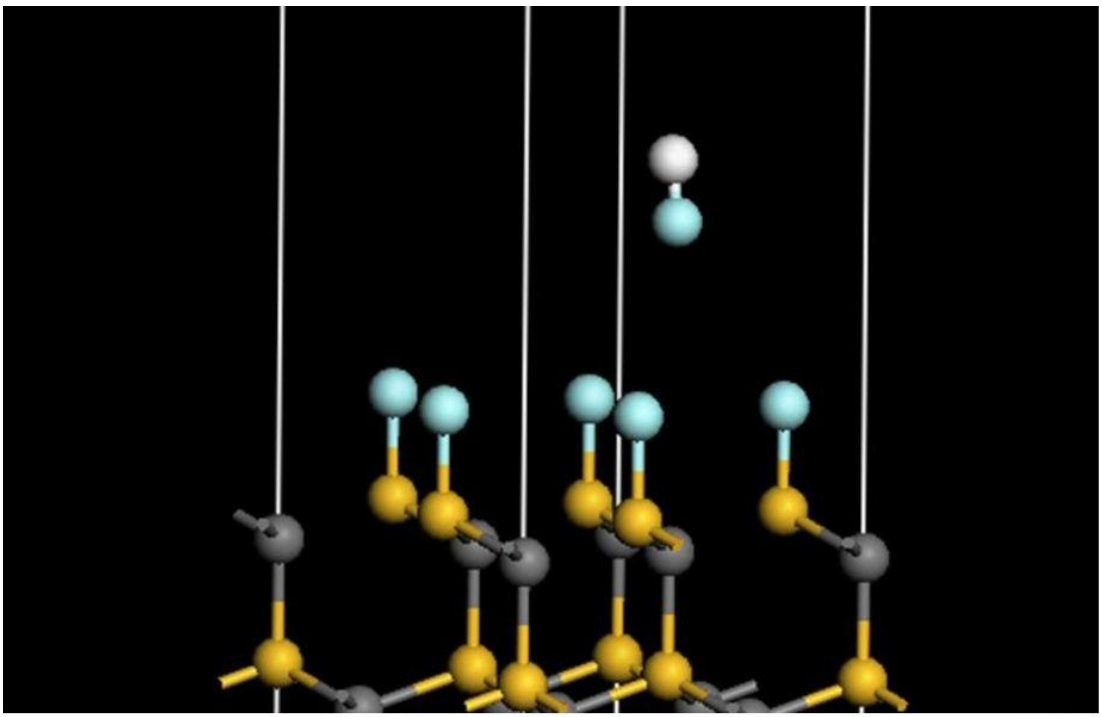

RE 4

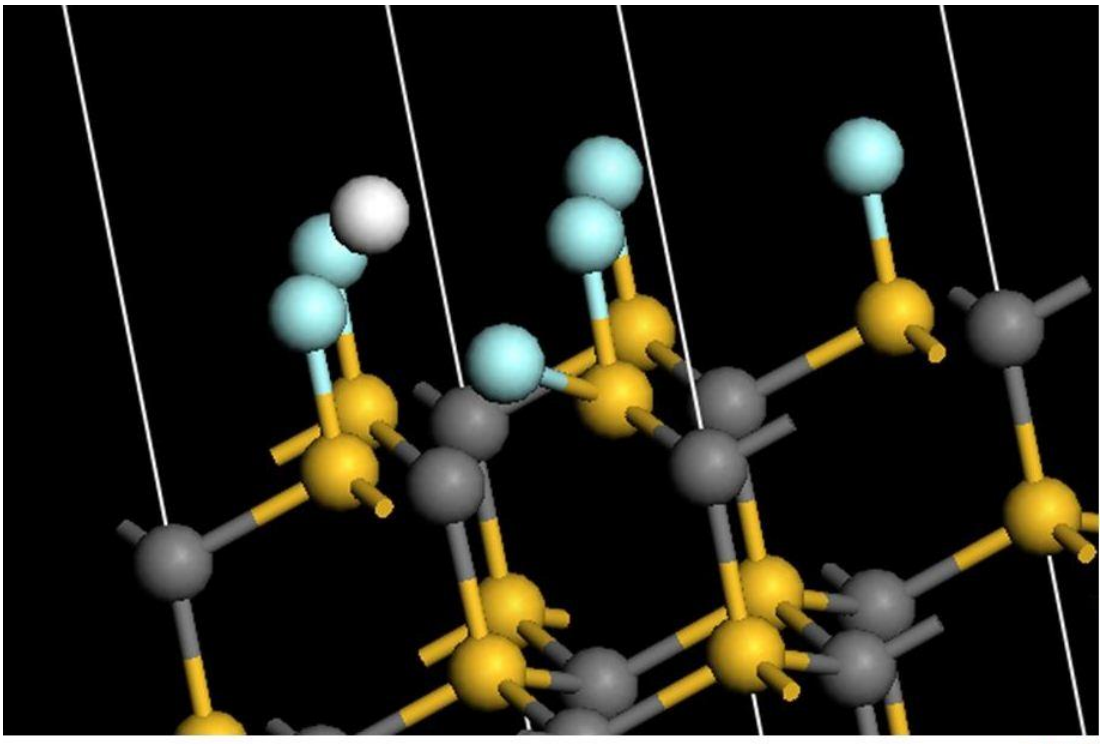

PR 4

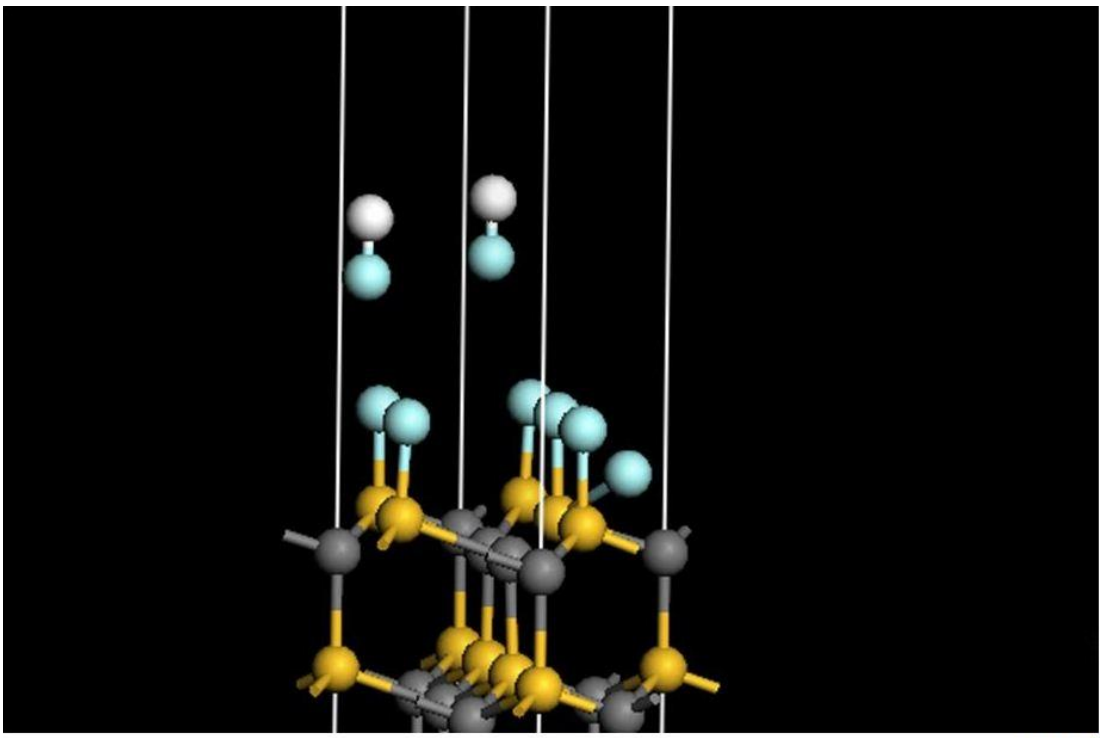

RE 5

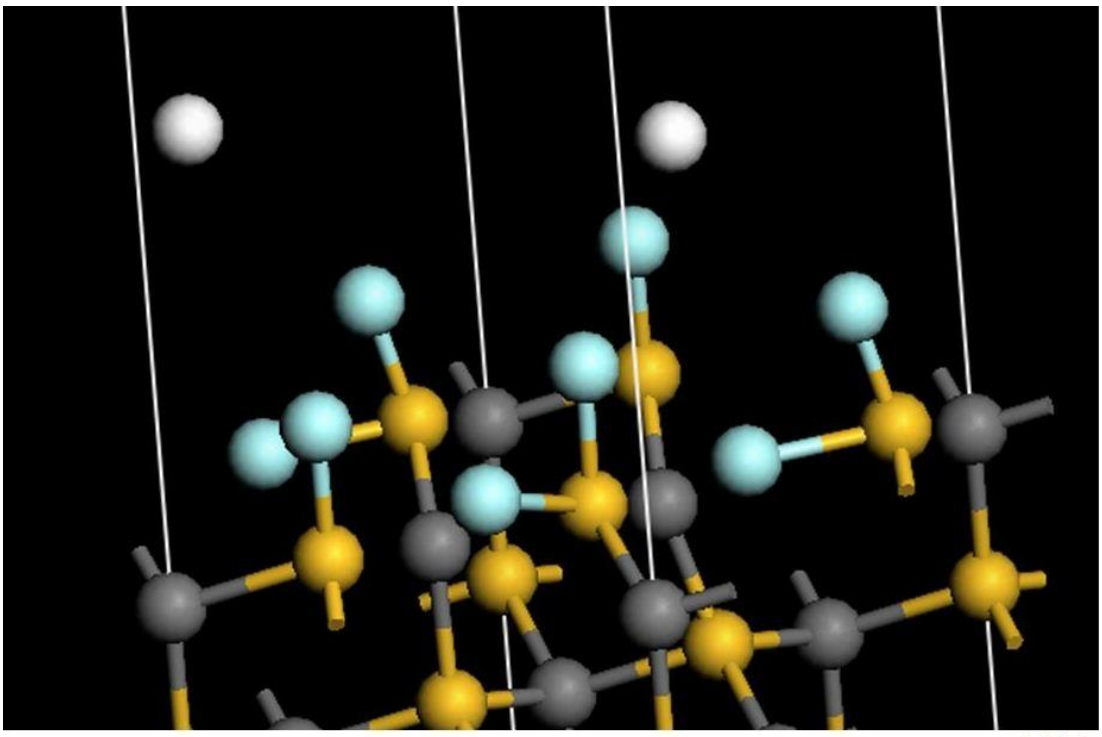

PR 5

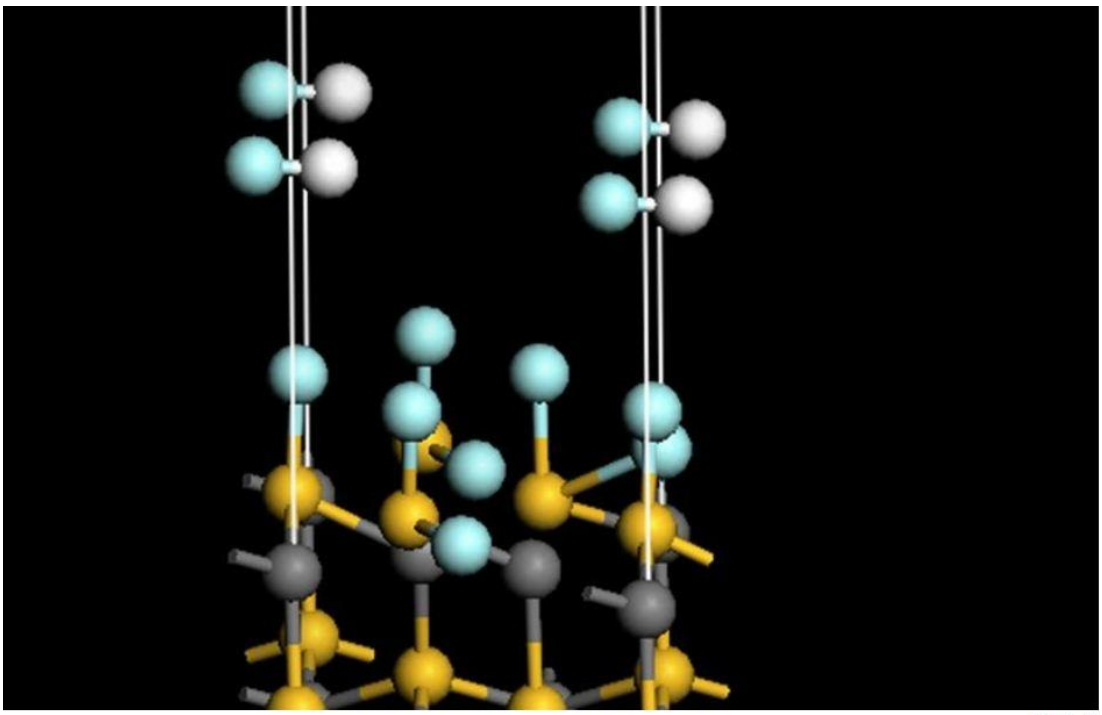

RE 6

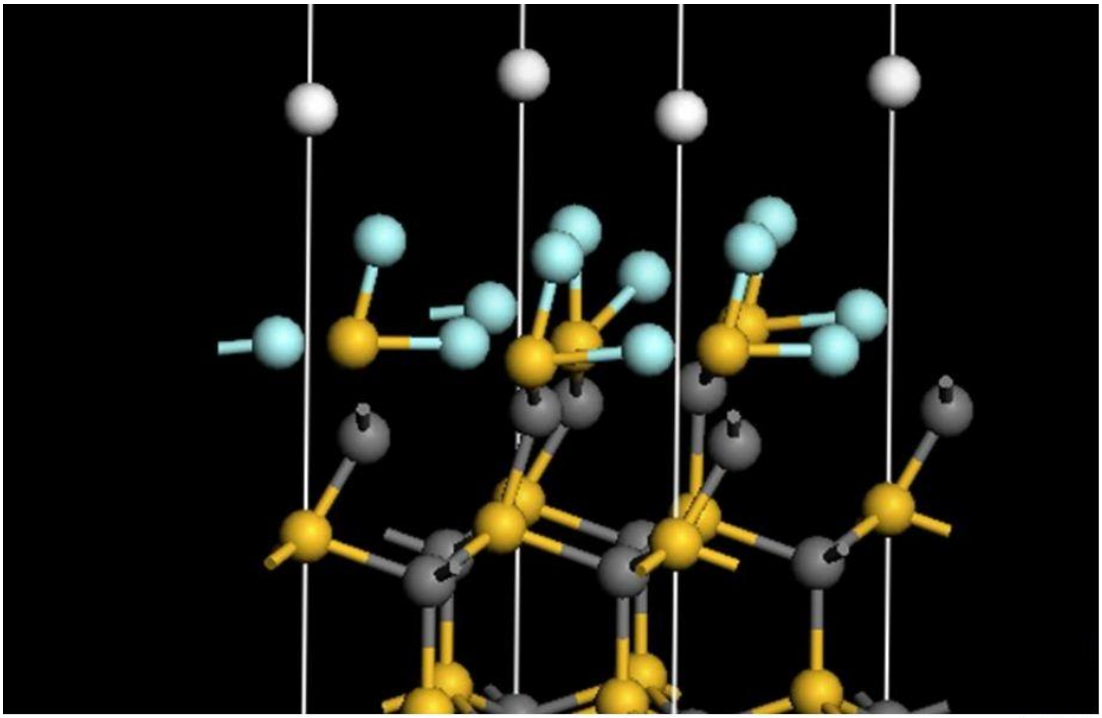

PR 6

Figure *S* 2. Fluorine attack on the 1st *SiC* bi-layer of 4H-*SiC* (0001) - $(\sqrt{3} \times \sqrt{3})R30°$ substrate surface forming SiF_2 group is demonstrated. RE – reactants, PR – products. The 4th, 5th and 6th *F*-atoms are added. The *Si* – *F* interaction by breaking S*i* – *C* bonds between the topmost *Si*-atoms (yellow) and *C*-atoms (grey) of substrate is shown. *C*-atoms are oxidised from -3 to -2. *F*-atoms (blue) are connected in the SiF_2 clusters. The reduced *H*-atoms (white) while connecting with the reduced *H*-atoms of the next (neighbour) unit cell escape as a volatile phase.

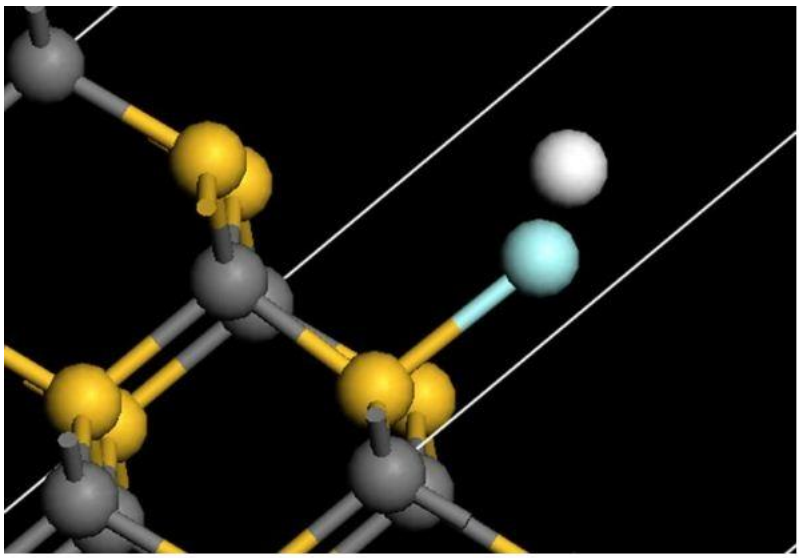

1

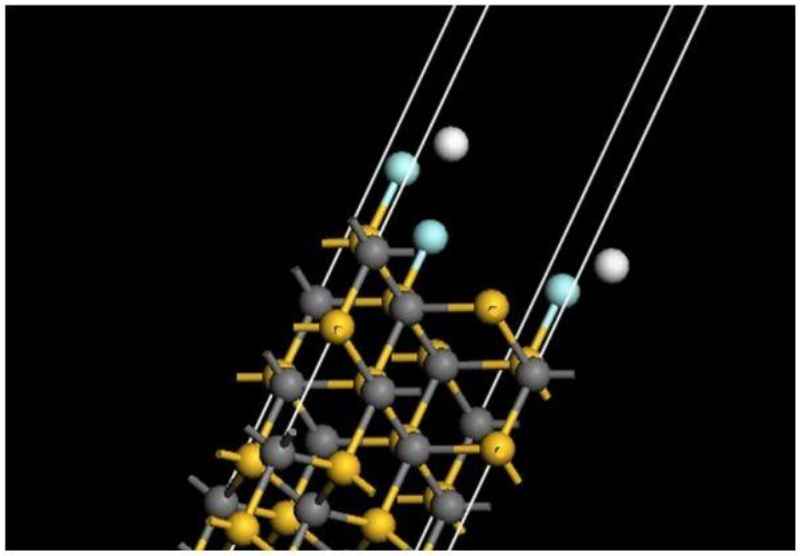

2

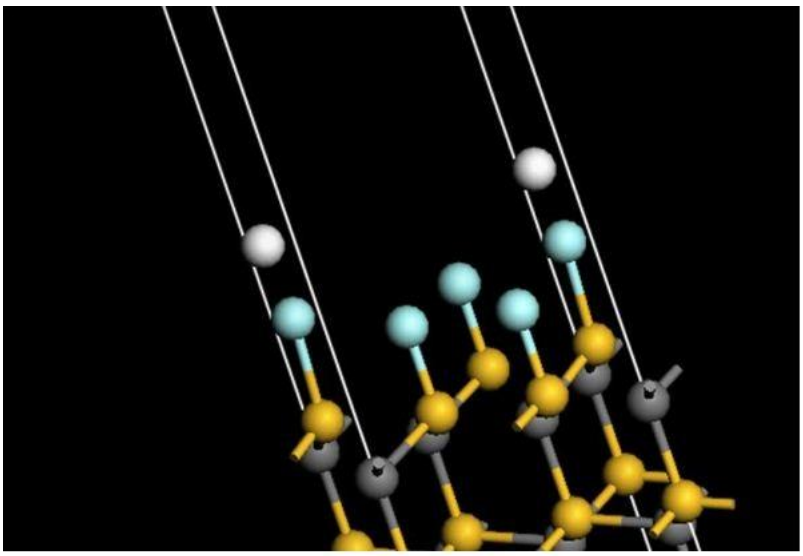

3

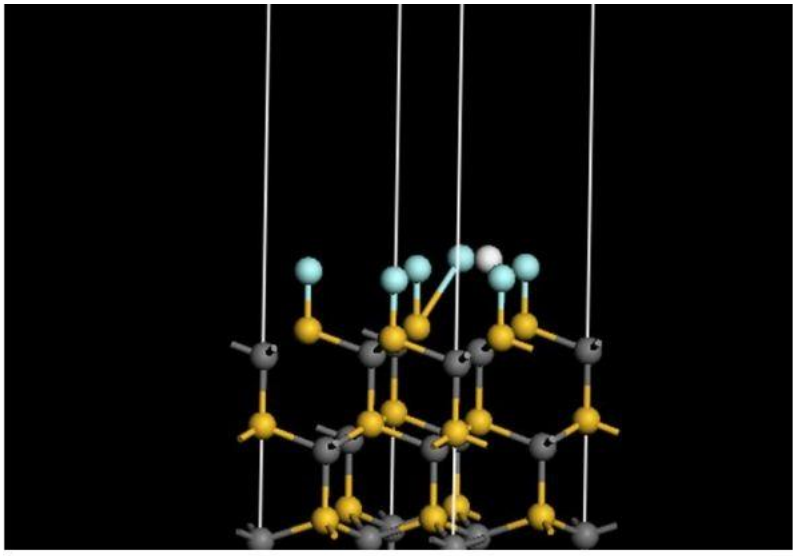

4

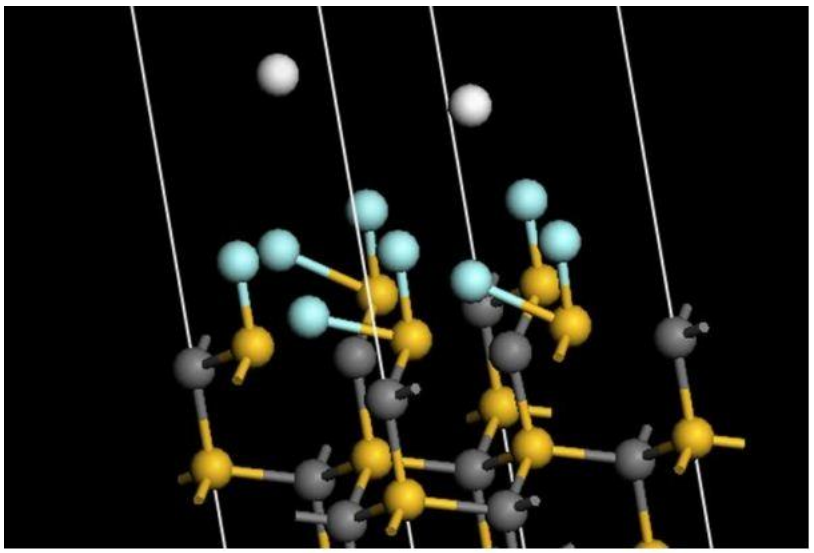

5

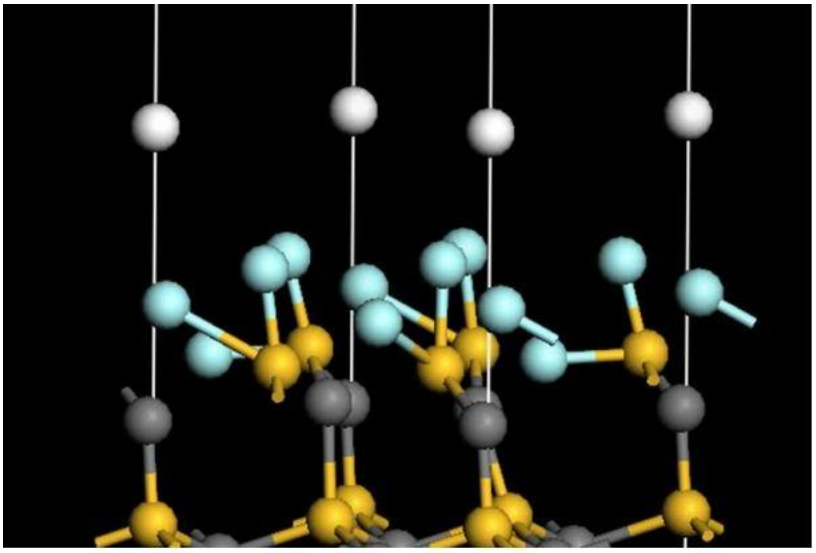

6

Figure *S* 3. Transition States for the *SiF* and SiF_2 group formations of the 1st *SiC* bi-layer, 4H-*SiC* (0001) - $\left(\sqrt{3}\times\sqrt{3}\right)R30°$ substrate surface: 1, 2, 3 – succession for the *SiF* group; 4, 5, 6 – succession for the SiF_2 group.

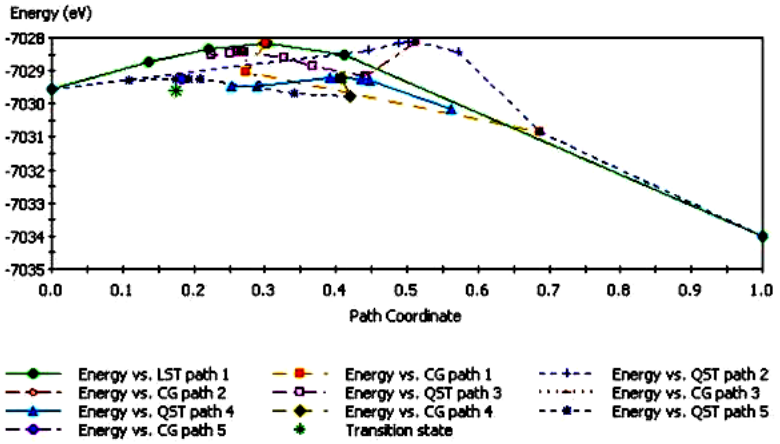
Energy (eV)
-7028
-7029
-7030
-7031
-7032
-7033
-7034
-7035
0.0 0.1 0.2 0.3 0.4 0.5 0.6 0.7 0.8 0.9 1.0
Path Coordinate
Energy vs. LST path 1
Energy vs. CG path 1
Energy vs. QST path 2
Energy vs. CG path 2
Energy vs. QST path 3
Energy vs. CG path 3
Energy vs. QST path 4
Energy vs. CG path 4
Energy vs. QST path 5
Energy vs. CG path 5
Transition state

1

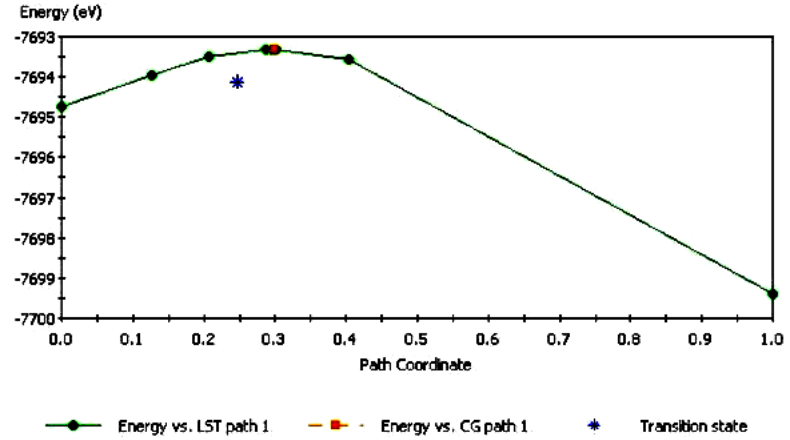
Energy (eV)
-7693
-7694
-7695
-7696
-7697
-7698
-7699
-7700
0.0 0.1 0.2 0.3 0.4 0.5 0.6 0.7 0.8 0.9 1.0
Path Coordinate
Energy vs. LST path 1
Energy vs. CG path 1
Transition state

2

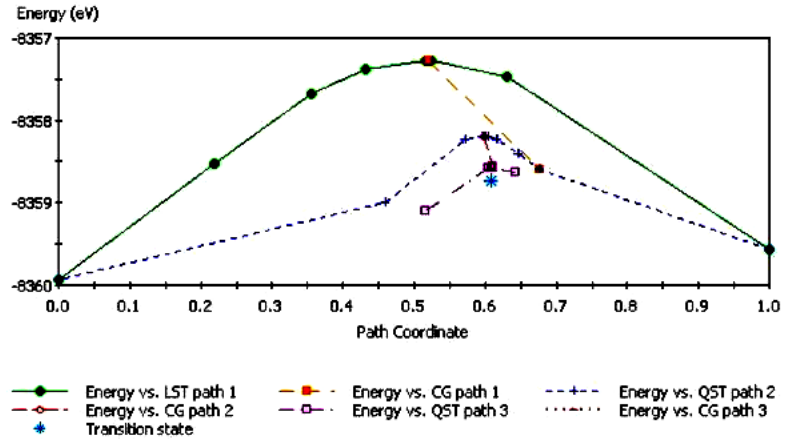
Energy (eV)
-8357
-8358
-8359
-8360
0.0 0.1 0.2 0.3 0.4 0.5 0.6 0.7 0.8 0.9 1.0
Path Coordinate
Energy vs. LST path 1
Energy vs. CG path 1
Energy vs. QST path 2
Energy vs. CG path 2
Energy vs. QST path 3
Energy vs. CG path 3
Transition state

3

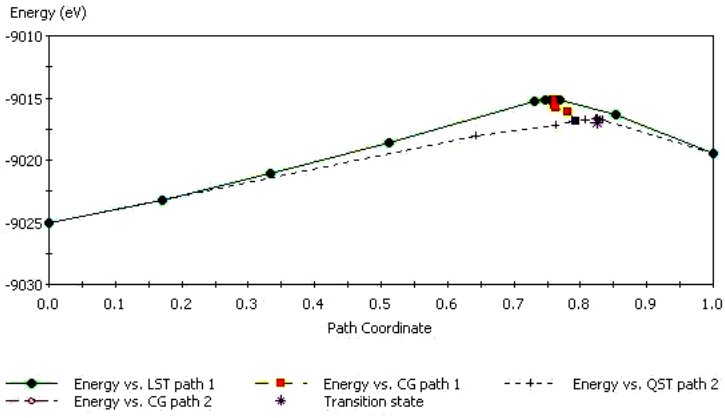

4

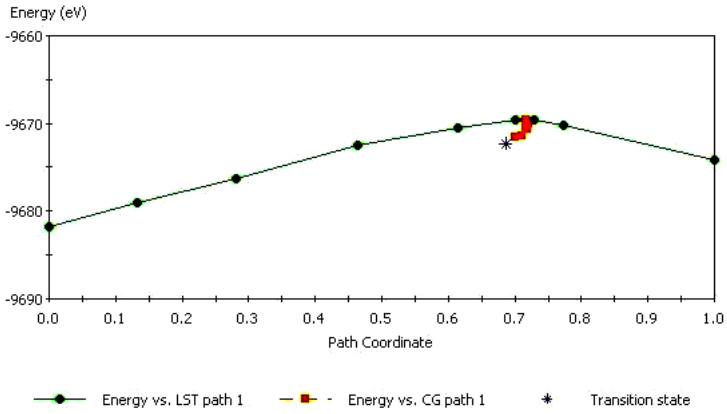

5

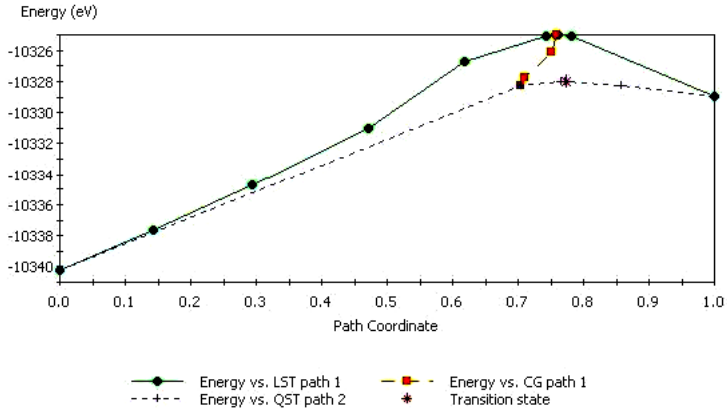

6

Figure *S* 4. Transition State diagrams for the *SiF* and SiF_2 group formations of the 1st *SiC* bi-layer, 4H-*SiC* (0001) - $\left(\sqrt{3}\times\sqrt{3}\right)R30°$ substrate surface reconstruction are placed; 1, 2, 3 – succession for the *SiF* group, 4, 5, 6 – succession for the SiF_2 group. The displacing locations of Transition States (shown by stars) are found under continuously reducing energy values. They move towards the high path coordinate region from the *SiF* group to the SiF_2 group.

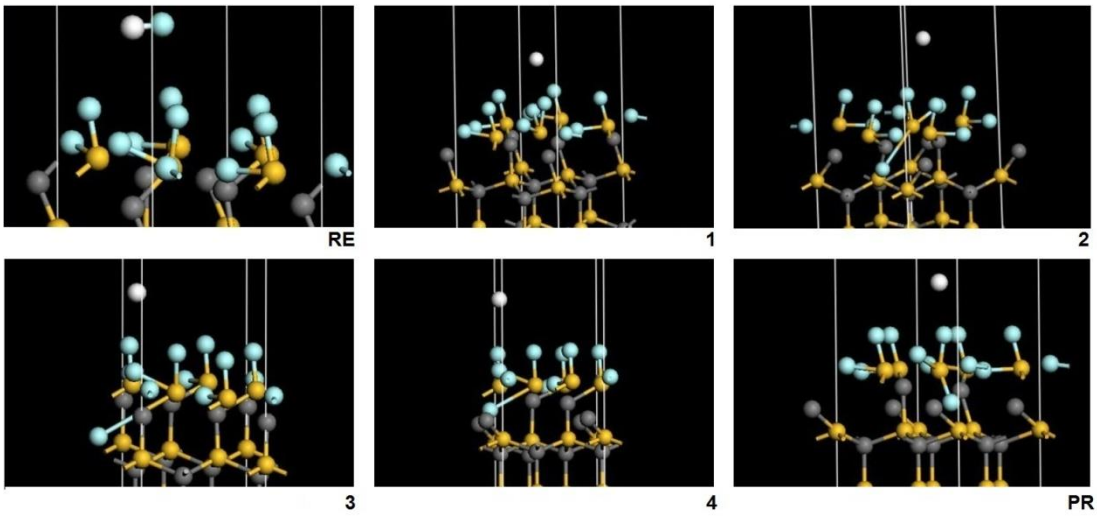

Figure *S* 5. SiF_3 group formation for the first *SiC* bi-layer is demonstrated. The 7th *F*-atom is added. 1, 2, 3 and 4 are pathway via interim products between the reactant (RE) and the product (PR). The *Si* – *F* interaction by breaking S*i* – *C* bonds between the topmost *Si*-atoms (yellow) and *C*-atoms (grey) of substrate is shown. *C*-atoms are oxidised from -2 to -1. *F*-atoms (blue) are connected in the SiF_3 clusters. The reduced *H*-atoms (white) while connecting with the reduced *H*-atoms of the next (neighbour) unit cell escape as a volatile phase.

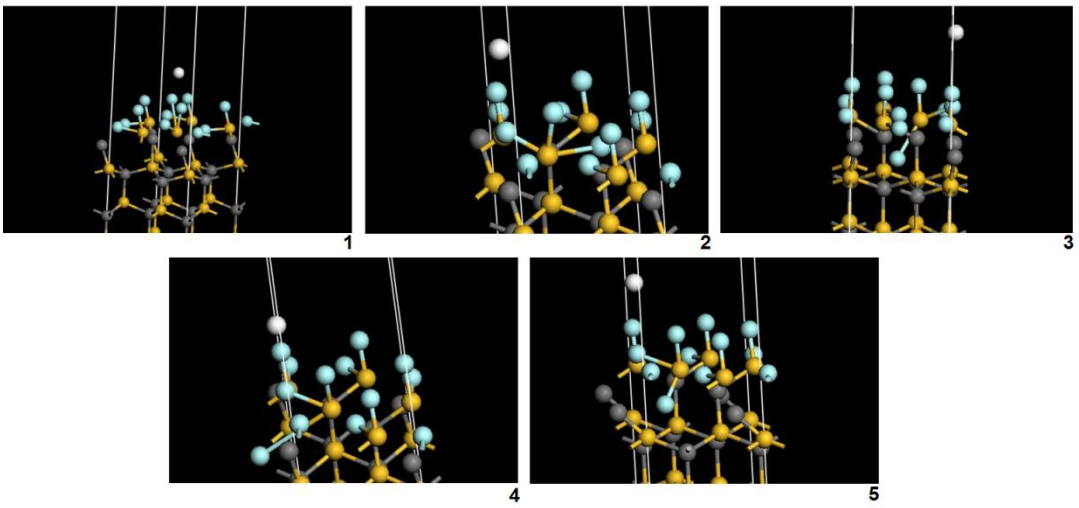

Figure *S* 6. Succession of Transition States separating four interim products while the 7th *F*-atom addition is shown.

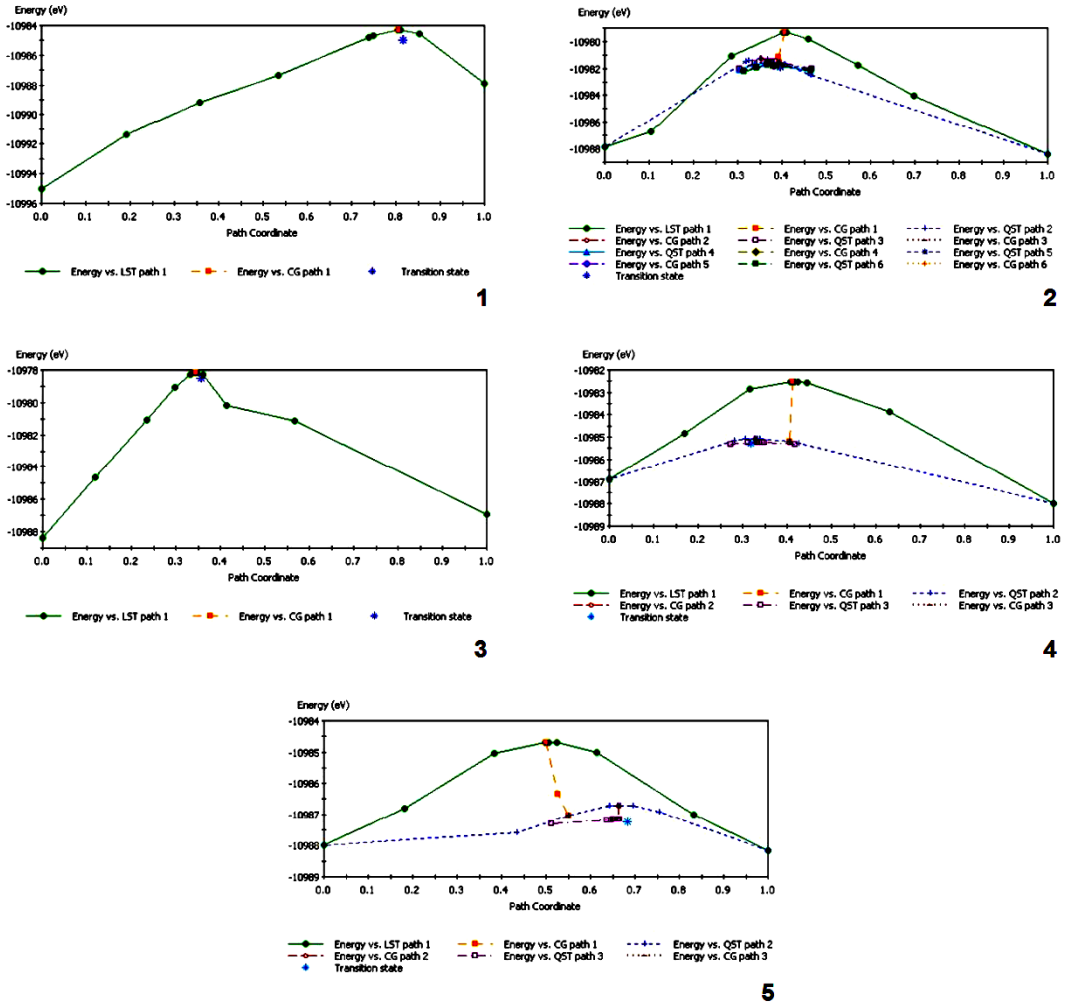

Figure *S* 7. Transition State diagrams for the 7th *F*-atom addition are placed. Adjustment for the initial cluster of the SiF_3 group for the first *SiC* bi-layer is found. Five Transition State locations are shown in the narrow energy interval and dispersing coordinates. The final state is found in the relatively high path coordinate region as a negligible decrease of energy values.

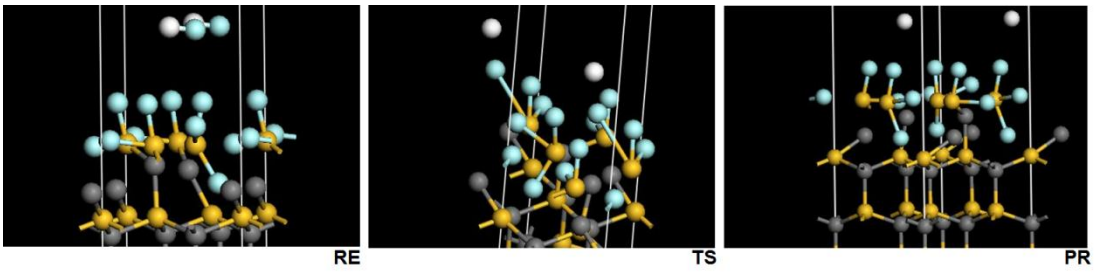

Figure *S* 8. SiF_3 group formation for the first *SiC* bi-layer is demonstrated. The 8th *F*-atom is added. RE – reactant, TS – transition state, PR – product. The *Si* – *F* interaction by breaking S*i* – *C* bonds between the topmost *Si*-atoms (yellow) and *C*-atoms (grey) of substrate is shown. *C*-atoms are oxidised from -2 to -1. *F*-atoms (blue) are connected in the SiF_3 clusters. The reduced *H*-atoms (white) while connecting with the reduced *H*-atoms of the next (neighbour) unit cell escape as a volatile phase.

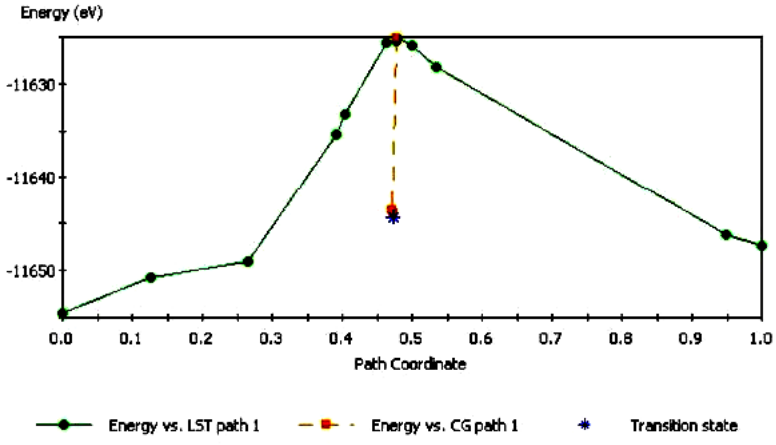

Figure *S* 9. The proper location of the Transition State is shown for the 8th *F*-atom addition. A decreasing energy value is found for the Transition State located in the middle path coordinate region.

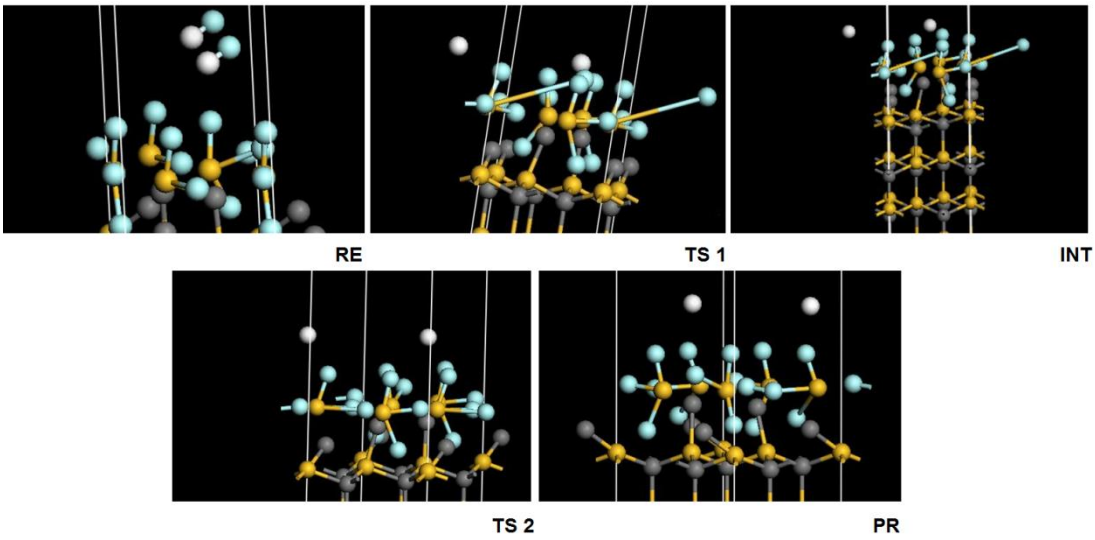

Figure *S* 10. SiF_3 group formation for the first *SiC* bi-layer is demonstrated. The 9th *F*-atom is added.
RE – reactant, TS – transition states, INT – interim product, PR – product. The *Si* – *F* interaction by breaking S*i* – *C* bonds between the topmost *Si*-atoms (yellow) and *C*-atoms (grey) of substrate is shown. *C*-atoms are oxidised from -2 to -1. *F*-atoms (blue) are connected in the SiF_3 clusters. The reduced *H*-atoms (white) while connecting with the reduced *H*-atoms of the next (neighbour) unit cell escape as a volatile phase.

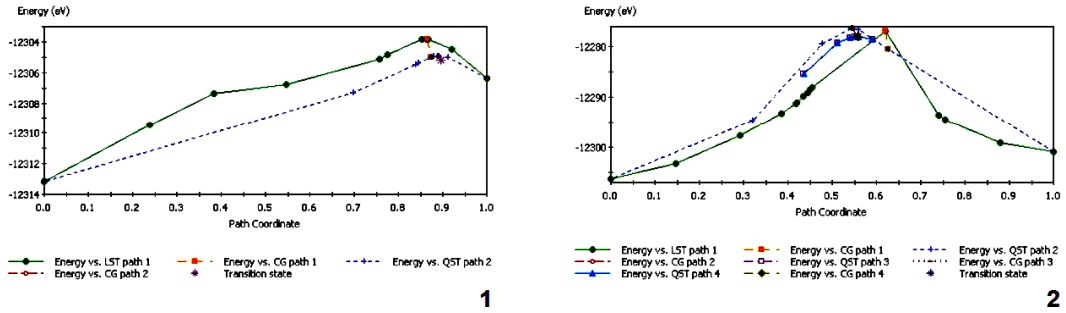

Figure *S* 11. Transition State diagrams for the 9th *F*-atom addition are placed. Search of proper adjustment for the final cluster of the SiF_3 group for the first *SiC* bi-layer is found under increasing Transition State energy values and in the middle path coordinate region.

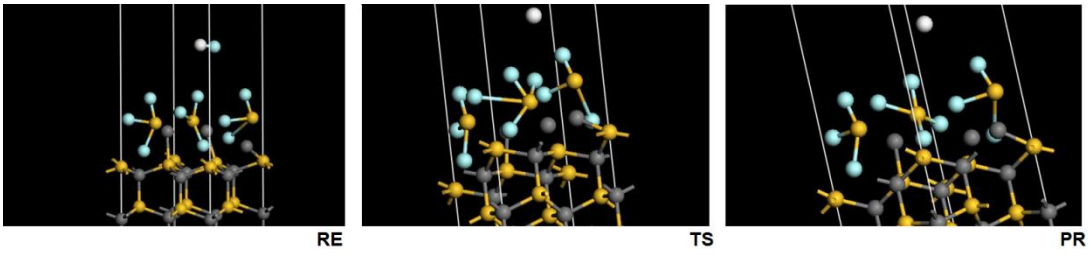

Figure *S* 12. SiF_4 molecules formation for the first *SiC* bi-layer is demonstrated. The 10th *F*-atom is added. RE – reactant, TS – transition state, PR – product. The *Si* – *F* interaction by breaking S*i* – *C* bonds between the topmost *Si*-atoms (yellow) and *C*-atoms (grey) of substrate is shown. *C*-atoms are oxidised from -1 to 0. Amorphous carbon is obtained. *F*-atoms (blue) are connected in the SiF_4 molecules. The SiF_4 molecules escape as a volatile phase. The reduced *H*-atoms (white) while connecting with the reduced *H*-atoms of the next (neighbour) unit cell escape as a volatile phase.

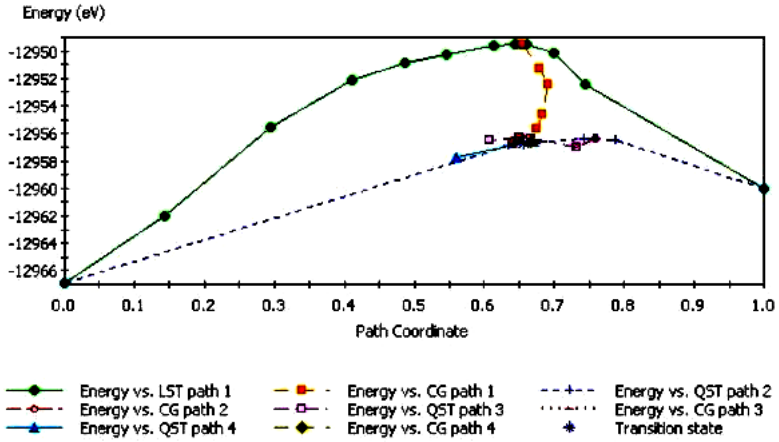

Figure *S* 13. Transition State diagram for the 10th *F*-atom addition is placed. Transition State is shown for the 10th *F*-atom adjustment (adjustment for the initial SiF_4 molecule for the first *SiC* bi-layer) before the SiF_4 molecules start to escape. The Transition State energy value decreases in anticipation of volatile phase. Transition State is located in the increased path coordinate region.

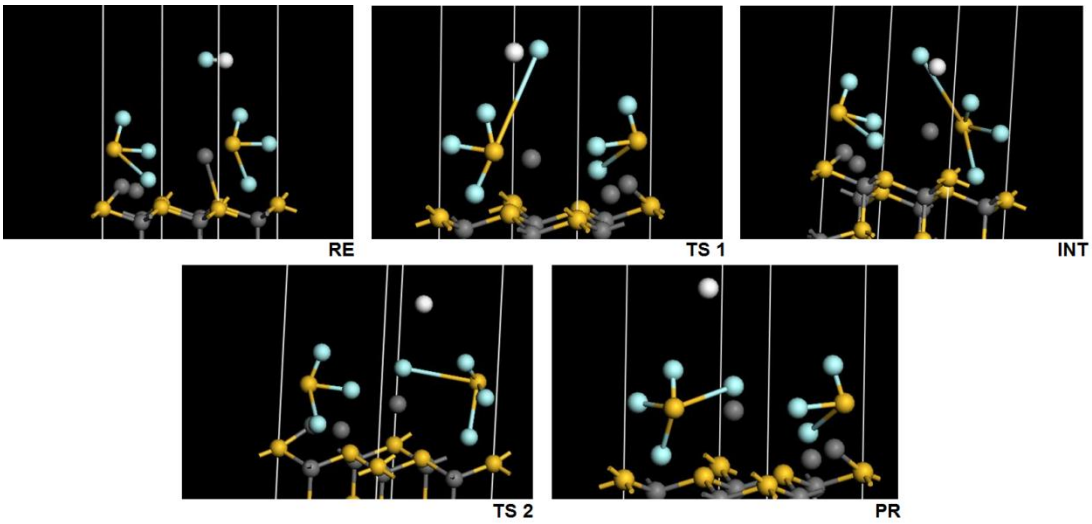

Figure *S* 14. SiF_4 molecules formation for the first *SiC* bi-layer is demonstrated. The 11th *F*-atom is added. RE – reactant, TS – transition states, INT – interim product, PR – product. The *Si* – *F* interaction by breaking S*i* – *C* bonds between the topmost *Si*-atoms (yellow) and *C*-atoms (grey) of substrate is shown. *C*-atoms are oxidised from -1 to 0. Amorphous carbon is obtained. *F*-atoms (blue) are connected in the SiF_4 molecules. The SiF_4 molecules escape as a volatile phase. The reduced *H*-atoms (white) while connecting with the reduced *H*-atoms of the next (neighbour) unit cell escape as a volatile phase.

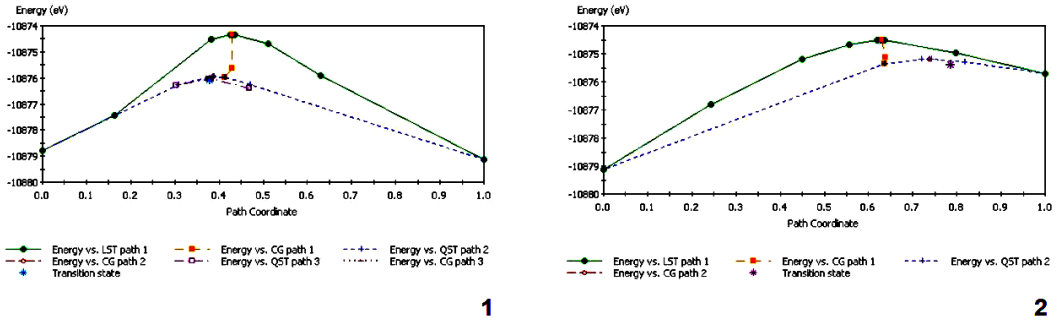

Figure *S* 15. Transition State diagrams for the 11th *F*-atom addition are placed. Two Transition States are shown to be separated by the interim product while the 11th *F*-atom adjustment (adjustment for the second SiF_4 molecule for the first *SiC* bi-layer) trends to the high path coordinate region. The Transition State energy values start to increase as the SiF_4 molecules escape.

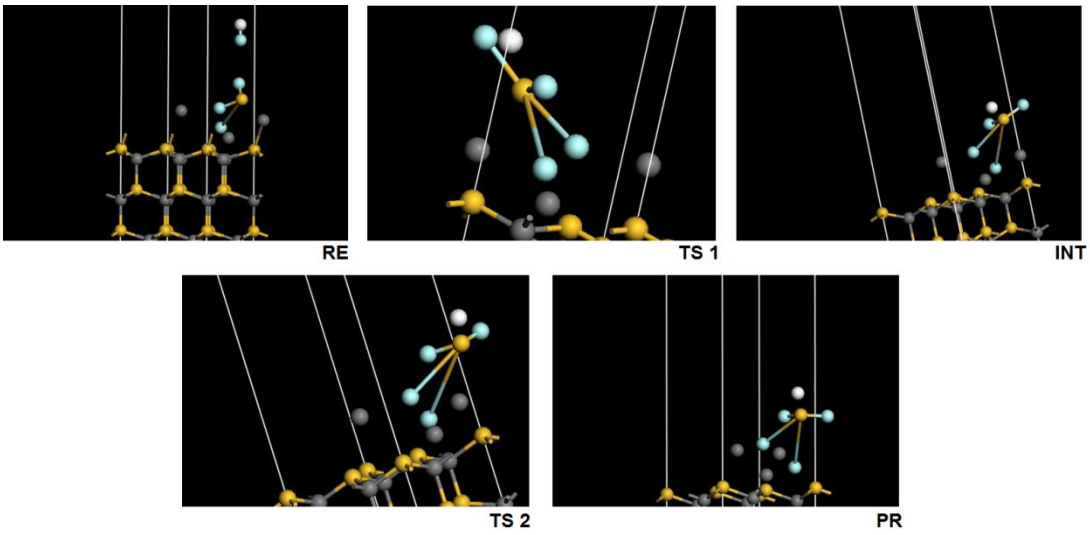

Figure *S* 16. SiF_4 molecules formation for the first *SiC* bi-layer is demonstrated. The 12th *F*-atom is added. RE – reactant, TS – transition states, INT – interim product, PR – product. The *Si* – *F* interaction by breaking S*i* – *C* bonds between the topmost *Si*-atoms (yellow) and *C*-atoms (grey) of substrate is shown. *C*-atoms are oxidised from -1 to 0. Amorphous carbon is obtained. *F*-atoms (blue) are connected in the SiF_4 molecules. The SiF_4 molecules escape as a volatile phase. The reduced *H*-atoms (white) while connecting with the reduced *H*-atoms of the next (neighbour) unit cell escape as a volatile phase.

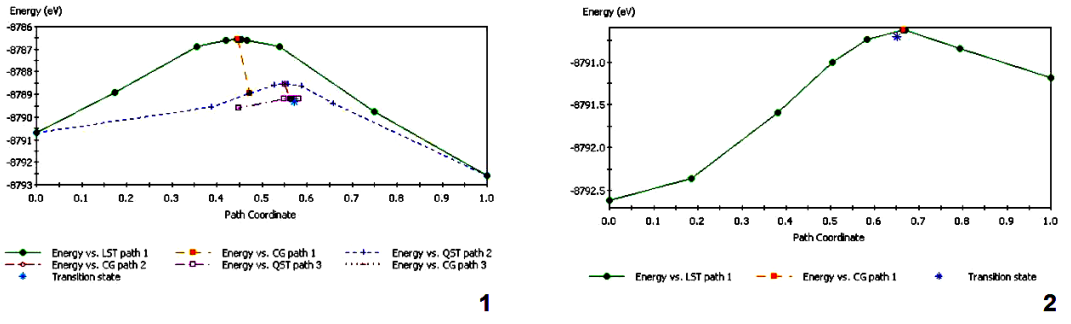

Figure *S* 17. Transition State diagrams for the 12th *F*-atom addition are placed. Two final Transition States for the first *SiC* bi-layer destruction are shown. In anticipation of the last SiF_4 molecule escape and three *C*-atoms release the Transition State energy value is advanced towards the initial level while locating in the middle path coordinate region.

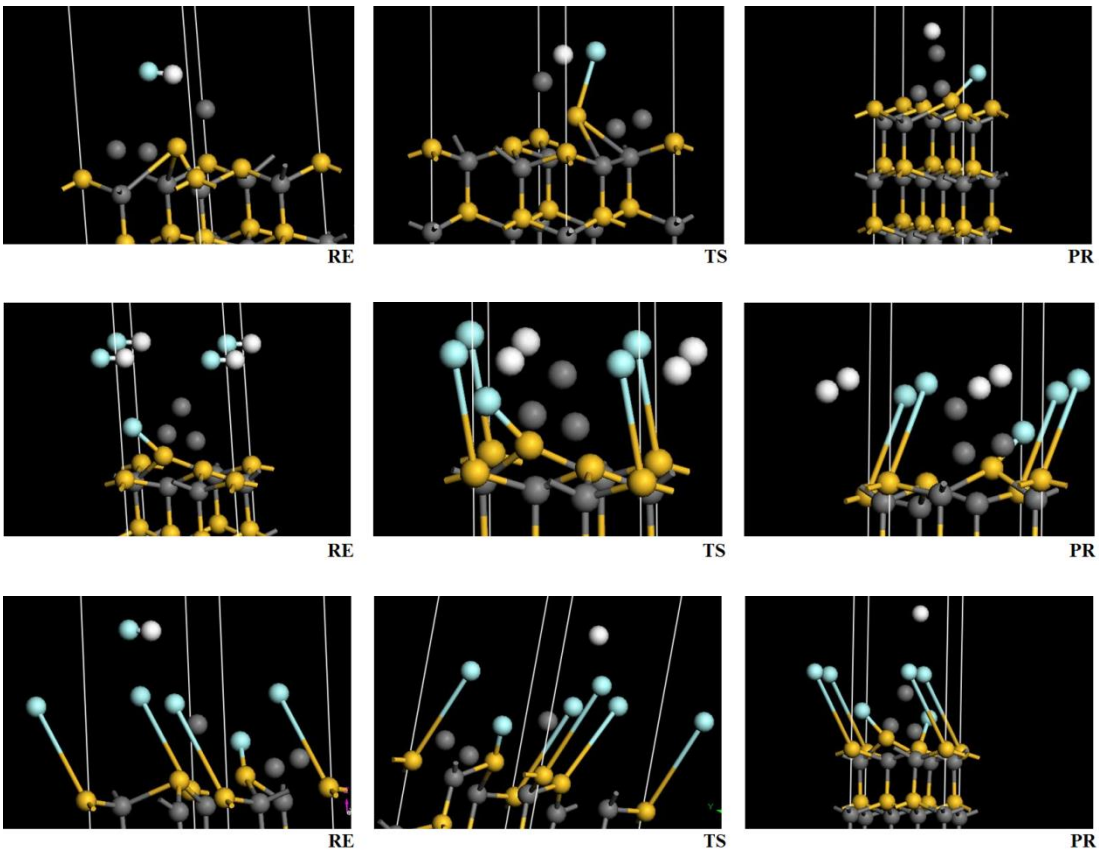

Figure *S* 18. *SiF* group formation for the second *SiC* bi-layer is demonstrated. 1st row: the 13th *F*-atom is added; 2nd row: the 14th *F*-atom is added; 3rd row: the 15th *F*-atom is added. RE – reactants, TS – transition states, PR – products. The *Si* – *F* interaction by breaking S*i* – *C* bonds between the *Si*-atoms (yellow) and *C*-atoms (grey) of the second *SiC* substrate bi-layer is shown. *C*-atoms are oxidised from -4 to -3. *F*-atoms (blue) are connected in the *SiF* clusters. The reduced *H*-atoms (white) while connecting with the reduced *H*-atoms of the next (neighbour) unit cell escape as a volatile phase.

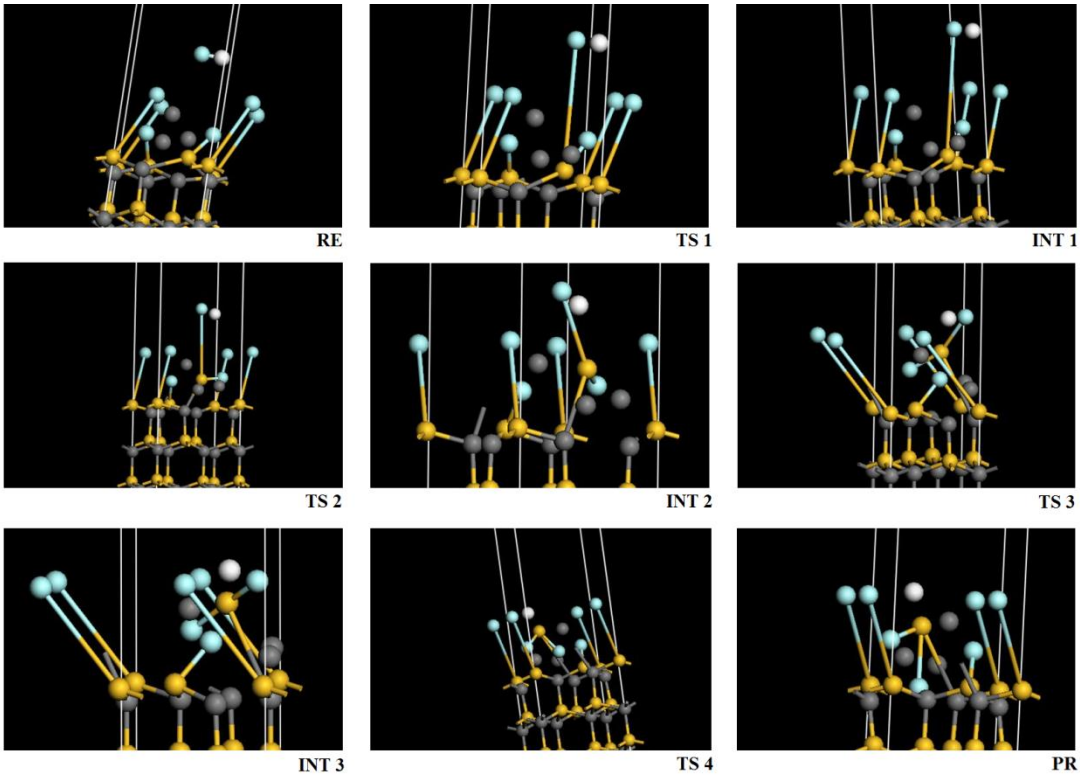

Figure *S* 19. SiF_2 group formation for the second *SiC* bi-layer is demonstrated. The 16th *F*-atom is added. RE – reactant, TS – transition states, INT – interim products, PR – product. The *Si* – *F* interaction by breaking S*i* – *C* bonds between the *Si*-atoms (yellow) and *C*-atoms (grey) of the second *SiC* substrate bi-layer is shown. *C*-atoms are oxidised from -3 to -2. *F*-atoms (blue) are connected in the SiF_2 clusters. The reduced *H*-atoms (white) while connecting with the reduced *H*-atoms of the next (neighbour) unit cell escape as a volatile phase.

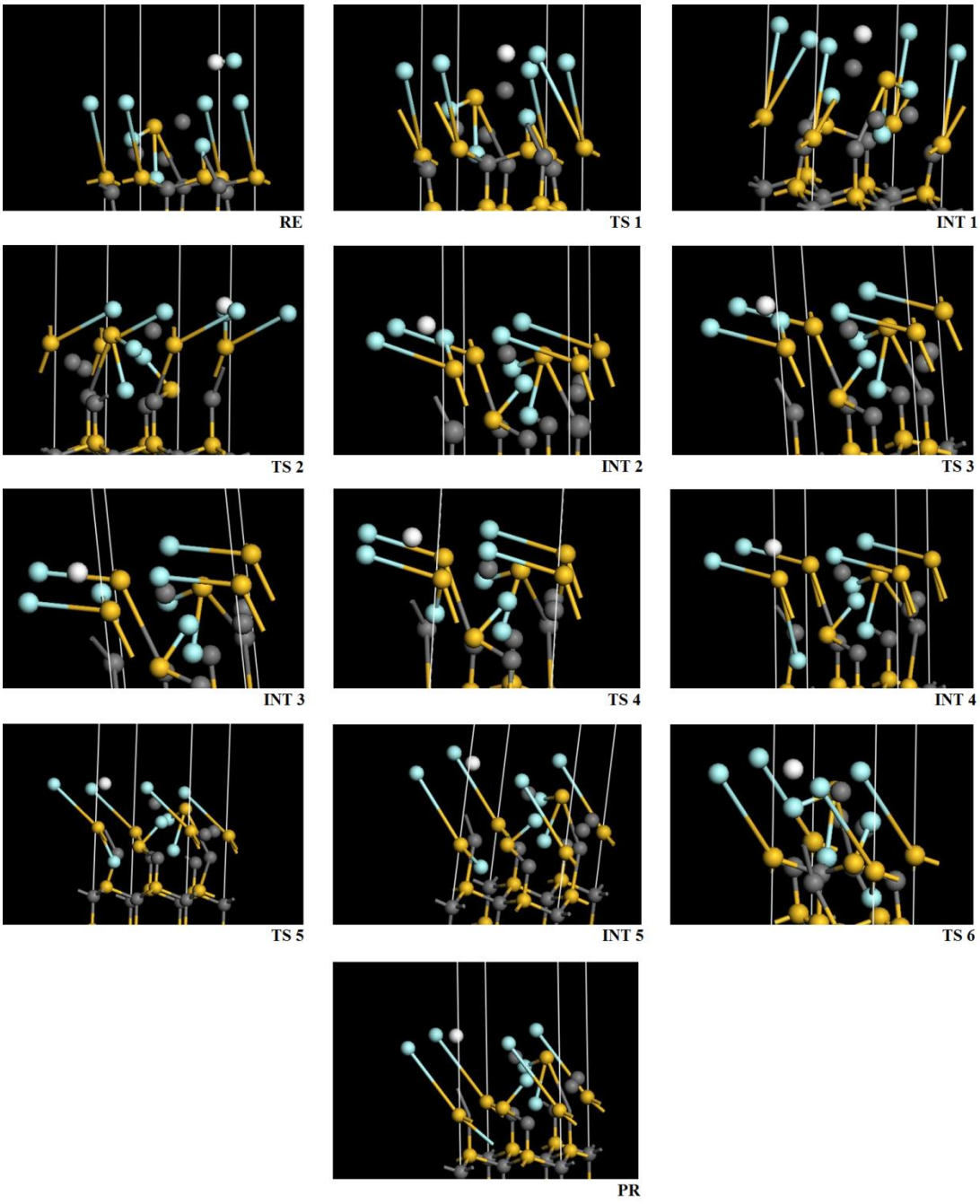

Figure *S* 20. SiF_2 group formation for the second *SiC* bi-layer is demonstrated. The 17th *F*-atom is added. RE – reactant, TS – transition states, INT – interim products, PR – product. The *Si* – *F* interaction by breaking S*i* – *C* bonds between the *Si*-atoms (yellow) and *C*-atoms (grey) of the second *SiC* substrate bi-layer is shown. *C*-atoms are oxidised from -3 to -2. *F*-atoms (blue) are connected in the SiF_2 clusters. The reduced *H*-atoms (white) while connecting with the reduced *H*-atoms of the next (neighbour) unit cell escape as a volatile phase.

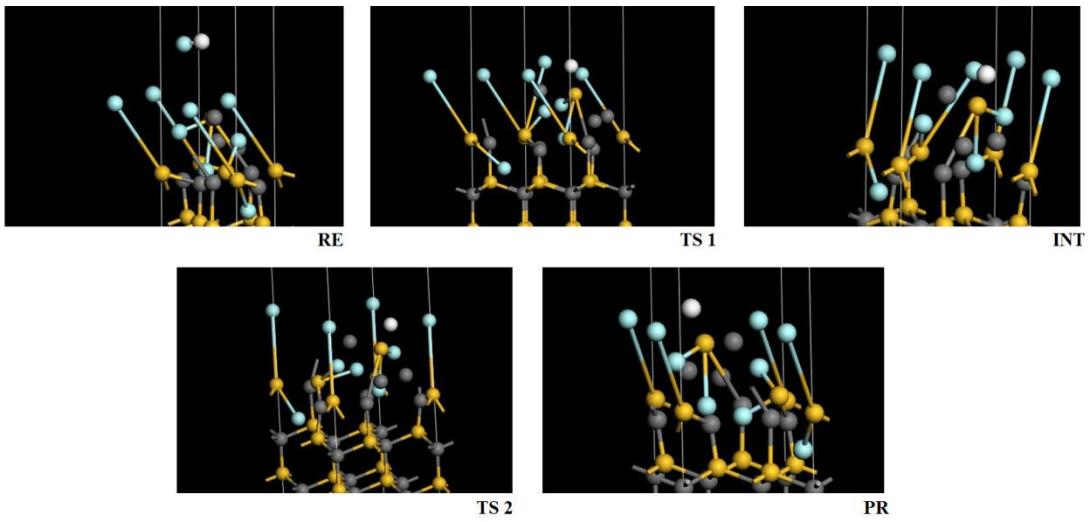

Figure *S* 21. SiF_2 group formation for the second *SiC* bi-layer is demonstrated. The 18th *F*-atom is added. RE – reactant, TS – transition states, INT – interim product, PR – product. The *Si* – *F* interaction by breaking S*i* – *C* bonds between the *Si*-atoms (yellow) and *C*-atoms (grey) of the second *SiC* substrate bi-layer is shown. *C*-atoms are oxidised from -3 to -2. *F*-atoms (blue) are connected in the SiF_2 clusters. The reduced *H*-atoms (white) while connecting with the reduced *H*-atoms of the next (neighbour) unit cell escape as a volatile phase.

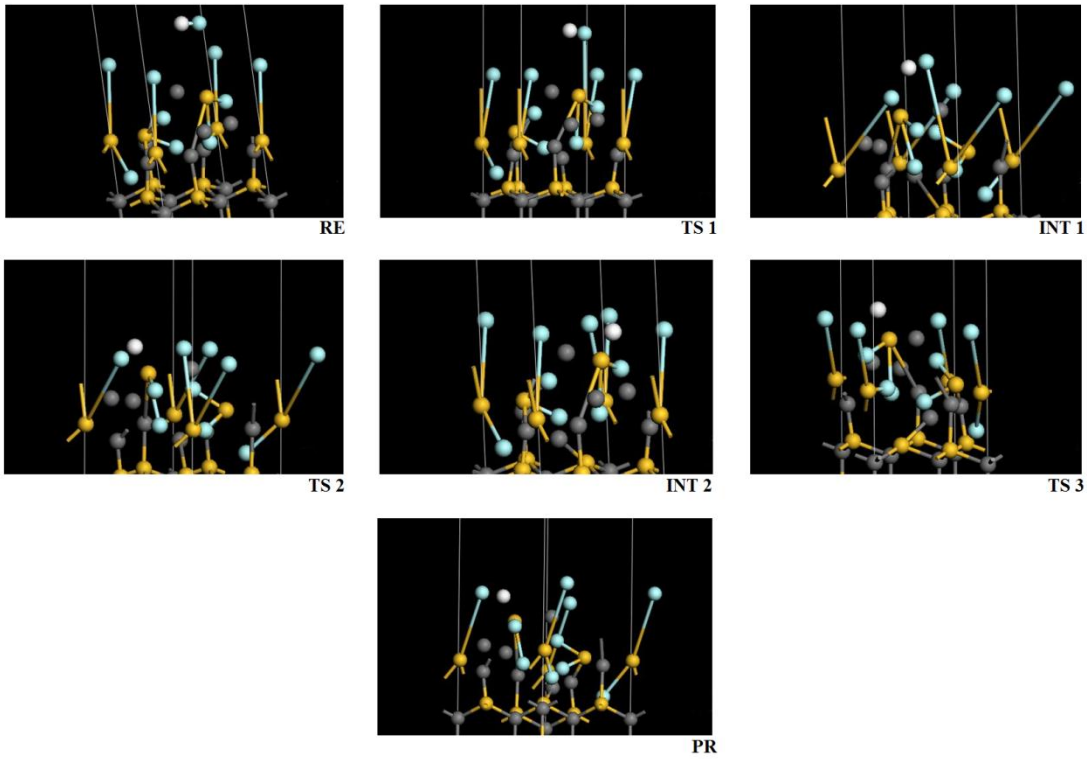

Figure *S* 22. SiF_3 group formation for the second *SiC* bi-layer is demonstrated. The 19th *F*-atom is added. RE – reactant, TS – transition states, INT – interim products, PR – product. The *Si* – *F* interaction by breaking S*i* – *C* bonds between the *Si*-atoms (yellow) and *C*-atoms (grey) of the second *SiC* substrate bi-layer is shown. *C*-atoms are oxidised from -2 to -1. *F*-atoms (blue) are connected in the SiF_3 clusters. The reduced *H*-atoms (white) while connecting with the reduced *H*-atoms of the next (neighbour) unit cell escape as a volatile phase.

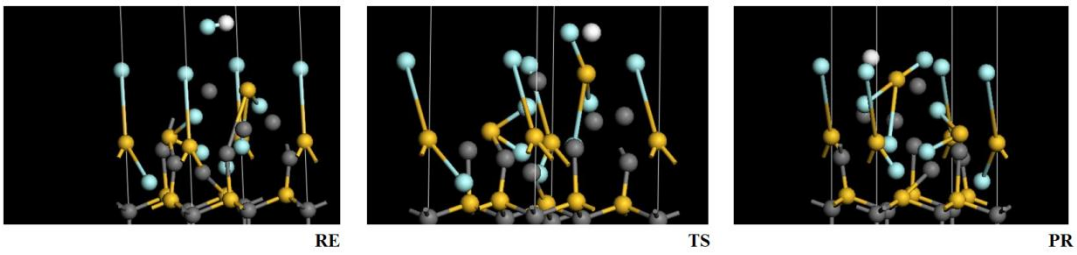

Figure *S* 23. SiF_3 group formation for the second *SiC* bi-layer is demonstrated. The 20th *F*-atom is added. RE – reactant, TS – transition state, PR – product. The *Si* – *F* interaction by breaking S*i* – *C* bonds between the *Si*-atoms (yellow) and *C*-atoms (grey) of the second *SiC* substrate bi-layer is shown. *C*-atoms are oxidised from -2 to -1. *F*-atoms (blue) are connected in the SiF_3 clusters. The reduced *H*-atoms (white) while connecting with the reduced *H*-atoms of the next (neighbour) unit cell escape as a volatile phase.

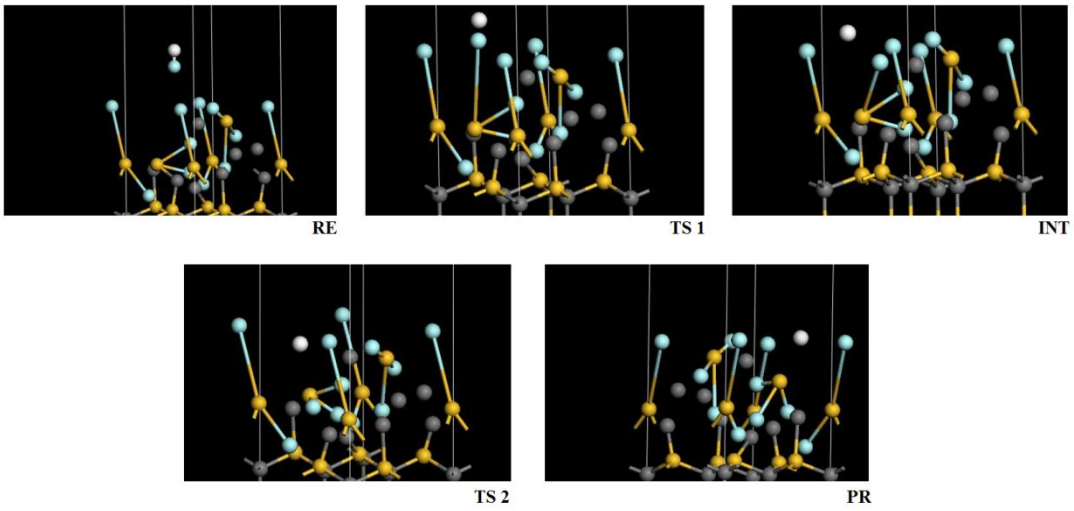

Figure *S* 24. SiF_3 group formation for the second *SiC* bi-layer is demonstrated. The 21st *F*-atom is added. RE – reactant, TS – transition states, INT – interim product, PR – product. The *Si* – *F* interaction by breaking S*i* – *C* bonds between the *Si*-atoms (yellow) and *C*-atoms (grey) of the second *SiC* substrate bi-layer is shown. *C*-atoms are oxidised from -2 to -1. *F*-atoms (blue) are connected in the SiF_3 clusters. The reduced *H*-atoms (white) while connecting with the reduced *H*-atoms of the next (neighbour) unit cell escape as a volatile phase.

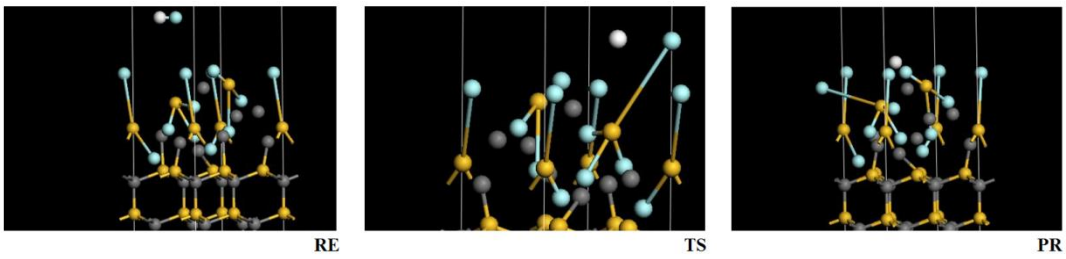

Figure *S* 25. SiF_4 molecules formation for the second *SiC* bi-layer is demonstrated. The 22nd *F*-atom is added. RE – reactant, TS – transition state, PR – product. The *Si* – *F* interaction by breaking S*i* – *C* bonds between the *Si*-atoms (yellow) and *C*-atoms (grey) of the second *SiC* substrate bi-layer is shown. *C*-atoms are oxidised from -1 to 0. Amorphous carbon is obtained. *F*-atoms (blue) are connected in the SiF_4 molecules. The SiF_4 molecules escape as a volatile phase. The reduced *H*-atoms (white) while connecting with the reduced *H*-atoms of the next (neighbour) unit cell escape as a volatile phase.

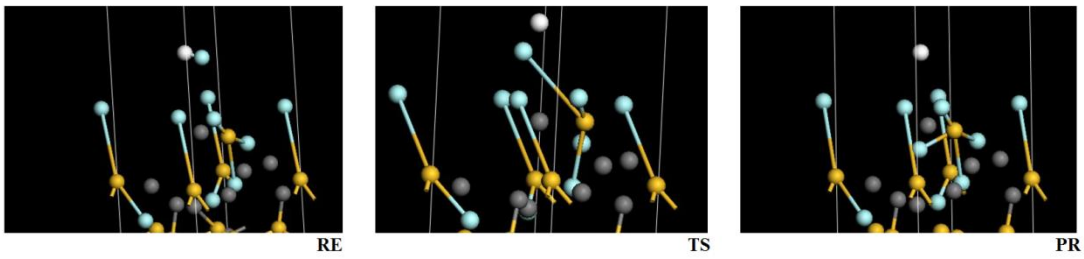

Figure *S* 26. SiF_4 molecules formation for the second *SiC* bi-layer is demonstrated. The 23rd *F*-atom is added. RE – reactant, TS – transition state, PR – product. The *Si* – *F* interaction by breaking S*i* – *C* bonds between the *Si*-atoms (yellow) and *C*-atoms (grey) of the second *SiC* substrate bi-layer is shown. *C*-atoms are oxidised from -1 to 0. Amorphous carbon is obtained. *F*-atoms (blue) are connected in the SiF_4 molecules. The SiF_4 molecules escape as a volatile phase. The reduced *H*-atoms (white) while connecting with the reduced *H*-atoms of the next (neighbour) unit cell escape as a volatile phase.

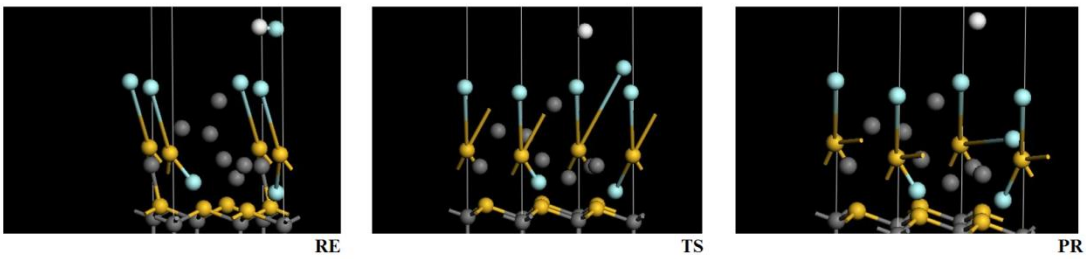

Figure *S* 27. SiF_4 molecules formation for the second *SiC* bi-layer is demonstrated. The 24th *F*-atom is added. RE – reactant, TS – transition state, PR – product. The *Si* – *F* interaction by breaking S*i* – *C* bonds between the *Si*-atoms (yellow) and *C*-atoms (grey) of the second *SiC* substrate bi-layer is shown. *C*-atoms are oxidised from -1 to 0. Amorphous carbon is obtained. *F*-atoms (blue) are connected in the SiF_4 molecules. The SiF_4 molecules escape as a volatile phase. The reduced *H*-atoms (white) while connecting with the reduced *H*-atoms of the next (neighbour) unit cell escape as a volatile phase.

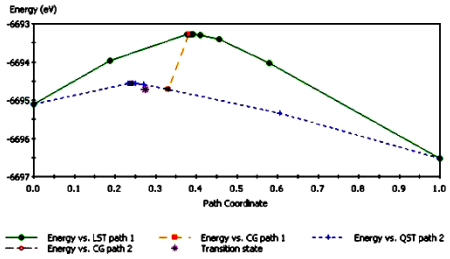

13

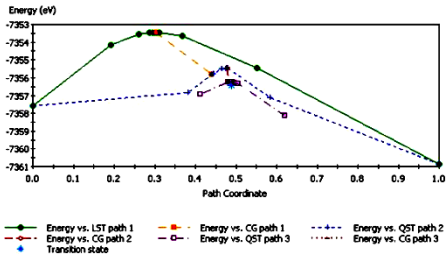

14

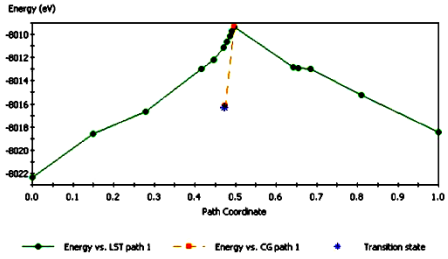

15

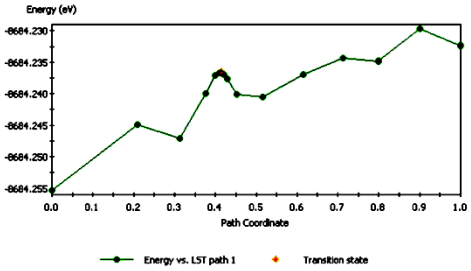

16_1

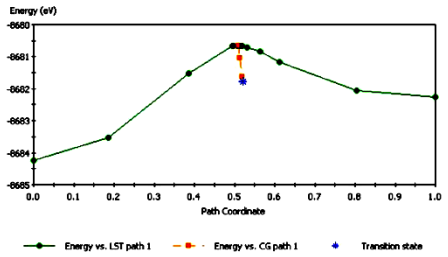

16_2

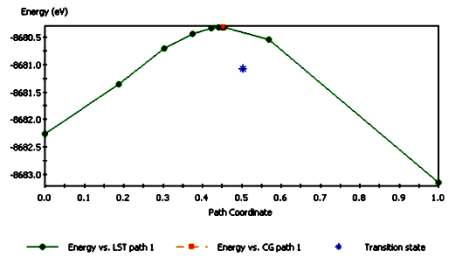

16_3

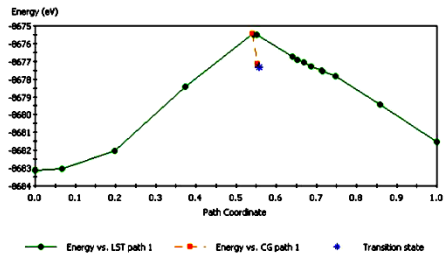

16_4

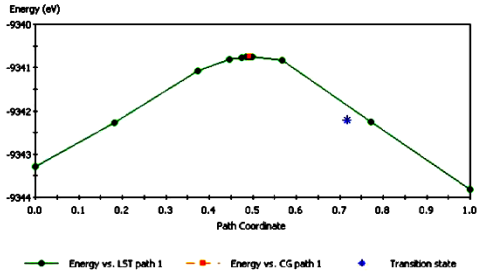

17_1

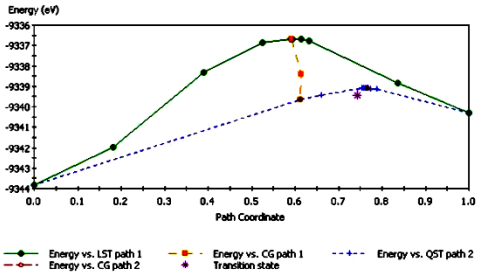

17_2

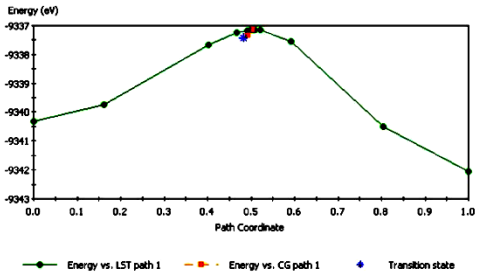

17_3

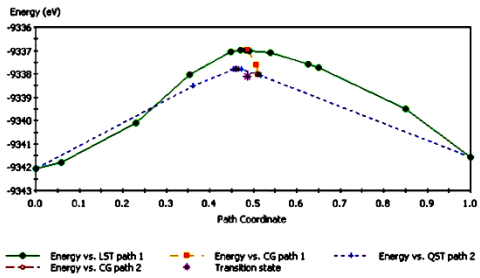

17_4

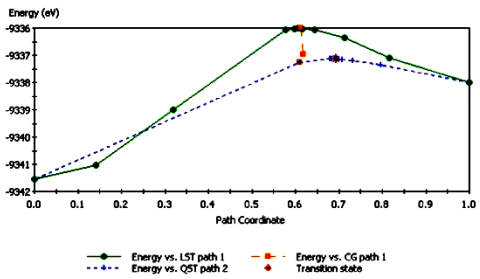

17_5

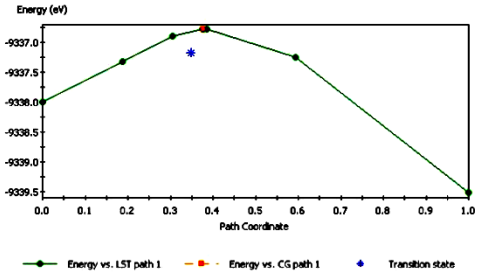

17_6

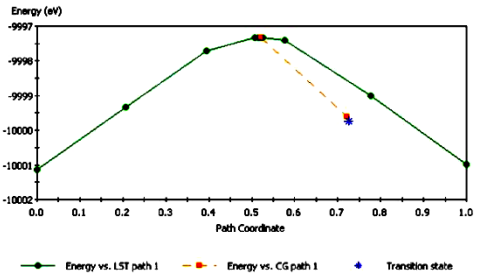

18_1

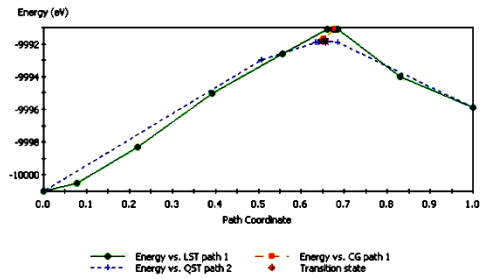

18_2

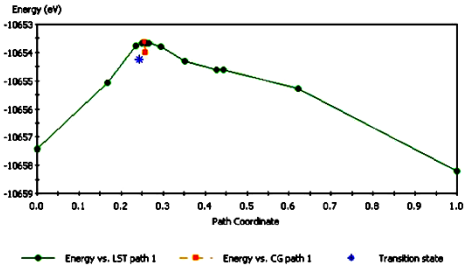

19_1

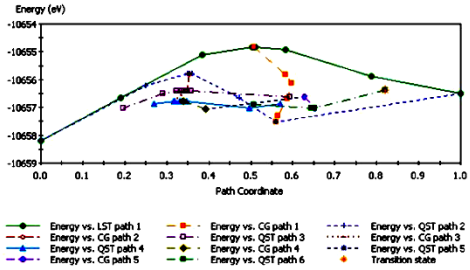

19_2

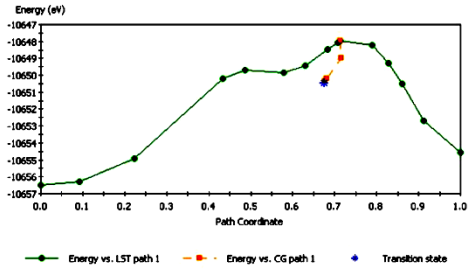

19_3

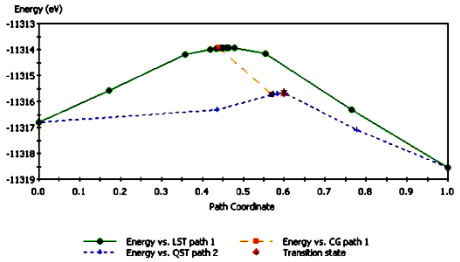

20

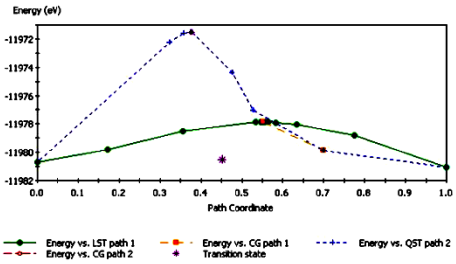

21_1

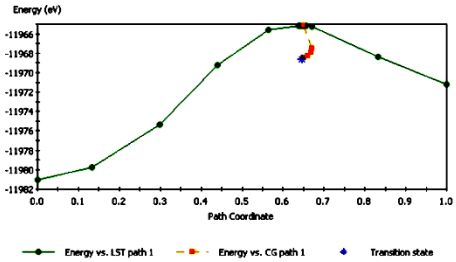

21_2

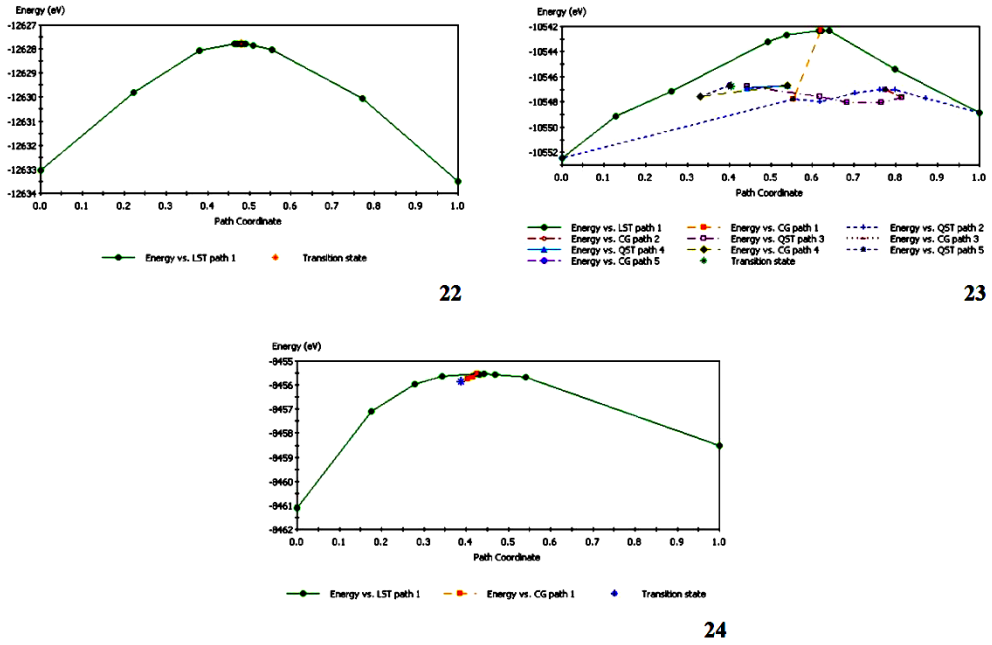

Figure *S* 28. Transition State diagrams for the second *SiC* bi-layer destruction are placed. The next twelve *F*-atoms are settled through the successive SiF_x groups by etching three *Si*-atoms of the (0001) - $\left(\sqrt{3}\times\sqrt{3}\right)R30°$ unit cell. The energy values are continuously decreased as propagation from *SiF* to SiF_4 groups and immediately return to initial value as the volatile phase escapes. The most complicated adjustment occurs for the SiF_2 and SiF_3 clusters including nine and three interim products respectively.

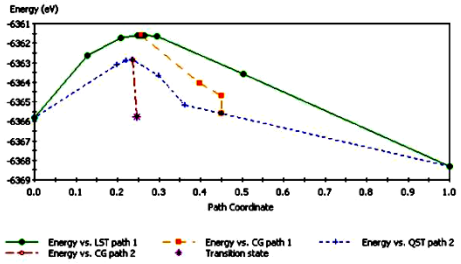

25

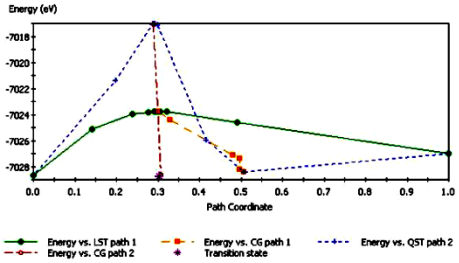

26

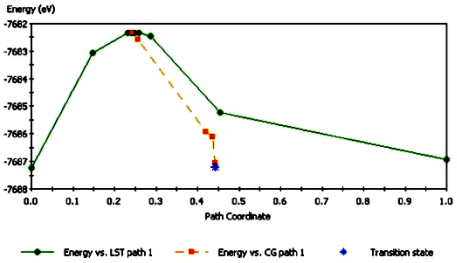

27

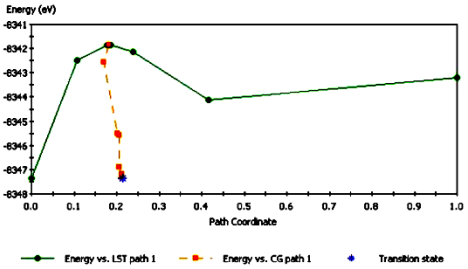

28

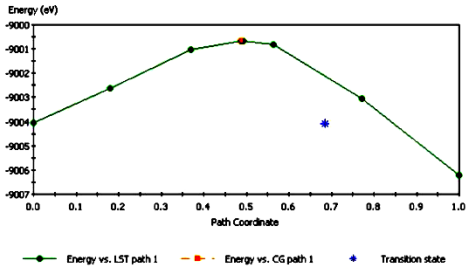

29_1

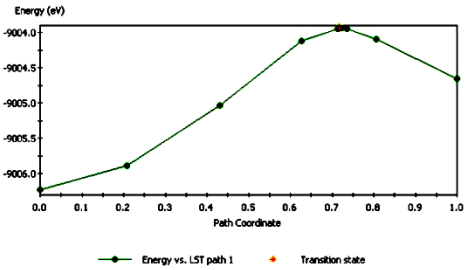

29_2

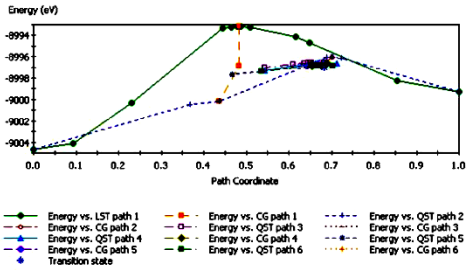

29_3

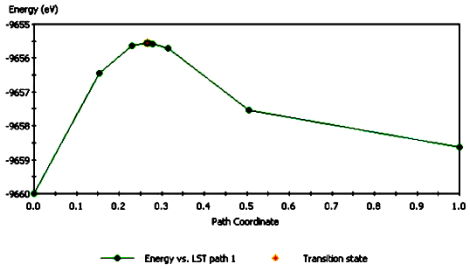

30

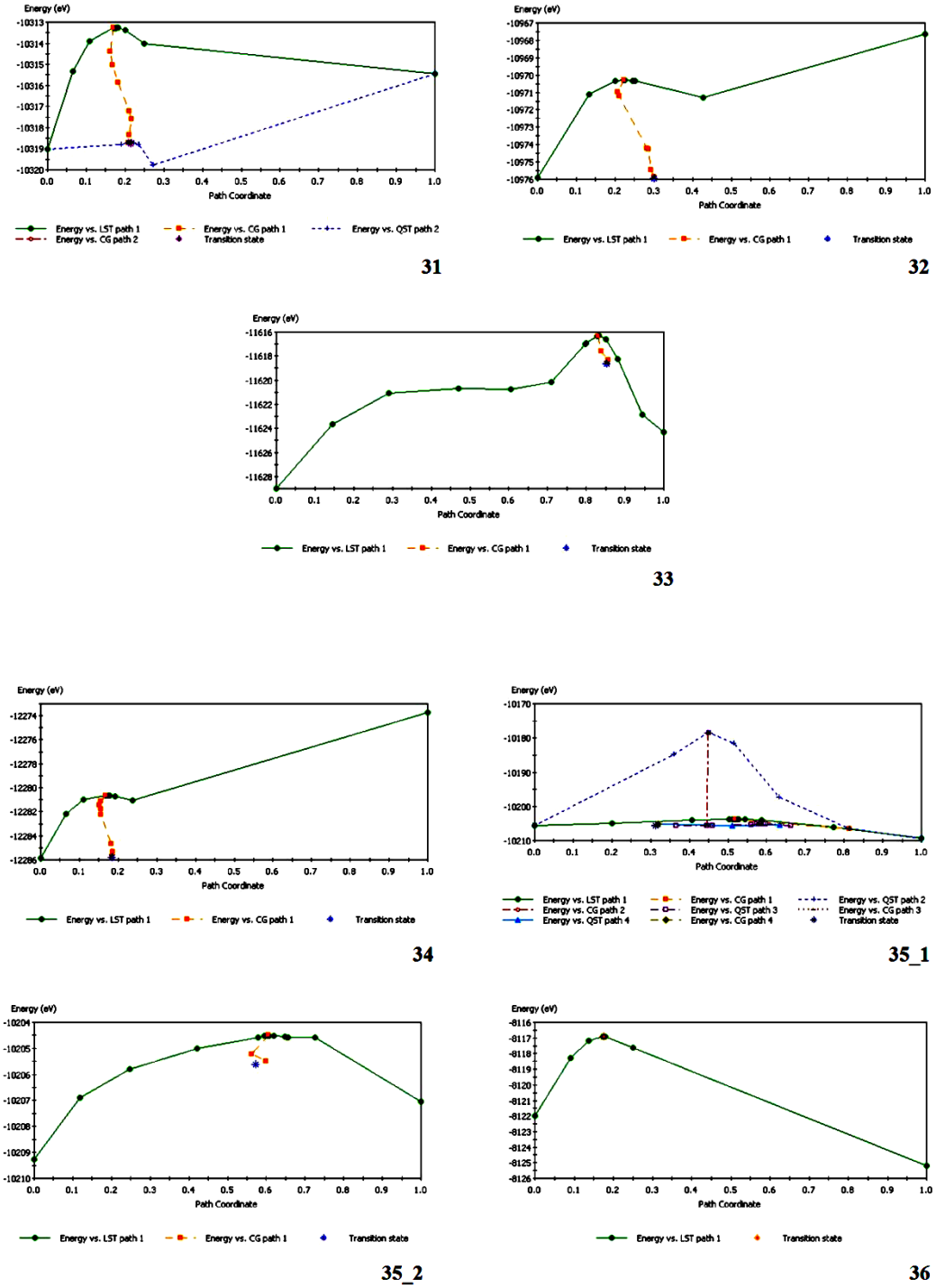

Figure *S* 29. Transition State diagrams for the third *SiC* bi-layer destruction are placed. Transition States while the (0001) - $\left(\sqrt{3}\times\sqrt{3}\right)R30°$ unit cell etching under *Si – F* interaction are shown. Transition State energy values decrease as the SiF_x propagation towards the volatile SiF_4 molecules. The Transition State location is traced in the highest path coordinate region for the SiF_3 group and returns to the initial minimal path coordinate region after the SiF_4 molecules escape.

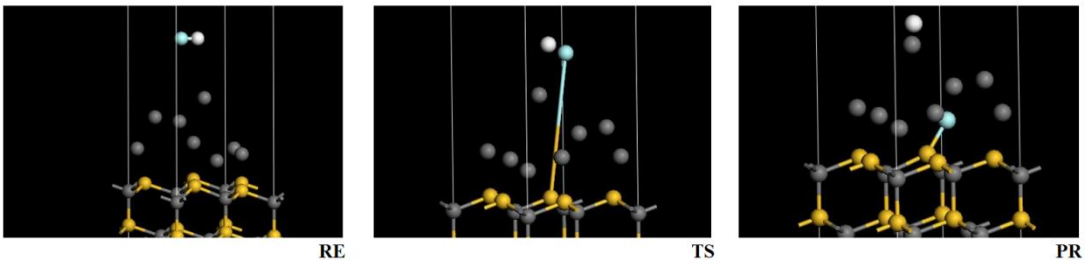

Figure *S* 30. *SiF* group formation for the third *SiC* bi-layer is demonstrated. The 25th *F*-atom is added. RE – reactant, TS – transition state, PR – product. The *Si* – *F* interaction by breaking S*i* – *C* bonds between the *Si*-atoms (yellow) and *C*-atoms (grey) of the third *SiC* substrate bi-layer is shown. *C*-atoms are oxidised from -4 to -3. *F*-atoms (blue) are connected in the *SiF* clusters. The reduced *H*-atoms (white) while connecting with the reduced *H*-atoms of the next (neighbour) unit cell escape as a volatile phase.

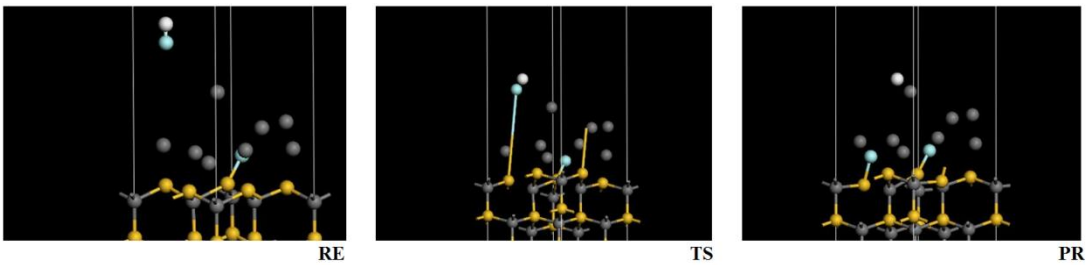

Figure *S* 31. *SiF* group formation for the third *SiC* bi-layer is demonstrated. The 26th *F*-atom is added. RE – reactant, TS – transition state, PR – product. The *Si* – *F* interaction by breaking S*i* – *C* bonds between the *Si*-atoms (yellow) and *C*-atoms (grey) of the third *SiC* substrate bi-layer is shown. *C*-atoms are oxidised from -4 to -3. *F*-atoms (blue) are connected in the *SiF* clusters. The reduced *H*-atoms (white) while connecting with the reduced *H*-atoms of the next (neighbour) unit cell escape as a volatile phase.

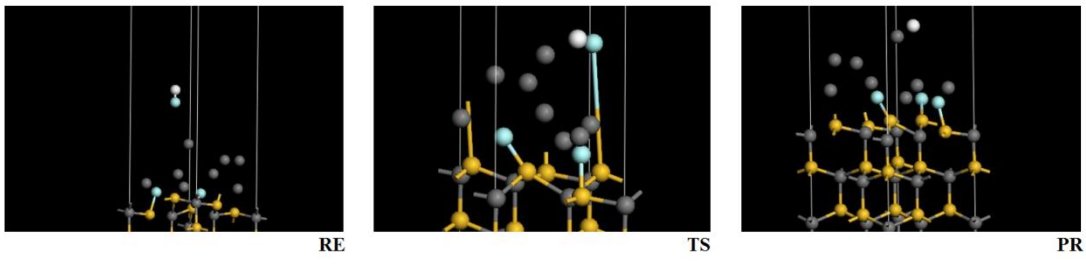

Figure *S* 32. *SiF* group formation for the third *SiC* bi-layer is demonstrated. The 27th *F*-atom is added. RE – reactant, TS – transition state, PR – product. The *Si* – *F* interaction by breaking S*i* – *C* bonds between the *Si*-atoms (yellow) and *C*-atoms (grey) of the third *SiC* substrate bi-layer is shown. *C*-atoms are oxidised from -4 to -3. *F*-atoms (blue) are connected in the *SiF* clusters. The reduced *H*-atoms (white) while connecting with the reduced *H*-atoms of the next (neighbour) unit cell escape as a volatile phase.

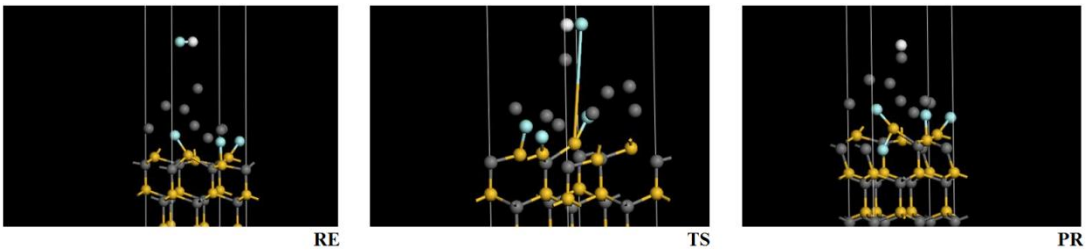

Figure *S* 33. SiF_2 group formation for the third *SiC* bi-layer is demonstrated. The 28th *F*-atom is added. RE – reactant, TS – transition state, PR – product. The *Si* – *F* interaction by breaking S*i* – *C* bonds between the *Si*-atoms (yellow) and *C*-atoms (grey) of the third *SiC* substrate bi-layer is shown. *C*-atoms are oxidised from -3 to -2. *F*-atoms (blue) are connected in the SiF_2 clusters. The reduced *H*-atoms (white) while connecting with the reduced *H*-atoms of the next (neighbour) unit cell escape as a volatile phase.

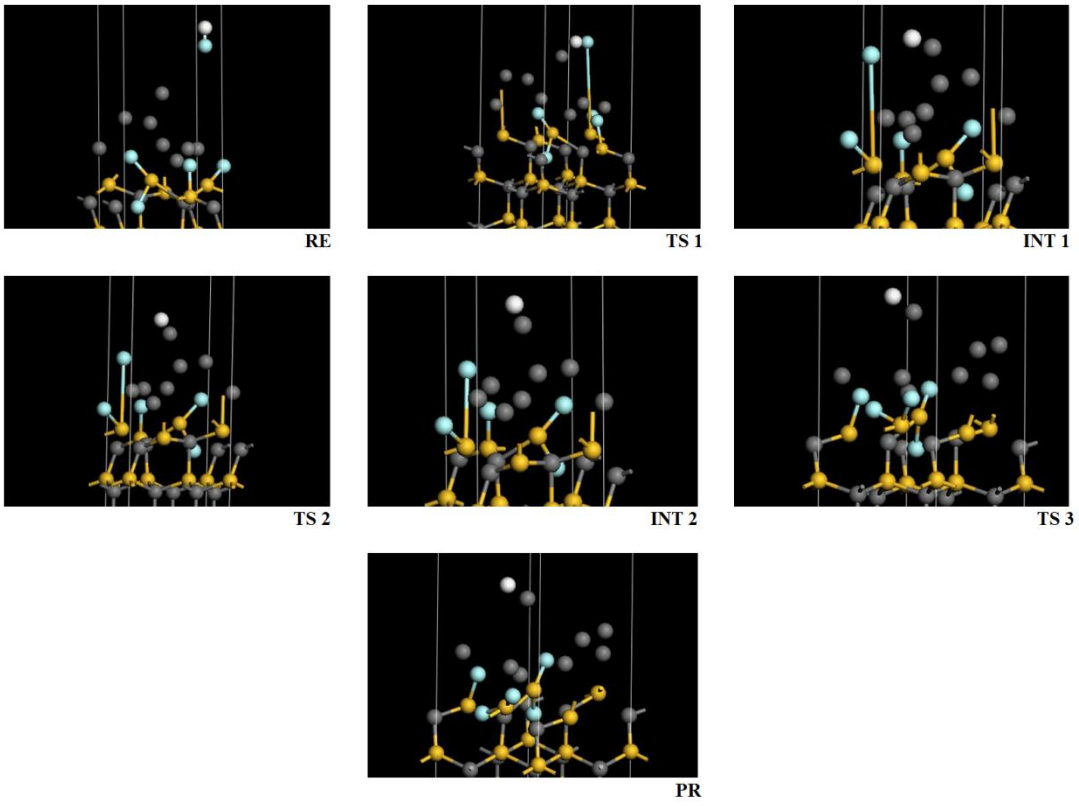

Figure *S* 34. SiF_2 group formation for the third *SiC* bi-layer is demonstrated. The 29th *F*-atom is added. RE – reactant, TS – transition states, INT – interim products, PR – product. The *Si* – *F* interaction by breaking S*i* – *C* bonds between the *Si*-atoms (yellow) and *C*-atoms (grey) of the third *SiC* substrate bi-layer is shown. *C*-atoms are oxidised from -3 to -2. *F*-atoms (blue) are connected in the SiF_2 clusters. The reduced *H*-atoms (white) while connecting with the reduced *H*-atoms of the next (neighbour) unit cell escape as a volatile phase.

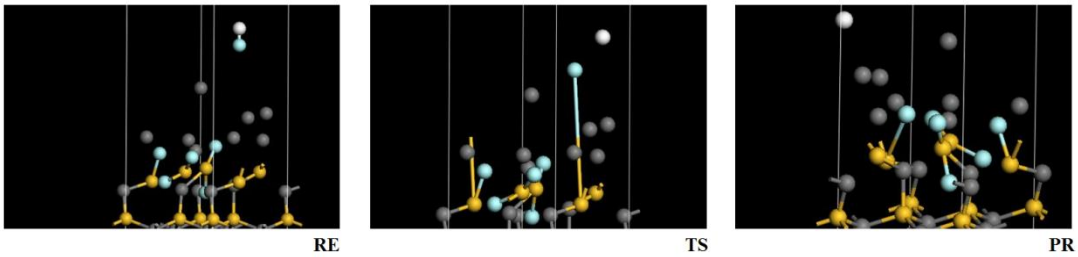

Figure *S* 35. SiF_2 group formation for the third *SiC* bi-layer is demonstrated. The 30th *F*-atom is added. RE – reactant, TS – transition state, PR – product. The *Si* – *F* interaction by breaking S*i* – *C* bonds between the *Si*-atoms (yellow) and *C*-atoms (grey) of the third *SiC* substrate bi-layer is shown. *C*-atoms are oxidised from -3 to -2. *F*-atoms (blue) are connected in the SiF_2 clusters. The reduced *H*-atoms (white) while connecting with the reduced *H*-atoms of the next (neighbour) unit cell escape as a volatile phase.

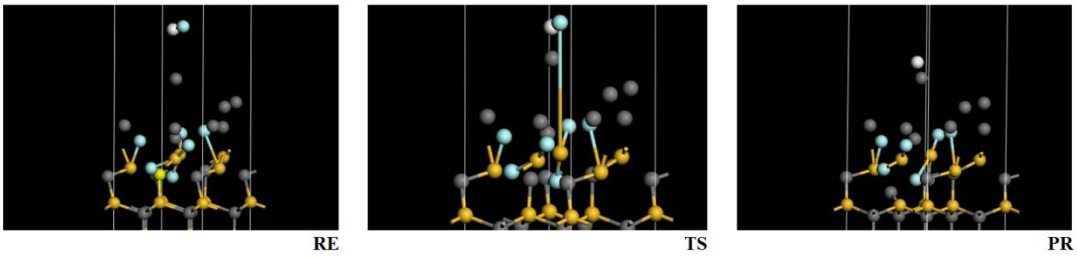

Figure *S* 36. SiF_3 group formation for the third *SiC* bi-layer is demonstrated. The 31st *F*-atom is added. RE – reactant, TS – transition state, PR – product. The *Si* – *F* interaction by breaking S*i* – *C* bonds between the *Si*-atoms (yellow) and *C*-atoms (grey) of the third *SiC* substrate bi-layer is shown. *C*-atoms are oxidised from -2 to -1. *F*-atoms (blue) are connected in the SiF_3 clusters. The reduced *H*-atoms (white) while connecting with the reduced *H*-atoms of the next (neighbour) unit cell escape as a volatile phase.

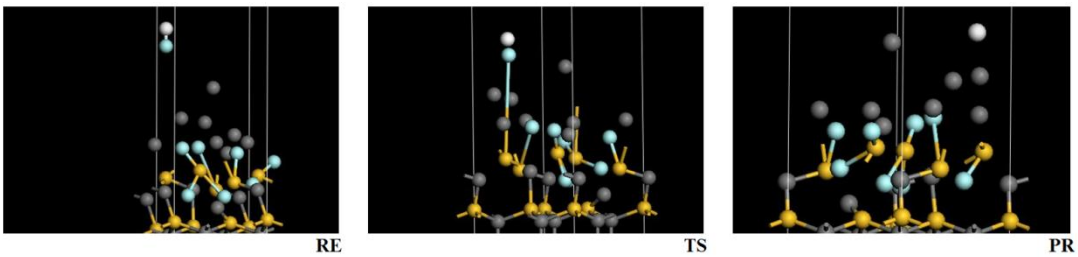

Figure *S* 37. SiF_3 group formation for the third *SiC* bi-layer is demonstrated. The 32nd *F*-atom is added. RE – reactant, TS – transition state, PR – product. The *Si* – *F* interaction by breaking S*i* – *C* bonds between the *Si*-atoms (yellow) and *C*-atoms (grey) of the third *SiC* substrate bi-layer is shown. *C*-atoms are oxidised from -2 to -1. *F*-atoms (blue) are connected in the SiF_3 clusters. The reduced *H*-atoms (white) while connecting with the reduced *H*-atoms of the next (neighbour) unit cell escape as a volatile phase.

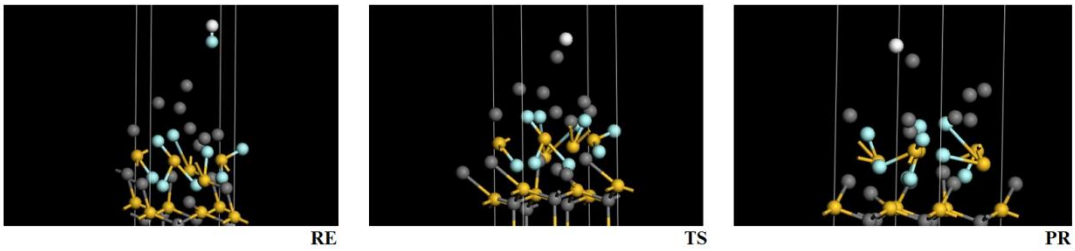

Figure *S* 38. SiF_3 group formation for the third *SiC* bi-layer is demonstrated. The 33rd *F*-atom is added. RE – reactant, TS – transition state, PR – product. The *Si* – *F* interaction by breaking S*i* – *C* bonds between the *Si*-atoms (yellow) and *C*-atoms (grey) of the third *SiC* substrate bi-layer is shown. *C*-atoms are oxidised from -2 to -1. *F*-atoms (blue) are connected in the SiF_3 clusters. The reduced *H*-atoms (white) while connecting with the reduced *H*-atoms of the next (neighbour) unit cell escape as a volatile phase.

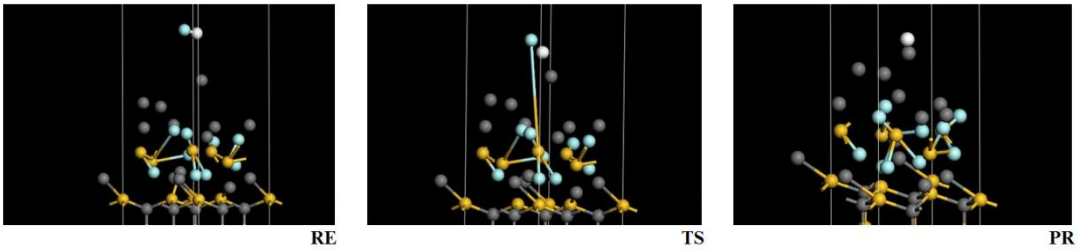

Figure *S* 39. SiF_4 molecules formation for the third *SiC* bi-layer is demonstrated. The 34th *F*-atom is added. RE – reactant, TS – transition state, PR – product. The *Si* – *F* interaction by breaking S*i* – *C* bonds between the *Si*-atoms (yellow) and *C*-atoms (grey) of the third *SiC* substrate bi-layer is shown. *C*-atoms are oxidised from -1 to 0. Amorphous carbon is obtained. *F*-atoms (blue) are connected in the SiF_4 molecules. The SiF_4 molecules escape as a volatile phase. The reduced *H*-atoms (white) while connecting with the reduced *H*-atoms of the next (neighbour) unit cell escape as a volatile phase.

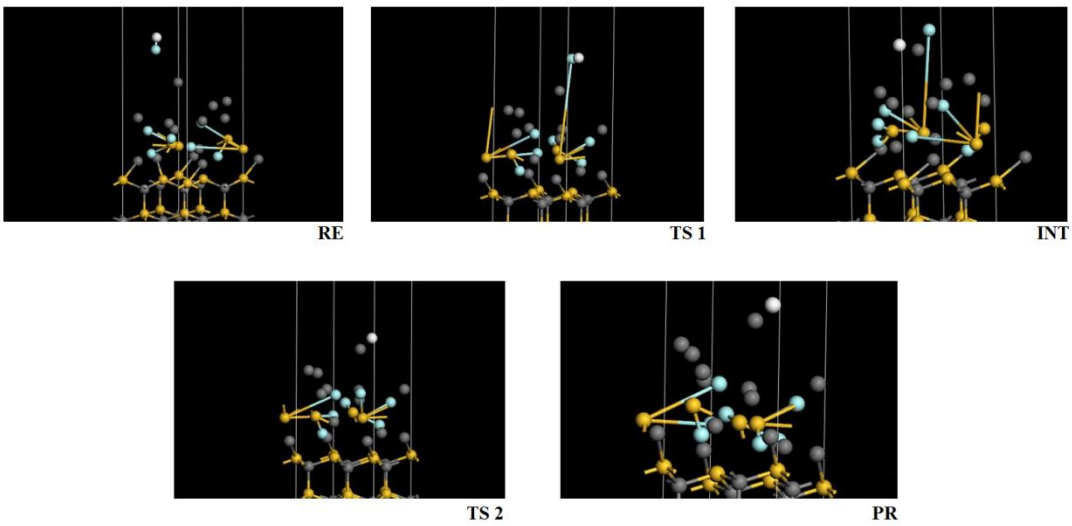

Figure *S* 40. SiF_4 molecules formation for the third *SiC* bi-layer is demonstrated. The 35th *F*-atom is added. RE – reactant, TS – transition states, INT – interim product, PR – product. The *Si* – *F* interaction by breaking S*i* – *C* bonds between the *Si*-atoms (yellow) and *C*-atoms (grey) of the third *SiC* substrate bi-layer is shown. *C*-atoms are oxidised from -1 to 0. Amorphous carbon is obtained. *F*-atoms (blue) are connected in the SiF_4 molecules. The SiF_4 molecules escape as a volatile phase. The reduced *H*-atoms (white) while connecting with the reduced *H*-atoms of the next (neighbour) unit cell escape as a volatile phase.

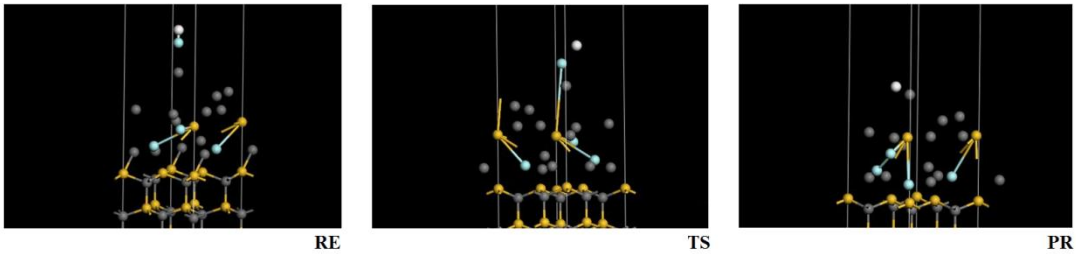

Figure *S* 41. SiF_4 molecules formation for the third *SiC* bi-layer is demonstrated. The 36th *F*-atom is added. RE – reactant, TS – transition state, PR – product. The *Si* – *F* interaction by breaking S*i* – *C* bonds between the *Si*-atoms (yellow) and *C*-atoms (grey) of the third *SiC* substrate bi-layer is shown. *C*-atoms are oxidised from -1 to 0. Amorphous carbon is obtained. *F*-atoms (blue) are connected in the SiF_4 molecules. The SiF_4 molecules escape as a volatile phase. The reduced *H*-atoms (white) while connecting with the reduced *H*-atoms of the next (neighbour) unit cell escape as a volatile phase.

Section 2

This section includes the explanatory illustrations for Chapter 9 concerning transformation of amorphous carbon into highly ordered graphene structure.

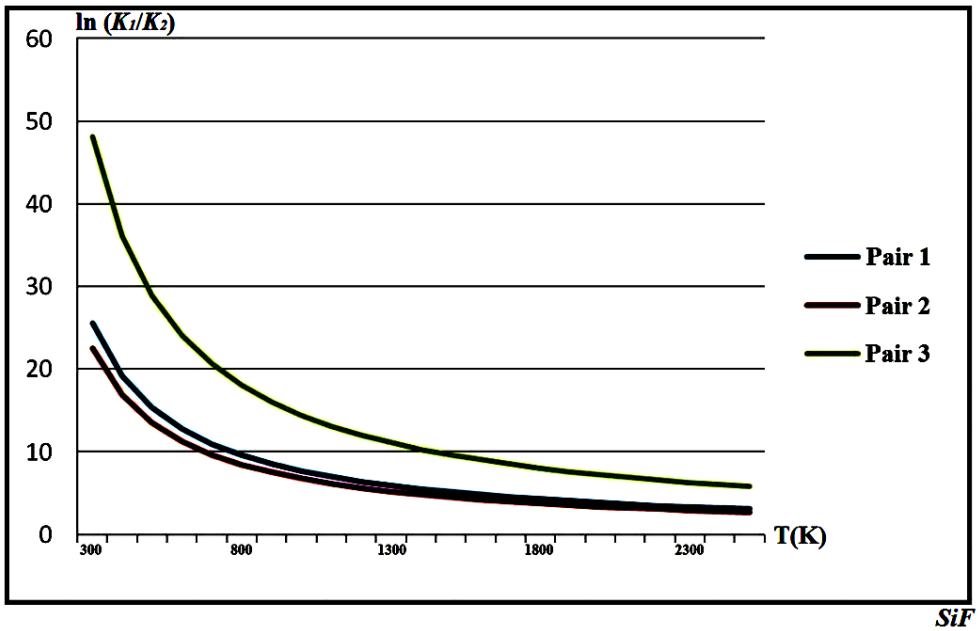
ln (K_1/K_2)
60
50
40
30
20
10
0
300
800
1300
1800
2300
T(K)
Pair 1
Pair 2
Pair 3

SiF

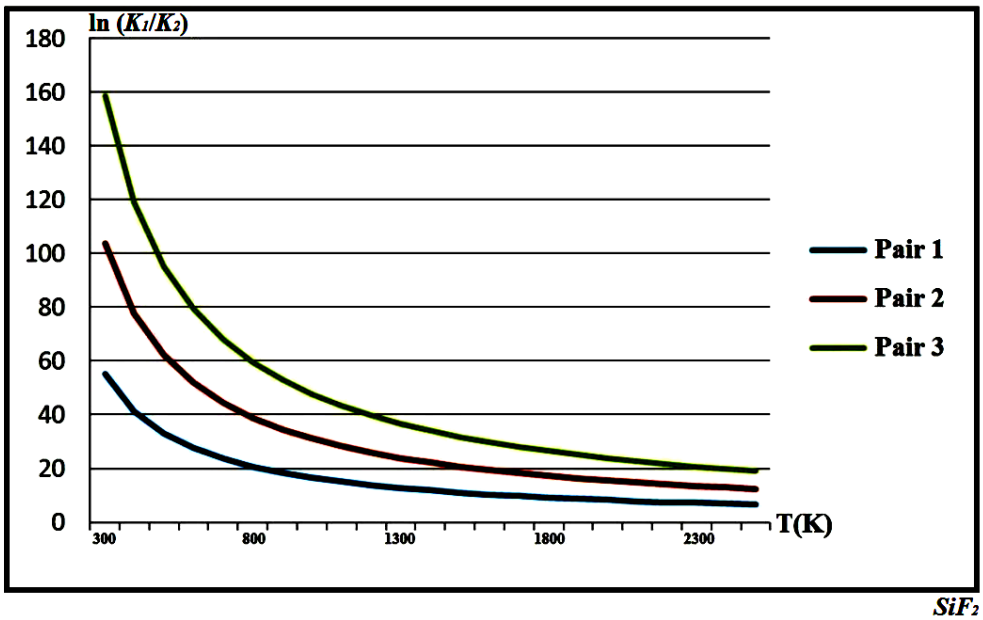
ln (K_1/K_2)
180
160
140
120
100
80
60
40
20
0
300
800
1300
1800
2300
T(K)
Pair 1
Pair 2
Pair 3

SiF_2

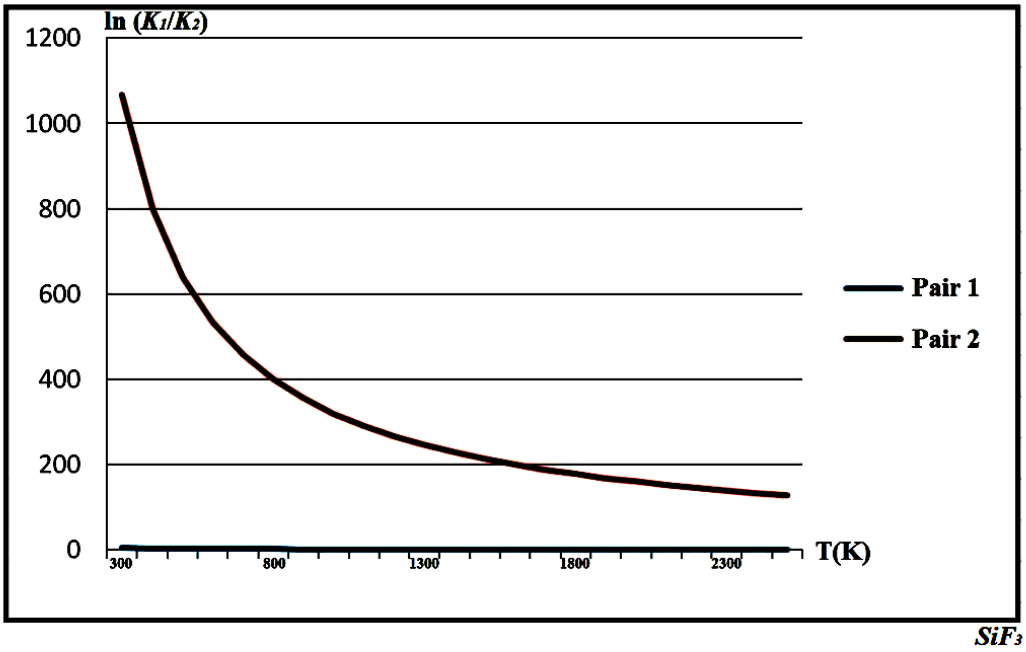

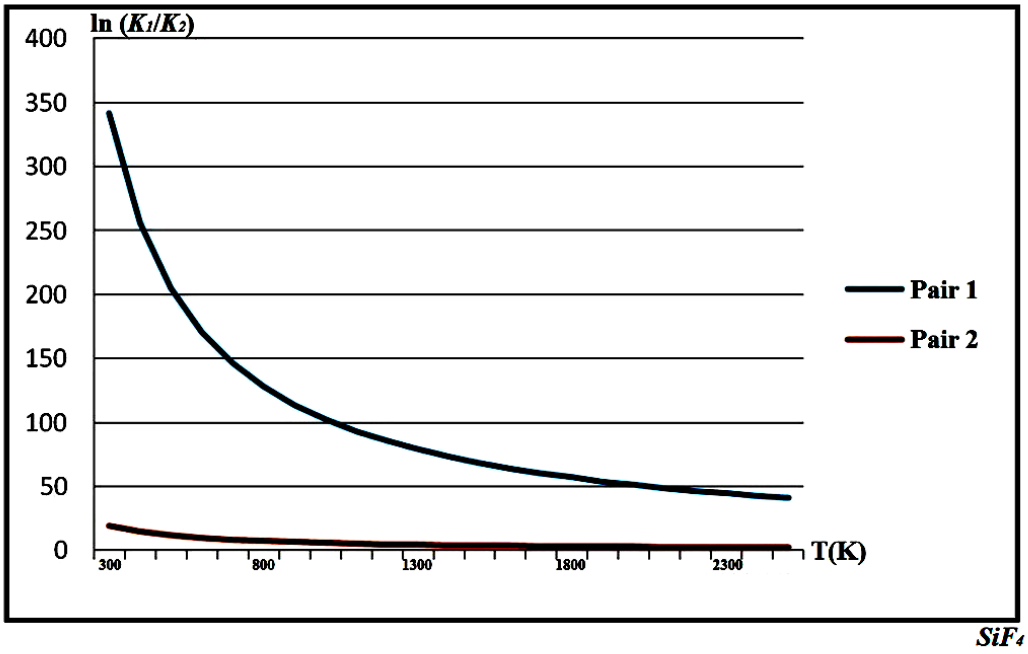

Figure S 42. Logarithm of rate constants ratio $ln\frac{K_1(T)}{K_2(T)}$ versus temperature is shown for the successive *SiF*, SiF_2, SiF_3 and SiF_4 group formations for the first *SiC* bi-layer. Temperature value of 300°K is taken as the initial point. The difference between the previous and next steps is equal to 100°. Gentle slope and steady rapprochement of different graphs start to appear from 1800°K. The best convergence is found for the *SiF* and SiF_4 groups.

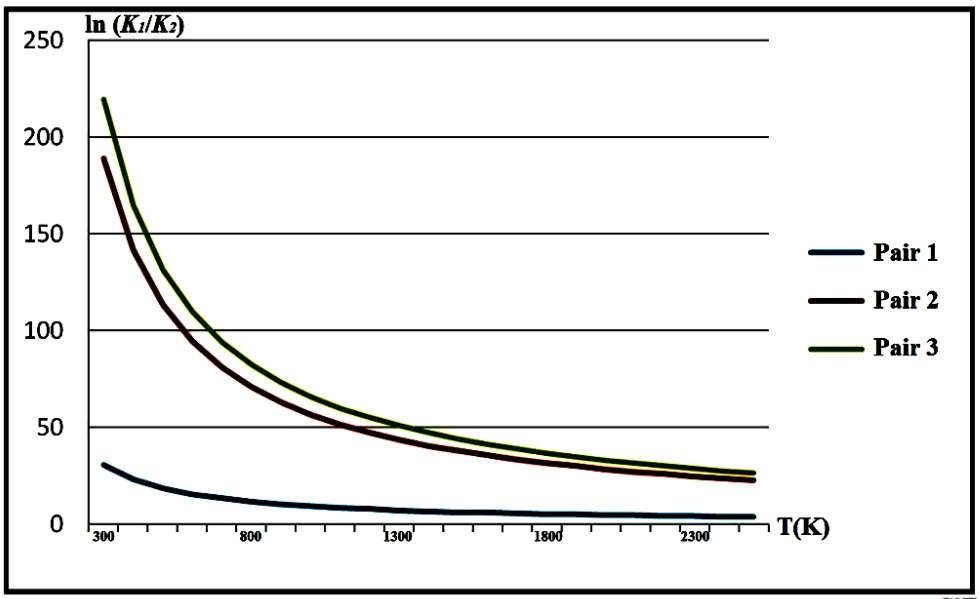
ln (K1/K2)
250
200
150
100
50
0
300
800
1300
1800
2300
T(K)
Pair 1
Pair 2
Pair 3

SiF

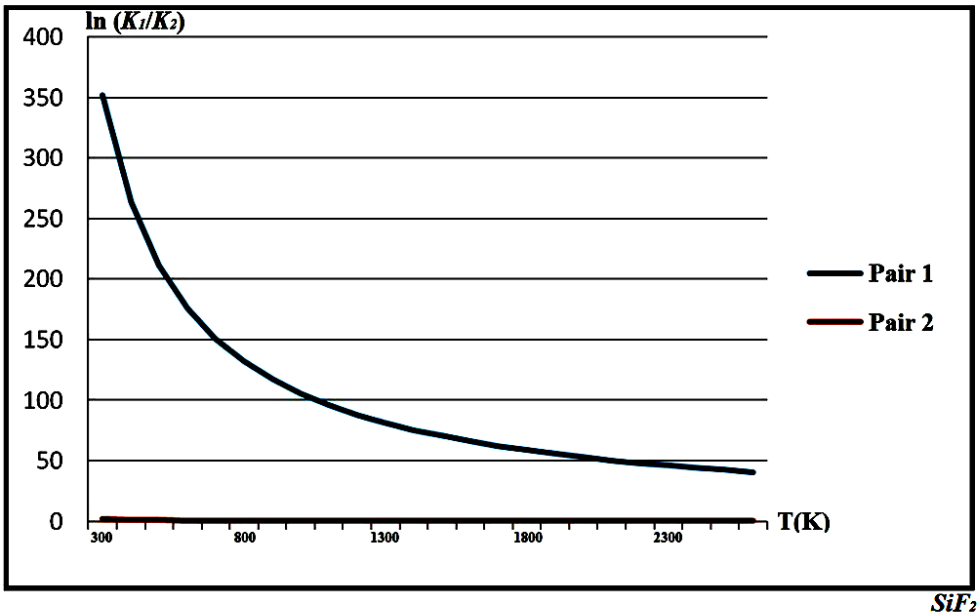
ln (K1/K2)
400
350
300
250
200
150
100
50
0
300
800
1300
1800
2300
T(K)
Pair 1
Pair 2

SiF₂

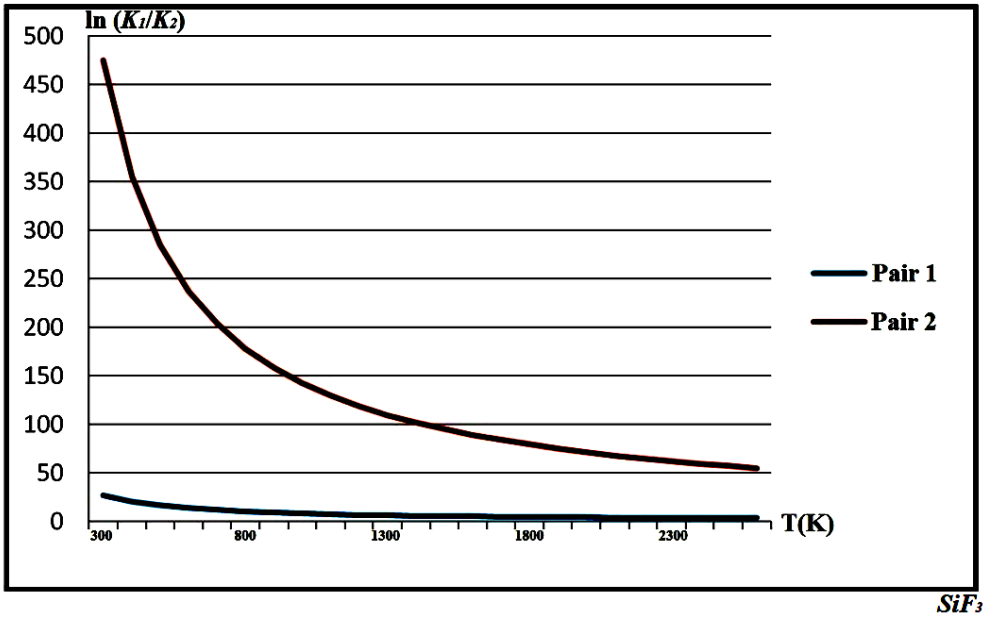

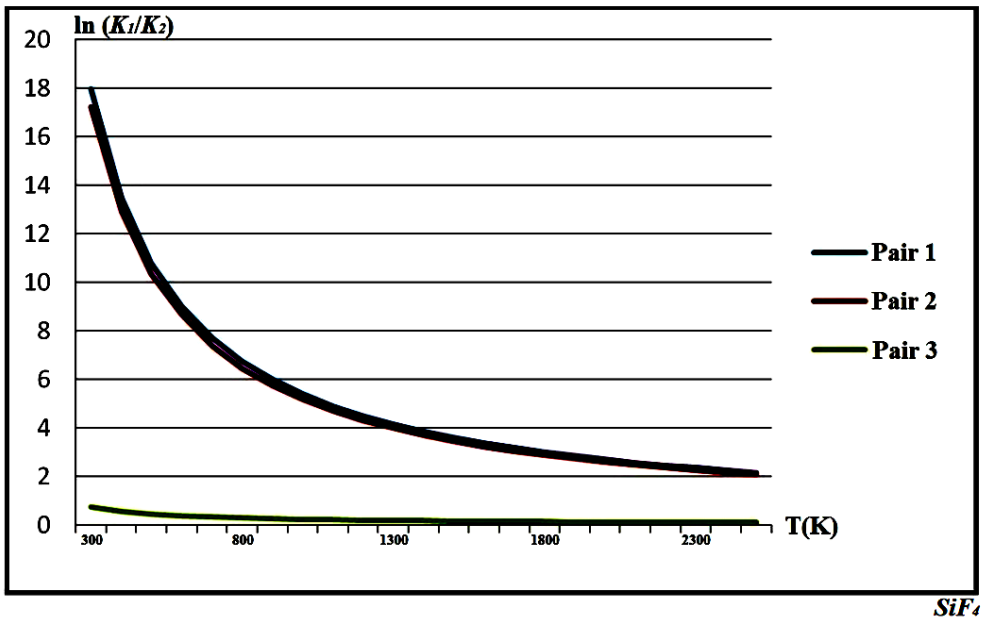

Figure S 43. Logarithm of rate constants ratio $ln\frac{K_1(T)}{K_2(T)}$ versus temperature is shown for the successive *SiF*, SiF_2, SiF_3 and SiF_4 group formations for the second *SiC* bi-layer. Temperature value of 300°K is taken as the initial point. The difference between the previous and next steps is equal to 100°. Gentle slope and steady rapprochement of different graphs start to appear from 1800°K. The best convergence is found for the *SiF* and SiF_4 groups.

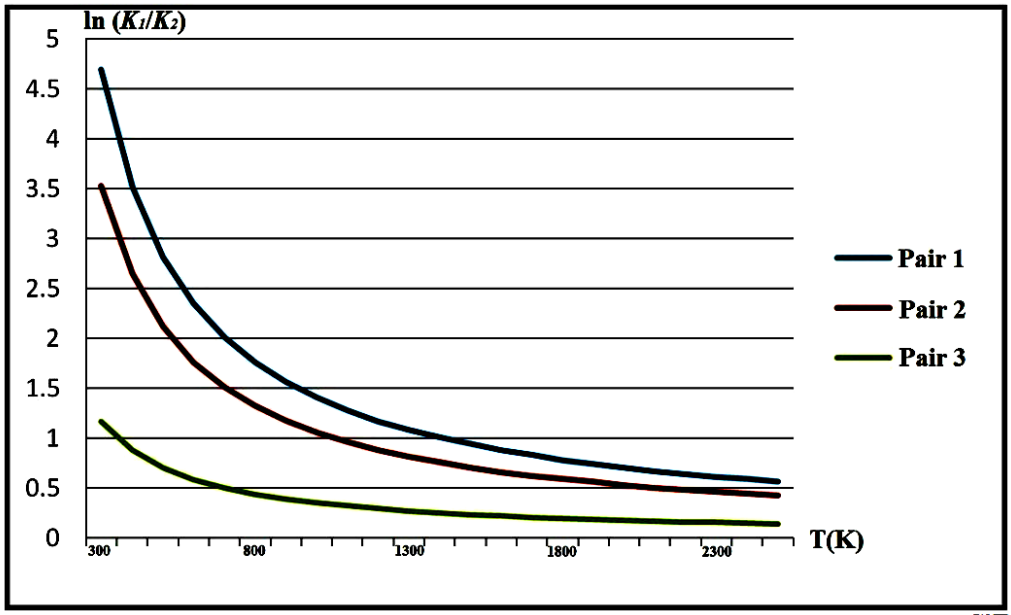
ln (K_1/K_2)
5
4.5
4
3.5
3
2.5
2
1.5
1
0.5
0
300
800
1300
1800
2300
T(K)
Pair 1
Pair 2
Pair 3

SiF

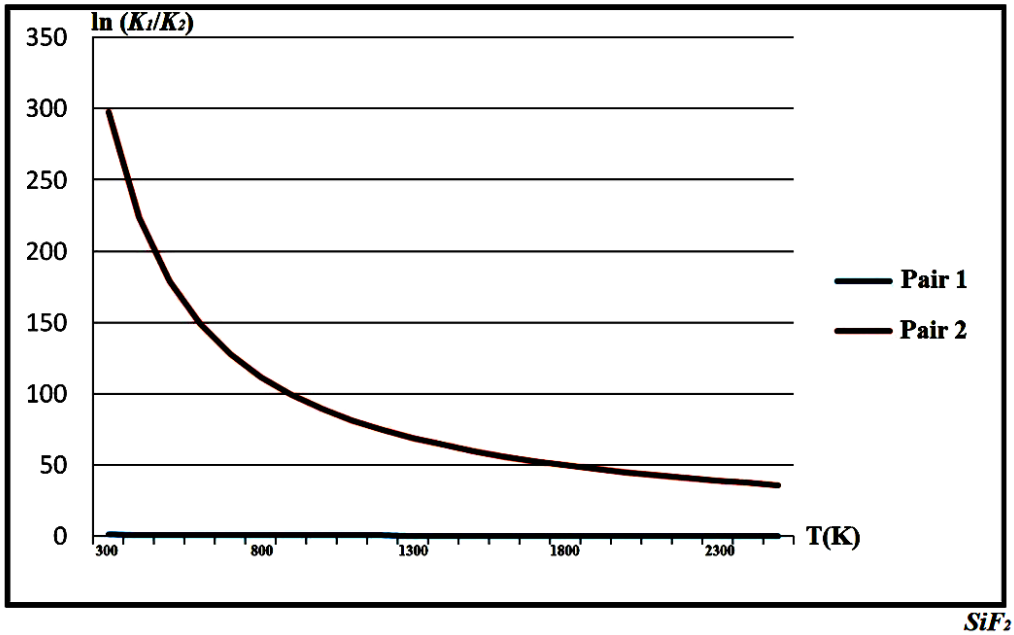
ln (K_1/K_2)
350
300
250
200
150
100
50
0
300
800
1300
1800
2300
T(K)
Pair 1
Pair 2

SiF₂

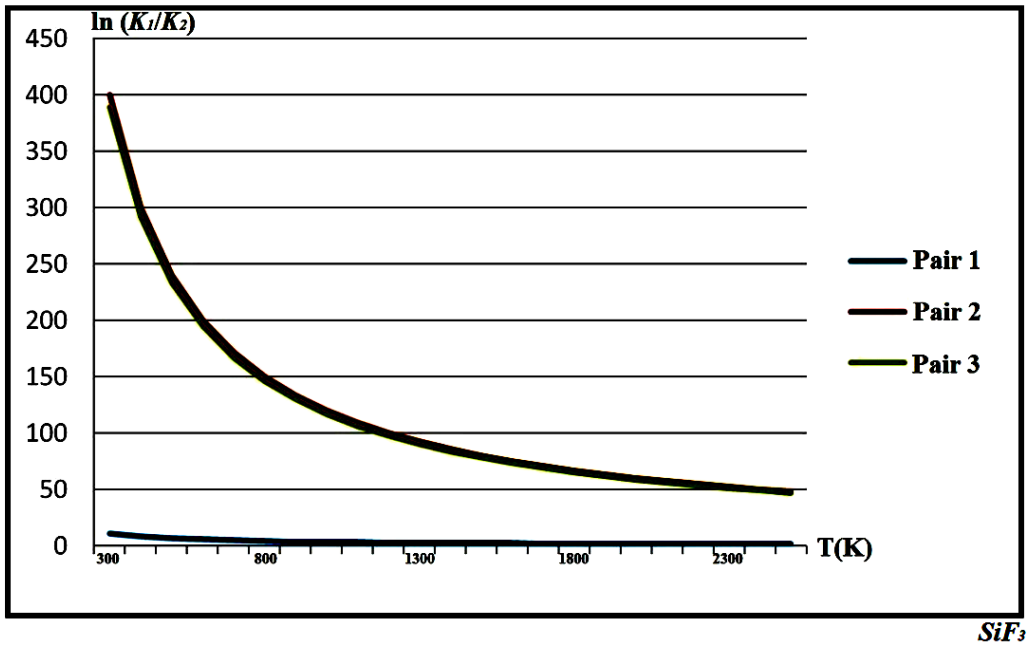

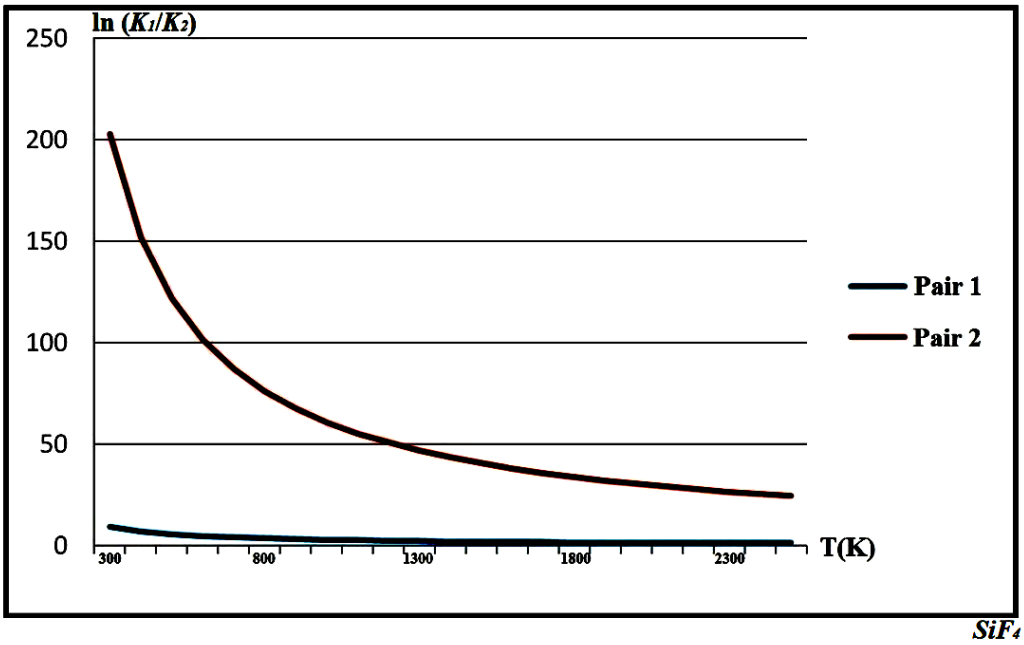

Figure S 44. Logarithm of rate constants ratio $ln\frac{K_1(T)}{K_2(T)}$ versus temperature is shown for the successive *SiF*, SiF_2, SiF_3 and SiF_4 group formations for the third *SiC* bi-layer. Temperature value of 300°K is taken as the initial point. The difference between the previous and next steps is equal to 100°. Gentle slope and steady rapprochement of different graphs start to appear from 1800°K. The best convergence is found for the *SiF* and SiF_4 groups.

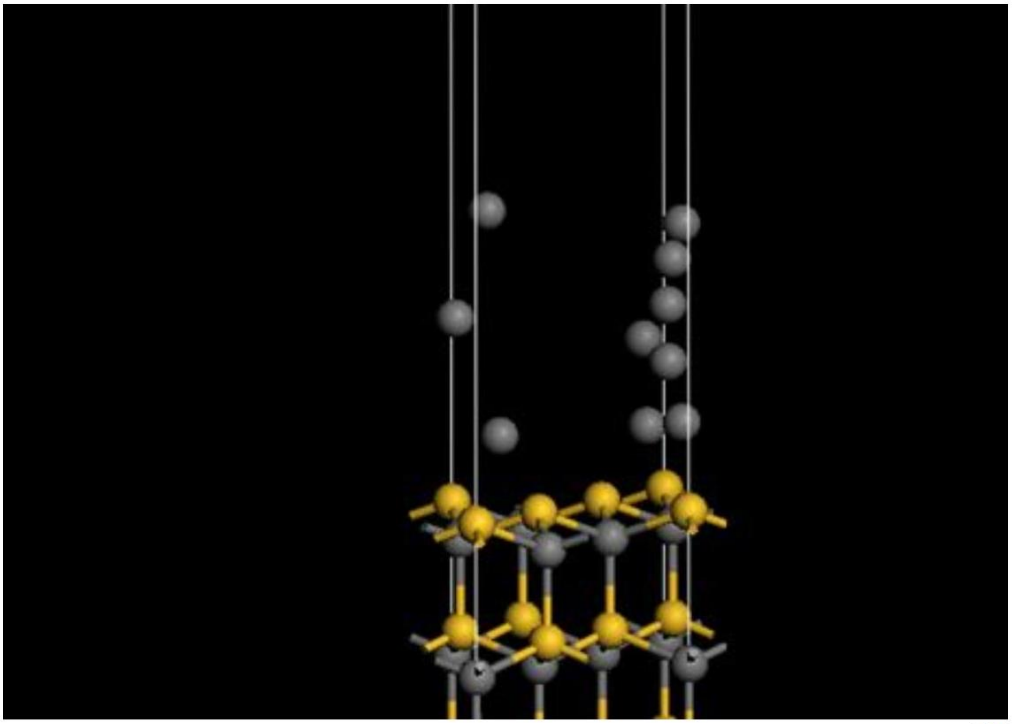

RE

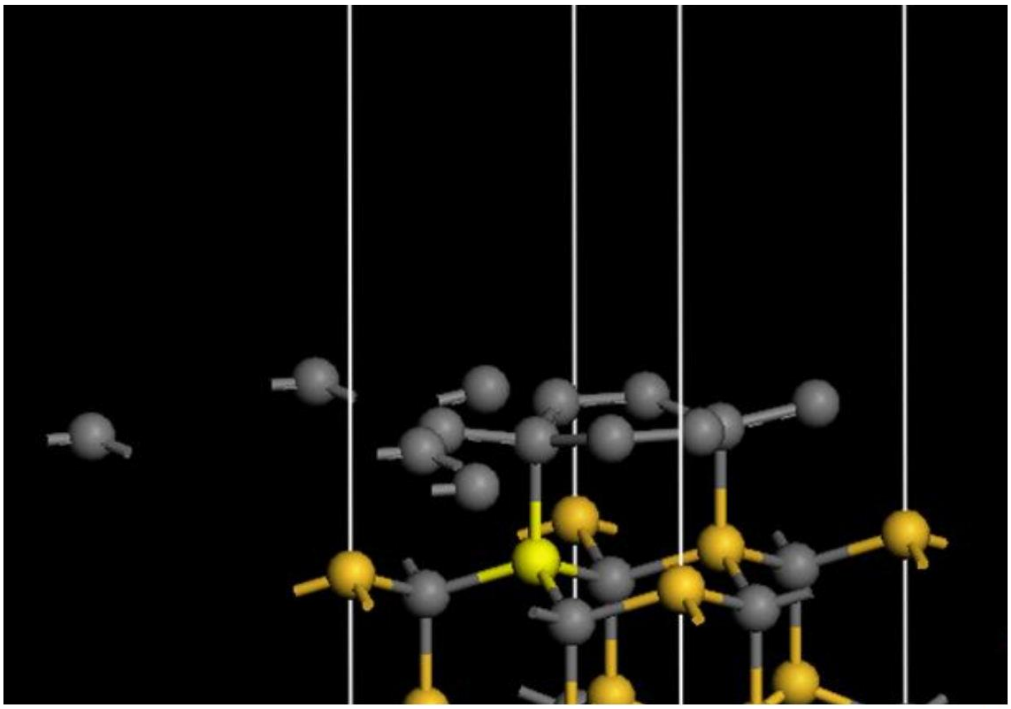

PR

Figure *S* 45. Initial reactant (RE) and final product (PR) for the transformation of amorphous carbon into highly ordered graphene structure are placed.

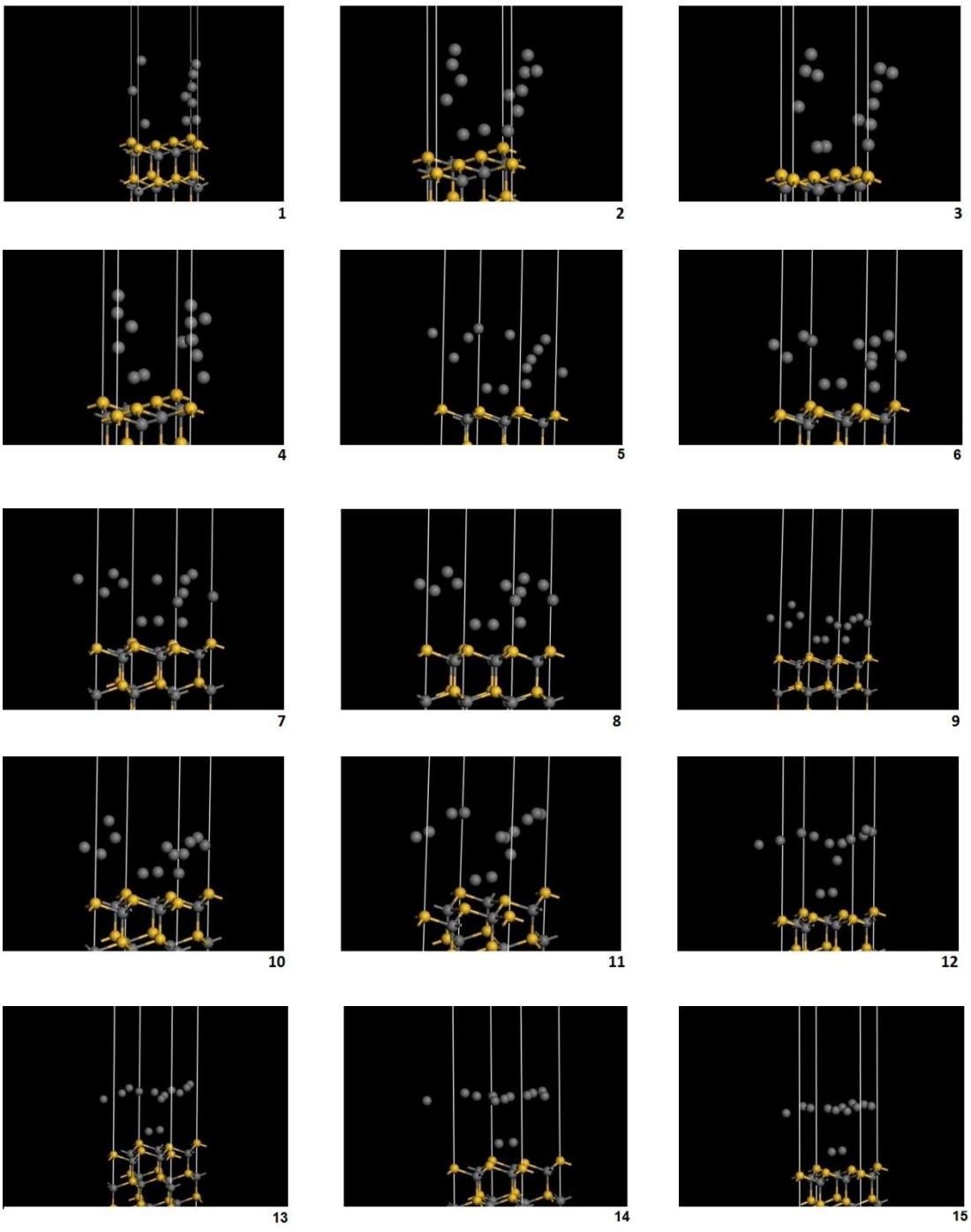
1
2
3
4
5
6
7
8
9
10
11
12
13
14
15

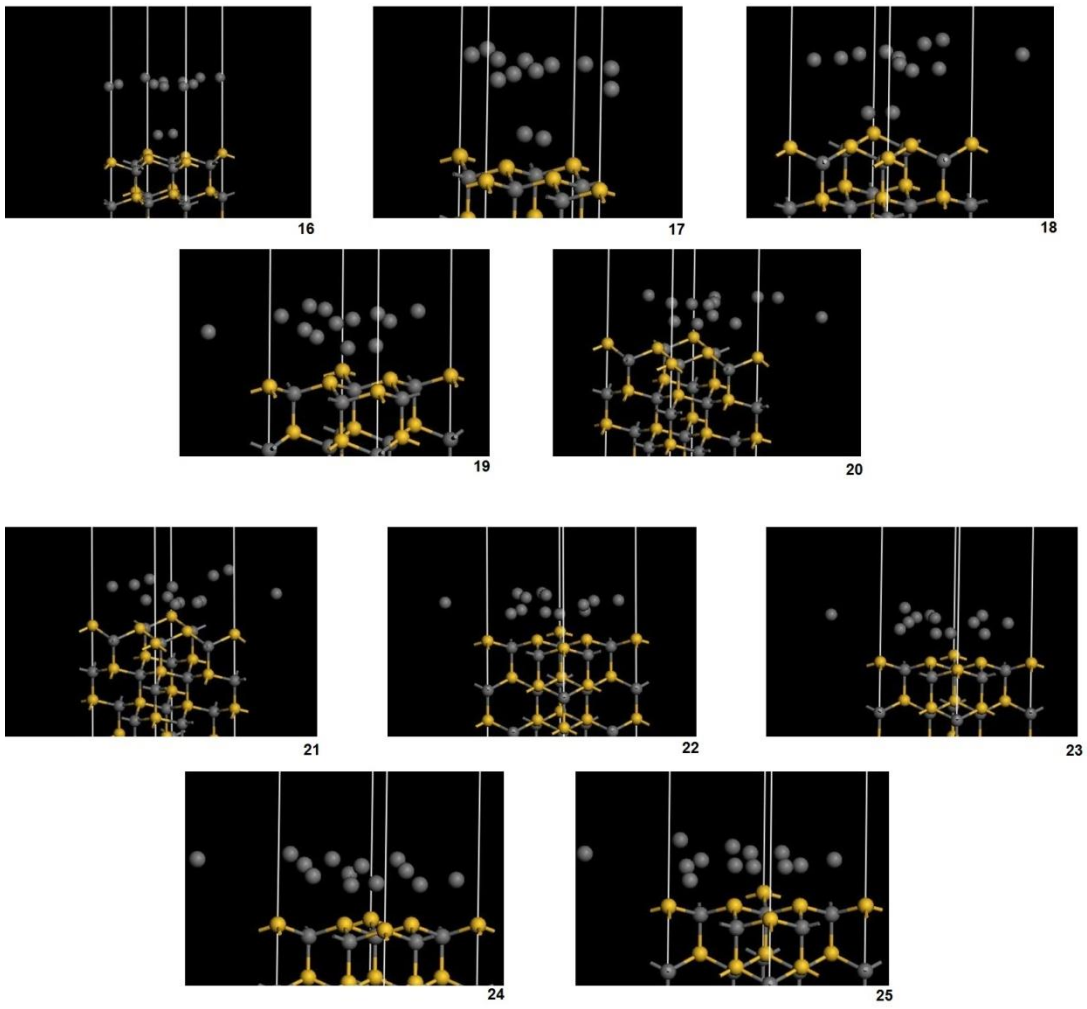

Figure *S* 46. Interim products between initial reactant and final product for the transformation of amorphous carbon into highly ordered graphene structure are placed. Number 1 corresponds to initial reactant. Number 25 corresponds to final product. Transformation of number 6 into number 7 runs spontaneously.

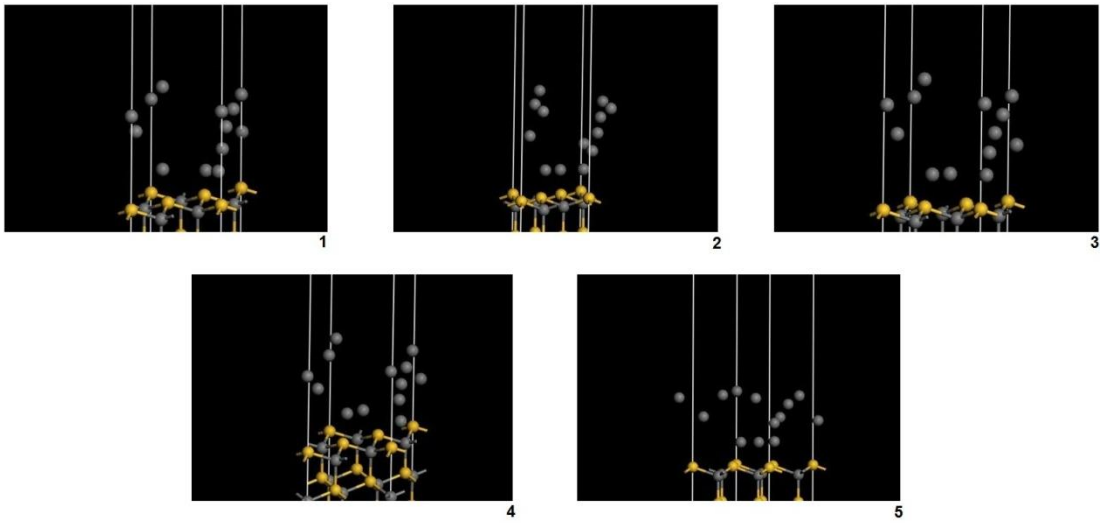
1
2
3
4
5
7
8
9
10
11
12
13
14
15

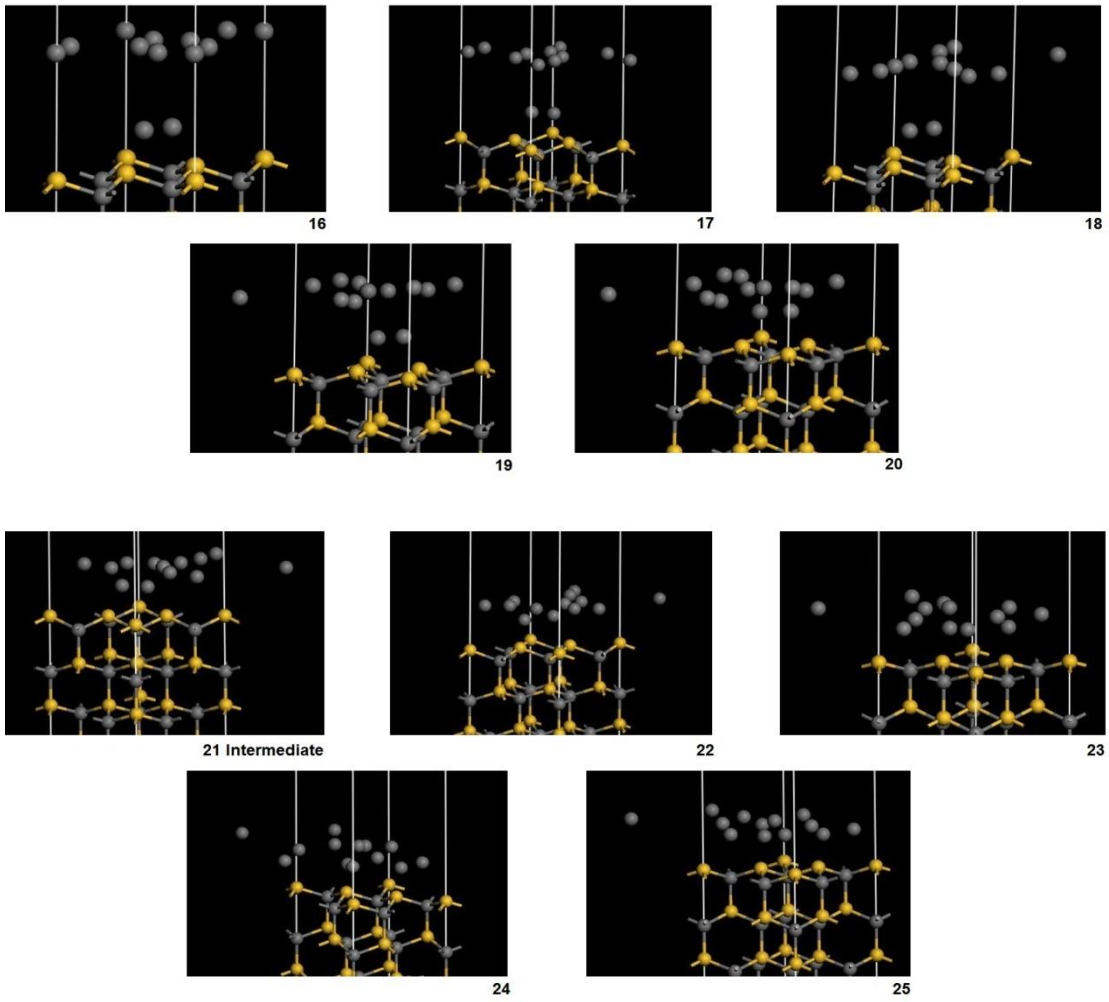

Figure *S* 47. Transition States between initial reactant and final product for the transformation of amorphous carbon into highly ordered graphene structure are placed. There is no 6th Transition State, because the reaction runs spontaneously. There is an intermediate product instead of 21st Transition State.

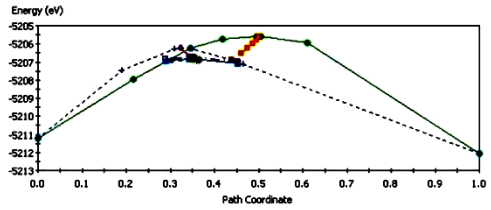

1

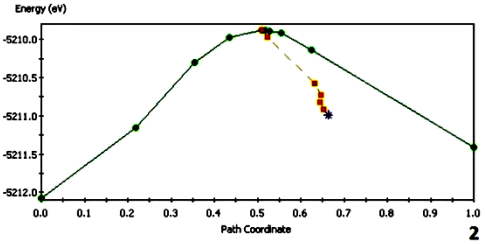

2

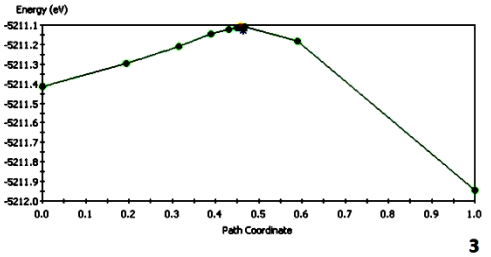

3

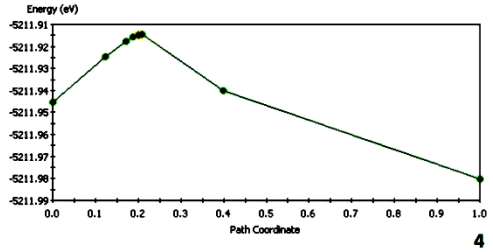

4

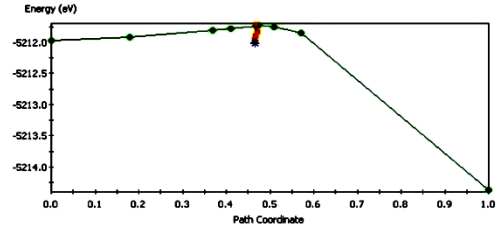

5

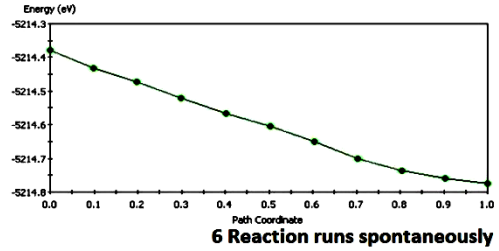

6 Reaction runs spontaneously

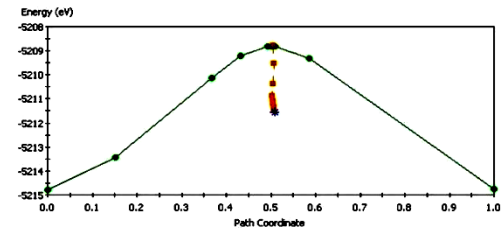

7

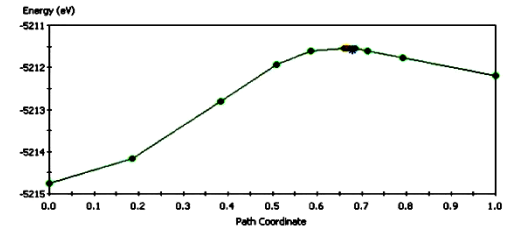

8

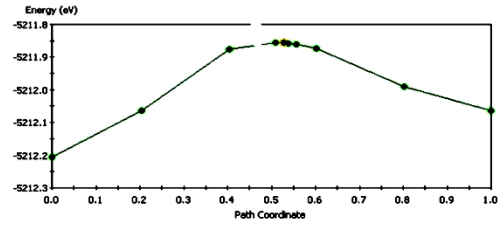

9

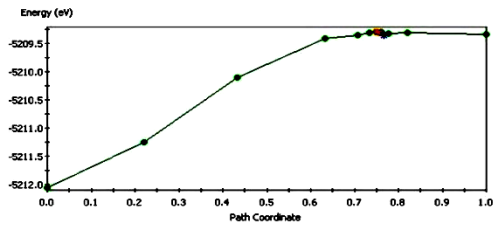

10

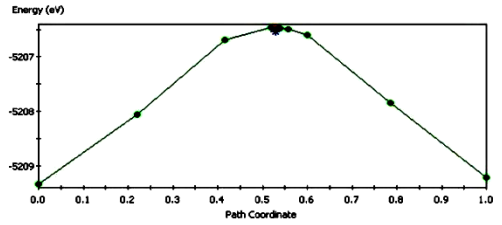

11

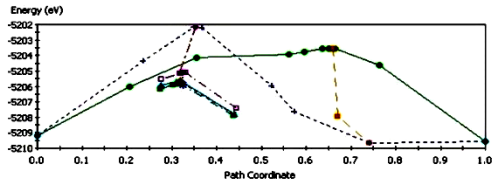

12

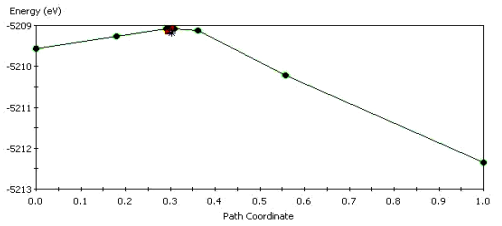

13

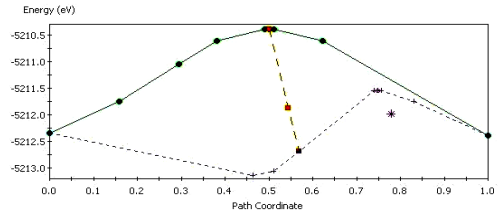

14

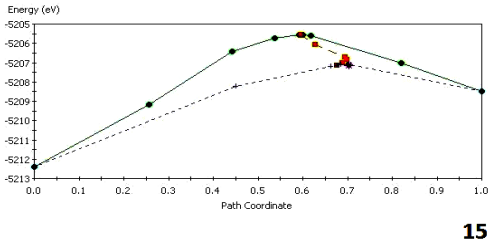

15

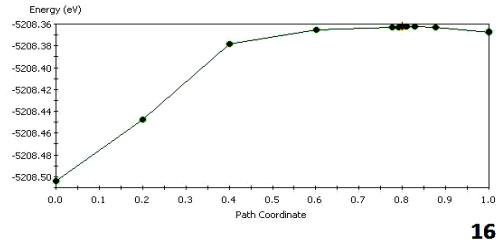

16

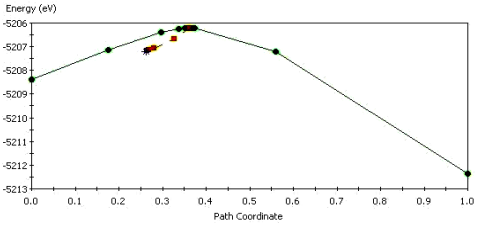

17

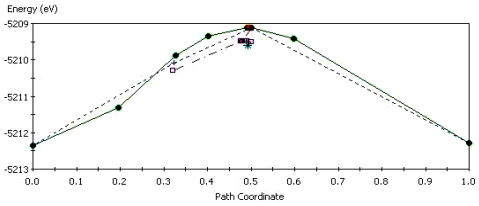

18

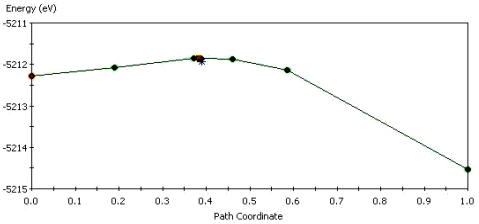

19

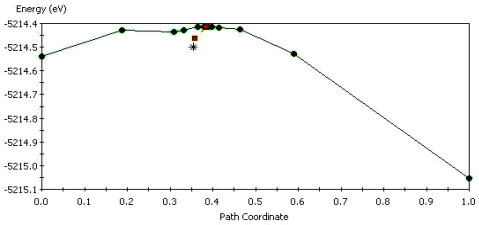

20

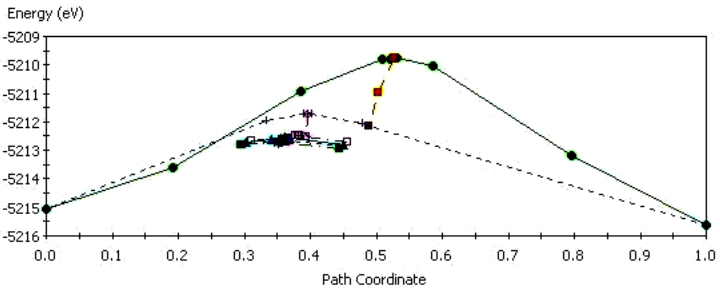

21 Intermediate

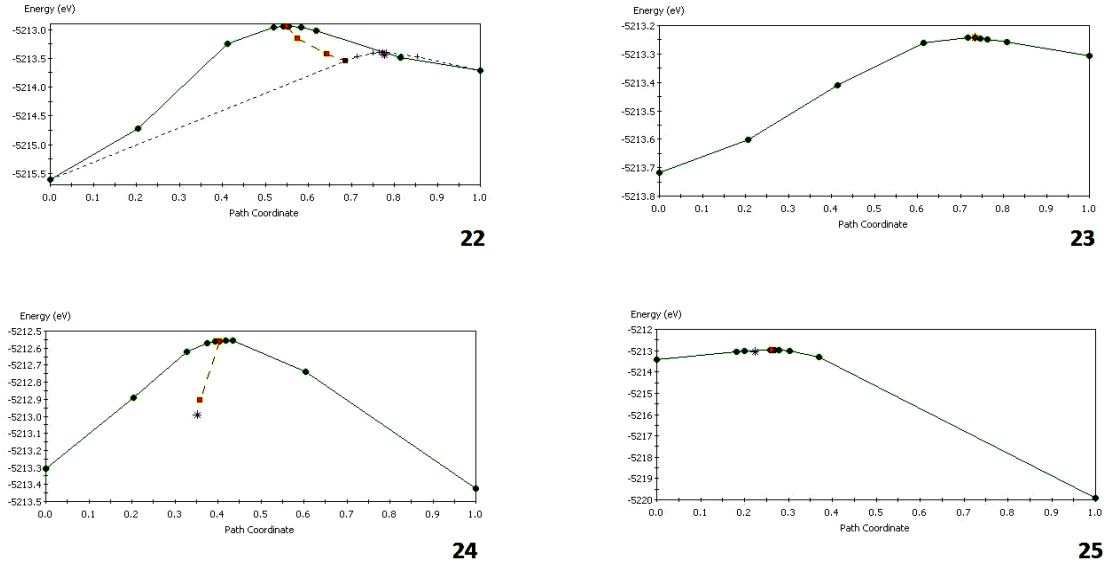

Figure *S* 48. Transition State diagrams for the transformation of amorphous carbon into highly ordered graphene structure are placed. There is no 6th Transition State, because the reaction runs spontaneously. There is no 21st Transition State, because it is intermediate product. The gradual Transition States for amorphous carbon transferring into highly ordered graphene structure are shown. Two stages are revealed at different energy levels. The first stage protracted from the beginning to the 20th step runs through the variable interim products towards the low Transition State and activation barrier (20th step). As a result, the process proves to be "suspended" around the 21st step. After interruption the second stage is restored. The new reconstruction under local endothermic effect and high activation barrier (22nd step) is advanced towards the decreasing energy of reaction and barrier from product values.

Appendix II

This supporting information contains the supplementary materials organised in a tabular form

Method	Crystallite size (μm)	Sample size (nm)	Charge carrier mobility (at ambient temperature)	Applications
Mechanical exfoliation	> 1000	> 1	> 200000 and at low temperature > 1000000	Research
Chemical exfoliation	< 0.1	Infinite as a layer of overlapping flakes	100 (for a layer of overlapping flakes)	Coatings, paint/ink, composites, transparent conductive layers, energy storage, bioapplications
Chemical exfoliation via graphene oxide	about 100	Infinite as a layer of overlapping flakes	1 (for a layer of overlapping flakes)	Coatings, paint/ink, composites, transparent conductive layers, energy storage, bioapplications
CVD	1000	about 1000	10000	Photonics, nanoelectronics, transparent conductive layers, sensors, bioapplications
SiC	50	100	10000	High-frequency transistors and other electronic devices

Table 1. Properties and applications of graphene obtained by different methods are placed (Novoselov et al., 2012).

Number of Step	Energy of Reactant	Energy of Product	Energy of Reaction	Energy of TS	Barrier from Reactant	Barrier from Product	Location of TS
			SiF group				
1_1	-7029.544	-7034.008	-4.463	-7029.578	-0.034	4.429	0.175
2_1	-7694.754	-7699.396	-4.642	-7694.127	0.627	5.269	0.248
3_1	-8359.94	-8359.566	0.374	-8358.729	1.211	0.837	0.608
			SiF_2 group				
4_1	-9025.081	-9019.44	5.641	-9016.971	8.11	2.469	0.826
5_1	-9681.843	-9674.093	7.749	-9672.308	9.535	1.785	0.688
6_1	-10340.24	-10328.94	11.295	-10328.02	12.215	0.919	0.773
			SiF_3 group				
7_1	-10995.04	-10987.88	7.155	-10984.97	10.073	2.917	0.815
7_2	-10987.89	-10988.37	-0.483	-10981.88	6.006	6.488	0.396
7_3	-10988.37	-10986.91	1.458	-10978.51	9.862	8.404	0.357
7_4	-10986.91	-10988	-1.09	-10985.29	1.616	2.706	0.319
7_5	-10988	-10988.17	-0.17	-10987.24	0.758	0.928	0.684
8_1	-11654.53	-11647.34	7.189	-11644.32	10.206	3.017	0.474
9_1	-12313.16	-12306.34	6.816	-12305.18	7.983	1.167	0.895
9_2	-12306.34	-12300.84	5.506	-12278.03	28.319	22.813	0.56
			SiF_4 group				
10_1	-12966.92	-12960	6.92	-12956.68	10.239	3.319	0.656
11_1	-10878.77	-10879.13	-0.354	-10876.07	2.701	3.055	0.379
11_2	-10879.13	-10875.72	3.409	-10875.39	3.735	0.326	0.785
12_1	-8790.713	-8792.612	-1.899	-8789.31	1.403	3.302	0.572
12_2	-8792.613	-8791.189	1.424	-8790.704	1.909	0.485	0.651

Table 2. Energy values found for the successive SiF_x formations on the 1st *SiC* bi-layer while destruction of the (0001) - $\left(\sqrt{3} \times \sqrt{3}\right)R30°$ unit cell under the *Si – F* interaction.

Number of Step	Energy of Reactant	Energy of Product	Energy of Reaction	Energy of TS	Barrier from Reactant	Barrier from Product	Location of TS
SiF group							
13_1	-6695.107	-6696.526	-1.419	-6694.721	0.386	1.804	0.274
14_1	-7357.595	-7360.857	-3.262	-7356.416	1.18	4.441	0.49
15_1	-8022.36	-8018.435	3.925	-8016.298	6.062	2.137	0.473
SiF_2 group							
16_1	-8684.256	-8684.233	0.023	-8684.237	0.019	-0.004	0.415
16_2	-8684.233	-8682.253	1.98	-8681.778	2.456	0.475	0.522
16_3	-8682.254	-8683.142	-0.889	-8681.077	1.177	2.066	0.503
16_4	-8683.143	-8681.542	1.601	-8677.345	5.798	4.197	0.558
17_1	-9343.285	-9343.817	-0.532	-9342.221	1.064	1.596	0.717
17_2	-9343.818	-9340.307	3.511	-9339.436	4.381	0.871	0.744
17_3	-9340.307	-9342.069	-1.762	-9337.423	2.884	4.646	0.484
17_4	-9342.069	-9341.565	0.505	-9338.118	3.952	3.447	0.487
17_5	-9341.564	-9338.001	3.563	-9337.143	4.421	0.857	0.693
17_6	-9338.001	-9339.516	-1.516	-9337.172	0.829	2.344	0.348
18_1	-10001.13	-10000.98	0.149	-9999.729	1.402	1.253	0.726
18_2	-10000.98	-9995.882	5.1	-9991.859	9.123	4.023	0.657
SiF_3 group							
19_1	-10657.43	-10658.21	-0.778	-10654.25	3.175	3.953	0.244
19_2	-10658.21	-10656.51	1.699	-10656.39	1.819	0.12	0.821
19_3	-10656.51	-10654.58	1.924	-10650.46	6.044	4.12	0.675
20_1	-11316.81	-11318.54	-1.73	-11315.68	1.122	2.852	0.599
21_1	-11980.7	-11981.08	-0.381	-11980.49	0.205	0.586	0.452
21_2	-11981.08	-11971.22	9.856	-11968.6	12.482	2.627	0.646
SiF_4 group							
22_1	-12633.03	-12633.5	-0.471	-12627.78	5.243	5.714	0.481
23_1	-10552.44	-10548.84	3.602	-10546.74	5.708	2.106	0.405
24_1	-8461.108	-8458.514	2.594	-8455.845	5.263	2.669	0.389

Table 3. Energy values found for the successive SiF_x formations on the 2nd *SiC* bi-layer while destruction of the (0001) - $\left(\sqrt{3}\times\sqrt{3}\right)R30°$ unit cell under the *Si – F* interaction.

Number of Step	Energy of Reactant	Energy of Product	Energy of Reaction	Energy of TS	Barrier from Reactant	Barrier from Product	Location of TS
			SiF group				
25_1	-6365.835	-6368.301	-2.467	-6365.769	0.066	2.533	0.247
26_1	-7028.657	-7027.009	1.648	-7028.712	-0.056	-1.703	0.304
27_1	-7687.252	-7686.941	0.311	-7687.216	0.036	-0.275	0.443
			SiF_2 group				
28_1	-8347.366	-8343.215	4.152	-8347.364	0.002	-4.15	0.214
29_1	-9004.051	-9006.231	-2.18	-9004.073	-0.022	2.159	0.684
29_2	-9006.231	-9004.659	1.573	-9003.94	2.291	0.719	0.718
29_3	-9004.659	-8999.294	5.365	-8996.978	7.681	2.316	0.683
30_1	-9659.99	-9658.621	1.369	-9655.561	4.43	3.061	0.266
			SiF_3 group				
31_1	-10319.03	-10315.46	3.573	-10318.78	0.257	-3.317	0.215
32_1	-10975.91	-10967.63	8.286	-10975.93	-0.022	-8.308	0.301
33_1	-11628.99	-11624.3	4.688	-11618.66	10.323	5.635	0.852
			SiF_4 group				
34_1	-12285.9	-12273.76	12.139	-12285.79	0.106	-12.033	0.184
35_1	-10205.52	-10209.27	-3.75	-10205.65	-0.129	3.621	0.314
35_2	-10209.27	-10207.05	2.217	-10205.62	3.654	1.437	0.573
36_1	-8122.015	-8125.188	-3.174	-8116.904	5.11	8.284	0.176

Table 4. Energy values found for the successive SiF_x formations on the 3rd *SiC* bi-layer while destruction of the (0001) - $\left(\sqrt{3}\times\sqrt{3}\right)R30°$ unit cell under the *Si – F* interaction.

Indexes	SiF group	SiF_2 group	SiF_3 group	SiF_4 group	Total
1st bilayer					
BR	1.80	29.86	74.82	19.99	126.47
BP	10.54	5.17	48.44	10.49	74.64
ER	-8.73	24.69	26.38	9.50	51.84
2nd bilayer					
BR	7.63	37.51	24.85	16.21	86.20
BP	8.38	25.77	14.26	10.49	58.90
ER	-0.76	11.73	10.59	5.73	27.29
3rd bilayer					
BR	0.05	14.38	10.56	8.74	33.73
BP	0.56	4.11	-6.00	1.31	-0.02
ER	-0.51	10.28	16.55	7.43	33.75

Table 5. Total BR, BP and ER values for the 1st, 2nd and 3rd *SiC* bi-layers are shown.

Temperature (K)	300	800	1300	1800	2300
Pair 1 *SiF* BL 1	25.58	9.59	5.9	4.26	3.34
Pair 2 *SiF* BL 1	22.56	8.46	5.21	3.76	2.94
Pair 3 *SiF* BL 1	48.15	18.06	11.11	8.03	6.28
Pair 1 SiF_4 BL 3	9.081	3.41	2.096	1.51	1.18
Pair 2 SiF_4 BL 3	202.7	76	46.77	33.78	26.43

Table 6. Dependence for the logarithm of rate constants ratio on temperature: 1st, 2nd and 3rd pairs for the *SiF* group of first *SiC* bi-layer; 1st and 2nd pairs for the SiF_4 group of third *SiC* bi-layer.

Number of Step	Energy of Reactant	Energy of Product	Energy of Reaction	Energy of TS	Barrier from Reactant	Barrier from Product	Location of TS
1	-5211.234	-5212.079	-0.845	-5206.868	4.366	5.211	0.359
2	-5212.08	-5211.415	0.664	-5210.992	1.087	0.423	0.664
3	-5211.416	-5211.945	-0.529	-5211.127	0.289	0.817	0.464
4	-5211.945	-5211.98	-0.035	-5211.915	0.03	0.065	0.2
5	-5211.98	-5214.379	-2.4	-5212.009	-0.03	2.37	0.465
6	-5214.379	-5214.775	-0.396	This reaction runs spontaneously			
7	-5214.775	-5214.765	0.009	-5211.567	3.208	3.199	0.508
8	-5214.765	-5212.207	2.558	-5211.58	3.186	0.628	0.678
9	-5212.208	-5212.063	0.144	-5211.857	0.35	0.206	0.527
10	-5212.063	-5209.339	2.724	-5209.35	2.714	-0.011	0.767
11	-5209.339	-5209.214	0.125	-5206.531	2.808	2.683	0.53
12	-5209.214	-5209.559	-0.345	-5205.894	3.32	3.665	0.324

Table 7. Energy values for the transformation of amorphous carbon into highly ordered graphene structure (steps 1 – 12) are shown.

Number of Step	Energy of Reactant	Energy of Product	Energy of Reaction	Energy of TS	Barrier from Reactant	Barrier from Product	Location of TS
13	-5209.559	-5212.344	-2.785	-5209.18	0.379	3.164	0.304
14	-5212.344	-5212.397	-0.053	-5211.987	0.357	0.41	0.78
15	-5212.396	-5208.504	3.892	-5207.156	5.24	1.347	0.703
16	-5208.504	-5208.367	0.137	-5208.363	0.142	0.004	0.8
17	-5208.368	-5212.363	-3.995	-5207.195	1.173	5.168	0.263
18	-5212.363	-5212.273	0.09	-5209.59	2.773	2.683	0.494
19	-5212.274	-5214.537	-2.264	-5211.938	0.336	2.6	0.391
20	-5214.538	-5215.054	-0.517	-5214.501	0.037	0.554	0.355
21	-5215.055	-5215.608	-0.553	This is intermediate of reaction			
22	-5215.608	-5213.719	1.889	-5213.439	2.168	0.28	0.777
23	-5213.719	-5213.307	0.412	-5213.244	0.475	0.063	0.735
24	-5213.307	-5213.423	-0.116	-5212.995	0.312	0.428	0.353
25	-5213.423	-5219.913	-6.49	-5213.063	0.36	6.85	0.224

Table 8. Energy values for the transformation of amorphous carbon into highly ordered graphene structure (steps 13 – 25) are shown. The energy value of intermediate product for the 21st step is -5212.732 eV.